Scott A. Lipson

MDCT and 3D Workstations

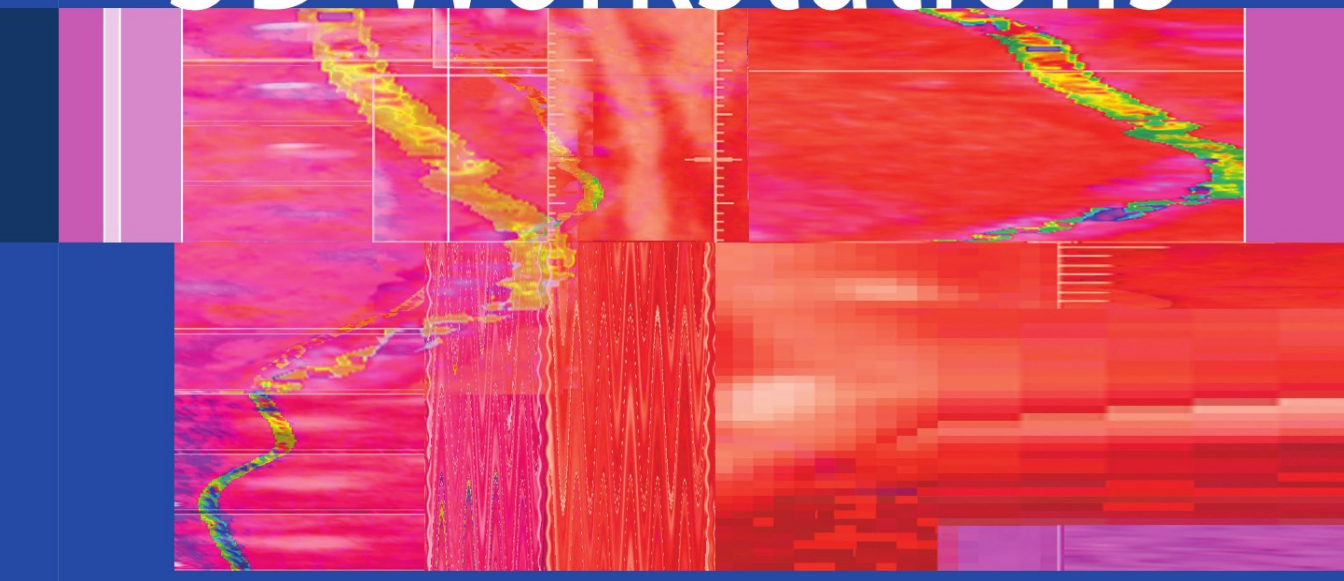

A Practical Guide and Teaching File

Springer

MDCT and 3D Workstations

Scott A. Lipson, MD
Associate Director of Imaging, Long Beach Memorial Medical Center, Long Beach, California

MDCT and 3D Workstations

A Practical How-To Guide and Teaching File

With 101 Figures in 379 Parts, 175 in Full Color

Springer

Scott A. Lipson, MD
Associate Director of Imaging
Long Beach Memorial Medical Center
Long Beach, CA 90806

Library of Congress Control Number: 2005924372

ISBN 10: 0-387-25679-2
ISBN 13: 978-0387-25679-5

Printed on acid-free paper.

Printed in China. (BS/EVB)

9 8 7 6 5 4 3 2 1

springeronline.com

To Nancy and Shelly and the memory of my father, Sheldon, who has been a constant source of inspiration throughout my life

Preface

Multidetector CT (MDCT) is much more than an incremental improvement over the previous technology. When compared with computed tomography (CT) imaging performed just 4 or 5 years ago, it is essentially a new modality. MDCT has significantly changed how I practice radiology and has reinvigorated my love for imaging. The images produced are not only clinically diagnostic, but they have an aesthetic beauty that is both accessible and enticing to radiologists, clinicians, and even patients.

The purpose of writing this book is twofold. The first section brings together into one source all the practical information needed to successfully set up a MDCT practice, operate the scanners and 3D workstations, manage workflow, and consistently produce high-quality diagnostic images.

The second section is a teaching file of volumetric cases. This is not intended to be a comprehensive collection of teaching material, but rather a showcase for the varied capabilities of current scanners and workstations. Each case is selected to demonstrate how the technology can improve the process of making a clinical diagnosis and then effectively relaying this information to other physicians in a format that is easy to understand.

I hope that readers of this book will not only get a better understanding of MDCT and 3D workstations, but also a better appreciation of the art of radiology expressed by the images.

Scott A. Lipson, MD

Acknowledgments

I owe a debt of gratitude to Chris Gordon and her team of excellent CT technologists at Long Beach Memorial Medical Center. Without their hard work, dedication, and friendship, this book would not have been possible. I want to acknowledge the invaluable contribution of Dr. John Renner, the director of radiology at Long Beach Memorial. It was his vision that enabled Long Beach Memorial to be one of the very first hospitals in the United States to own and operate a 16-detector multi-detector CT (MDCT). I also thank the administration at Long Beach, particularly Richard Decarlo and Terry Ashby for their support of this project. I am also indebted to my friends and collaborators from Toshiba America Medical Systems: Mike MacLeod, Bryan Westerman, Doug Ryan, and Jeff Hall, and from Vital Images, Vikas Narula. They have assisted and supported me over the years and have all contributed their expertise to this book in different ways. Finally, I would like to thank the following radiologists who contributed images or case discussions used in this book: Dr. Ruben Sebben, Dr. Hirofumi Anno, Dr. Albert de Roos, Dr. Stanley Laucks, Jr., and Dr. Alisa Watanabe.

Contents

Part I

How-to Guide to MDCT and 3D Workstations

Chapter 1

Introduction

Just a few years ago three-dimensional (3D) imaging with computed tomography (CT) was a tool used primarily at a few select academic centers, often by specially trained technologists working in a dedicated 3D imaging lab. This situation has changed rapidly, however, and with the proliferation of multidetector CT (MDCT) scanners and advanced workstations, CT angiography (CTA) and volumetric imaging are now routine practice in community hospitals and imaging centers all over the world. This transition has been extremely rapid and for many radiologists quite difficult. Advances in CT and workstation technology have moved much faster than physician training and education.

The equipment needed to perform volumetric imaging is straightforward. An MDCT scanner is essential, as is a 3D workstation. The images and cases that are used in this article were primarily acquired on a 16-slice MDCT (Aquilion 16, Toshiba Medical Systems, Japan), but the concepts and principles are applicable with minor modifications to 4-slice MDCT, as well as to the new generation of 32-, 40-, and 64-slice scanners.

Acquiring the proper hardware is essential, but it is just the first step in the process. With the new equipment must also come a new philosophic approach to CT imaging. Volumetric imaging requires a paradigm shift in how radiologists acquire and review CT data. It is easy with MDCT to become overwhelmed by the amount of information that is available. Data sets now routinely number from several hundred to thousands of images. A coordinated and thoughtful approach is needed to handle this information. The goal is to provide higher quality imaging and to translate this into more accurate radiologic diagnosis and better patient care than ever before. The dilemma is how to accomplish all this without sacrificing work efficiency.

To achieve these goals, radiologists must adapt how they review and think about CT data. Axial CT images remain important, but they are just one tool among many for case review. As radiologists become more comfortable with volumetric data, they rely less on any one imaging plane or reconstruction algorithm. Radiologists can choose the most appropriate imaging plane or planes for a given examination to review

the data. Advanced picture archives and communication systems (PACS) and 3D workstations allow for volumetric image review that seamlessly integrates multiplanar data with the capability for volume rendered reconstructions and other advanced tools. The concept of slices becomes outdated.

Volumetric data sets affect not only how we review the data but the type of examinations we perform with CT and how we scan the patients. The most dramatic impact is in the area of CTA. CT angiography is rapidly replacing diagnostic catheter angiography throughout the body (and perhaps soon even in the heart). The purely diagnostic catheter angiogram may soon become a rarity, gone the way of the exploratory laparotomy. Performing and processing CTA images has become dramatically easier as workstation technology has improved. Done correctly, it is an extremely powerful and accurate tool for evaluating the vascular tree. Many of those who use CTA routinely believe that in many cases it is truly the gold standard, replacing the catheter angiogram. Having said that, I must also admit that CTA is often not as easy as it looks. It requires careful attention to detail and a full knowledge of the strengths and weakness of different reconstruction techniques. Many significant pitfalls can lead an inexperienced user to make clinically important errors.

The benefits of volumetric imaging are not limited to CTA, however. Every facet of CT imaging can be improved dramatically. For example, for musculoskeletal imaging, volumetric data sets from a single acquisition can be reconstructed in any conventional or oblique plane with no loss of resolution. Patient positioning is no longer of major importance, and the need to obtain direct coronal or sagittal scans no longer exists. Simple surface rendering techniques coupled with basic segmentation can provide a tremendous amount of information very quickly. For trauma patients, this has been an amazing revolution. With a single data acquisition, multiple examinations can be rapidly generated and interpreted.

The goal of this book is to help guide radiologists, students, and technologists through the often complex and difficult areas of CT data acquisition, protocols, image reconstruction and review, and efficient workflow. Descriptions of how to effectively use 3D workstations to interpret and process images are also given, and practical examples for different types of cases are provided. The teaching file is designed to show interesting cases that illustrate how the technology can be used on a daily basis to improve diagnosis, patient care, and communication among radiologists, referring doctors, and patients.

Chapter 2

MDCT Data Acquisition

Volumetric imaging requires routine acquisition of high-resolution data sets. The principles apply not just to cases such as CTA, but can be used for virtually every study performed. One major difference between single-slice CT and MDCT is a fundamental separation between how data are acquired and how they are reviewed. With single-slice CT there is frequently little difference between the slice thickness images are acquired at and the thickness in which they are reviewed. Volumetric MDCT depends on acquiring very thin section data sets that are used to generate thicker axial slices as well as multiplanar and volume images. Review of the very thin section axial images is less efficient and usually unnecessary, but the information remains available for those instances where it is needed.

The goal of volumetric imaging with MDCT should be to acquire data sets with isotropic (or near-isotropic) voxels whenever possible. An isotropic voxel is a cube, measuring the same in the x, y, and z planes. A typical single-slice voxel has a dimension much longer in the z-axis than the x- or y-axis. This leads to adequate resolution in the plane of acquisition (usually axial) but poor-quality images for multiplanar reconstructions (MPRs) and 3D reconstructions. Isotropic voxels allow for true 3D imaging. No matter how the data set is projected, there is no significant loss in resolution.

The size of the field of view (FOV) affects voxel size and, therefore, spatial resolution. With a standard CT imaging matrix of 512×512 pixels and a FOV of 25 cm, the pixel size in the x and y dimensions is approximately 0.5 mm (Figure 2.1). Therefore, to achieve an isotropic voxel the z-axis resolution would need to be 0.5 mm also. With a larger FOV such as 50 cm, the in-plane pixel size increases to 1.0 mm and an isotropic voxel would only require 1-mm slice thickness. This fact can be incorporated into protocol design. The FOV chosen should always be as small as possible to accommodate the anatomy of interest. Corresponding slice thickness should also be used to maximize resolution, given limitations in anatomic coverage needed or scan duration.

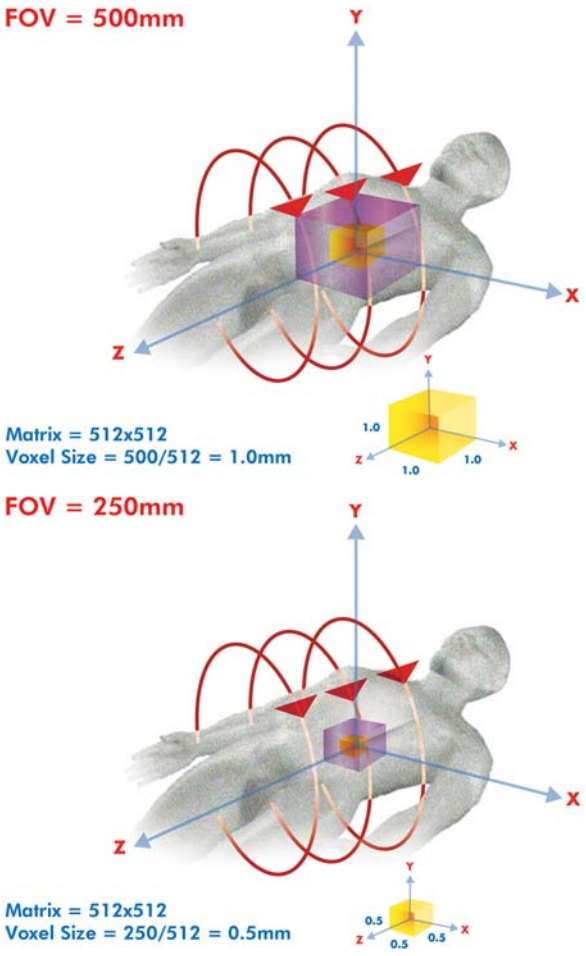

Figure 2.1. Isotropic voxels at two different fields of view (FOV). With a large FOV (50 cm) and a 512 × 512 matrix, isotropic voxels are achieved with 1-mm slice thickness. With a smaller FOV (25 cm), 0.5-mm slice thickness is needed to achieve isotropic voxels.

MDCT Scan Protocols

Multidetector CT scanners offer a dizzying number of protocol options. Some of the major scan acquisition variables that the user must consider include scan mode (sequence vs. helical), slice number and thickness, helical pitch, FOV, rotation time, radiation dose parameters, and coverage needed (scan length). Once the data have been acquired, there are an equally large number of variables to consider in how the data are reconstructed and presented for viewing. These variables, such as reconstruction thickness and algorithm, and multiplanar reconstructions, are discussed separately. It is important to remember with MDCT that there is a fundamental difference in how the images are acquired and how they are viewed.

Scan Mode

Helical scanning is preferred for almost all cases and is essential for volumetric imaging. Sequence scanning can have a small role. Some sites prefer to scan the brain in sequence rather than helical mode. Traditionally, this has produced sharper images with fewer artifacts; however, with current MDCT scanners, equal or superior images can be obtained in helical mode in most cases. This will be variable, depending on the scanner and the individual radiologist's preferences. I suggest that each site individually evaluate brain scans done in sequence and helical mode and choose the method that produces the best quality images. In cases in which image quality is similar, I strongly recommend helical scanning because of the increased flexibility this allows for volumetric imaging. Other types of scans that may have been performed with sequence scanning in the past such as spine examinations, should all be performed helically with MDCT scanners.

The other major use for sequence scanning is for coronary calcium scoring when performed in conjunction with prospective gating. This is discussed further later in this chapter (see Cardiac Gating).

Slice Thickness

Multidetector CT scanners have a limited, fixed number of slice-thickness options to choose from when operating in full helical mode. Most 16-slice scanners offer two slice options: 0.5 mm to 0.75 mm for the highest *z*-axis resolution, or 1.0 mm to 1.5 mm for faster table speeds at lower resolution (Figure 2.2). Some scanners also offer an even faster, lower *z*-axis resolution setting which is used predominately to obtain very fast scans in acutely ill or uncooperative patients. Four-slice scanners also can be operated in a higher-resolution mode (0.5 mm–1.25 mm) or a faster mode to increase coverage (2 mm–2.5 mm). Eight-slice scanners have options somewhere in between those of 4- and 16-slice scanners. The newer 32- and 40-slice scanners are similar to 16-detector scanners and can obtain 32 images at a very high or slightly lower resolution. The 64-detector scanners have only one slice-thickness option in 64-detector mode; however, if thicker images are desired, they can also be operated in 32-detector mode.

As a general rule, protocol design should incorporate the highest resolution setting that will provide the coverage needed in an acceptable time frame (breath hold or contrast media injection duration).

The FOV should also be considered. There is little reason to use 0.5-mm slice thickness on an abdominal CT in an obese patient with a 50-cm FOV. As a general rule, studies done with small FOV and/or small anatomic coverage should be done at the highest resolution setting available on the scanner. This would include examinations such as head, sinus or facial bones, neck, and most musculoskeletal cases. Body examinations including the chest, abdomen, and pelvis can be done with either high- or medium-resolution slice thickness depending on patient factors such as size, ability to hold breath, and length of anatomic coverage needed. Most routine body examinations are performed with 1.0- to 1.5-mm slice thickness. Submillimeter slice-

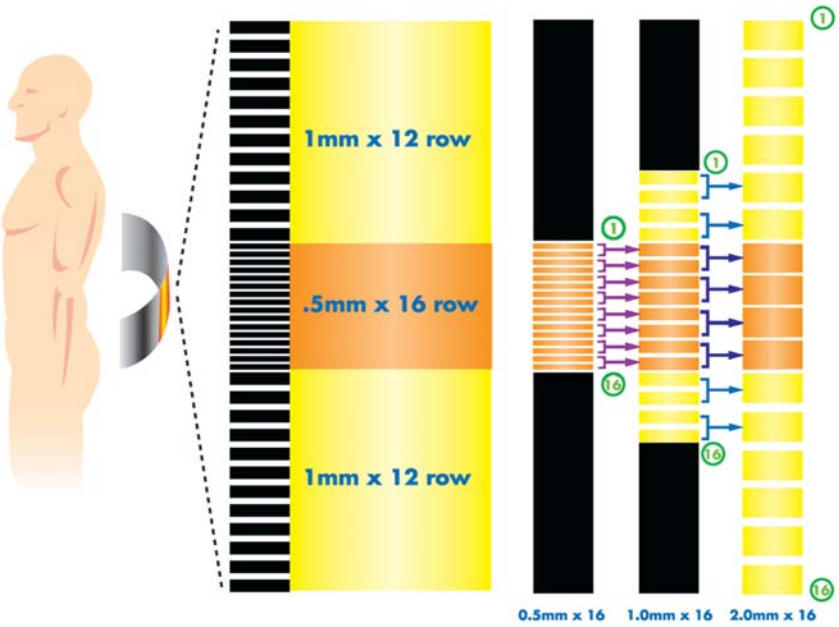

Figure 2.2. Sample detector for a 16-detector array scanner. The detector has 16 central 0.5-mm elements surrounded by 12 1-mm elements on each side for a total length of 32 mm. Sixteen data-acquisition channels are connected to the detector. By using detector elements alone or by combining elements together, different slice thickness options are available as shown.

thickness protocols can be reserved for smaller patients or specific examination types such as lung nodule detection or high-resolution pancreas imaging. One obvious benefit of 32- to 64-detector scanners is that all studies can be performed with slice thickness of 0.5 mm to 0.625 mm, depending on the scanner.

When designing a protocol, it is also important to consider the purpose of the examination. Examinations intended for 3D imaging, such as CTA or orthopedic cases, should be performed using the highest resolution setting whenever possible. Since there are many instances where a different slice thickness may be selected for the same type of examination, it is often beneficial to have two protocols available: a high-resolution protocol for optimal isotropic volumetric imaging and a faster, lower-resolution protocol to maximize coverage and shorten examination time. This classic trade-off between resolution and speed is still an important issue in the MDCT era, particularly with 4- and 8-slice scanners. For 16-slice scanners, this trade-off is clinically important only for a few examinations, such as aortogram with runoff, or gated cardiac or aorta CTA. As the number of slices available increases over 16, this issue becomes largely unimportant.

High-resolution imaging does come with a few downsides. In addition to longer scan times, there are radiation and signal-to-noise issues to consider. Thin slice scans do subject patients to higher radiation doses because of the overlapping penumbra of the x-ray beam. This

effect is significant with 4-slice scanners but is minimal with scanners with 16 or more detectors. High-resolution images are also grainier, with lower signal-to-noise ratios. This can be quite noticeable when looking at the thinnest slice source images, but is usually not significant when looking at thicker axial or multiplanar image reconstructions and volumes, except in very large patients.

Helical Pitch

Helical pitch for MDCT scanners has been defined in two different ways: detector pitch and beam pitch. Detector pitch is the less commonly used method and is defined as table movement (mm) per rotation/the selected slice thickness of the detector. Beam pitch is the preferred and most commonly used method to describe helical pitch. Beam pitch can be defined as table movement (mm) per rotation/beam width. The beam width can be determined by multiplying the number of slices (detectors used) by slice thickness (mm). For example, for a 16-detector scanner at 0.5-mm slice thickness and table movement of 10 mm per rotation, Pitch = $10/(16 \times 0.5) = 1.25$.

$$\text{Beam Pitch} = \text{Table Travel (mm) per Rotation} / \text{Number of Slices (Detectors Used)} \times \text{Slice Thickness (mm)}$$

At a pitch value of 1, each detector will record data from one full rotation of the x-ray tube. At pitch values of greater than 1, there is relative undersampling of the data, with a gap between consecutive scans. Conversely, with pitch values of less than 1, there is overlap of the data acquisition.

Changing the helical pitch will affect the scan acquisition in several ways. Increasing the pitch will speed up the scan, allowing for more anatomic coverage with some penalty in image noise (related to data under-sampling) although this effect is usually small at pitch levels below 1.5. Increased pitch will also decrease radiation dose to the patient as long as the technique remains constant. Some scanners will automatically compensate for the increased noise seen with higher pitch by automatically increasing the tube current as long as it is not at maximum. There can also be some increase in helical streak (windmill) artifacts at higher pitch values. This is most detectable as streak artifacts at high contrast borders such as air–bone interfaces.

Decreasing the helical pitch will reduce anatomic coverage but can produce higher quality images by obtaining more data per rotation. This can be very useful in orthopedic imaging to obtain higher quality images, particularly when hardware is present, and for cardiac gated acquisitions where pitch values between 0.2 and 0.4 are commonly used. Cardiac gating will be discussed in a following section. Most scanners come with recommended pitch values that optimize speed and image quality. For most general examinations and CTA, a helical beam pitch between 1.2 and 1.4 is ideal. For orthopedic imaging and some neuroimaging, a pitch value of 1 or less than 1 may be used.

Dose Parameters

Much attention (appropriately so) has been focused recently on radiation dose in CT. Computed tomography is the leading source of medical radiation exposure in developed countries. Radiation dose is of particular concern in pediatric imaging but is also of high importance in adult imaging. Reducing the radiation exposure to the population related to CT scanning requires a multifaceted approach. There needs to be scrutiny of ordering practices with elimination of unnecessary examinations that offer little likelihood of clinical benefit. As MDCT proliferates, this is becoming a significant issue as overutilization becomes the norm in many practices. When a CT examination is to be performed, care must be taken to insure that the patient receives the lowest possible dose to provide a fully diagnostic study. This requires careful attention to protocol details, including slice thickness (particularly with 4-detector scanners), acquisition parameters, and number (phases) of scans done.

With MDCT, slice thickness and detector number can have an impact on radiation dose. It is impossible to collimate an x-ray beam to the exact margin of the x-ray detector; therefore, there is a tail (penumbra) of radiation on each side of the beam that represents excess radiation that does not contribute to image quality (Figure 2.3). During a helical acquisition, this penumbra will overlap and build up, increasing the dose for the entire examination. The size of this effect is closely related to slice thickness and detector number. With a 4-slice scanner and submillimeter slice thickness, a narrowly collimated x-ray beam is used, and this effect becomes significant and can even result in doubling the dose for the study. Buildup of the radiation penumbra decreases in importance as both slice thickness and detector number increase because the x-ray beam is much wider and therefore there is much less overlap. With scanners with 16 or more detectors, the overlap is small, even with 0.5-mm images.

Recognizing the importance of dose management in MDCT, CT manufacturers have focused extensive attention recently on methods to control, monitor, and reduce dose from CT examinations (independent of factors already discussed). There are two primary methods to reduce CT dose for an individual examination. The first way is for the CT technologist to individually tailor the dose parameters for each patient based on the patient's weight and the body part being imaged. This method is often quite arbitrary and may result in substantially different techniques being used for the same examination, depending on the technologist. Alternatively, multiple examination protocols can be created in the scanner for each type of examination based on the patient's size and weight with appropriate kV/mA parameters built directly into each protocol. Although this technique can be effective if the protocols are built correctly and guidelines for use are diligently followed, it is somewhat cumbersome and is easily subject to error if the technologist chooses the wrong protocol.

Recognizing the limitations of the above methods, most scanners now have some form of automatic exposure control (AEC) available.

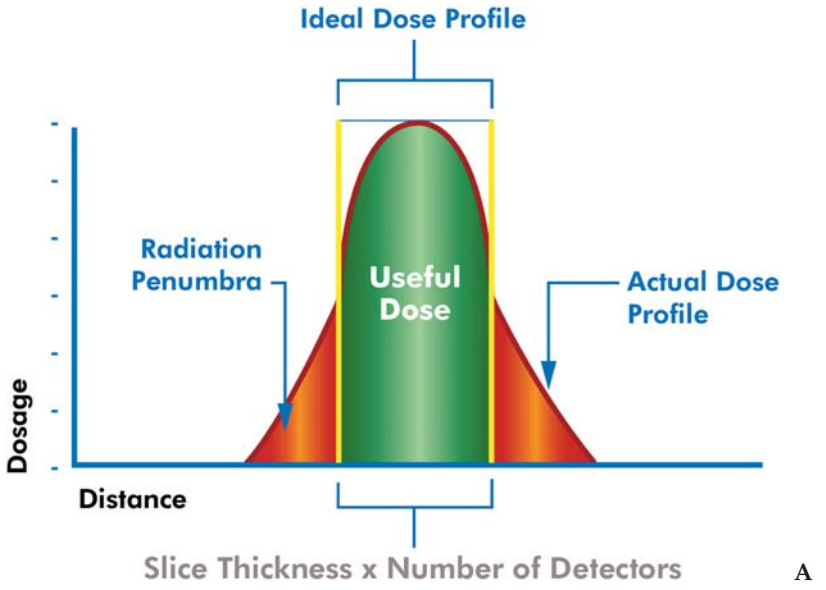

A

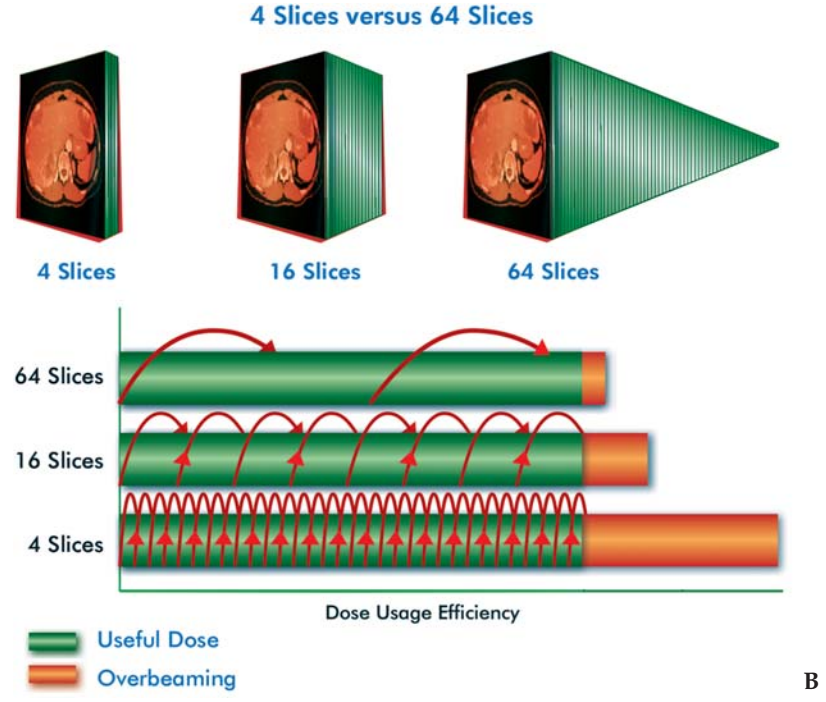

B

Figure 2.3. Radiation penumbra and dose buildup. (A) Radiation penumbra. Overbeaming occurs with each rotation of the x-ray tube. The penumbra does not contribute to image quality and will increase dose to the patient for the examination. The effective dose delivered to the desired detector elements is shown in green, with the penumbra shown in orange. (B) Graphical demonstration of the dose-buildup effect of the radiation penumbra with 4-, 16-, and 64-slice CT. Dose buildup occurs when volumes of tissue are scanned. With thin section imaging, the dose buildup is substantial with 4-slice scanners, markedly reduced with 16-slice scanners, and negligible with 64-slice scanners.

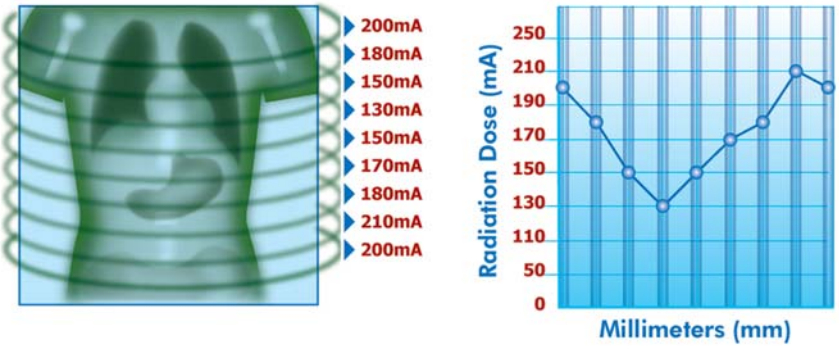

Figure 2.4. Automated exposure control: demonstration of *z*-axis dose modulation. The scout view is used to determine attenuation coefficients for each anatomical region, and the scanner modulates the mA value for different regions according to attenuation while maintaining uniform image quality throughout the volume. The graph shows the fluctuating mA values delivered during the scan.

These techniques are designed to automatically modulate the x-ray dose given to the patient depending on specific information obtained by the scanner about that patient. There are two principal methods for automatic exposure control: *z*-axis modulation and *xy*-axis modulation.

The *z*-axis modulation typically relies on attenuation measurements derived from the actual patient obtained during the scout image acquisition, to create a radiation dose profile for the examination that is individually tailored to that patient (Figure 2.4). The dose administered will actually vary dynamically during the examination depending on the attenuation of the patient's body. For example, in a chest study, the radiation dose will be much higher through the shoulders and much lower through the lungs. The most sophisticated systems now allow the operator to preselect the desired image quality based on noise levels and the scanner will then apply the appropriate tube current for the study regardless of the patient's size. This relieves the operator of the need to vary conditions based on patient size or weight.

The *x-y* tube current modulation refers to exposure control that varies during the gantry's 360-degree rotation. It is designed to change tube current in response to changes in patient shape. This technique takes advantage of the fact that most patients are significantly thinner front to back than they are side to side. Therefore, the scanner can reduce mA for the AP and PA projections of the body while increasing mA for the lateral views.

In some advanced systems, *xy*- and *z*-axis modulation are combined for the most effective automatic exposure control. The operator can still control the appearance of the final image by overriding or limiting the parameters of the scan to convert images that are very low dose but somewhat noisy to images that are high quality but higher dose.

A further variant on automatic exposure control is the ECG modulated tube current sometimes used in cardiac imaging. If images do not

need to be reconstructed at certain cardiac phases, then the tube current can be reduced to reduce patient dose. This technique is effective for calcium scoring but less practical for coronary angiography where images may need to be reconstructed at multiple cardiac phases.

Rotation Time

Along with advances in detector technology, improvements in CT gantry rotation time and tube technology have been key factors in the MDCT revolution. Improved temporal resolution has many benefits, including shorter examination times, reduced motion, peristaltic and pulsation artifacts, and better visualization of a rapid, dynamic contrast bolus. These factors have greatly improved CT for a wide variety of patients particularly for pediatrics, trauma, and critically ill people. Improved temporal resolution is also important for good-quality CTA throughout the body and essential for cardiac CTA.

Rotation times of 0.5 sec are now routine for many examinations, and many scanners have capability of rotation times of 0.4 sec or even less. Do not look for continued dramatic improvement in gantry rotation time in the future. Current scanners are approaching an absolute physical limitation of the technology. As the gantry rotation time increases, the gravitational forces (g-forces) that the x-ray tube is subjected to increase exponentially (Figure 2.5). Further significant improvements in temporal resolution will need software solutions (partial scanning,

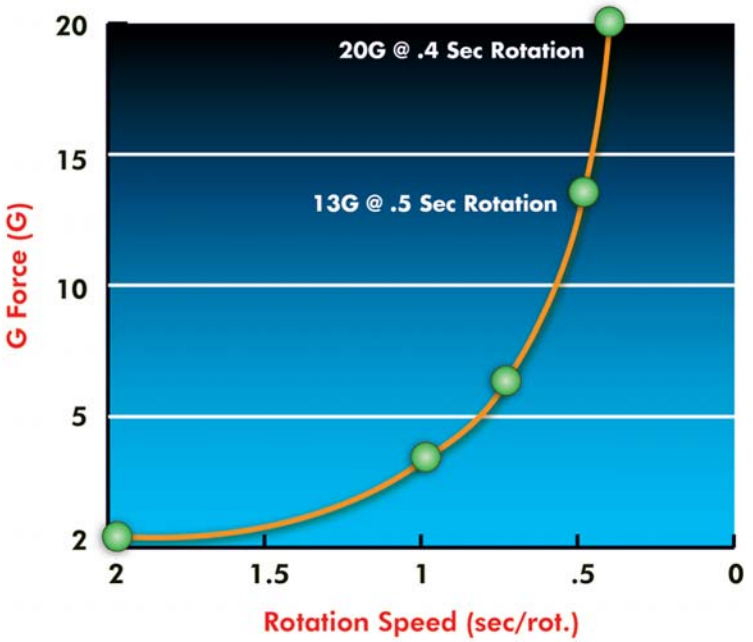

Figure 2.5. Plot of g-force against rotation time. As the rotation time decreases below 0.5 sec, there is an exponential increase in g-force applied to the x-ray tube.

adaptive segmented reconstruction—refer to the section on cardiac gating) or a dramatic change in x-ray tube and gantry design.

In addition to affecting temporal resolution, changing the rotation time also affects the radiation dose and signal-to-noise ratio of the study. Faster gantry rotation effectively reduces both radiation dose and image quality. This is often unimportant when high-contrast vessels are being imaged for CTA, but can be important when low-contrast resolution is needed. To compensate for faster rotation times, dose parameters may need to be increased. Using longer rotation times is also another way to improve image quality in large patients where technique is already maximal, or for studies that need high image quality such as musculoskeletal examinations, particularly if hardware is present.

Patients with Metal Hardware/Prostheses

Scans performed in patients with indwelling metal hardware or joint prostheses require special consideration. With current MDCT scanners, it is possible to obtain high-quality images in these patients if the proper technique is utilized. Increasing kV from the standard 120 to 135 will give less beam-hardening artifact from metal. Increasing rotation time from .5 sec to .75 sec or 1 sec while maintaining mA will improve image quality but at the expense of increased radiation dose to the patient. The longer rotation time allows for a higher sampling rate per time (more views per rotation). When the images are reconstructed, many scanners have special reconstruction kernels or artifact-suppression software that helps suppress metal artifact and should be used in these patients.

Cardiac Gating

Involuntary patient motion has been a problem for CT since its inception. However, as gantry rotation times have decreased and slice number has increased, patient movement, respiratory motion, and bowel peristalsis have all become progressively less important causes of significant artifact. The heart however, has remained a difficult organ to image because of the speed and complexity of its motion, even with gantry rotation times of the order of 0.4 sec and 64-detector row scanners. Effective cardiac imaging requires both high spatial resolution isotropic data sets to visualize small arteries down to 1 mm to 2 mm and high temporal resolution to minimize pulsation artifacts.

The temporal resolution needed to image the heart is significantly affected by heart rate. At heart rates less than 70 beats per minute (bpm) motion–free images can be obtained during diastole with temporal resolution of less than 250 msec. At higher heart rates this time decreases further and even better temporal resolution is needed. In addition, all of the data needed must be acquired during a single breath hold.

Despite the difficulties, the combination of multislice scanners and electrocardiogram (ECG) gating has made CT imaging of the heart and associated vessels a reliable diagnostic tool, provided that careful atten-

tion is paid to hardware and software selection. ECG gating of CT images can be done in two ways. These are termed prospective and retrospective gating.

Prospective gating works by turning on the x-ray beam for a short time at a preselected stage of the cardiac cycle (Figure 2.6). Scan timing is generally set to approximately 70% to 80% of the R-R interval so that images will coincide with diastole and have the fewest motion artifacts. Temporal resolution is optimized by using a partial scan reconstruction algorithm. This can be achieved using parallel-beam–based *half-scan* reconstruction algorithms that provide a temporal resolution of approximately one half of the rotation time. For current scanners, this translates to a temporal resolution of approximately 200 msec to 320 msec.

Using prospective gating, multiple slices are acquired in sequence mode triggered from the ECG. Following the acquisition the table moves, and the next acquisition is performed during the subsequent cardiac cycle as triggered by the ECG. The number of slices acquired per rotation is equal to the number of detectors available on the scanner. The total time needed to cover the heart will depend on the heart rate and number of detectors on the scanner, but the heart can be easily covered with a 16-detector scanner with 1-mm to 1.5-mm slice thickness in one breath hold; however, this may be a challenge with a 4-detector scanner unless thicker collimation is used (2 mm–2.5 mm).

Prospective gating is used primarily for coronary artery calcium scoring and has the added benefit of providing the patient with a low radiation dose, which is important for a screening test. Reconstructed slice thickness for calcium scoring examinations is typically 2 mm to 3 mm because of the extensive electron-beam CT (EBCT) database acquired at 3 mm. Calcium scoring is generally performed on the workstation using dedicated software. The operator identifies individual calcium deposits and the software calculates the total score, using either the Agatston, volume, or calcium mass methods (see Case 12.1). Since the images are obtained as an axial sequence acquisition, they are not suitable for 3D reconstruction.

The biggest problems associated with prospective gating are high or irregular heart rates. A heart rate of 60 bpm, with an R-R interval of 1 sec enables a 200-msec image to be acquired with little motion artifact. Heart rates over 90 bpm may result in failure of the acquisition. Also, heart rates which vary during the examination, such as in atrial fibrillation or other arrhythmias, may seriously reduce image quality and the accuracy of the results.

The second technique of cardiac gating with CT is referred to as retrospective gating. This technique allows for volumetric data acquisition and can be used for evaluation of the coronary arteries or veins, the thoracic aorta, and the pulmonary veins (Figure 2.6). The technical demands of coronary artery CTA differ considerably from those of calcium scoring. Thin slice isotropic acquisition is essential because of the small size and tortuosity of the coronary vessels. Efficient evaluation of the coronary arteries requires the use of both multiplanar reconstruction (MPR) and 3D images.

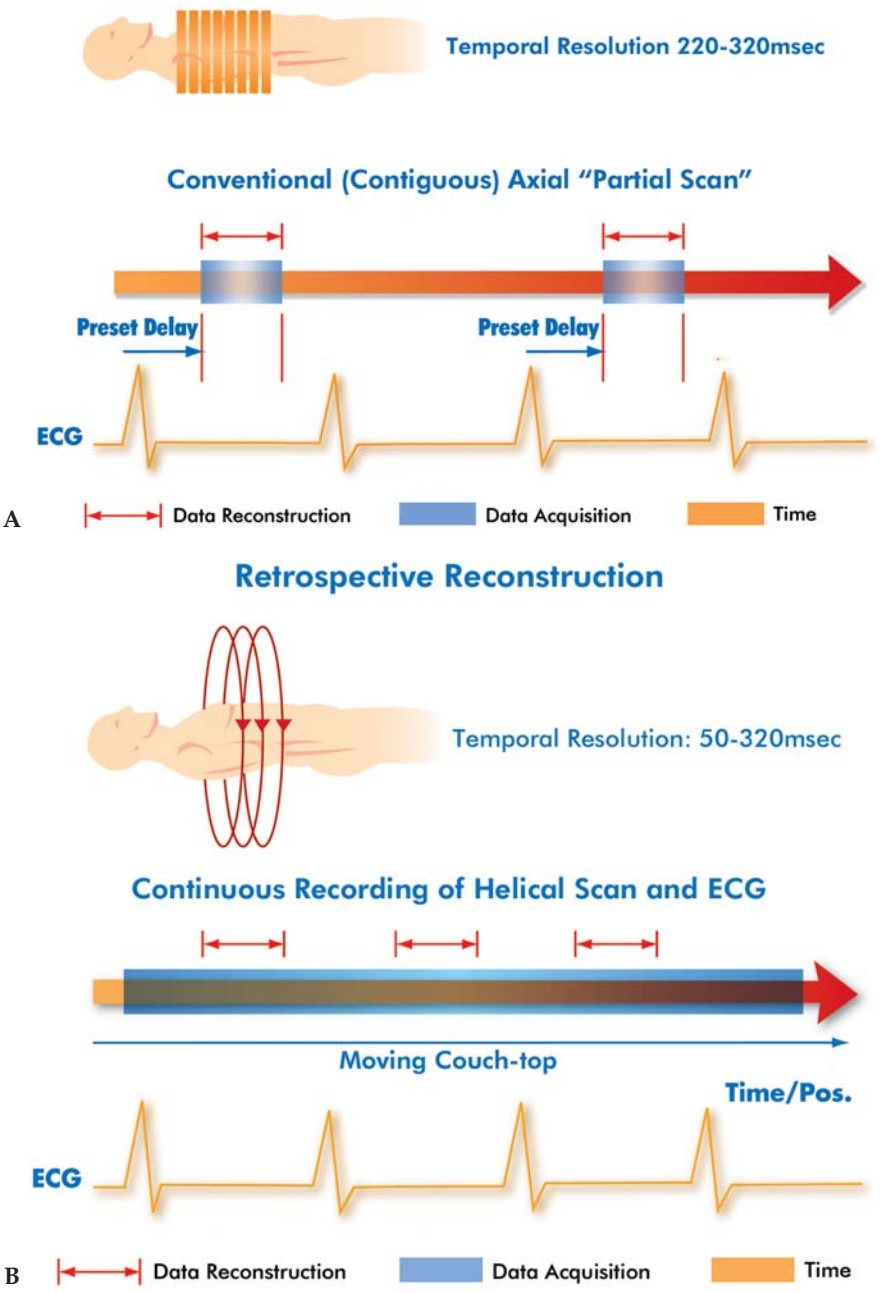

Figure 2.6. Gating techniques. (A) Prospective gating. The patient is scanned in sequence mode. The scan acquisition is triggered at a preset (diastole) phase of the ECG. Partial reconstruction is used to improve temporal resolution. After the scan is completed, table movement occurs, and the next scan is triggered by a subsequent heartbeat. (B) Retrospective gating. The patient is scanned in helical mode. The ECG tracing is recorded continuously during the acquisition. After the entire scan is completed, the images are reconstructed retrospectively at one or multiple phases of the ECG. Partial reconstruction and segmented reconstruction can be used to improve temporal resolution.

For retrospectively gated studies, the heart is scanned helically, and the ECG is recorded. After data acquisition, images are reconstructed at selected cardiac phases identified on the recorded ECG. A typical examination may generate nine or more data sets reconstructed at 10% intervals from a value of 10% R-R interval to 90% R-R interval. This examination provides the high level of image quality demanded for the evaluation of coronary artery disease.

Data acquisition requires that every position of the heart must be covered by a detector row at every point during the cardiac cycle. This means that the scanner table must not advance more than the total width of the active detectors for each heartbeat. It is therefore necessary to acquire overlapping data sets with helical pitches much lower than those for non-gated studies. Typical helical beam pitch values for a retrospectively gated study are between 0.2:1 and 0.4:1. The helical pitch must also be adapted to the heart rate to ensure complete phase-consistent coverage of the heart with overlapping image sections. Consequently, patient dose increases significantly for retrospectively gated studies, and the examination time is prolonged. Coronary CT angiography has an approximate dose exposure of 10 mSv, which is equal to or exceeds the expected dose from a traditional diagnostic catheter coronary angiogram.

The radiation dose from this examination can be reduced by dynamic reduction of tube output in each cardiac cycle during phases of the R-R interval that are of less importance for ECG-gated reconstruction (*ECG-gated dose modulation*). With this approach, the full tube output is applied only during the diastolic phase of the cardiac cycle, at which time images are most likely to be reconstructed. For the rest of the cardiac cycle (systole), the tube output is reduced. Depending on the heart rate, an overall exposure savings of 30% to 50% can be achieved without compromising image quality. In this way, it is possible to reduce the radiation exposure for CT coronary angiography to a level of 5 mSv to 7 mSv, depending on patient heart rate. One downside of this technique is that images from all cardiac phases are not available, and therefore, dynamic movie loops of the cardiac wall motion cannot be viewed.

The combination of thin slices and low pitch means that a minimum of 16 detector rows is needed to complete the cardiac study within an acceptable breath-hold of approximately 30 sec. Scanners with 32 and 64 detectors can bring the scan time down to much more comfortable levels. Scanners with 4 and 8 detectors, which can be used for calcium scoring, are generally not suitable for good-quality coronary CT angiography.

Reconstruction of the data to produce an acceptable image requires sophisticated software. Two main algorithmic approaches are used to perform retrospective cardiac gating: partial scan reconstruction and segmented adaptive reconstruction. Whichever technique is used is largely dependent on the patient's heart rate.

Partial scan reconstruction takes advantage of the fact that an acceptable image can be reconstructed from data acquired from approximately one half of a gantry rotation or a temporal resolution of 200 msec to 250 msec (Figure 2.7). When all of these data must be

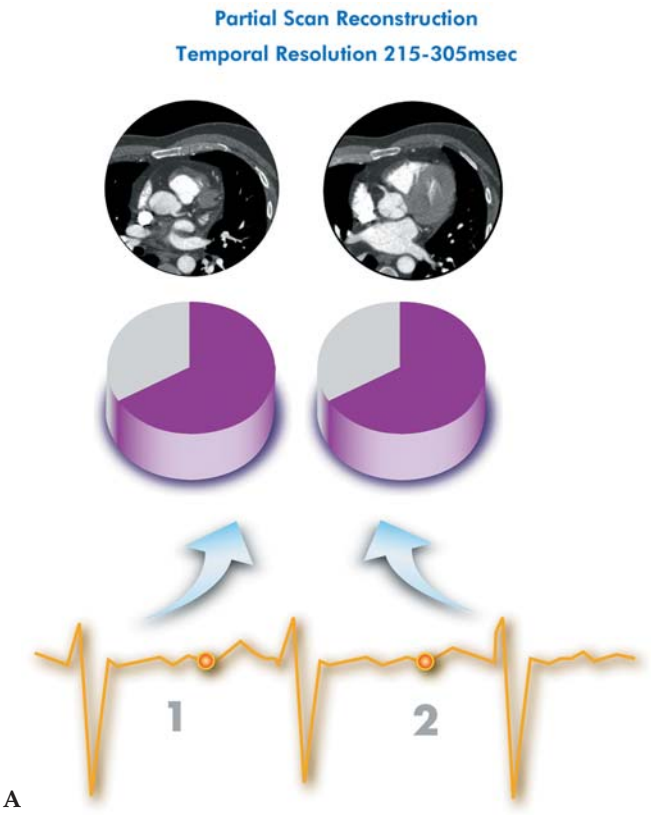

A

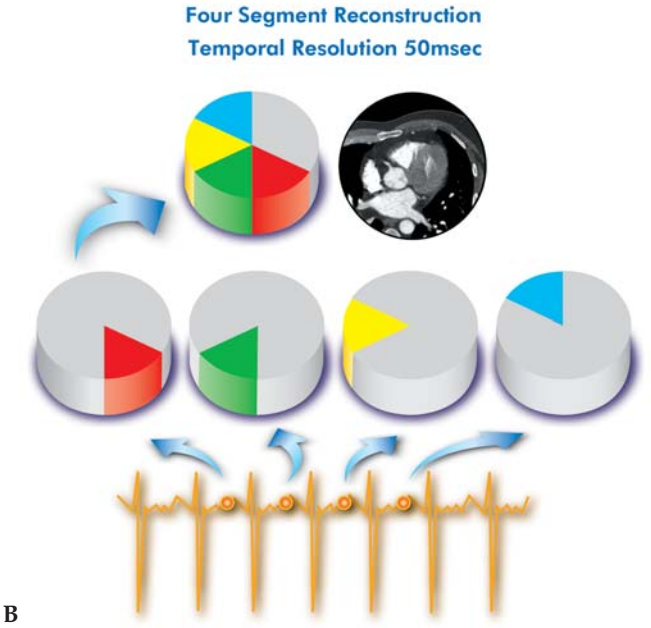

B

Figure 2.7. Retrospective reconstruction techniques. (A) Low heart rate partial reconstruction. At low heart rates a single complete image is generated for each heart beat. To improve temporal resolution the image is reconstructed from a partial rotation of the x-ray tube. (B) High heart-rate adaptive segmented reconstruction. At higher heart rates, there are not enough data to produce an image from a single heartbeat. To further improve temporal resolution the image can be generated by combining data from multiple heartbeats and using partial scan reconstruction. Adaptive reconstruction from four segments is demonstrated in the figure.

acquired within a single cardiac cycle, heart rate becomes a limiting variable. This technique works well with heart rates up to approximately 70 bpm for existing scanners. Many centers will therefore administer beta-blockers to patients to decrease the heart rate below 70 bpm to allow for partial scanning.

The segmented adaptive reconstruction algorithm allows patients with higher heart rates to be scanned. This technique uses software to take data collected from consecutive cardiac cycles and combines them into a single image. Breaking down the image acquisition into as many as 4 or 5 segments in this way reduces the temporal resolution of the image and allows patients with higher heart rates to be scanned successfully at a cost of decreased longitudinal coverage (which may require increasing slice thickness for 16-detector scanners). Partial scan reconstruction is also utilized to further improve temporal resolution. Utilizing these techniques, if two segments are combined, an effective temporal resolution of 100 msec to 125 msec can be achieved, and with four segments, 50 msec to 60 msec.

Heart rates that vary during the scan still represent a problem for image quality with retrospective gating. As with prospective gating, the presence of arrhythmias may produce artifacts or cause a complete failure of the scan acquisition. Heart rate variability is more pronounced at the beginning and end of a long breath hold. Therefore, the shorter scan times needed by the 32- and 64-slice scanners can improve image quality by allowing the acquisition of more consistent data from the center of the breath hold and also reducing the need to administer beta-blockers.

Once the data have been collected, images at many cardiac phases can be reconstructed. This will increase the likelihood of generating the best images for the diagnosis of CAD, and also allows cine loops of the beating heart to be displayed. It is not uncommon for the phase of the study with the least motion to vary from patient to patient. In addition, when evaluating individual coronary arteries in the same patient, different phases may be better for the right and left arteries. Specialized software can also use the reconstructed images to calculate ejection fraction, cardiac output, and wall motion.

Selected Readings

1. Boone JM, Geraghty EM, Seibert JA, Wootton-Gorges SL. Dose reduction in pediatric CT: a rational approach. Radiology 2003;228:352–360.
2. Brenner D, Elliston C, Hall E, Berdon W. Estimated risks of radiation-induced fatal cancer from pediatric CT. Am J Roentgenol 2001;176:289–296.
3. Cademartiri F, Luccichenti G, van Der Lugt A, et al. Sixteen-row multislice computed tomography: basic concepts, protocols, and enhanced clinical applications. Semin Ultrasound CT MR 2004 Feb;25(1):2–16.
4. Cody DD, Moxley DM, Krugh KT, O'Daniel JC, Wagner LK, Eftekhari F. Strategies for formulating appropriate MDCT techniques when imaging the chest, abdomen, and pelvis in pediatric patients. Am J Roentgenol Apr 2004;182:849–859.

5. Crawley MT, Booth A, Wainwright A. A practical approach to the first iteration in the optimization of radiation dose and image quality in CT: estimates of the collective dose savings achieved. Br J Radiol 2001;74: 607–614.
6. Fishman EK. From the RSNA refresher courses: CT angiography: clinical applications in the abdomen. Radiographics 2001;21:3–16.
7. Fleischmann D, Rubin GD, Paik DS, et al. Stair-step artifacts with single versus multiple detector-row helical CT. Radiology 2000;216:185–196.
8. Flohr T, Stierstorfer K, Bruder H, Simon J, Schaller S. New technical developments in multislice CT. Part 1. Approaching isotropic resolution with sub-millimeter 16-slice scanning. Rofo 2002;174:839–845.
9. Flohr T, Bruder H, Stierstorfer K, Simon J, Schaller S, Ohnesorge B. New technical developments in multislice CT. Part 2. Sub-millimeter 16-slice scanning and increased gantry rotation speed for cardiac imaging. Rofo 2002;174:1022–1027.
10. Flohr TG, Schoepf UJ, Kuettner A, et al. Advances in cardiac imaging with 16-section CT systems. Acad Radiol 2003;10:386–401.
11. Flohr T, Kuttner A, Bruder H, et al. Performance evaluation of a multi-slice CT system with 16-slice detector and increased gantry rotation speed for isotropic submillimeter imaging of the heart. Herz 2003;28:7–19.
12. Gies M, Kalender WA, Wolf H, Suess C. Dose reduction in CT by anatomically adapted tube current modulation. I. Simulation studies. Med Phys 1999;26:2235–2247.
13. Greess H, Wolf H, Baum U, et al. Dose reduction in computed tomography by attenuation-based on-line modulation of tube current: evaluation of six anatomical regions. Eur Radiol 2000;10:391–394.
14. Greess H, Nomayr A, Wolf H, et al. Dose reduction in CT examination of children by an attenuation-based on-line modulation of tube current (CARE dose). Eur Radiol 2002;12:1571–1576.
15. Halliburton S, Stillman A, Flohr T, et al. Do segmented reconstruction algorithms for cardiac multi-slice computed tomography improve image quality? Herz 2003;28:20–31.
16. Hamberg LM, Rhea JT, Hunter GJ, Thrall JH. Multi–detector row CT: radiation dose characteristics. Radiology 2003;226:762–772.
17. Hong C, Becker CR, Huber A, Schoepf UJ, Ohnesorge B, et al. ECG-gated reconstructed multi–detector row CT coronary angiography: effect of varying trigger delay on image quality. Radiology 2001;220:712–717.
18. Horton KM, Sheth S, Corl F, Fishman EK. Multidetector row CT: principles and clinical applications. Crit Rev Comput Tomogr 2002;43(2):143–181.
19. Jakobs TF, Becker CR, Ohnesorge B, et al. Multislice helical CT of the heart with retrospective ECG gating: reduction of radiation exposure by ECG-controlled tube current modulation. Eur Radiol 2002;12:1081–1086.
20. Jones TR, Kaplan RT, Lane B, Atlas SW, Rubin GD. Single- versus multidetector row CT of the brain: quality assessment. Radiology 2001;219: 750–755.
21. Kalender WA, Wolf H, Suess C, Gies M, Greess H, Bautz WA. Dose reduction in CT by on-line tube current control: principles and validation on phantoms and cadavers. Eur Radiol 1999;9:323–328.
22. Kalender WA, Wolf H, Suess C. Dose reduction in CT by anatomically adapted tube current modulation. II. Phantom measurements. Med Phys 1999;26:2248–2253.
23. Kalra MK, Maher MM, Sahani DV, et al. Low-dose CT of the abdomen: evaluation of image improvement with use of noise reduction filters—pilot study. Radiology 2003;228:251–256.

24. Kalra MK, Maher MM, D'Souza R, Saini S. Multidetector computed tomography technology: current status and emerging developments. J Comput Assist Tomogr 2004 Jul–Aug;28(suppl 1):S2–S6.
25. Kalra MK, Maher MM, Toth TL, et al. Strategies for CT radiation dose optimization. Radiology 2004;230:619–628.
26. Klingenbeck-Regn K, Schaller S, Flohr T, Ohnesorge B, Kopp AF, Baum U. Subsecond multi-slice computed tomography: basics and applications. Eur J Radiol 1999;31:110–124.
27. Kopp AF, Schroeder S, Kuettner A, et al. Coronary arteries: retrospectively ECG-gated multi-detector row CT angiography with selective optimization of the image reconstruction window. Radiology 2001;221:683–688.
28. Mahesh M, Scatarige JC, Cooper J, Fishman EK. Dose and pitch relationship for a particular multislice CT scanner. Am J Roentgenol 2001;177: 1273–1275.
29. Mahesh M. Search for isotropic resolution in CT from conventional through multiple-row detector. Radiographics 2002;22:949–962.
30. McNitt-Gray MF, Cagnon C, Solberg TD, Chetty I. Radiation dose from spiral CT: the relative effects of collimation and pitch. Med Phys 1999;26:409–414.
31. Napoli A, Fleischmann D, Chan FP, et al. Computed tomography angiography: state-of-the-art imaging using multidetector-row technology. J Comput Assist Tomogr 2004 Jul–Aug;28(suppl 1):S32–S45.
32. Pappas JN, Donnelly LF, Frush DP. Reduced frequency of sedation of young children with multisection helical CT. Radiology 2000 Jun;215(3): 897–899.
33. Prokop M. General principles of MDCT. Eur J Radiol 2003 Mar;45(suppl 1): S4–S10.
34. Roos JE, Willmann JK, Weishaupt D, et al. Thoracic aorta: motion artifact reduction with retrospective and prospective electrocardiography assisted multi-detector row CT. Radiology 2002;222:271–277.
35. Rubin GD. Three-dimensional helical CT angiography. Radiographics 1994;14:905–912.
36. Rydberg J, Buckwalter KA, Caldemeyer KS, et al. Multisection CT: scanning techniques and clinical applications. Radiographics 2000;20: 1787–1806.
37. Rydberg J, Liang Y, Teague SD. Fundamentals of multichannel CT. Semin Musculoskelet Radiol 2004 Jun;8(2):137–146.
38. Schoepf UJ, Becker CR, Ohnesorge BM, Yucel EK. CT of coronary artery disease. Radiology 2004;232:18–37.
39. Wang G, Vannier MW. The effect of pitch in multislice spiral/helical CT. Med Phys 1999 Dec;26(12):2648–2653.
40. Wildberger JE, Mahnken AH, Schmitz-Rode T, et al. Individually adapted examination protocols for reduction of radiation exposure in chest CT. Invest Radiol 2001;36:604–611.
41. van Gelder RE, Venema HW, Serlie IW, et al. CT colonography at different radiation dose levels: feasibility of dose reduction. Radiology 2002;224: 25–33.

Chapter 3

Delivery of Contrast Media for MDCT

Proper delivery of iodinated contrast is extremely important for MDCT. All of the amazing advantages of MDCT can be nullified by improper contrast administration. The faster acquisitions possible with MDCT have many benefits for contrast delivery, including greater coherency of the contrast bolus and the ability to reduce contrast dose. At the same time, these faster acquisitions can be less forgiving, and it is possible to completely miss or outrun a contrast bolus.

To understand protocols for contrast administration, it is important to consider early contrast medium (CM) dynamics. When CM is injected intravenously, it travels from the veins at the injection site to the right heart, the pulmonary arteries, and then to the pulmonary veins and the left heart before it reaches the arterial system for the first time (*first pass*). After the CM is distributed throughout the body, it reenters the right heart (equilibrium phase). Therefore, what we identify as arterial enhancement for CTA includes both a first-pass and an equilibrium or recirculation contribution. The first-pass effect produces much denser contrast enhancement as a result of less dilution (Figure 3.1). As a result of this, uniphasic (constant rate) injections do not lead to an arterial enhancement plateau, but rather to a hump-shaped time enhancement curve. Plateau-like arterial enhancement can only be achieved with biphasic or multiphasic injection protocols.

Injection duration also affects the cumulative arterial enhancement and peak enhancement. Both will be smaller if the injection duration is shortened. The maximal arterial enhancement response is also directly proportional to the iodine administration rate (*iodine flux*) and can be controlled by increasing the injection rate and/or the iodine concentration of the contrast used. In practical terms, similar peak enhancement can be obtained by using lower density contrast (300 mg I/mL) at a faster rate or higher density contrast (350 mg I/ml or 370 mg I/ml) at a lower rate.

When designing contrast administration protocols, the main variables to consider are amount and density of contrast, rate of injection, proper timing of the bolus, and whether to use a uniphasic or multi-

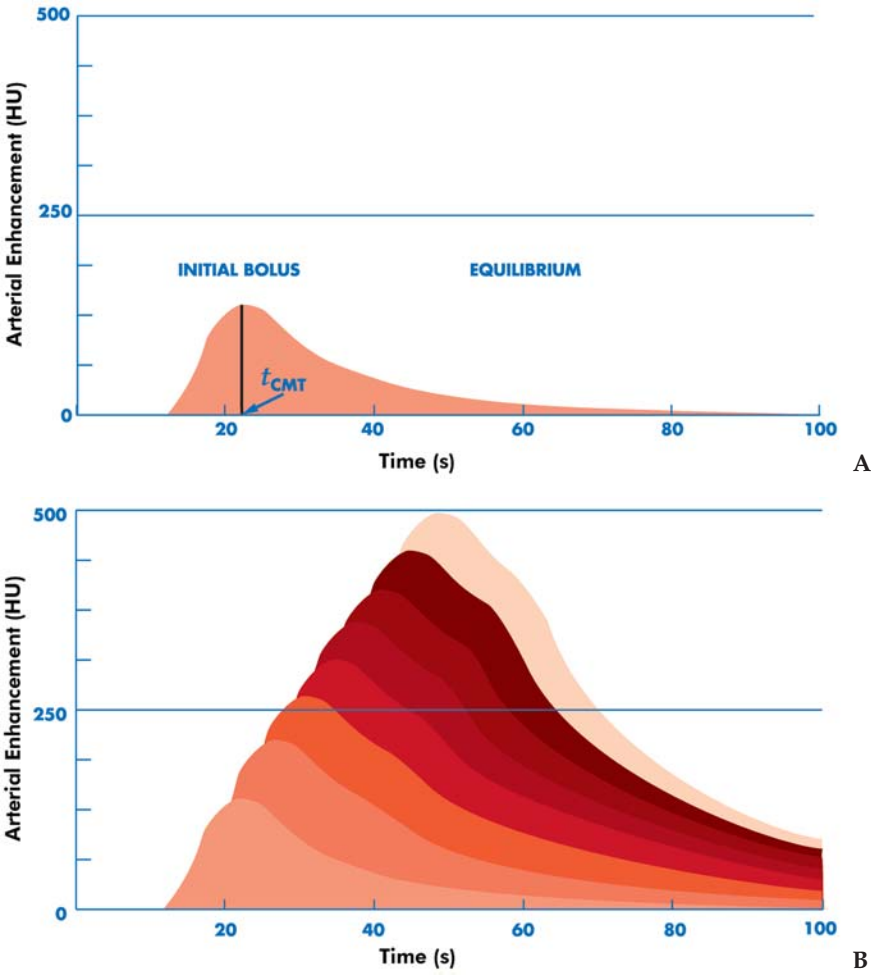

Figure 3.1. Contrast enhancement curve. Demonstration of first-pass effect and continued uniphasic contrast injection over time. (A) A short, rapid contrast injection such as a test bolus will produce a rapid increase in arterial density related to the first-pass effect with progressive decay in density in the equilibrium phase. The time to peak arterial enhancement is demonstrated as t_{CMT}. (B) A rapid, continuous contrast injection produces progressively increasing arterial density over the duration of the injection related to a summation of first-pass and equilibrium phases as the contrast recirculates throughout the body.

phasic injection. For sites that have a dual head injector, there is also the impact of a saline flush injection to consider.

Scan Timing

Successful CT angiography requires careful attention to scan timing. Fortunately, all current 16-slice scanners offer contrast timing programs that can eliminate most of the guesswork from the process. The process

can work several different ways, depending on the scanner and the option chosen. The purpose of these programs is to take away the guesswork in the calculation of the patient's contrast media transit time (t_{CMT}).

Test Bolus Method

The test bolus method uses a small test injection and multiple low dose scans performed over the artery of interest until the contrast is visualized. This gives an accurate value of time to arrival for the contrast in that artery. The t_{CMT} is defined as the time to peak enhancement in that vessel. Scan delay for that patient is then determined by taking the t_{CMT} of the contrast and adding an additional small delay factor of a few seconds.

Bolus Triggering Method

This technique eliminates the test injection. The injection is begun, and the scanner obtains multiple images over an artery of interest (Figure 3.2). The t_{CMT} for the scan is determined automatically when the con-

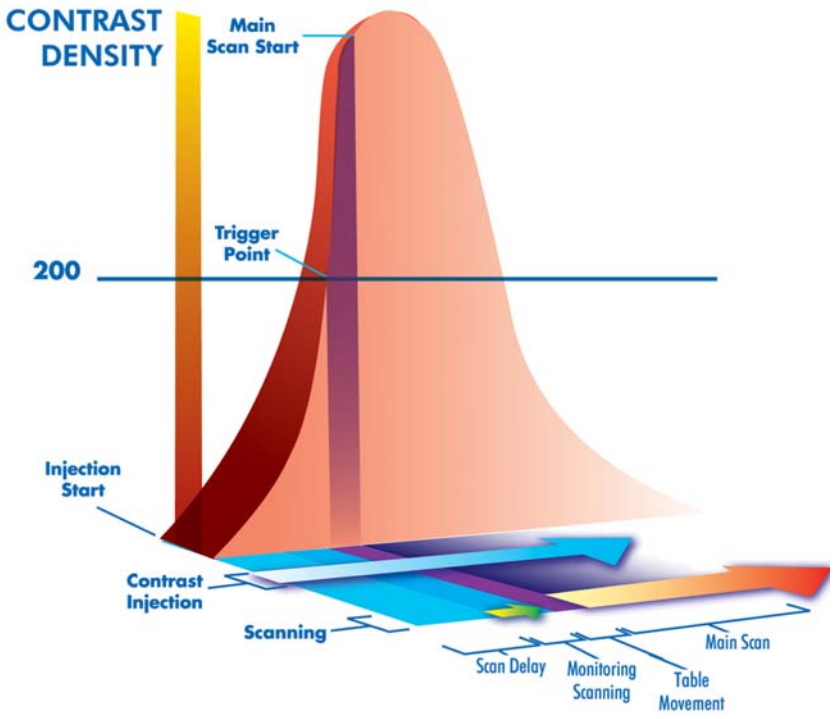

Figure 3.2. Illustration of the bolus triggering technique. Contrast injection is begun, and there is an initial scan delay until a monitoring scan begins. The monitoring scan tracks arterial density until the predetermined trigger point (200 HU) is reached. Once the trigger point is reached, there is a short delay to allow for table movement, and then the main scan begins. The scan and contrast injection proceed according to the preset parameters.

trast density in the artery exceeds a predetermined Hounsfield unit (HU) value (automatic triggering) or can be determined manually by the technologist based on the visual appearance of the contrast in the vessel (manual triggering). The scan will be initiated when either the predetermined HU or visual threshold is reached. There is an additional delay factor built into the test bolus method as it generally takes approximately 4 sec to 8 sec for the table to move and the scanning to begin once the triggering event has occurred.

Timing for most CTA examinations is fairly straightforward. A major vessel such as the aorta or pulmonary artery is selected to monitor the injection using either the test injection or bolus triggering method. The vessel chosen is important. It should be as large as possible if automatic triggering is used and either within or very close to the area of scanning interest. Smaller vessels can be chosen if manual visualization triggering is used.

One study where timing can be more difficult is the aortogram with runoff. Flow to the lower extremities can be asymmetric and highly variable. With current 16-slice scanners, it is possible to outrun the contrast bolus to the feet and end up with no contrast in the distal vessels. This can occur in the presence of significant arterial disease, and the problem is even more important with 32- and 64-detector scanners. It is also possible to over delay and end up with venous contamination. One trick is to use a slightly slower injection (3 mL/sec) and to trigger the scan from the common femoral artery in the groin rather than the aorta. Triggering on the femoral artery will account for the marked heterogeneity that can be seen in flow through the aorta and iliacs. On rare occasions, it is still possible to outrun the contrast with this technique, and a second run through the lower leg may be needed.

Scan timing for parenchymal organ studies of the abdomen is more forgiving than for CTA, but must still be done properly to be successful routinely. The standard fixed delay methods used traditionally for abdominal CT can still be used with MDCT with several modifications. Generally, all of the contrast should be in the patient before the scan is begun. A 70-sec delay for the abdomen and a 45- to 50-sec delay for the chest generally works well at a 2 mL/sec injection rate. At an injection rate of 3 mL/sec, the scan delays can be decreased by 10 sec to 15 sec for the abdomen and 5 sec to 10 sec for the chest, depending on injection duration (contrast volume). This can give a nice mix of vascular and organ enhancement.

Some studies, such as a dual-phase liver, require images in both the arterial and portal venous phase. The arterial portion of the scan can be triggered using an automatic method, but it is important to add at least 10 sec to 15 sec of additional delay onto the scan once contrast appears in the aorta. The goal is to image the liver in the late arterial phase, which usually occurs between 25 sec and 30 sec following injection at 4 mL/sec to 5 mL/sec or approximately 10 sec after dense contrast appears in the aorta. The second scan can be performed at 70 sec after the start of the injection. For a pancreatic study, an even longer delay is needed. The pancreatic phase occurs at approximately 40 sec or 20 sec to 25 sec after contrast first appears in the aorta.

Contrast Amount and Density

The amount of contrast used for a CT examination generally varies with the type of examination and often with patient factors. In choosing an effective amount and density of contrast, it is important to consider the main purpose of the contrast injection: Is it primarily for vascular (arterial) enhancement or for parenchymal organ or venous enhancement? To maximize arterial enhancement for vascular CTA studies, high-density contrast (≥350 mg I/mL) is recommended and should be paired with rapid injection rates of 4 mL/sec to 5 mL/sec. When high-density contrast is injected at a rapid rate, excellent arterial enhancement can be reliably achieved. Lower density contrast can be used, but then injection rates of 5 mL/sec to 6 mL/sec are needed to achieve the same degree of arterial contrast enhancement.

For CTA, the principal objective is to achieve and maintain optimal arterial enhancement throughout the scan. The length of the scan and the injection rate needed can determine the volume of contrast to be used. It is best to think in terms of flow rate and injection duration rather than contrast volume. A good rule of thumb to follow for MDCT is that the contrast injection time should last for the scan duration plus a small delay factor. The delay factor is generally between 4 sec and 10 sec and may correspond to the triggering delay seen with a bolus triggered scan between the triggering event and the initiation of scanning. This factor is, in effect, a contrast buffer to help insure that high-quality scans are consistently obtained and contrast enhancement does not fade out at the end of the study. When the bolus triggering method is used, the delay factor chosen can equal the expected time it takes the scanner to move the table and initiate scanning once the trigger threshold has been reached. It is possible to use the formula injection duration as the scan time without adding an additional delay. This reduces contrast dose, but for CTA, it leaves little room for error. This is just a basic guideline to be used as a starting point and is not meant to be followed precisely for all examinations without consideration of other variables.

$$\text{Injection Duration} = \text{Scan Duration} + \text{Delay Factor}$$

Scan duration for a study is provided at the scan console when the technologist plans the examination but can also be calculated with the following formula:

$$\text{Total Scan Time} = (\text{Total Distance Covered} \times \text{Rotation Time})/(\text{Pitch} \times \text{No. of Detector Rows} \times \text{Slice Thickness})$$

$$\text{Contrast Volume (mL)} = \text{Injection Duration} \times \text{Injection Rate (mL/sec)}$$

For example, to scan a thoracic and abdominal aorta (600-mm coverage) with a 16-detector scanner, 1-mm slices, rotation time of 0.5 sec, and a pitch value of 1.2, the scan would take approximately 15.6 sec. Scan duration + 5-sec delay factor = 20-sec contrast injection. At 4 mL/sec injection rate, a total of 80 mL would be needed, and at 5 mL/sec, 100 mL would be used. In patients who have low cardiac

output or in large patients, this amount should be increased, since it frequently takes longer to achieve adequate aortic enhancement. The minimum amount of contrast needed for CTA is approximately 75 mL for normal sized adults. Below this level, adequate vascular enhancement cannot always be obtained. Volumes can potentially be reduced even further if a saline flush is used. The maximum needed is usually 150 mL to 175 mL. Most examinations can be done with 75 mL to 125 mL of contrast.

For studies of the abdomen, it is very important to achieve good organ enhancement. Visualization of liver lesions can be difficult if adequate liver parenchymal enhancement is not obtained. There is a minimum amount of iodine needed to achieve this enhancement. At least 100 mL of 350 mg I/mL or 125 mL of 300 mg I/mL is suggested for good quality abdomen scans. This is the minimum requirement, and in fact, better visualization of lesions can be obtained by giving more contrast. When the liver is the target organ of the examination, increasing the amount of iodine used for the examination to at least 125 mL of 350 mg I/mL contrast is recommended. Timing and injection duration are less critical for venous or parenchmal studies than they are for CTA.

Injection Rate and Technique

Standard injection rates for CTA are 3 mL/sec to 6 mL/sec depending on the study performed. The faster the contrast is injected, the higher the peak aortic enhancement achievable. As described already, contrast density affects the peak enhancement possible, and less dense contrast needs to be injected faster to achieve the same enhancement level. Peak enhancement is also related to duration of injection. At a uniform injection rate, the aortic enhancement will continue to increase during the course of the injection.

Biphasic contrast injections can produce a more uniform plateau of contrast enhancement. This is achieved by injecting contrast at two different rates. The initial 25 mL of contrast is injected faster than the remainder of the contrast. A typical protocol for 350 mg I/mL contrast would be 30 mL at 5 mL/sec and 75 mL to 100 mL at 3.5 mL/sec. For 300 mg I/mL of contrast, the corresponding injection rates would be 6 mL/sec and 4 mL/sec.

Saline Flush

Dual head injectors are now becoming widely available. They offer the ability to inject a saline flush immediately following the contrast injections. Usually approximately 25 mL to 50 mL of saline is injected. Saline can also be used as a large-volume test bolus prior to contrast injection to, test the patient's IV line. This can help reduce the incidence of contrast extravasations.

Saline flush provides several benefits. It will clear the residual contrast from the IV tubing and accelerate washout from the arm veins. This can provide an effective 10 mL to 25 mL of additional usable con-

trast for CT examinations. This will improve organ enhancement and slightly prolong the vascular phase for angiography examinations. This benefit can effectively reduce the amount of contrast needed for both body CT examinations and CT angiography by approximately 25 mL. This will result in a cost savings and will potentially lessen the risk of contrast nephrotoxicity. Saline flush also reduces the very dense contrast seen in the subclavian vein, brachiocephalic vein, and superior vena cava (SVC). This helps reduce streak artifacts.

Pediatric Patients

Please refer to Appendix 1 for a discussion about administering contrast in children.

Selected Readings

1. Bae KT, Tran HQ, Heiken JP. Uniform vascular contrast enhancement and reduced contrast medium volume achieved by using exponentially decelerated contrast material injection method. Radiology 2004 Jun;231(3): 732–736.
2. Bae KT, Tran HQ, Heiken JP. Multiphasic injection method for uniform prolonged vascular enhancement at CT angiography: pharmacokinetic analysis and experimental porcine model. Radiology 2000 Sep;216(3):872–880.
3. Bae KT. Peak contrast enhancement in CT and MR angiography: when does it occur and why? Pharmacokinetic study in a porcine model. Radiology 2003 Jun;227(3):809–816.
4. Catalano C, Laghi A, Reitano I, Brillo R, Passariello R. Optimization of contrast agent administration in MSCT angiography. Acad Radiol 2002 Aug;9(suppl 2):S361–S363.
5. Choe YH, Phyun LH, Han BK. Biphasic and discontinuous injection of contrast material for thin-section helical CT angiography of the whole aorta and iliac arteries. Am J Roentgenol 2001 Feb;176:454–456.
6. Dorio PJ, Lee FT Jr., Henseler KP, et al. Using a saline chaser to decrease contrast media in abdominal CT. Am J Roentgenol 2003 Apr;180:929–934.
7. Eastwood JD, Lev MH, Provenzale JM. Perfusion CT with iodinated contrast material. Am J Roentgenol 2003;180:3–12.
8. Fleischmann D. Present and future trends in multiple detector-row CT applications: CT angiography. Eur J Radiol 2002;12(suppl):S11–S16.
9. Fleischmann D, Rubin GD, Bankier AA, Hittmair K. Improved uniformity of aortic enhancement with customized contrast medium injection protocols at CT angiography. Radiology 2000;214:363–371.
10. Fleischmann D. High-concentration contrast media in MDCT angiography: principles and rationale. Eur Radiol 2003 Nov;13(suppl 3):N39–N43.
11. Frush DP, Spencer EB, Donnelly LF, Zheng JY, DeLong DM, Bisset GS III. Optimizing contrast-enhanced abdominal CT in infants and children using bolus tracking. Am J Roentgenol 1999 Apr;172(4):1007–1013.
12. Haage P, Schmitz-Rode T, Hubner D, et al. Reduction of contrast material dose and artifacts by a saline flush using a double power injector in helical CT of the thorax. Am J Roentgenol 2000;174:1049–1053.
13. Herman S. Computed tomography contrast enhancement principles and the use of high-concentration contrast media. J Comput Assist Tomogr 2004 Jul–Aug;28(suppl 1):S7–S11.

14. Hopper KD, Mosher TJ, Kasales CJ, et al. Thoracic spiral CT: delivery of contrast material pushed with injectable saline solution in a power injector. Radiology 1997;205:269–271.
15. Hsu RM. Computed tomographic angiography: conceptual review of injection and acquisition parameters with a brief overview of rendering technique. Appl Radiol 2002;31(suppl):33–39.
16. Kirchner J, Kickuth R, Laufer U, et al. Optimized enhancement in helical CT: experiences with a real-time bolus tracking system in 628 patients. Clin Radiol 2000;55:368–373.
17. Luboldt W, Straub J, Seemann M, Helmberger T, Reiser M. Effective contrast use in CT angiography and dual-phase hepatic CT performed with a subsecond scanner. Invest Radiol 1999 Dec;34(12):751–760.
18. Luker GD, Siegel MJ, Bradley DA, Baty JD. Hepatic spiral CT in children: scan delay time-enhancement analysis. Pediatr Radiol 1996;26(5):337–340.
19. Mehnert F, Pereira PL, Trubenbach J, Kopp AF, Claussen CD. Biphasic spiral CT of the liver: automatic bolus tracking or time delay? Eur Radiol 2001;11(3):427–431.
20. Mehnert F, Pereira PL, Trubenbach J, Kopp AF, Claussen CD. Automatic bolus tracking in monophasic spiral CT of the liver: liver-to-lesion conspicuity. Eur Radiol 2001;11(4):580–584.
21. Napoli A, Fleischmann D, Chan FP, et al. Computed tomography angiography: state-of-the-art imaging using multidetector-row technology. J Comput Assist Tomogr 2004 Jul–Aug;28(suppl 1):S32–S45.
22. Ono S, Akaizawa T, Gotou R, et al. Analysis of time-density curves of contrast media for improvement of chest dynamic incremental CT. J Comput Assist Tomogr 1999 Sep–Oct;23(5):753–757.
23. Platt JF, Reige KA, Ellis JH. Aortic enhancement during abdominal CT angiography: correlation with test injections, flow rates, and patient demographics. Am J Roentgenol 1999 Jan;172:53–56.
24. Schoellnast H, Tillich M, Deutschmann HA, et al. Abdominal multidetector row computed tomography: reduction of cost and contrast material dose using saline flush. J Comput Assist Tomogr 2003 Nov–Dec; 27(6):847–853.
25. Tublin ME, Tessler FN, Cheng SL, Peters TL, McGovern PC. Effect of injection rate of contrast medium on pancreatic and hepatic helical CT. Radiology 1999 Jan;210(1):97–101.
26. van Hoe L, Marchal G, Baert AL, Gryspeerdt S, Mertens L. Determination of scan delay time in spiral CT-angiography: utility of a test bolus injection. J Comput Assist Tomogr 1995;19:216–220.

Chapter 4

Image Reconstruction and Review

Data acquisition with MDCT scanners is relatively straightforward. Scanners offer a fixed number of slice thickness options, and other variables are controlled in predictable ways for different examinations. When it comes to image reconstruction and review however, the opposite is true. There are almost an unlimited number of ways to reconstruct and view an MDCT data set, and no one right way to do it. Many of the choices made depend on variables that are site and radiologist dependent and have nothing to do with the scanner or the examination performed. Questions to consider when designing reconstruction protocols include the following: How will the images be viewed—on a PACS monitor, on film, or directly on a 3D–capable workstation? What is the archival method—film or electronic storage? If the storage is electronic, is it on-site or remote? What is the cost structure for the storage? Finally, many of the choices will come down to the personal preferences of individual radiologists. These preferences frequently change and evolve as radiologists gain experience with volumetric imaging.

Image Reconstruction

If you could summarize a basic principle of time-efficient volumetric imaging with MDCT in a few words, they would be scan thin, view thick. It is important to remember that the thinnest images that can be reconstructed for a data set is predetermined by the slice thickness used for the scan. Also, the thinner the sections available, the better the quality of derived multiplanar and 3D reconstruction. Once these thin sections are obtained, all scanners offer tremendous flexibility in the way images are reconstructed and reviewed. Some of the parameters to consider when reconstructing the data set include reconstruction method and algorithm, FOV, slice thickness, and automated or manual creation of MPR, volume, or maximum intensity projection (MIP) images.

Reconstruction Algorithm

Image reconstruction with 16-slice and higher MDCT scanners is much more complicated than with single-slice or even 4-slice scanners. Axial scanning with single-slice scanners is relatively straightforward, as all of the views needed to reconstruct an image are acquired in the image plane, since the table does not move while the image is being acquired. With the introduction of helical or spiral scanning, image reconstruction had to take a considerable leap forward, because now the table was moving continuously during data collection, and the views needed to reconstruct the axial image were not all in the same plane. To overcome this problem, views in the image plane were interpolated from measurements on either side of the image plane. The most practical result of helical image reconstruction was a broadening of the slice sensitivity profile for a given image. This means that the actual reconstructed image was thicker than the slice thickness at which it was acquired, particularly with higher pitches. This effect was small with single-detector scanners. The advent of 4-slice scanners required minor modifications to the existing helical reconstruction algorithms, which were still functional.

The introduction of scanners with more than 4 simultaneous slices created further complications. Existing algorithms that assumed the x-ray source, imaging range of interest (ROI), and the detector were all in the same plane were no longer completely valid. Newer algorithms that accounted for the fact that the imaging ROI actually projected onto multiple detector rows in different planes were needed. Trying to reconstruct axial images without taking these various view angles (cone beam) into account produced significant artifacts. In order to maintain image quality, various cone beam reconstruction algorithms were developed. Because these new techniques are very computer intensive, image reconstruction times tended to be significantly longer than for single- and 4-slice scanners. Manufacturers have compensated for this by incorporating faster processing boards into the 16-, 32-, and 64-slice scanners.

It is important to appreciate that the reconstruction algorithm chosen can have a significant effect on image quality and artifacts. Artifacts become more pronounced as the cone angle increases, and at the periphery of the field of view. Edge distortions and blurring at high-contrast interfaces are common examples of reconstruction artifacts. It is not uncommon for current systems to provide both cone beam and conventional reconstruction (fan beam approximation) algorithms, giving the operator a choice between reconstruction speed and image quality (Figure 4.1). Many scan manufacturers quote very high reconstruction rates for CT images that are not based on using a full cone beam algorithm. These reconstruction speeds may be useful in some cases, but the majority of cases should be reconstructed with the best quality algorithm.

Reconstruction Filters

Once the basic reconstruction algorithm is chosen, a choice of filter kernel to be applied to the raw data must also be made. There are mul-

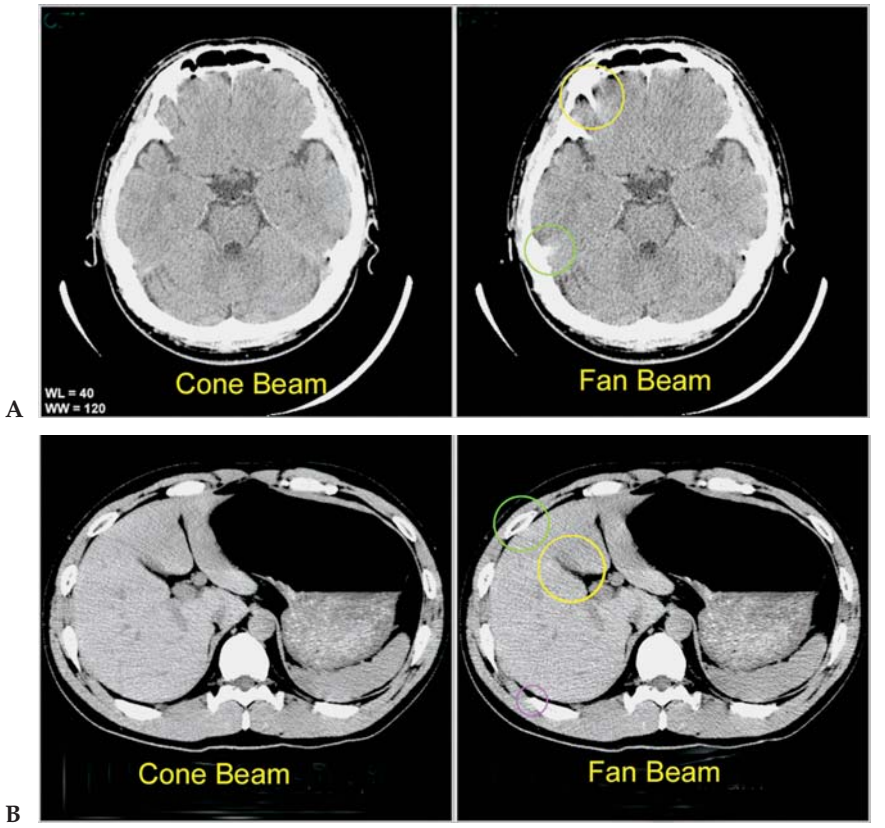

Figure 4.1. Reconstruction artifacts. (A and B) Brain and abdomen CT images reconstructed with two different algorithms (cone beam and fan beam approximation). Note the more pronounced artifacts with the non–cone beam reconstruction. Windmill and streak artifacts are most pronounced at the periphery, best noted involving the skull and ribs. Note also the blurring of the liver margin (yellow circle). (Courtesy of Ilmar A. Hein, PhD.)

tiple filter options varying between the extremes of very smoothing to very sharpening filters. These filters can have a tremendous effect on how the final images look. In general, smoother (soft tissue) filters are more often used to reconstruct the raw data, as sharper filters will often produce images that are unacceptably grainy, particularly when looking at very thin slice sections. Smoother soft tissue reconstruction kernels also generally produce better-looking 3D volume and surface reconstructions.

The raw data can be reconstructed with as many different filter kernels as necessary to provide the desired information. For example, chest scans can be routinely reconstructed with both a soft tissue filter as well as a sharper filter to better see lung detail. Another way to achieve a similar look and save storage space and reconstruction time is to apply an edge enhancement algorithm to the images after they are reconstructed. Most PACS systems allow for a sharpening filter to be applied to the images as a postprocessing feature. This approach is not

quite as good as applying the filter directly to the CT raw data, but it can be a good compromise for sites that want to decrease the number of images reviewed and stored and speed up reconstruction times. Special filters can also be applied on the scanner for orthopedic cases to reduce artifacts from metal in patients being scanned with rods or joint prostheses in place.

Manufacturers of CT scanners can recommend certain kernels for reconstruction of images for different types of cases, but I recommend that each site work with its applications people to try out various options and choose the filters that they like best for each different examination. Applications specialists can take the same data set and reconstruct images using different filters for direct comparison by the radiologists. The decision whether to reconstruct the data in a single (soft tissue) algorithm or multiple algorithms (soft tissue, lung, bone) must be decided by each site. The benefits of multiple reconstructions are better image quality for bone studies and lung, but the disadvantages are significant and include longer reconstruction times for each case and much more data to review and archive. Also, much of the same effect can be achieved using postprocessing features on a PACS workstation.

While discussing image reconstruction, real-time, or continuous, imaging should be considered. This specialized algorithm allows CT images to be viewed as rapidly as 12 frames per second. Originally developed for CT fluoroscopy to facilitate and speed up CT-guided interventions, the technique has other valuable applications. It can show the operator the results of a helical scan in real time, providing greater control over when to terminate or extend the scan. On occasion, physicians are able to make important decisions about trauma patient care even before the final images are reconstructed. Perhaps the most valuable application, however, is the use of real-time imaging for contrast tracking. Scan timing to achieve optimum contrast enhancement has been getting more and more difficult since the introduction of helical scanning. Considering the scan speed of 16 and higher slice scanners, the situation is even more critical. Real-time reconstruction is able to monitor contrast with CT number measurements as high as 12 frames per second, thus eliminating any uncertainty in scan timing. The more sophisticated of these software packages can start the helical scan automatically or show the operator the best time for manual initiation. The software can be sufficiently robust and reliable for all contrasted CT studies, including coronary angiography. Real-time reconstructions also allow a CT technologist to instantly evaluate a contrast injection for quality of vascular enhancement. For example, when performing a CT runoff, if the scanner has "outrun" the contrast bolus to the legs, a second scan can be performed immediately to identify the vessels (Figure 4.2).

Slice Thickness

Thin (submillimeter) images are wonderful for generating volume reconstructions but are less than ideal for primary image review. These

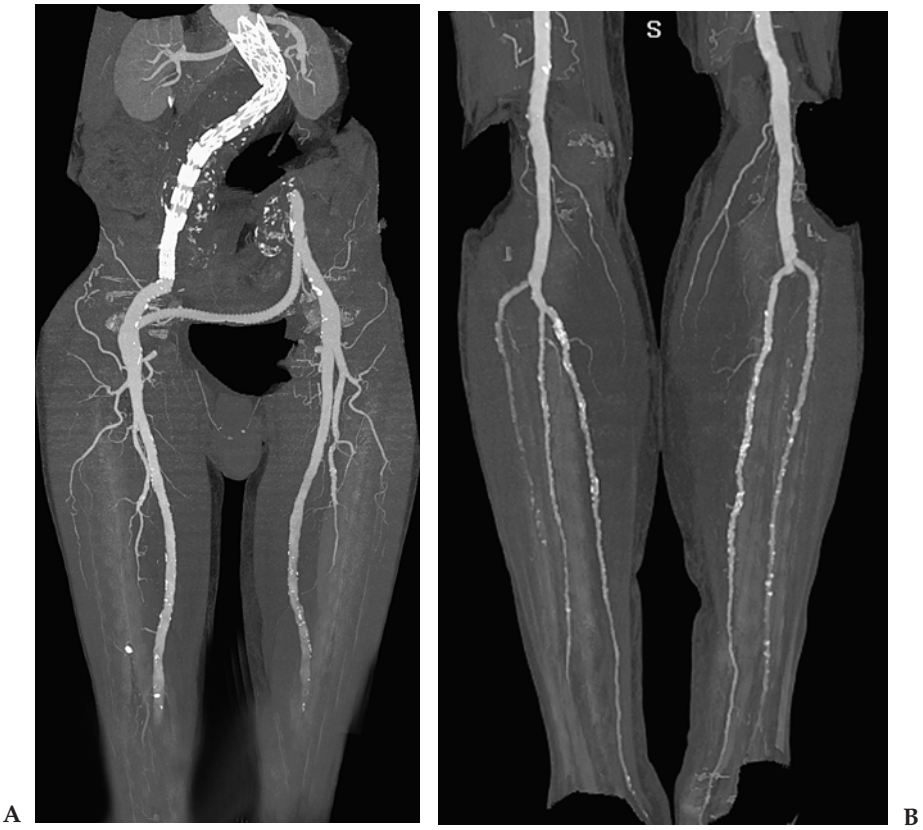

Figure 4.2. Runoff with second pass through the lower legs. (A) An 88-year-old man with severe generalized arteriomegaly and prior aorto-right femoral graft with femoral-femoral crossover graft. Segmented MIP image demonstrates no flow below the distal superficial femoral arteries. Because of the generalized arteriomegaly, flow is extremely slow and the scanner has outrun the contrast bolus. (B) Additional scan obtained through the lower legs immediately following the initial runoff. Utilizing the real-time reconstruction feature, the technologist could see the absence of contrast in the calves and performed a second pass. Segmented MIP image shows the distal runoff.

data sets are large and cumbersome to review even on the best PACS systems. The images tend to be noisier, and pathology is frequently better identified on thicker section images. Radiologists are generally more likely to identify important findings when looking at 200 images as opposed to 800 images. The goal is to maintain the advantage of high-resolution imaging but to create image files that are manageable and easily reviewed, and to prevent the eyestrain and fatigue associated with viewing huge data sets. Time-efficient review is critical to gaining acceptance of MDCT. When presented with overly large data sets, both radiologists and clinicians will eventually become frustrated, and error rates may increase because of image fatigue.

Another important characteristic of multislice image reconstruction was alluded to at the beginning of this chapter. Since the acquired data

sets are highly sampled volumes, it is quite feasible to construct images that are considerably thicker than the slices used during scanning. The technique is similar to averaging or filtering the raw data over any desired image thickness. This can have considerable value when thin images are needed for MPR or 3D reconstructions, but thicker images are preferred for interpretation and archiving. It has become convenient to distinguish between slice thickness (how the data were acquired) and image thickness (how the data are reconstructed). Keep in mind that image thickness may be greater than—but can never be less than—the slice thickness at which the data were acquired. Review of thicker slice axial and multiplanar images is a fundamental component of time-efficient CT workflow.

The image thickness chosen for reconstruction is a highly individual decision and may depend on the type of examination, indication, and how the images are reviewed (soft versus hard copy). For soft copy viewing on PACS, reconstruction slice thickness between 3 mm and 5 mm will cover the vast majority of examinations. This is perfectly adequate for the majority of body, neurology, spine, and extremity studies. There are certain examinations, however, in which review of thinner reconstructions (1.5 mm to 2 mm) may be useful. Some examples include chest angiogram for pulmonary embolism, pancreas evaluation, peripheral joints, and chest for lung nodule or high-resolution evaluation.

If image review must be done on hard copy, then even thicker reconstructions are generally used to keep film number and cost more reasonable. It should be emphasized that no matter what image thickness is chosen for viewing, the thin section data remain available and can be reviewed in any case in which there is a question or problem that might be answered by very high resolution images.

Overlapping Reconstructions

Conventional CT wisdom dictates that to achieve high-quality multiplanar and 3D reformations the images should be reconstructed with an overlap of approximately 50%. Therefore, for cases scanned at 1.5-mm collimation, the images should be reconstructed every 0.75 mm. For the example cited, this would in fact improve quality of MPR and volume images. The down side is, of course, larger data sets that take up more memory and storage.

With current generation 16 or higher detector scanners, overlapping reconstructions are often unnecessary. When scans are generated with isotropic voxels, improvement in reconstruction quality from overlapping reconstructions is often quite minimal. In patients scanned with smaller FOV and resolution of 0.5 mm, overlapping reconstructions are generally not worth the extra difficulty generated by the larger data sets. The same is also true of larger FOV examinations with resolution up to 1 mm. Different scan manufacturers have different recommendations regarding overlapping reconstructions. With scanners having a maximal resolution of 0.75 mm, overlap is generally recommend, whereas with scanners having a resolution of 0.5 mm, this has been

found to be unnecessary in most cases. I would recommend that each site experiment with several different types of CTA cases and reconstruct the same data set with and without overlap and compare the quality of the MPR and volume images for themselves to make a final determination.

Multiplanar Reconstructions

A fundamental benefit of volumetric data sets is the ability to quickly and easily review very high quality multiplanar images. With MDCT, multiplanar imaging should be part of the routine practice and incorporated into almost all CT examinations in some form. Standard thicker section (3 mm) coronal and sagittal images are simple to create and can be reviewed quickly and efficiently (Figures 4.3 and 4.4). For years radiologists relied on axial images for primary diagnosis. Although multiplanar reconstructions were available, there was substantial image quality degradation between the axial and the reconstructed images. Few radiologists in this setting felt comfortable relying primarily on the reconstructions for diagnosis. MDCT has completely changed this. Radiologists are now free to interpret images in whatever plane is most appropriate. In this respect CT now has the same capability as MRI.

As radiologists become more comfortable with multiplanar imaging, diagnostic accuracy and confidence unquestionably improves. Many diagnoses are much easier to make in nonaxial planes. This can be difficult to fully understand and appreciate until it becomes a routine part

A B

Figure 4.3. Acute epiglottitis. (A) Axial 3-mm image of a 25-year-old man having difficulty swallowing, neck pain, and fever. Enlargement of the epiglottis is present on this image but can be easily overlooked on the axial slices. (B) Sagittal reconstruction makes identification of the abnormal epiglottis much easier and more obvious.

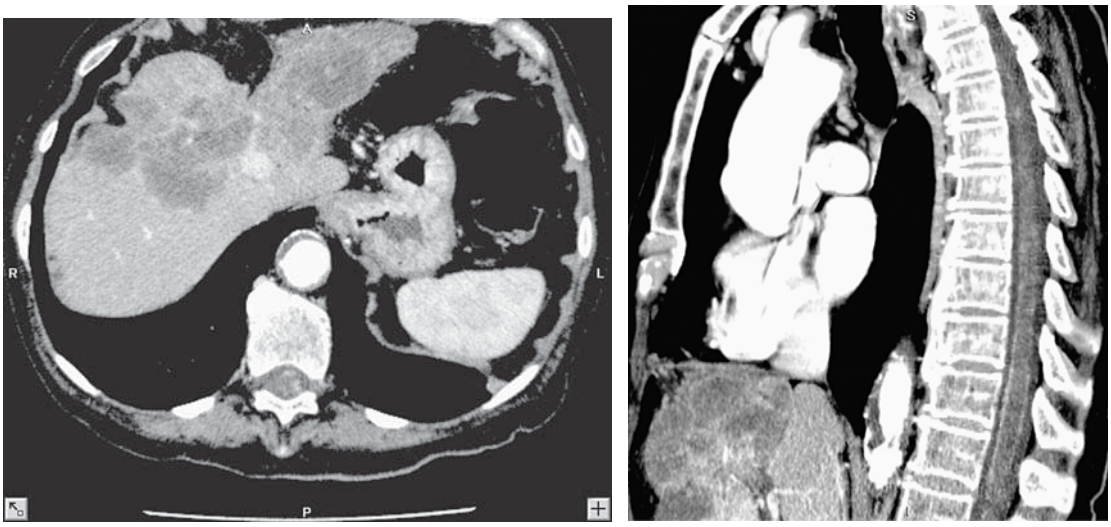

Figure 4.4. Leptomeningeal carcinomatosis from breast carcinoma. (A) Axial 3-mm image shows extensive liver metastasis. Nodular enhancement is present on the surface of the spinal cord, but this is very difficult to detect on the axial images. (B) Sagittal reconstruction shows linear and nodular enhancement on the surface of the cord. Findings are less likely to be missed on the sagittal images.

of your practice. Also, with isotropic imaging, any oblique plane can be easily created and reviewed with no loss of image quality.

There is no question that routine review of multiplanar images is beneficial, but there are significant choices to be made as to how they should be created. The two major options are to create the MPRs on the scanner console directly and send them to PACS, or to create the MPRs directly on the PACS system or workstation from the thin section data. Both options have certain advantages and disadvantages.

Scanner-Created MPRs

With current MDCT scanners, creation of sagittal and coronal images on the scanner is easy. The images can be manually created by the technologist or automatically generated by the scanner software and built directly into the examination protocol. Automatically generated reconstructions ensure that the MPRs are always done and are time efficient for the technologist. These images are generally straight sagittal and coronal planes. If oblique images are desired, the technologist generally must create them manually.

For the radiologist, MPR images created by the scanner and sent to PACS have many advantages. Foremost among them is that the images are routinely and immediately available for review. Most modern PACS systems allow the user to display and link multiple sequences at once. This allows the radiologist to quickly and efficiently review and compare images in multiple planes. The most appropriate plane can be chosen for primary review and pathology can be easily correlated into three planes. The process is simple, reliable, and effective.

The main disadvantage of scanner-created MPRs is a lack of flexibility. Radiologists are limited to predetermined reconstruction planes for a given examination. If the radiologist wants to see the images in a nonstandard or oblique plane, he must either ask the technologist to create the desired images on the scanner and send them to PACS, or have the data transferred to a workstation that will allow interactive reconstruction of the data by the radiologist or technologist. In either situation there is some delay and inconvenience in reviewing the case.

PACS/Workstation-Created MPRs

Many PACS systems now allow users to interactively create multiplanar reconstructions directly on the PACS monitor. In the future it is likely that all new systems will have this feature. It is important to remember that to create high-quality reconstructions the thinnest possible slice reconstruction (equal to the thickness the image was acquired at) must be sent to the PACS system or workstation. Since data sets are frequently huge (hundreds or even thousands of images), they have the potential downside of slowing down the network, causing cases to take much longer to load onto PACS, creating cumbersome data sets to review, and increasing storage costs. As networks and computers rapidly improve and get faster, and storage costs fall, these issues will likely become trivial, but at this time this remains an important consideration for many sites that must utilize computers and networks that are less than state of the art.

The main advantage of creating MPRs on PACS or a workstation is the flexibility and interactivity it provides. Radiologists have at their fingertips the ability to create images in any plane. This can be a powerful tool in some cases. The main disadvantage is that this generally requires the radiologist to perform a few extra steps in order to see the MPR images. Even if the time involved is minimal, many radiologists will fail to use this feature routinely and save it for only select cases. Both radiologists and clinicians like to have the images immediately available and accessible. As software continues to improve this will likely cease to be an issue. In the future I suspect all radiologists will have immediate access to multiplanar, volume, and MIP images directly on the PACS system, and the separation between PACS monitors and dedicated 3D workstations will continue to blur. Once this occurs it will no longer be necessary or advantageous to create reconstructions on the scanner console.

Image Review

Effective use of a MDCT scanner requires soft copy image review. Even sites that are unable to install a full PACS system can institute a system to review images on computer at a relatively small cost (film archival and storage is a different story, however). The number of different options for soft copy image review is huge, and a full discussion of PACS systems is beyond the scope of this book. However, there

are some general concepts that are widely applicable and worth discussing.

One of the great benefits of soft copy review is the ability to rapidly scroll through large data sets. The transition from a sheet-based review to a scrolling-based review can initially be challenging for some radiologists, but once made is well worth the effort. Gains in efficiency and accuracy can be expected. Pathology is much easier to identify, and there is less fatigue on the eye and mind when images are reviewed in this manner.

Another great benefit of computer-based image review is having an electronic toolset at your fingertips. Almost all systems allow the user to easily window images manually or with presets, measure objects and Hounsfield units, annotate, adjust image sharpness and contrast, and magnify images. Other available features include the ability to easily compare images, check prior reports, link images, and save select images for teaching or conferences. Select image files can also be printed or emailed to referring doctors, and even incorporated directly into the radiology report. Many current PACS systems also include advanced tools such as ones providing the ability to create MPR, volume, or MIP images directly on the PACS. Systems are also available that have all of the functionality of both a PACS monitor and a 3D workstation seamlessly integrated into one unit.

An important and often overlooked part of utilizing PACS effectively is setting up user-friendly hanging protocols. Most systems allow for some degree of customization when setting up protocols. Individual preferences will vary, but when viewing MDCT it is helpful to have each series loaded in a different screen partition for easy scroll review and comparison. If possible, having the sequences automatically linked and cross-referenced is extremely helpful. Cross-referencing allows users to localize findings between axial, sagittal, and coronal images. Linking can allow direct comparison of images pre- and postcontrast or between different window settings. The number of separate partitions the monitor is divided into should vary depending on the number of different series available and whether or not a comparison is being loaded. The downside of having multiple partitions open per monitor is that the image size gets smaller and smaller. This is usually not a significant factor for CT until more than four to six partitions per monitor are used.

Selected Readings

1. Fuchs T, Krause J, Schaller S, Flohr T, Kalender WA. Spiral interpolation algorithms for multislice spiral CT—part II: measurement and evaluation of slice sensitivity profiles and noise at a clinical multislice system. IEEE Trans Med Imaging 2000 Sep;19(9):835–847.
2. Grass M, Manzke R, Nielsen T, et al. Helical cardiac cone beam reconstruction using retrospective ECG gating. Phys Med Biol 2003 Sep; 48(18):3069–3084.

3. Hobbs WC. Taking digital imaging to the next level: challenges and opportunities. Radiol Manage 2004 Mar–Apr;26(2):16–20.
4. Hu H. Multi-slice helical CT: scan and reconstruction. Med Phys 1999 Jan;26(1):5–18.
5. Kohler T, Proksa R, Bontus C, Grass M, Timmer J. Artifact analysis of approximate helical cone-beam CT reconstruction algorithms. Med Phys 2002 Jan;29(1):51–64.
6. Kohler TH, Proksa R, Grass M. A fast and efficient method for sequential cone-beam tomography. Med Phys 2001 Nov;28(11):2318–2327.
7. La Riviere PJ, Pan X. Longitudinal aliasing in multislice helical computed tomography: sampling and cone-beam effects. IEEE Trans Med Imaging 2002 Nov;21(11):1366–1373.
8. Mathie AG, Strickland NH. Interpretation of CT scans with PACS image display in stack mode. Radiology 1997 Apr;203(1):207–209.
9. Proksa R, Kohler T, Grass M, Timmer J. The n-PI-method for helical cone-beam CT. IEEE Trans Med Imaging 2000 Sep;19(9):848–863.
10. Reiner BI, Siegel EL, Hooper FJ, Pomerantz S, Dahlke A, Rallis D. Radiologists' productivity in the interpretation of CT scans: a comparison of PACS with conventional film. Am J Roentgenol 2001 Apr;176(4):861–864.
11. Reiner BI, Siegel EL, Hooper FJ. Accuracy of interpretation of CT scans: comparing PACS monitor displays and hard-copy images. Am J Roentgenol 2002 Dec;179(6):1407–1410.
12. Reiner BI, Siegel EL, Hooper FJ, Glasser D. Effect of film-based versus filmless operation on the productivity of CT technologists. Radiology 1998 May;207(2):481–485.
13. Tamm EP, Thompson S, Venable SL, McEnery K. Impact of multislice CT on PACS resources. J Digit Imaging 2002;15(suppl 1):96–101.
14. Van Ooijen PM, Bongaerts AH, Witkamp R, Wijker A, Tukker W, Oudkerk M. Multi-detector computed tomography and 3-dimensional imaging in a multi-vendor picture archiving and communications systems (PACS) environment. Acad Radiol 2004 Jun;11(6):649–660.

Chapter 5

3D Workstations: Basic Principles and Pitfalls

It was only a few years ago that 3D workstations were slow, cumbersome, and difficult to use. Unless you had special training and a large block of time available (research fellows), they were of limited use. Many clinical departments had them, but they mostly served to collect dust. Things are now dramatically different. There has been tremendous improvement in the technology, both hardware and software. Workstations are now much more user-friendly, flexible, and powerful. Many have significant automated features that perform complex operations in one or two mouse clicks that would previously have taken minutes.

One or more workstations are now an essential part of any MDCT service. In many departments they are used on a daily basis by a wide range of people, including technologists, radiologists, and even referring physicians. The workstation has become an essential tool in the radiology reading room for interpreting cases and reviewing findings with referring doctors. Some systems can even be accessed remotely over the Internet , allowing complex 3D manipulations to be performed from any connected computer.

Effective use of a 3D workstation requires a basic understanding of the concepts and tools that are used to generate the images. Many radiologists are familiar with the terminology used: volume rendering, surface shading, MIP, segmentation, etc., but they have little idea of the differences between them, how they are produced, and when best to use them. Misuse of these techniques can easily generate misleading images that result in incorrect diagnosis. Even in centers that are fortunate enough to have trained 3D technologists to process images, it is still important for the radiologist to understand the type of images they are viewing, and the various limitations and strengths of different rendering and segmentation techniques. All rendering techniques have the ability to introduce significant artifacts or distortions of the data. Careful attention to detail and understanding of the basic concepts is necessary to reliably generate high-quality work.

Image Rendering Techniques

Image rendering refers to the algorithm that the workstation uses to process the data set and generate an image. There are substantial differences between the different rendering techniques. Each technique has advantages and disadvantages. Knowing when to use a particular technique and when not to is crucial to successful volumetric imaging (Table 5.1).

Table 5.1. Image Rendering Techniques

Technique	Best Use	Advantages	Limitations
Multiplanar reconstructions	**All general body, orthopedic, and neurological/spine cases (except routine brain).**	**Improves quality of almost every case. Should be part of the routine image review for almost every type of examination. No learning curve required.**	**Not a 3D imaging technique.**
Maximum intensity projection	**Blood vessels.**	**Versatile, simple, and quick technique to demonstrate vessels. Vary the thickness of the MIP slab to show more or less anatomy.**	**Other dense structures in the same image, such as bone, may obscure the vessels. Dense vessel calcification renders MIP images almost useless.**
Curved planar reconstruction	**Tortuous and calcified vessels. Many uses in general imaging, such as pancreas, bile ducts, ureters, spine, mandible and many others.**	**Single best way to show luminal narrowing in calcified or tortuous vessels or stent patency. Also has many useful applications in nonvascular imaging.**	**Can be time consuming and cumbersome to generate images if automated software not available. Learning curve may be significant, particularly for nonvascular uses.**
Surface rendering	**Musculoskeletal (MSK) imaging.**	**Excellent 3D technique to demonstrate anatomy and pathology of osseous structures. Short learning curve.**	**Much of the data are discarded to produce the image. Volume rendering is superior for almost all non-MSK applications**
Volume rendering	**Any examination that would benefit from 3D imaging.**	**Most versatile and useful 3D imaging technique. Can benefit a wide range of vascular and nonvascular cases, particularly when combined with effective segmentation techniques.**	**Effective use improves significantly with experience. Knowledge of segmentation important. Vessel calcification a significant limitation.**
Endoluminal imaging	**Colon, airways, blood vessels, and other hollow organs.**	**Allows user to look inside a blood vessel or hollow organ at the surface of that structure.**	**Use limited to certain types of examinations. Can be time consuming to be used effectively. Learning curve is significant.**

Figure 5.1. Postoperative evaluation of an odontoid fracture. (A) Oblique sagittal MPR oriented through the plane of the screw. Mild residual displacement of the odontoid is present. Position of the screw relative to the bone is well seen. (B) Oblique coronal MPR oriented through the plane of the screw. Screw is well positioned within the odontoid.

Multiplanar Reconstructions

This is the postprocessing technique most familiar to radiologists and still the most useful and versatile. In the previous chapter, methods to incorporate MPRs into routine daily practice were discussed. The quality of multiplanar reconstructions is directly related to the image slice thickness. When isotropic voxels (0.5 mm–1 mm, depending on the FOV) are used the quality of a reconstructed image in any plane is virtually identical to the original axial reconstruction. If the voxel depth is larger than isotropic, image quality can be improved by overlapping the reconstructions by approximately 50%.

Varying the amount of data to be included within each slice can easily control the thickness of MPRs. This is akin to averaging several thin slices to generate a thicker slice. One of the main advantages of reviewing images on a workstation is the flexibility to instantly create and review MPRs in any plane. Oblique and double oblique reconstructions can be helpful in many types of cases. Some examples include extremity scans, spine, cardiac, facial bones/sinuses, and even body cases to look at specific structures like the common bile duct, ureters, pancreas etc. (Figure 5.1).

Surface Rendering

Surface rendering (SR), also known as surface-shaded display, is a 3D rendering method that has been in use for many years. Early on it was used to show all types of anatomy and pathology, including vascular studies, body cases, and bone cases. Its popularity was due in large part

to the fact that SR requires a smaller amount of data than volume rendering (VR) and can therefore be implemented more rapidly and on less powerful computers. Once computers and workstations became more powerful, most of the uses of surface rendering were replaced by volume rendering. Surface rendering has remained a very useful technique for orthopedic imaging, however. It excels at showing bone surfaces and anatomy (Figure 5.2). For almost all other indications, volume-rendering techniques are generally preferred.

Surface-rendered images are created by comparing the intensity of each voxel in the data set to some predetermined threshold. The computer will include or exclude the voxel depending on whether its CT number is above or below the threshold and use this information to

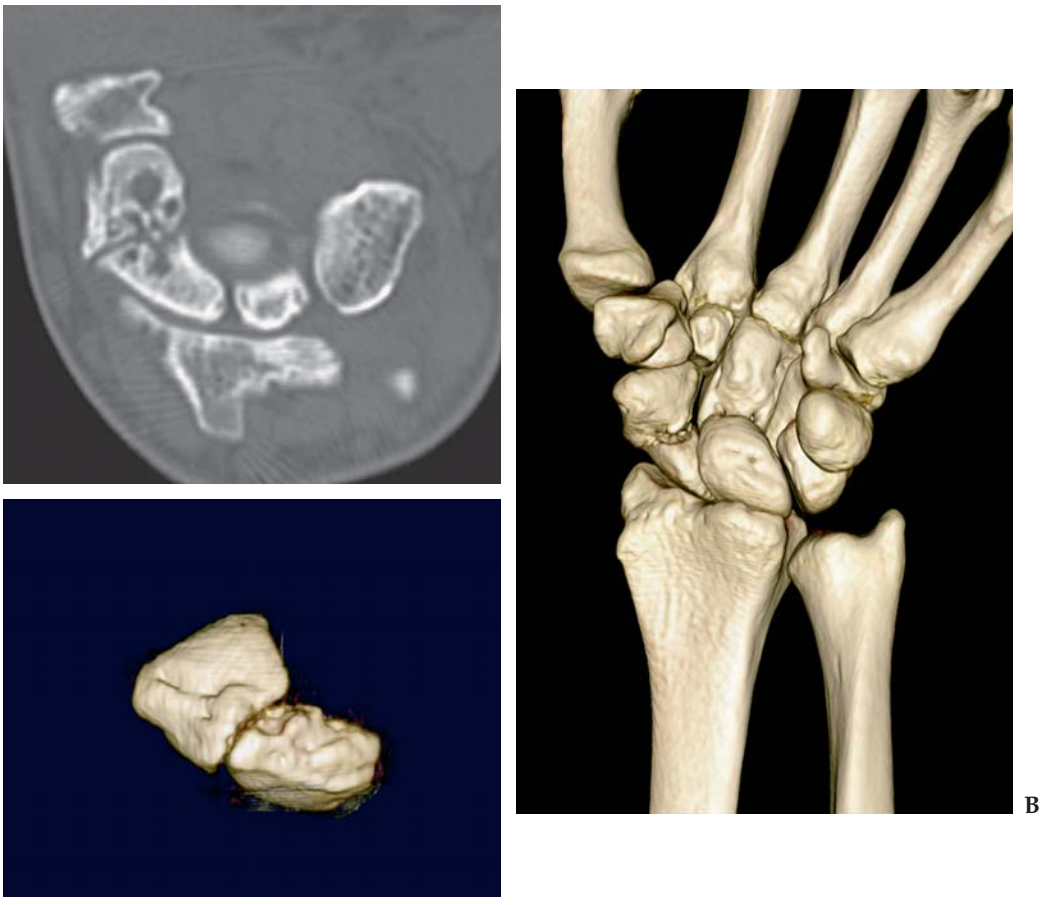

Figure 5.2. A 25-year-old with a nonunion scaphoid fracture. (A) Oblique coronal MPR along the long axis of the scaphoid. There is a scaphoid waist nonunion fracture with cystic degenerative changes in the bone. (B) Frontal surface-rendered projection image. Excellent detail of the fractured bone is present. However, none of the internal cystic changes can be appreciated on this surface view. (C) Isolated view of the scaphoid following manual segmentation of the other wrist bones. The scaphoid was manually sculpted from a series of 2D images, leaving the isolated bone. The bone can now be easily viewed from any projection to optimally demonstrate the fracture and degree of displacement.

create a surface of an object. Surface contours are then modeled as a collection of polygons and displayed with surface shading. All data that do not contribute to the surface of an object are discarded. This technique works well when surfaces are very clearly defined and there is a large density difference between an object and the adjacent tissues. This is generally the case for bone imaging.

The SR image takes on a 3D quality when a gray or color scale value is assigned to each surface that is proportional to the distance between the hypothetical vantage point and that surface. An object may be rotated in space and viewed from different vantage points, and the computer will recalculate the surface display by determining the distance between the new vantage point and the surface of the tissue of interest.

Surface rendering is an excellent way to show bony anatomy and many types of pathology as long as the bone surface is involved. The images can be rotated and viewed from any angle. Trimming or segmenting the data set to remove unwanted bone or other overlying tissues from the area of interest can make this technique even more useful.

A major drawback of SR is that the data set is converted from a volume to a surface representation, and much of the available information is discarded. As a result, surface-shaded reconstructions should not be widely used except to demonstrate anatomy of osseous structures. Even in musculoskeletal imaging this technique is limited, as any pathology that does not substantially alter the surface contour of the bone will not be shown.

Maximum Intensity Projection

Maximum intensity projection has been the most widely used technique for visualization of blood vessels for both CT and MR angiography (Figures 5.3 and 5.4). It has been widely studied and evaluated and remains a very important tool.

Maximum intensity projection images are created using a computer algorithm that evaluates each voxel along a line from the viewer's eye through the image and selects the voxel with the maximum intensity as the value of the corresponding display pixel. The resulting image is displayed as a collapsed or two-dimensional representation of the maximal intensity voxels that were present in the selected data set.

The MIP images can be generated from the entire data set or only a portion of it. Current MR angiography techniques provide excellent background suppression which allows MIP images to be easily created from the entire data set. Unfortunately, with CT angiography there is significant nonvascular background which makes MIP imaging of the entire data set frequently limited. When other high-density structures such as bone, enhancing organs, or calcifications are present and overlying the blood vessels, these structures will be averaged in with the vessels and obscure them.

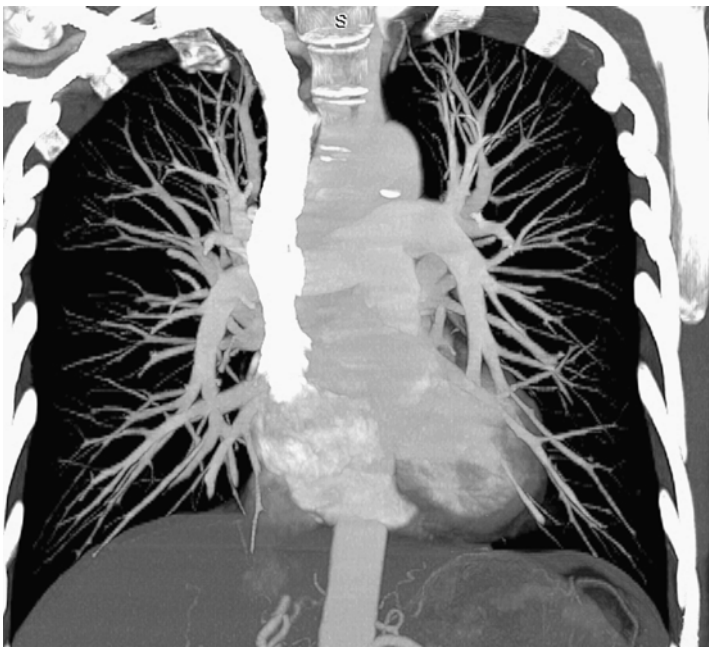

Figure 5.3. Pulmonary vessels from a pulmonary CTA. Coronal thick slab MIP image (50 mm). Exquisite detail of the branching peripheral pulmonary arteries is shown in this normal study.

Figure 5.4. Superficial femoral artery (SFA) occlusions. Volume MIP image with the bones removed. There are bilateral SFA occlusions with distal reconstitution. MIP images are superior to VR images for demonstrating the small collateral vessels.

There are two major methods for overcoming averaging effects. The first way is to segment the data set prior to display with the MIP algorithm. By removing all other high-density structures from the data set, superimposition effects can be minimized, and the remaining vessels can be displayed as a maximum intensity projection. The second method is to create the MIP image from only a portion of the data set. This has been called the variable sliding slab method. On the workstation a slab thickness can be set and the computer will use only that slab to generate the MIP image. The operator can slide through the entire data set, from one end to the other, during which time the computer will continuously update the image. The operator also has control over the slab thickness at any time. Increasing the slab will demonstrate more vessels and anatomy, but also significantly increases the likelihood of superimposition which may cause difficulty in interpretation. Thinner sections are useful to view single vessels and minimize effects of adjacent bone or calcium.

The major limitation of the MIP algorithm is vessel calcification. Neither segmentation nor thin slab MIP techniques can reliably eliminate the averaging that occurs when vessels are densely calcified. This is a major potential pitfall of the MIP technique and must be recognized by the user. In these instances other techniques such as curved planar reconstruction (CPR) must be used.

Curved Planar Reconstruction

Curved planar reconstruction is a very powerful technique that is particularly useful for demonstrating anatomy and stenosis of very tortuous and calcified vessels. It can also be applied to nonvascular anatomy and has applications throughout the body (Figures 5.5 and 5.6).

Curved planar reconstructions allow the user to designate a centerline path around which the image will be reconstructed. It is similar to a multiplanar reconstruction, but unlike that technique the reconstruction can follow any type of curve defined by the user rather than a flat plane. The images can be generated either manually or automatically, using vessel-tracking software. Manual CPRs allow the user to deposit a series of points that will define the path of the reconstruction. The points are chosen from the most appropriate plane to see the anatomy. The user can deposit points along the course of a blood vessel or along nonvascular structures such as the pancreas, common bile duct, ureter, or mandible. The primary orientation of the curved reconstruction (axial, sagittal, or coronal) is selected by the user depending on the anatomy or pathology to be demonstrated.

Many current workstations contain software applications that can substantially automate the process of generating a centerline path for curved reconstruction or vascular analysis. The function is different on different workstations, but the basic principle requires the user to select a vessel or deposit a couple of seed points along a contiguous vascular segment. The software will then automatically trace the vessel and determine the centerline path. From this information the computer can

Figure 5.5. Right iliac stents. Manually generated curved planar reconstruction through the right common and external arteries. The CPR allows a centerline reconstruction through the iliac stents which clearly demonstrates that both stents are widely patent.

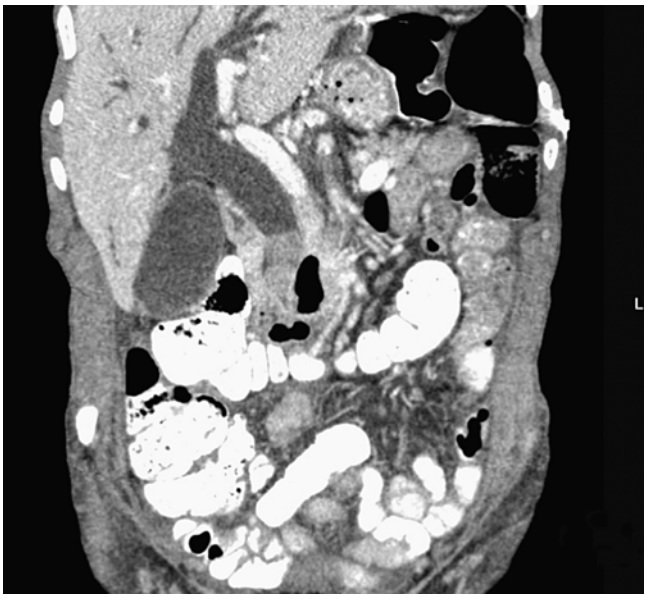

Figure 5.6. Common bile duct (CBD) stones. Coronal curved planar reconstruction through the CBD. There are two large noncalcified stones in the distal CBD with marked biliary duct dilatation.

generate a curved reconstruction along that path. Some software will also allow the user to view this reconstruction from multiple angles and generate a short axis image through the vessel to assist in measurement of luminal diameter and stenosis. Automated vessel analysis and measurement tools can also be incorporated into the software.

Volume Rendering

In recent years volume rendering has become the single most useful and versatile 3D imaging technique. It has applications in every type of examination performed with CT. With current workstations VR is quick, versatile, and extremely powerful when used as an interactive tool by an experienced user. Volume rendering is even more powerful when combined with other tools such as data set segmentation.

A great advantage of VR over other viewing techniques is that the entire volume of the data set is rendered without discarding any information. The resulting images therefore contain more information and are potentially much more clinically useful. This allows volume-rendered images to display multiple tissues and show their relationships to one another.

Volume-rendering techniques sum the contributions of each voxel along a line from the viewer's eye through the data set. This is done repeatedly for every pixel in the displayed image. The image is generated by assigning each voxel in the image an opacity value based on its Hounsfield units that will determine its contribution, along with other voxels in the same projection ray, to the final image. Unlike a MIP image that takes only the highest density value for a given ray, with VR no information is lost or discarded, and every voxel contributes to the final image. The intensity of each pixel can be determined for a tissue and applied to an arbitrary heat scale where it is assigned a color, brightness, and degree of opacity based on that scale. Usually, the tissue of most interest is rendered as the most opaque and other tissues are rendered as less opaque.

The look of the volume image can be easily varied by the computer or the user by changing variables such as the color scale, applied lighting, opacity values and window/level settings. Changing these values can have a dramatic effect on the appearance of the VR image. Changing the color scale changes the color scheme of the image. By varying opacity and window/level functions, structures can be brought in or out of view, and anatomy can be demonstrated or removed at will. This gives the user the ability to quickly classify structures based on their attenuation. For example, soft tissue can often be windowed out of volume-rendered data sets to reveal the contrast-enhanced vascular structures, without having to do time-consuming or complicated segmentation.

Most workstations contain multiple presets with predetermined values for heat scale, opacity, brightness, lighting, and window/level function. These presets are used to emphasize different tissue types for

different examinations, such as bone, soft tissue, tendons, vascular contrast, airways, or colon. The user can select a defined preset to achieve a desired look, or interactively change parameters until the desired effect is achieved. Either the image itself or a histogram of the CT data set may be used to refine the tissue definitions. From the image even simple variation in window/level settings is an easy way to emphasize or de-emphasize certain anatomy. With the use of a histogram, the height and shape of the brightness and opacity curves may be changed interactively to optimize tissue display.

A great strength of volume rendering is its interactivity. The image can be rotated and viewed from any angle. Volumes can be manipulated in many different ways to demonstrate the desired anatomy. Parts of the data set can be edited out (segmentation) or windowed out so they are transparent. In addition, a viewer can define slabs to view only a portion of the data set at a time or define cut-planes to interactively slice into the data set from any angle. These techniques are useful both for vascular imaging and general body imaging (Figure 5.7).

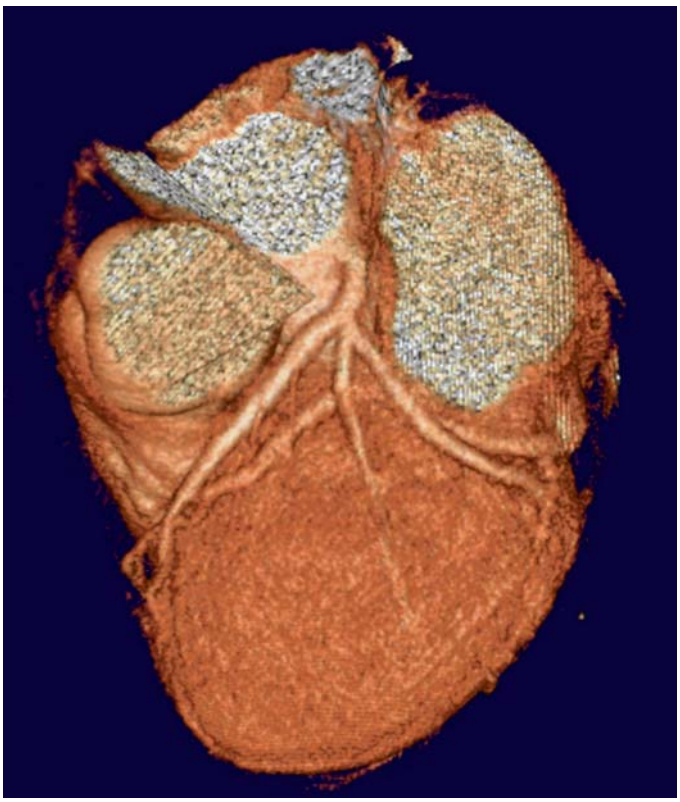

Figure 5.7. Coronary blood vessels. VR image of the heart with the aorta, pulmonary artery, and part of the left atrium segmented out to show the origin of the left coronary artery. The left main, left anterior descending, and circumflex arteries are shown. There is also a large first obtuse marginal branch from the circumflex.

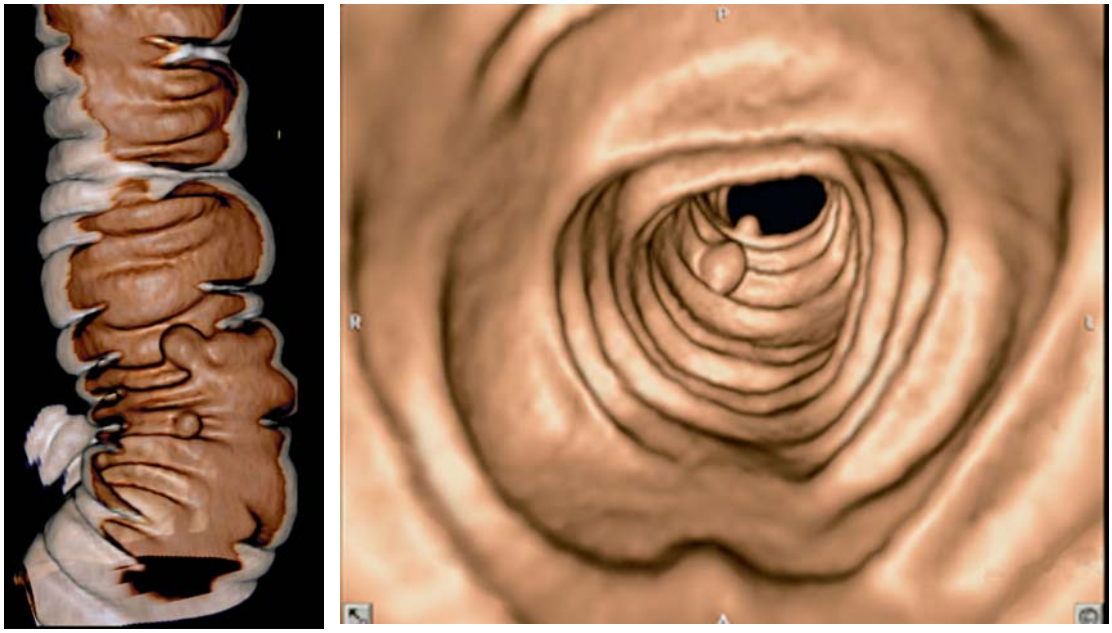

Figure 5.8. Colon polyps. (A) Endoluminal image of the descending colon which demonstrates two adjacent polyps measuring 10 mm and 6 mm. (B) Image from the endoluminal colon "fly-through" again shows the two polyps.

Endoluminal Imaging

This technique, also called perspective volume rendering, allows a user to look inside the lumen of a structure as if it were hollow and the user were inside of it. It can be applied to air-containing structures such as the colon, stomach, or trachea, or structures with high density inside such as enhanced blood vessels or a contrast-filled bladder (Figure 5.8). Once inside, a user can "fly through" the structure, giving the appearance of a virtual colonoscopy or virtual bronchoscopy.

On some workstations the software is able to automatically calculate a centerline path through the air or contrast-containing structure, allowing the user to easily negotiate the structure with minimal effort. Users also have the ability to change their virtual field of view lens, which helps them see more or less of the internal surroundings. Direction of viewing can also be easily adjusted, allowing viewers to see both forward and reverse directions. Software also helps correlate findings noted on the 3D perspective view with standard 2D images to allow better characterization of abnormalities. In addition to the standard endoluminal images, some software has features that will open up or fillet the colon, giving the appearance of a virtual pathologic specimen.

Segmentation Techniques

Segmentation refers to the process of selectively removing or isolating information from the data set with the purpose of better demonstrating certain areas of anatomy or pathology. Segmentation can be

a relatively simple process, such as trimming the CT table out of the data set or sculpting out a large structure on a 3D volume image. It can also be an elaborate and time-consuming process of manually sculpting out an entire vascular tree in a diseased aortogram and runoff.

Fortunately, current 3D workstation manufacturers have developed many powerful tools to make the segmentation process simpler and more automated. These workstations provide a myriad of post-processing techniques for editing and analyzing patient data. Manual, automatic, and semiautomatic image processing tools have been incorporated in many 3D workstations for the purposes of refining and enhancing 3D volume-rendered, surface-rendered, or MIP images. When properly performed, segmentation is an extremely helpful process that improves diagnosis and generates images that are more clinically useful and familiar to both radiologists and referring doctors.

Manual Segmentation

Manual segmentation refers to the process by which a user interactively outlines the information that is to be removed. Manual segmentation can be performed on either 2D or 3D images. For 2D sculpting, the user can outline the anatomy to be saved or discarded by drawing contour lines on a series of axial or MPR images. It is not necessary to draw contour outlines on each individual image, as the computer is able to interpolate the information from a select series of outlines for the entire data set. The number of individual image outlines needed depends on how significantly the anatomy changes from slice to slice. Once the user has specified the region or volume of interest, the software is able to apply transparency and/or color to the selected region, thereby making it invisible, semi-visible, or a distinctly different color. The user can specify whether to keep the outlined region and discard the background or to make the outlined region transparent and keep the background.

Manual sculpting can also be performed on 3D volume- or surface-rendered images. The procedure is essentially identical. The user will interactively draw contour lines around the region to be edited, and the computer will isolate or discard this region as directed by the user. Three-dimensional sculpting is generally quicker but is often less precise than a careful manual 2D segmentation.

Automated Segmentation Techniques

Automated segmentation has been one of the most important advances made recently by workstation software companies. These techniques are extremely powerful and can produce substantial time savings when a large data set is edited. All editing and rendering techniques have limitations that can lead to errors if they are not properly used, but

automated segmentation techniques are particularly prone to errors if they are not used correctly. The images generated must be carefully reviewed for accuracy by comparing them with unsegmented data.

Current 3D workstations rely on highly complex mathematical algorithms to automate the segmentation process. This is a rapidly changing area, and a complete discussion is beyond the scope of this book. Although this is a simplification, automatic segmentation relies on two basic techniques to generate an effect. These are connectedness (also known as region growing or seed detection) and thresholding. The basic concept is to select a starting point or series of several points (usually a blood vessel, bone, or other very high or very low density structure), and have the computer grow a region of interest based on contiguous pixels that fall with a specified Hounsfield unit range (threshold). In this way the computer is able to track a blood vessel or a bone and follow it as long as there are contiguous pixels that fall within a specified range. Once the region has been completed the computer can render either the selection or background transparent or semitransparent as directed by the user.

Using this technique, one is often able to track an entire vascular tree or segment out the entire skeleton with a few mouse clicks. The user is able to exert some control over how much is included or removed by varying the threshold used by the computer to connect the points. If the upper limit HU is increased, more high-density structures will be included, and if the lower limit is decreased, then more low-density structures will be included. Using blood vessels as an example, decreasing the lower HU number will help include smaller, more peripheral vessels that are less dense than the larger vessels. The tradeoff is that as the lower limit is decreased, more soft tissue background is likely to be included in the segmentation result. The same is true at the upper limit. Increasing the upper limit is necessary if the contrast is very dense, but it also increases the chance that bone will also be included in the result.

This process tends to works very well when there is a significant difference in density between structures such as soft tissue, contrast-enhanced vessels, and bone. When this is not the case, automated segmentation will often fail. Another problem is noncontiguous pixels which can occur when there are vascular occlusions or very high grade stenoses. In this case vessels may not be included in the final result. It is therefore always important to compare the segmentation result with the original data set to make sure that desired structures have not been inadvertently removed by the computer.

Seed detection or vessel-tracking software can be taken even one step further. Once a vessel has been selected and tracked by the computer, software can calculate a centerline path and generate an automatic curved multiplanar reconstruction through that vessel. It is also possible to automatically measure maximal and minimal areas of vessel diameter or area and calculate a percentage diameter or area stenosis of the opacified lumen.

Pitfalls with 3D Evaluation

As powerful as 3D workstations have become, there are numerous pitfalls that can affect both novice and veteran users. Avoiding these pitfalls is essential to providing high-quality service to patients and referring doctors. Errors related to the use of the workstation generally fall into four main categories: errors related to misuse or misunderstanding of a rendering technique, errors introduced by segmentation, errors related to artifacts in the data set, and errors caused by excessive image noise.

Rendering Errors

These errors most commonly occur when a user relies on a single 3D rendering technique without first carefully reviewing the source data or correlating with other techniques. These errors can occur in both vascular and orthopedic applications. In vascular imaging this frequently involves vessel calcification (Figure 5.9). When significant calcium is present, both volume-rendered images and thick-slab MIPs are essentially useless to evaluate the vessel lumen. It is very easy to both under- and overcall stenosis on MIP and volume images. Evaluation of the true vascular lumen requires correlation with thin-slice axial or MPR images or curved planar reformations. The MIP images are also highly susceptible to errors introduced by superimposition of other high-density structures in the same volume.

In orthopedic imaging, when viewing both volume- and surface-rendered images, one can easily miss nondisplaced fractures and bone lesions that do not involve the outer cortex. Again, correlation must be made with thin slice multiplanar reconstructions.

Segmentation Errors

Segmentation can easily introduce errors by inadvertently removing important vessels or other structures from the data set. Many times it is quite obvious that important anatomy has been inadvertently removed, but much more frequently than many users realize, this goes unnoticed. When viewed as a volume it is often impossible to identify that an important structure is absent, particularly if it is unexpected. This is especially common when automatic segmentation and vessel-tracking techniques are used. Small arteries and arteries that are stenotic may be excluded from the final reconstruction. In this way it is possible to misinterpret a stenotic vessel as occluded, or completely overlook an accessory artery (Figure 5.10). Segmentation methods can also create false areas of narrowing by removing a portion of the vessel lumen. This may occur when there is heterogeneous enhancement of the vessel caused by laminar or turbulent flow or streak artifacts from adjacent structures. On 3D reconstructions this could mimic a true stenosis.

Many of the artifacts or inadvertent exclusions introduced by segmentation are easily identified by the absence of an expected structure, but many cases are quite subtle. Errors can be introduced simply by

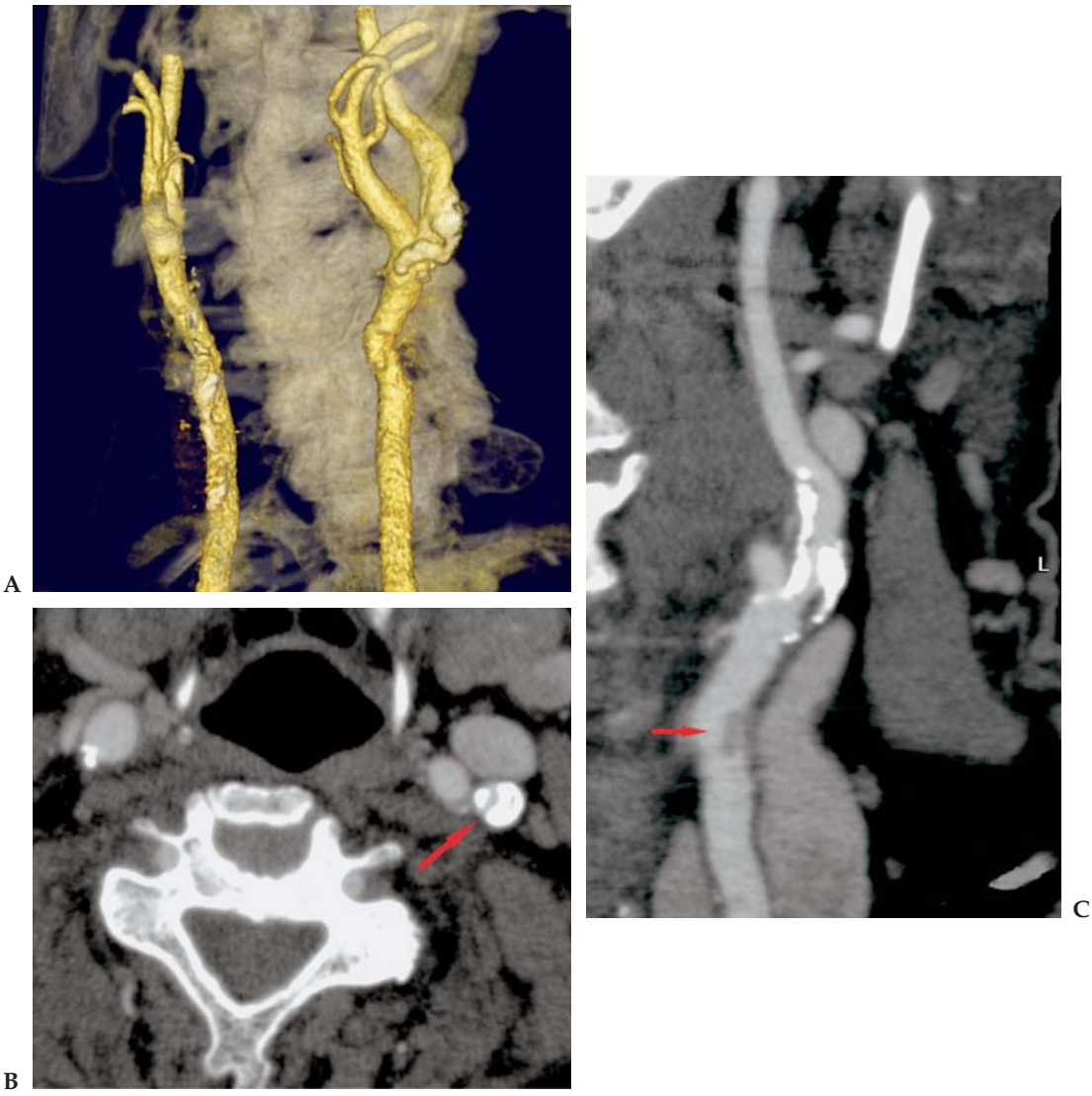

Figure 5.9. Left internal (ICA) carotid artery critical stenosis. (A) VR segmented image of the carotid arteries. The left ICA demonstrates calcific plaque. There appears to be at least some degree of stenosis, but it is impossible to accurately grade on the VR image. (B) Axial 0.5-mm image through the proximal left internal carotid artery (ICA). Circumferential calcific plaque surrounds the ICA, causing at least 90% stenosis (arrow). (C) CPR through the left carotid. The critical ICA stenosis is now demonstrated in long axis. Soft plaque in the common carotid artery (CCA) is also present (arrow).

trimming the data set. For example, when reviewing a circle of Willis CTA it is fairly common practice to trim the upper brain to better see the circle vessels on 3D. This act might exclude a pericallosal aneurysm from the data set which could then be missed by the radiologist.

The solution is again straightforward. Never depend solely on segmented images. Always review unsegmented volumes or MIPs and the thin section data. This minimizes the chance that an important finding will be inadvertently excluded and overlooked.

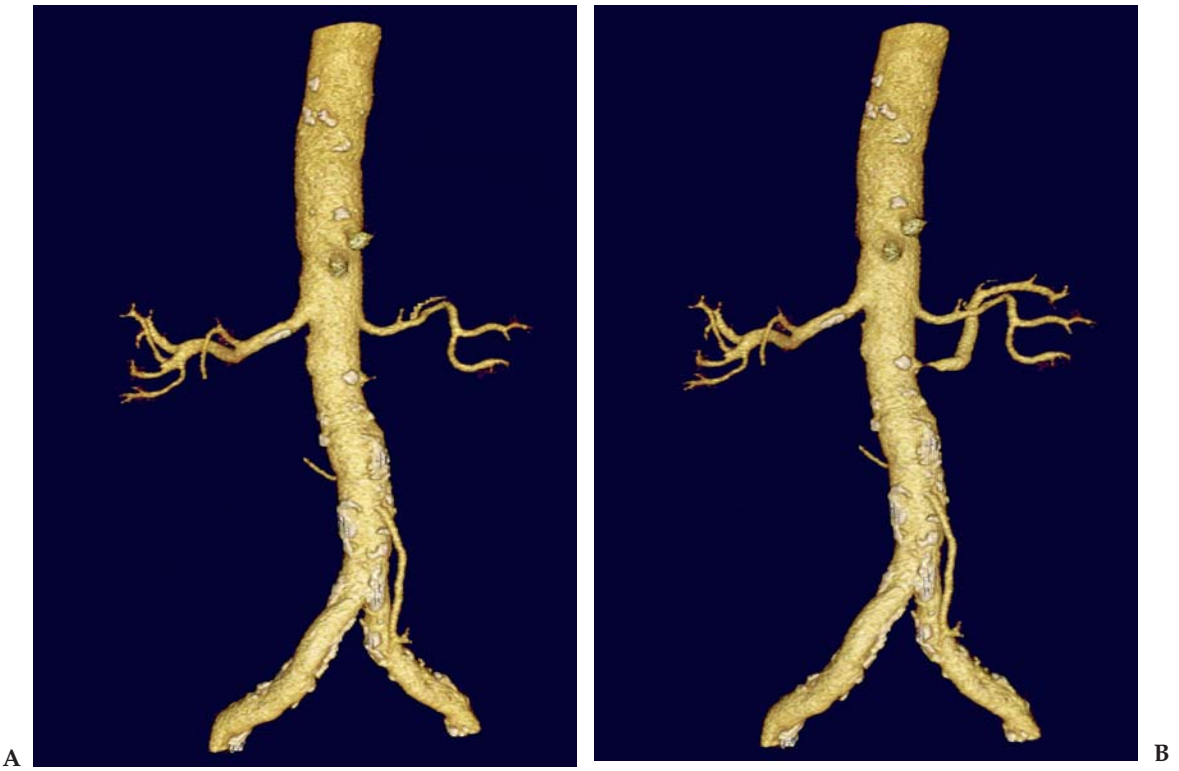

Figure 5.10. Accessory renal artery with high-grade stenosis. (A) Segmented VR image obtained after using automatic vessel-tracking software to isolate the blood vessels. Single normal-appearing renal arteries are noted to each kidney. (B) Segmented VR image after restoring the missing artery. The initial segmentation removed the stenotic accessory left renal artery. This is not unusual when severely diseased vessel segments are present. If only segmented volume or MIP images were reviewed, this vessel could easily be overlooked. Reviewing unsegmented multiplanar or MIP images will avoid this type of pitfall.

Artifacts

Artifacts in the data set that affect advanced rendering are most often associated with either some type of motion or high-density material that generates streak artifact. Motion type artifacts result from patient movement, breathing, and pulsation (Figures 5.11 and 5.12). Most of the time these artifacts are obvious and cause no problem, but more often than people realize, they can be subtle and introduce interpretation errors if careful review is not done. Motion artifacts are particularly dangerous on multiplanar reconstructions. Subtle motion can easily mimic a fracture or a vascular lesion on reconstructions. Review of the axial source image can almost always resolve the question. Motion has a typical appearance on the thin slice image with double lines and ghosting or blurring of the image outside the expected margin of the structure.

Pulsation artifacts most commonly affect the ascending thoracic aorta and are well known to generate artifacts that can mimic aortic

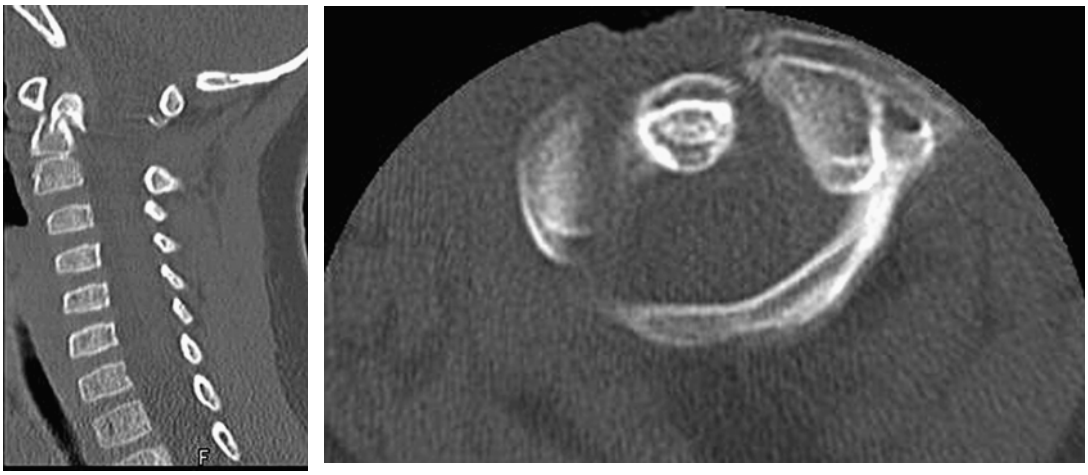

Figure 5.11. Six-year-old with a cervical spine pseudofracture. (A) Sagittal MPR shows an apparent odontoid fracture. This is an unusual fracture in children. (B) Axial 0.5-mm source image at the level of the fracture. Obvious motion artifact is present with double cortical lines and an image ghost anterior to the vertebral body. This accounts for the misregistration seen on the sagittal MPR. No fracture is present.

dissection on all images (Figure 5.13). Knowledge of this artifact and careful review of the axial images can usually distinguish a pulsation artifact from a true dissection. The artifacts are often seen on several slices involving the aortic root. They typically cause lines both anteriorly and posteriorly, often in a one o'clock and seven o'clock position. Look for extension of artifact outside the confines of the aorta.

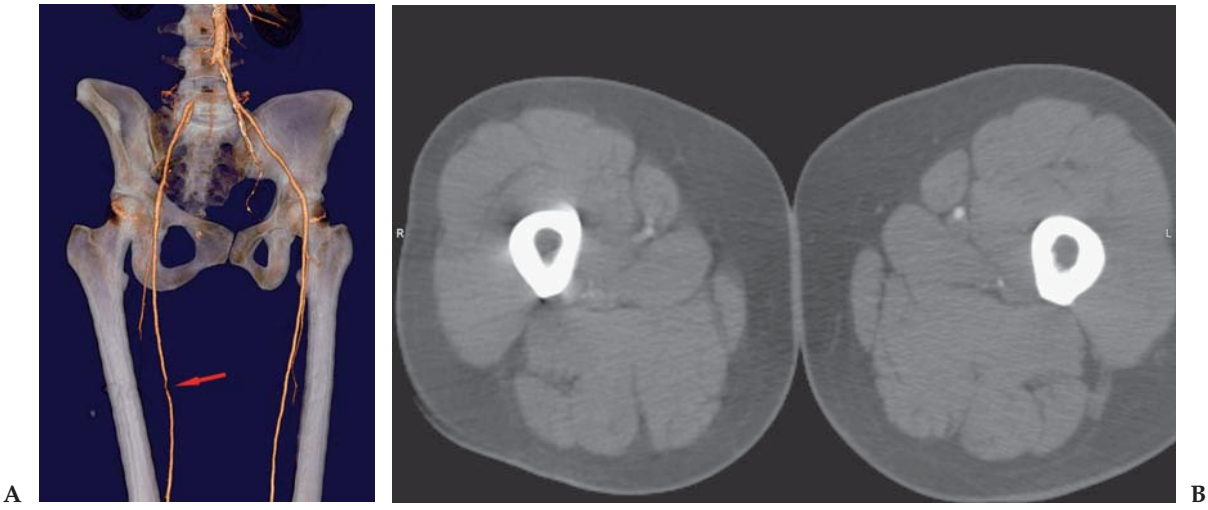

Figure 5.12. Pseudostenosis of right superficial femoral artery (SFA). (A) Volume-rendered image from a CT runoff study. The right common iliac artery is occluded. There is also an apparent high-grade stenosis of the mid right superficial femoral artery. (B) Axial 1.0-mm image. There is motion of the right leg that occurred resulting in the apparent stenosis of the SFA. Note the streak artifact from the femur and the different sharpness between the right and left legs.

This can be one of the most difficult types of artifact to recognize, even by experienced observers. In cases where a definite diagnosis cannot be made, consider repeating the examination, as the artifact rarely looks identical twice in a row. The best option is to perform or repeat the study using ECG gating, as this will generally eliminate or reduce pulsation artifacts.

Streak artifacts most often arise from metal but can also occur from dense contrast (usually in the brachiocephalic vein) and other high-density structures. Current MDCT scanners are much better at minimizing metal artifacts than previous scanners. Because of this we can now routinely image patients with joint prostheses and other types of metal hardware in place (Figure 5.14). As a result of this, many examinations demonstrate streak artifacts in the data set. These artifacts have a very characteristic appearance on source and MPR images, which is easily identified. Streak artifacts appear as straight parallel or radiating lines coming from a defined source. They are not confined to any anatomic structure.

On volume or surface images however, the appearance may be somewhat misleading. Artifacts may appear as areas of dropout, which can mimic vessel stenosis or occlusion. It is very important not to overinterpret images when excessive streak artifact is present. For orthopedic cases the 3D images can be rewindowed to minimize the artifacts and still demonstrate the relevant anatomy and pathology. In vascular cases it is best to study the vessels on the 2D source images to most accurately evaluate for disease.

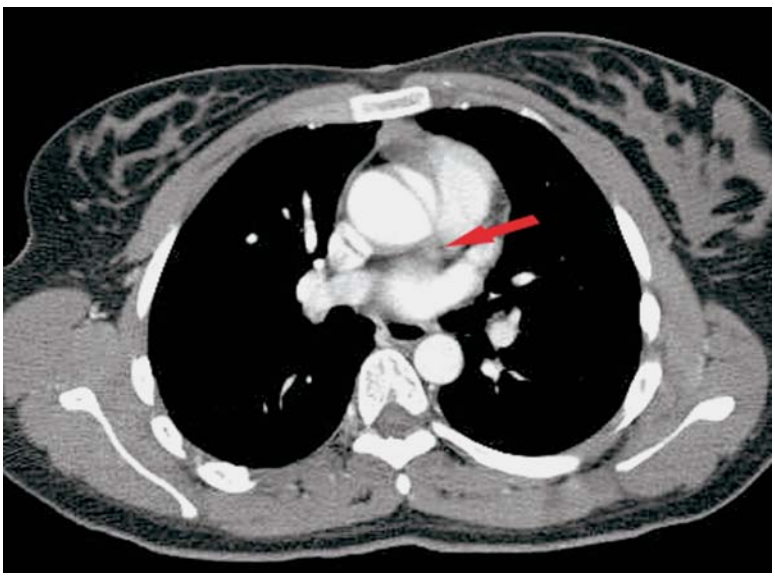

Figure 5.13. Aortic pulsation artifact mimicking a type A aortic dissection. Axial 2-mm image through the ascending aorta. There is an apparent intimal flap in the ascending aorta that is related to pulsation artifact. Notice how the line extends outside the confines of the aorta (arrow) and how artifact is also present in the SVC. This allows a correct diagnosis to be made.

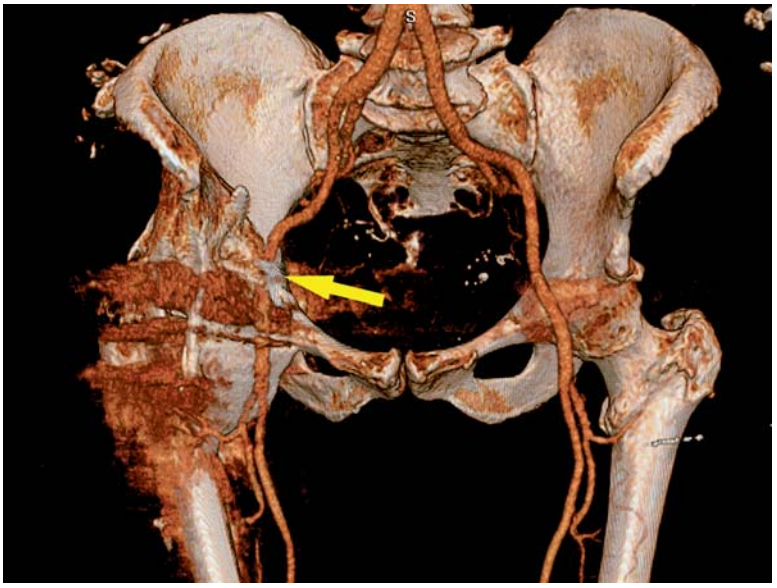

A

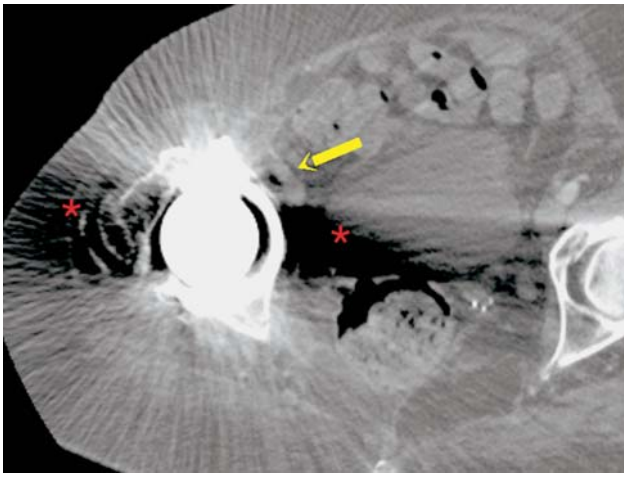

B

C

Figure 5.14. Streak artifact mimicking an iliac occlusion. (A) VR image of the pelvis from a CTA study. There is apparent occlusion of the right external iliac artery (EIA). (B) Axial 1-mm image. Extensive streak artifact is noted surrounding the patient's hip prosthesis. Typical radiating parallel lines are present as well as a dense horizontal band of signal dropout (*). The EIA (arrow) is just anterior to this band and is significantly affected by the artifact. (C) CPR through the iliac shows multiple areas of artifactual dropout, but the vessel is clearly patent.

Excessive Image Noise

This is a common problem in very large patients, even when maximal technique is used. Since current MDCT scanner tables have much higher weight limits (up to 450 pounds) than previous generation tables, much larger patients than ever before are being scanned. Excessive image noise significantly limits the utility of 3D rendering techniques. This is particularly problematic for vascular examinations and causes limitation similar to a very poor contrast bolus (Figure 5.15). The

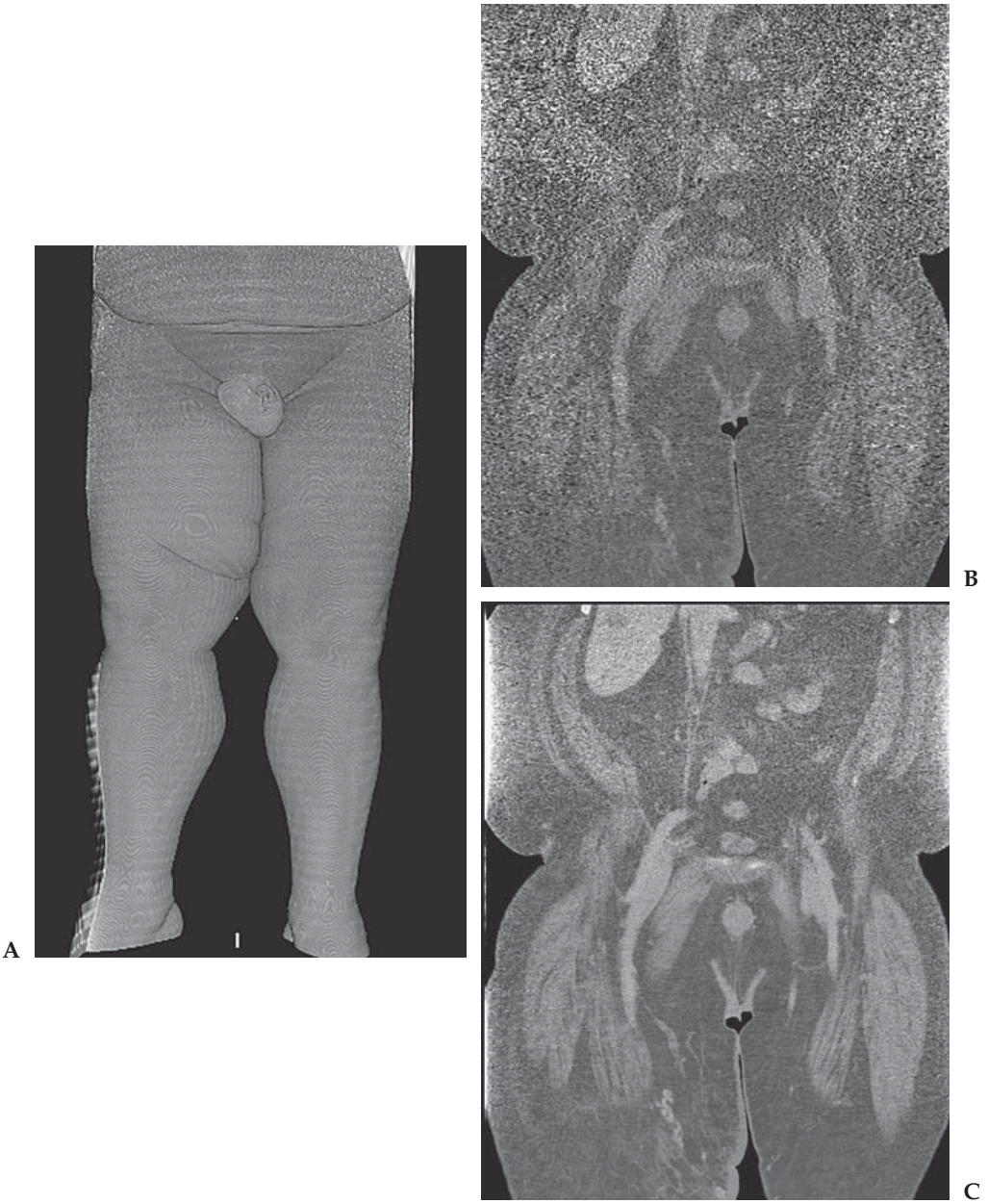

Figure 5.15. Lower extremity CT venogram in a 425-pound man. (A) SR image of the lower extremities in this morbidly obese man with leg swelling. Ultrasound could not adequately identify the veins to exclude deep vein thrombosis (DVT). The patient was also too big to fit in the magnet for an MR venogram. (B) Coronal 1-mm image from the CT venogram. Excessive image noise makes it difficult to evaluate the veins. (C) Coronal 5-mm image. Improved signal-to-noise ratio in the averaged image allows for adequate screening to exclude DVT in this man.

ability of the workstation to distinguish differences in density between the soft tissues and the contrast is poor, and the reconstructed volumes are grainy and show poor distinction between tissue types. Automatic segmentation techniques also tend to work poorly in this situation.

When faced with a very noisy study it is best to go back to MPR-type images for review. The best image quality will be obtained by reviewing thicker images than those of the original collimation. For example, if the data were acquired at 0.5 mm to 1.5 mm, then reviewing summed or averaged 2-mm to 5-mm images will produce better image quality with less noise.

The best solution for noisy images is to maximize the CT acquisition protocols for large patients. In addition to using high mAs values, other tricks include lowering the pitch and using a longer rotation speed. These modifications will also effectively increase dose to the patient, but at the expense of scan duration or coverage. Also, do not try to obtain maximal image resolution in these patients. Larger FOV with thicker slices is preferable. Careful attention should be made when using automatic exposure control techniques to insure that the images retain diagnostic quality.

Archival and Communication of 3D Images

This is an important but often overlooked step in the process of volumetric imaging. Many of the 3D images generated are of more practical use to referring doctors, such as vascular and orthopedic surgeons, than they are to radiologists. Therefore, it is very important to ensure that these images are available and communicated to the appropriate people.

Long-term storage of patient data on the workstation itself is impractical as even the largest hard drives can rapidly fill up. The easiest way to archive images from the workstation is to export them directly back to the PACS system. A collection of representative images from the examination can be selected and exported to PACS. It is also possible to export images to a color paper printer or laser printer for film archive, but this is a less desirable archival method. A CD-ROM–based archive can also be created for each patient although this is somewhat cumbersome. It is up to either the interpreting radiologist or a trained technologist to create and export the images to be archived for each patient.

Successful MDCT practices also need creative solutions to get the beautiful workstation images to their referring doctors. There are many different ways to do this. Many PACS systems have a Web-based product that will allow physicians to view images over the internet once they have been archived back to PACS. Some hospitals also have an intranet onto which images can be posted directly for review. Imaging centers and even hospitals can also use other creative approaches. A CD-ROM with the images can be created and delivered to the referring doctor. Images can be printed on a color printer and incorporated directly into the report that is mailed to the physician. Images can even be sent out with a report via email. Many options are available and different physicians will prefer to receive images in different ways, but it is up to the center to find an effective way to make them available for review.

Selected Readings

1. Addis KA, Hopper KD, Lyriboz TA, et al. CT angiography: in vitro comparison of five reconstruction methods. Am J Roentgenol 2001; 177:1771–1776.
2. Batra P, Bigoni B, Manning J, et al. Pitfalls in the diagnosis of thoracic aortic dissection at CT angiography. Radiographics 2000;20:309–320.
3. Beaulieu CF, Jeffrey RB Jr, Karadi C, Paik DS, Napel S. Display modes for CT colonography. II. Blinded comparison of axial CT and virtual endoscopic and panoramic endoscopic volume-rendered studies. Radiology 1999;212:203–212.
4. Black MJ, Sapiro G, Marimont DH, et al. Robust anisotropic diffusion. IEEE Trans Image Process 1998;7(3):421–432.
5. Choi HS, Choi BW, Choe KO, et al. Pitfalls, artifacts, and remedies in multidetector row CT coronary angiography. Radiographics 2004;24:787–800.
6. Desser TS, Sommer FG, Jeffrey RB Jr. Value of curved planar reformations in MDCT of abdominal pathology. Am J Roentgenol 2004 June;182(6): 1477–1484.
7. Farag AA, Hassan H, Falk R, et al. 3D volume segmentation of MRA data sets using level sets: image processing and display. Acad Radiol 2004; 11:419–435.
8. Gonzalez RC, Woods RE. Digital Image Processing. 2nd ed. Boston, MA: Addison-Wesley; 2002.
9. Kirchgeorg MA, Prokop M. Increasing spiral CT benefits with postprocessing applications. Eur J Radiol 1998;28:39–54.
10. Napel S, Marks MP, Rubin GD, et al. CT angiography with spiral CT and maximum intensity projection. Radiology 1992;185:607–610.
11. Nino-Murcia M, Jeffrey RB Jr, Beaulieu CF, Li KC, Rubin GD. Multidetector CT of the pancreas and bile duct system: value of curved planar reformations. Am J Roentgenol 2001;176:689–693.
12. Prokop M, Shin HO, Schanz A, Schaefer-Prokop CM. Use of maximum intensity projections in CT angiography: a basic review. Radiographics 1997;17:433–451.
13. Raman R, Napel S, Rubin GD. Curved-slab maximum intensity projection: method and evaluation. Radiology 2003 Oct;229(1):255–260.
14. Raman R, Napel S, Beaulieu CF, Bain ES, Jeffrey RB Jr, Rubin GD. Automated generation of curved planar reformations from volume data: method and evaluation. Radiology 2002;223:275–280.
15. Robb RA. Biomedical Imaging, Visualization, and Analysis. New York, NY: Wiley-Liss; 1999.
16. Roos JE, Willmann JK, Weishaupt D, et al. Thoracic aorta: motion artifact reduction with retrospective and prospective electrocardiography assisted multi-detector row CT. Radiology 2002;222:271–277.
17. Rubin GD, Dake MD, Napel S, et al. Spiral CT of renal artery stenosis: comparison of three-dimensional rendering techniques. Radiology 1994;190: 181–189.
18. Schreiner S, Paschal CB, Galloway RL. Comparison of projection algorithms used for the construction of maximum intensity projection images. J Comput Assist Tomogr 1996;20:56–67.
19. Sommer FG, Jeffrey RB Jr, Rubin GD, et al. Detection of ureteral calculi in patients with suspected renal colic: value of reformatted noncontrast helical CT. Am J Roentgenol 1995;165:509–513.
20. Sonka M, Hlavac V, Boyle R. Image Processing, Analysis and Machine Vision. 2nd ed. Pacific Grove, CA: Brooks/Cole Publishing Co; 1999.

21. Suri JS, Setarehdan SK, Singh S. Advanced Algorithmic Approaches to Medical Image Segmentation: State Of The Art Applications in Cardiology, Neurology, Mammography and Pathology. New York, NY: Springer-Verlag; 2002.
22. Udupa JK. Three-dimensional visualization and analysis methodologies: a current perspective. Radiographics 1999;19:783–806.
23. van Bemmel CM, Viergever MA, Niessen WJ. Semiautomatic segmentation and stenosis quantification of 3D contrast-enhanced MR angiograms of the internal carotid artery. Magn Reson Med 2004;51:753–760.
24. van Ooijen PM, Ho KY, Dorgelo J, Oudkerk M. Coronary artery imaging with multidetector CT: visualization issues. Radiographics 2003 Nov–Dec;23(6):e16.
25. Vos FM, van Gelder RE, Serlie IWO, et al. Three-dimensional display modes for CT colonography: conventional 3D virtual colonoscopy versus unfolded cube projection. Radiology 2003;228:878–885.
26. Whitaker RT, Breen DE, Museth K, et al. A Framework for Level Set Segmentation of Volume Datasets. Proceedings of the International Workshop on Volume Graphics. 159–168, 2001.

Chapter 6

Guide to Clinical Workstation Use

The previous chapter discussed the basic principles and concepts needed to understand and effectively use a 3D workstation. This knowledge, coupled with training on how to operate and navigate the specific functionality of the workstation, is essential to proceed with evaluation of clinical cases. Unfortunately, this is not enough. Many radiologists or technologists, when first faced with a large, unprocessed data set and a workstation, feel somewhat lost as to where to start and how to proceed. When evaluating clinical cases on a workstation it is important to have a clear plan of action for each type of case. The next section discusses the general approach to CT angiography, orthopedic imaging, and body imaging.

CT Angiography

CTA has rapidly become the single most important new technique driving the multidetector CT revolution. CTA is now widely considered to be equal if not superior to catheter digital subtraction angiography (DSA) in terms of diagnostic accuracy for many types of examinations. CTA offers certain information about anatomy and vascular pathology that simply cannot be obtained with DSA. CTA shows not only vascular anatomy and stenosis but plaque morphology and in many instances plaque characterization. The ability to view vessels in three dimensions and rotate them at will has proved extremely valuable to both radiologists and surgeons.

The diagnostic catheter angiogram is rapidly becoming an unnecessary test, and over the next few years will likely go the way of the diagnostic laparotomy. Noninvasive vascular imaging with CTA and MRA is already the norm in many institutions throughout the country. In almost all cases adequate information for diagnosis, prognosis, and treatment planning of vascular disease throughout the body can be obtained with noninvasive imaging. The one exception to this remains the coronary arteries. Cardiac CTA is steadily improving and is already a very powerful test, but at this time it is not ready to

challenge cardiac catheterization for most patients with suspected coronary disease.

Interventional radiologists should not fear a shift to noninvasive diagnostic imaging. Many more patients can and should be evaluated with CTA or magnetic resonance angiography (MRA) than were ever previously evaluated by DSA. These studies will identify many more patients with treatable lesions that can be referred for angioplasty and stent procedures. Ideally, patients will be identified earlier in the disease process while nonsurgical treatment is still possible. The vascular radiologist's focus will primarily become treatment rather than diagnosis.

General Approach to CTA

CTA is an extremely powerful tool and can be highly accurate, but it requires a certain amount a patience, dedication, and attention to detail. The process may seem deceptively simple, but there are multiple pitfalls that can lead to inaccurate diagnosis. Compared with MRA, CTA is both more powerful and more difficult. The higher resolution of CT can make more accurate diagnosis, but the lack of inherent background suppression requires much more postprocessing to be performed.

When processing and reviewing CTA, there are two separate but very important goals to keep in mind. The first goal is to make an accurate diagnosis. This goal is frequently straightforward and in many instances a diagnosis can be accurately made from the thin section or multiplanar data alone without any additional processing. The second goal is to produce images that are understandable and useful to referring and treating doctors, particularly surgeons and interventional imagers. Radiologists often overlook this goal, but it is essential to maintain a busy and sustainable CTA practice. Surgeons must have images that are familiar to them and will allow them to operate without the need for any additional imaging. If this is not accomplished they will have no motivation to refer patients for CTA. These two goals can be met routinely by following a few basic steps in every case.

The three basic steps to successful CTA are as follows: always review the thin section axial or multiplanar data, make frequent use of segmentation, and always make a diagnosis based on a combination of different methods rather than relying solely on any single rendering technique. These guidelines are true regardless of whether a technologist or radiologist initially processes the data set.

Step 1: Review the Data Set

Review of the data set should be the first step performed when reviewing a CTA examination, and it is also useful as the final step in the process before (or during) reporting of the case. During the initial review, attention should be directed to several issues. First, what is the overall quality of the examination? Focus on the degree of vascular enhancement and the presence of motion or other artifacts. Is excessive image noise present? Second, it is important to get a general idea of the extent and location of vascular pathology and, in particular, the extent of vascular calcification. This information will help guide how the

images should be processed and what techniques will be most useful. For example, if the vessels show minimal calcification, volume rendering or MIP images alone will suffice for postprocessing. However, when the vessels are heavily calcified, there is no reason to spend a lot of time with MIP or VR images, and attention should be focused on producing curved planar reconstructions.

It is generally possible to formulate a very accurate assessment of the vascular pathology in a given patient simply by reviewing the axial thin section data. Knowing where the disease is will help guide the additional processing of the case.

Finally, reviewing the source images is essential for identifying comorbid nonvascular pathology. Radiologists are responsible for everything on the images, and the number of patients with significant incidental pathology is huge. Common incidental pathology includes not only tumors of the thyroid, lung, liver, adrenal glands, and kidney, but also common benign entities such as gallstones, renal stones, hydronephrosis, bowel disease, and many other entities too numerous to name (see Figure 8.1.1E).

Step 2: Segment the Data Set

This step is not absolutely necessary in every case, and there are some cases that can be well demonstrated without using any segmentation, but in general, proper use of segmentation will improve image interpretation and is a key step to generating the kind of clinically relevant images that will satisfy referring doctors.

The task of segmenting the data set is made much easier by the use of automatic segmentation algorithms. Automatic segmentation for CTA can be performed with two different approaches. One approach is to isolate certain unwanted structures such as bone and preferentially exclude them from the data set, leaving everything else. This usually works best for patients with highly diseased vascular structures with densely calcified vessels and multiple high-grade stenoses or occlusions. The second technique is to use the contrast in the vessels to isolate the vascular tree and remove all other structures. This works best in less severely diseased vessels where flow continuity is preserved. Not every case can be successfully processed with automatic segmentation (or this option may not be available on your workstation). For these cases it is important to fall back on manual segmentation methods. Most cases can benefit from a combination of both techniques. Automated methods are used first, but then manual techniques are employed to finish cleaning up the data set and remove or isolate unwanted structures that remain.

Both 3D volume and thick slab MIP techniques benefit significantly from segmentation. The vessels are more easily visualized and can be freely rotated without overlapping high-density bone. The images generated are highly familiar to surgeons and interventional radiologists. They mimic a DSA examination but actually contain more information and allow true 3D visualization. The interactive evaluation of a segmented 3D volume rendered image is perhaps the single best feature of multidetector CTA.

There are rendering methods available that do not require the data to be presegmented. These include MPR images, thin slab MIP, and curved planar reconstructions. All of these techniques have a significant role in vascular evaluation but none of them will generate 3D images of the vascular tree that mimic a high quality DSA evaluation or allow unimpeded 3D visualization of the vessels.

Step 3: Use Multiple Rendering Techniques for Diagnosis

The importance of this cannot be overstated. Most interpretation errors with CTA result when a radiologist depends on a single rendering technique such as MIP or volume rendering to make a diagnosis. With both of these techniques, one can easily overlook significant vessel stenosis, particularly when calcification is present. Segmented volumes are even more dangerous to interpret alone, as the segmentation process can introduce many errors such as cutting off or artificially narrowing important vessels. Most of these errors can be eliminated by also reviewing one or more of the following: source axial data, MPRs, thin slab MIP, or curved planar reformations.

Realizing the limitations of relying on volume images, many radiologists find themselves reading only source and MPR images. This is also a mistake. Many types of vascular pathology are much more easily identified and diagnosed on volume images. Examples include small aneurysms, variant anatomy, collateral vessels, and often, vascular irregularity and stenosis. Full and accurate diagnosis generally requires combining review of thin section images (MIP or MPR) with some type of volume, thick slab MIP, or curved planar reconstruction. This approach should be familiar to anyone who regularly reads MRA, but I believe it is even more important for CTA.

Suggested Approach for Specific CTA Examinations

Remember the three-step approach for all examinations. I generally begin and end each evaluation with a review of the thin section axial or multiplanar images, and no examination is complete until all the images are reviewed for incidental nonvascular pathology.

Circle of Willis

Circle of Willis (COW) examinations are most frequently performed to look for aneurysms or vascular malformations or as part of the workup for stroke or TIA (Figure 6.1). They can also be performed in patients with tumors to evaluate vascularity, perform vessel mapping before surgery, and look for vascular involvement by the tumor. A good starting point is to review thin and thick slab MIP images of the circle of Willis. Slab thickness between 10 mm and 20 mm is usually best. Images should be reviewed in all three planes as these are complementary and different vessels are easier to see in different planes. After review of the circle of Willis vessels, special attention must be made to areas that are difficult to visualize. These include the petrous and cavernous carotids in the skull base as well as the ophthalmic and PICA arteries. These areas are blind spots on MIP and volume images that can hide an

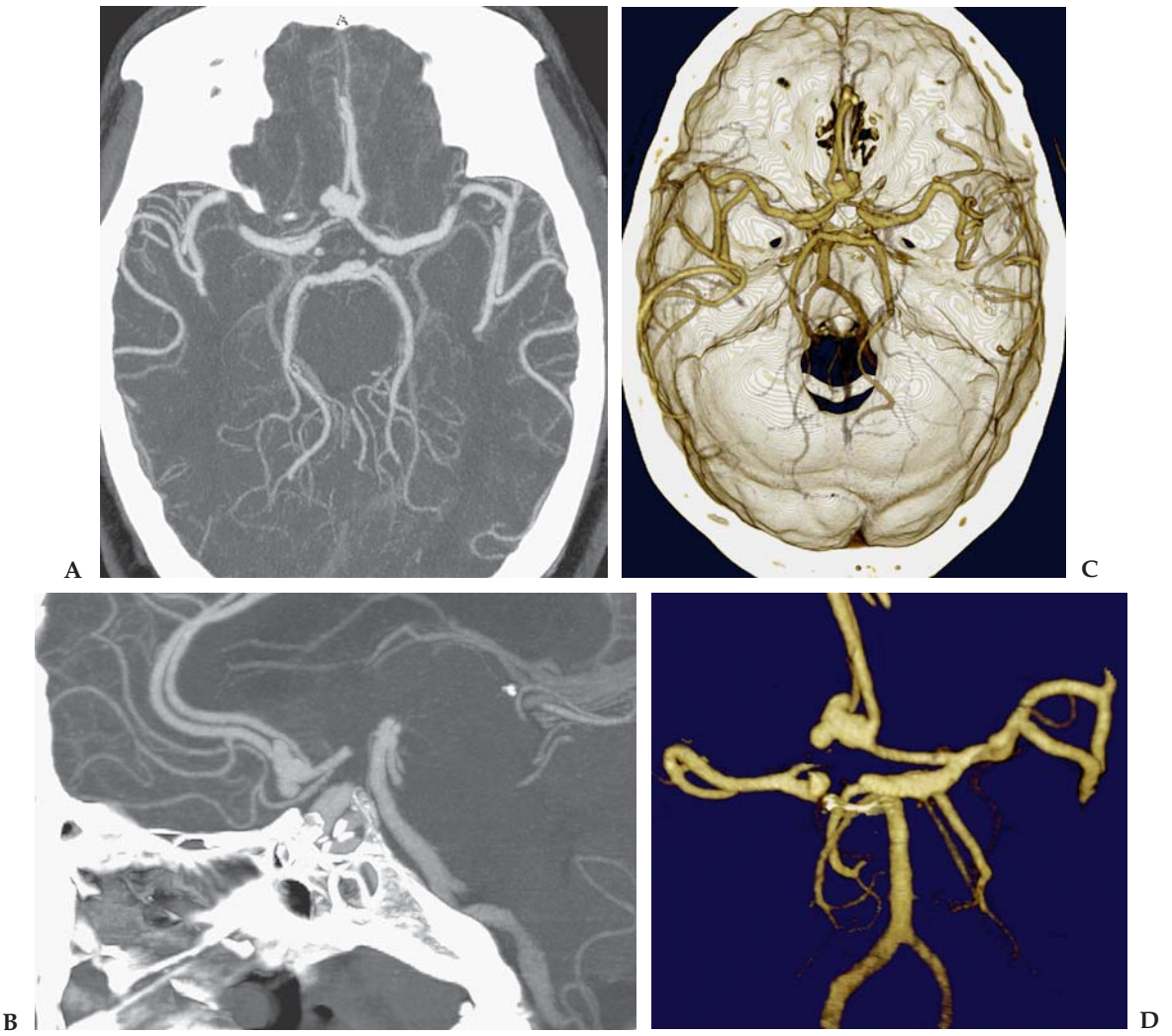

Figure 6.1. Anterior communicating artery aneurysm. (A) Axial MIP with 15-mm slab thickness. Aneurysm arising from the anterior communicating artery (ACOM) is identified. (B) Sagittal MIP with 7-mm slab thickness. This thinner slab MIP better shows the bilobed appearance of the aneurysm. (C) VR image of the circle of Willis. The top of the skull has been trimmed down to better show the vessels, but no additional segmentation has been done. Window/level has been adjusted to de-emphasize the veins. The origin of the aneurysm is now better seen. This view is also useful to the surgeon for showing the position of the aneurysm relative to other vessels. (D) Segmented VR image. The skull has been sculpted away from the circle using manual sculpting. The neck of the aneurysm can now be optimally evaluated by rotating the vessels into the most advantageous projection.

aneurysm or stenosis. Review of MPR or very thin slab MIP images of these areas must be done.

After review of multiplanar and variable-slab MIP images, focus on volume-rendered images. Volume images may demonstrate small aneurysms or areas of vascular narrowing that can be more difficult to identify on MIP or source images. Unsegmented volume images can be rapidly reviewed by trimming the data set on the top and bottom. This

allows for easy 3D visualization of the circle of Willis with the bony landmarks of the skull base in place.

Segmentation of the data set can be extremely helpful and allows the circle of Willis to be rotated along any axis in three dimensions. The COW is a challenging area to segment and automated methods do not work well for many cases. I prefer to manually segment the data, including the circle and as much of the vertebrobasilar system as possible. These images are excellent for identifying small aneurysms. The vessels in the skull base are generally not visualized with this method, however, and must be viewed separately.

Arch and Carotids

The challenge for this examination lies in the dense calcification that is often present at the carotid bifurcation. For evaluation of the aortic arch, coronal thin slab MIPs (10 mm–20 mm) are easily done and usually are all that is needed. Attention should be focused on the origins of the common carotid arteries and the vertebral origins. Correlation with axial, sagittal, and coronal MPRs can be made in difficult cases with calcified vessel origins.

Evaluation of the carotid bifurcation when calcification is present is best done with curved planar reformations with axial and oblique MPR correlation (Figure 6.2). Tools that generate automatic curved reconstructions are extremely helpful for the carotids. Curved reconstructions are very useful for measuring the diameter of stenosis. Measurements are obtained at the narrowest point of the vessel lumen, and again where the vessel appears to be normal in caliber distal to the stenosis. Confirmation of the stenosis measurement should also be made on a true axial cross-section image. Patients without calcification can be evaluated with either volume rendering or MIP images.

Volume images are useful in all patients to demonstrate the anatomy and show the surgeon where the bifurcation is relative to important bony landmarks. I always take either unsegmented volume images or images with a ghost of the bony landmarks in place for this purpose, but I rarely try to interpret the extent of disease based on the volume images alone.

Chest CTA

Chest CTA is generally done either to rule out pulmonary embolus (PE) or to evaluate the thoracic aorta (or sometimes both) (Figure 6.3). Chest CTA for pulmonary embolus is best evaluated by review of thin slice axial and coronal images. These images are the most sensitive for identifying filling defects within the vessels. Accuracy can be improved even further by also reviewing sliding thin and thick slab MIP reconstructions. Thicker slab MIPs (20 mm) are best for identifying abrupt vessel cutoffs in smaller peripheral pulmonary arteries. Volume images add little to a PE study.

Thoracic aorta studies are approached differently than a PE study. Axial and oblique sagittal images are first reviewed to evaluate for aortic dissection. If a dissection is present, axial, oblique sagittal, and slab MIPS are most useful for evaluation. Volume images are best to show the anatomy of the aorta and great vessels and to demonstrate

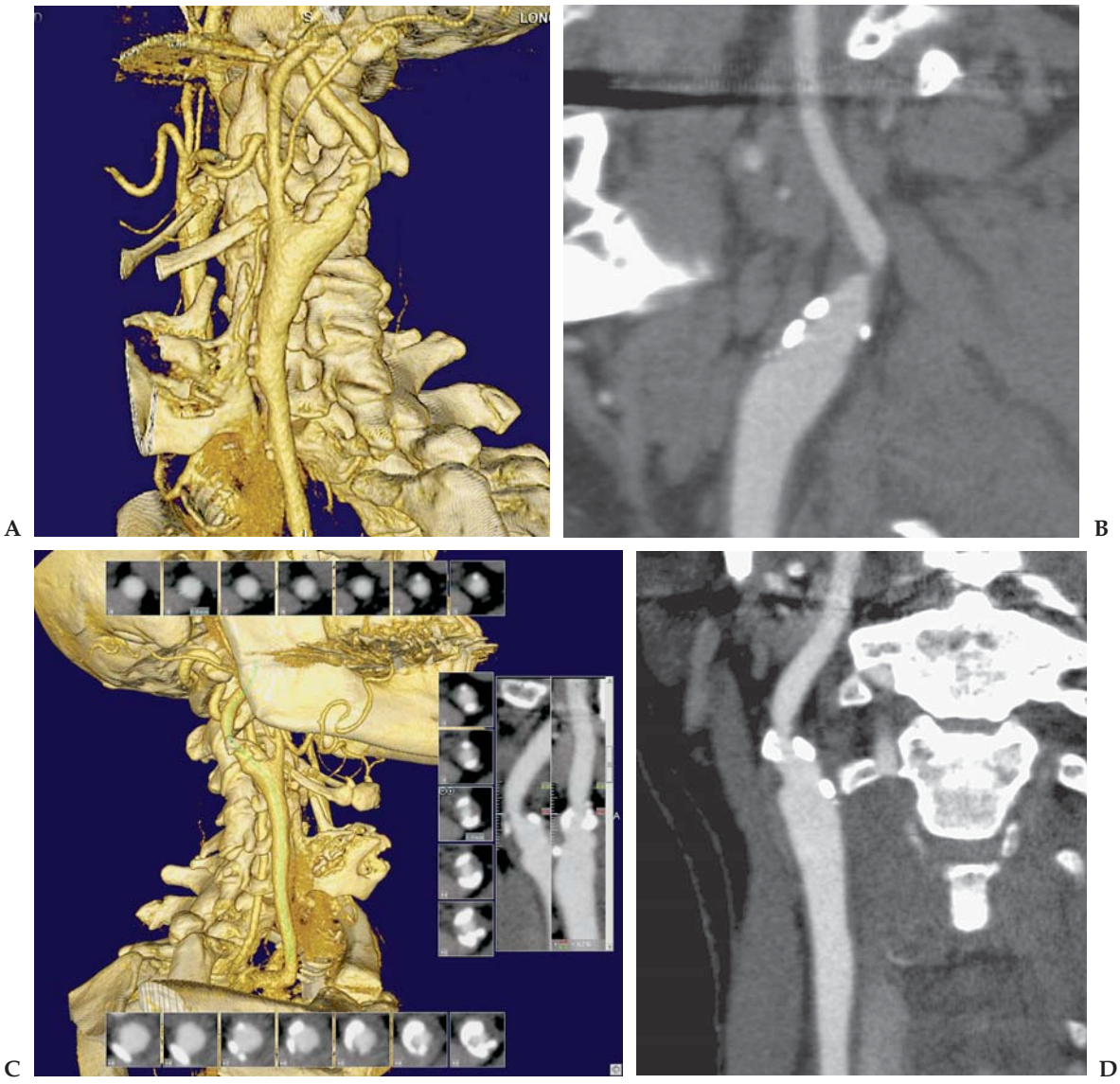

Figure 6.2. Bilateral carotid artery stenosis. (A) Lateral unsegmented VR view of the left carotid artery. A critical stenosis of the ICA is present 1.5 cm distal to the origin. (B) Sagittal CPR through the left ICA. Vessel-tracking software has been used to create this curved image. The stenosis is near occlusive, approximately 95%. (C) Volume-rendered view of the right ICA using the vessel probe tool (vessel tracking) to produce two orthogonal curved reconstructions with corresponding axial cross-sections through the centerline path. The right ICA demonstrates extensive calcified plaque. The vessel lumen is measured in the stenotic region on the short axis cross-sections and compared with the vessel diameter where it appears normal. This allows for calculation of 62% stenosis in this patient. (D) Corresponding coronal CPR of the right ICA stenosis. This image is another way to display the vessel using the same tool as in image C. Stenosis could also be measured and calculated on this image.

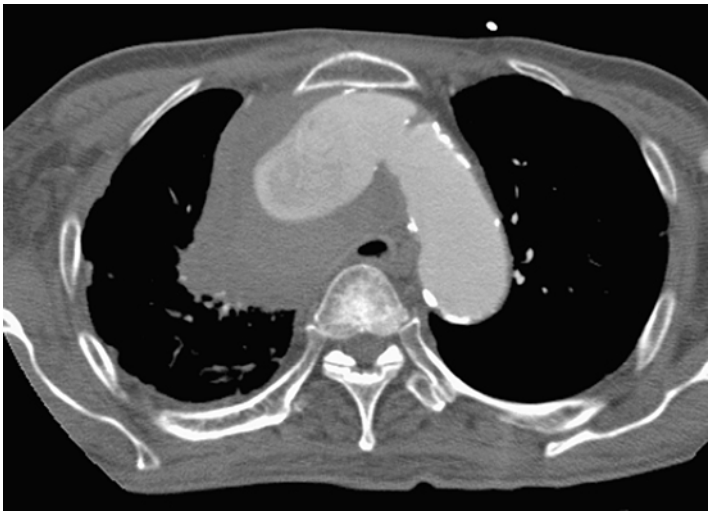

A

B

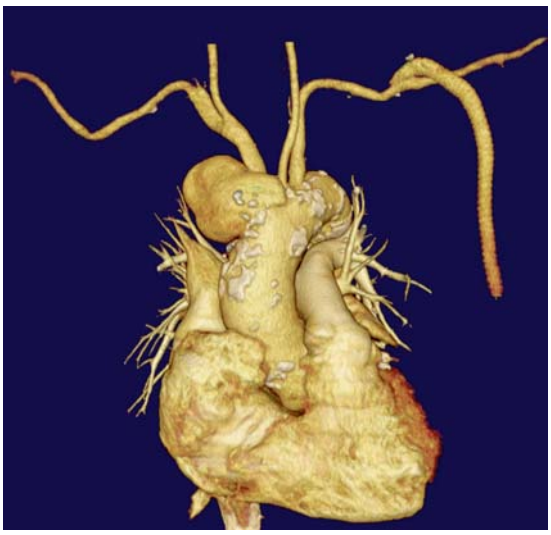

C

Figure 6.3. Ruptured mycotic aortic aneurysm. (A) Axial 3-mm image through the aortic arch. There is a large mediastinal hematoma present adjacent to a large saccular aneurysm of the aortic arch. (B) Coronal MIP image of the aorta. The hematoma and large aneurysm adjacent to the brachiocephalic artery is demonstrated. (C) Volume rendered image of the chest vessels using automated segmentation to isolate the vessels from the bony thorax. The volume image better shows the saccular nature of the aneurysm and its relationship to the aorta and great vessels. The MIP images have the advantage of also showing the mediastinal hematoma. Also note the presence of a left axillary-femoral graft. The graft has slow flow and is incompletely filled.

an aortic aneurysm. Segmentation to remove portions of the heart, pulmonary arteries, and bony structures will optimize depiction of the aorta on the volume-rendered images when pathology is present. Automated segmentation methods generally work quite well for the thoracic aorta. Visualization of the origins of the great vessels may require the use of oblique thin section data or curved planar reformations, particularly if the vessel origins are narrowed and heavily calcified.

Coronary Artery CTA

Coronary CTA is now commonly performed to screen patients for coronary artery disease or anomalies, to evaluate patency of bypass grafts or stents, to evaluate coronary veins for pacemakers or pulmonary veins prior to an ablation procedure, or to evaluate for cardiac masses. Current 64-channel scanners now even make it possible to evaluate patients with acute chest pain as part of a comprehensive CT evaluation of the aorta, pulmonary arteries, and heart in a single acquisition.

Review of coronary artery CT is best done with a combination of 3D and MIP/curved reconstructions. Three-dimensional volume rendering is useful for demonstrating the coronary anatomy and can also show stenosis if there is not significant calcification present. Manual segmentation is generally needed to remove a portion of the pulmonary artery and left atrial appendage in order to see the left main and proximal anterior descending and circumflex arteries. In addition, the diaphragm must be removed to show the right coronary artery (RCA) along the base of the heart and the posterior descending artery.

To evaluate for stenosis, oblique thin slab MIP or curved MIP images are most useful (Figure 6.4). Curved reconstructions are generally superior and can be generated manually or by using advanced vessel-tracking software to automatically calculate the centerline path through the vessel. In this way, the entire vessel can be depicted on one image showing vessel lumen as well as the presence of soft or calcific plaque.

Evaluation of the pulmonary veins prior to radiofrequency ablation depends on segmented MIP and volume-rendered images to demonstrate the 3D anatomy of the veins. Vessel origins are measured and reviewed from thin section axial or coronal images. In addition, endoluminal imaging to demonstrate the ostia of the vessels is also commonly performed.

Abdominal Aorta and Peripheral Runoff

Common indications for these studies include abdominal aortic aneurysm, renal artery stenosis, mesenteric ischemia, abdominal bleeding, claudication, leg ulcers, and other manifestations of peripheral vascular disease (Figure 6.5). The coverage of the study will depend on the indication, but the postprocessing approach is similar. The difficulty of processing these examinations can be highly variable, ranging from straightforward to highly complex, and a somewhat methodical approach is needed. When evaluating a full aortogram and runoff, it is often helpful to break up the data set into two or three more manageable segments (again mimicking a conventional DSA examination).

After reviewing the axial data, I suggest segmenting the data set using either an automated vessel-tracking tool or a threshold tool to remove bone. Once segmented, 3D volume-rendered images should be reviewed. In patients with mild disease and minimally calcified vessels the volume images may be all that is needed, but in patients with calcified vessels and more extensive plaque, more work is needed. Volume images are optimal for demonstrating general vascular anatomy, occlusions, and collateral vessels. Focal stenosis may or may not be adequately demonstrated with volume rendering.

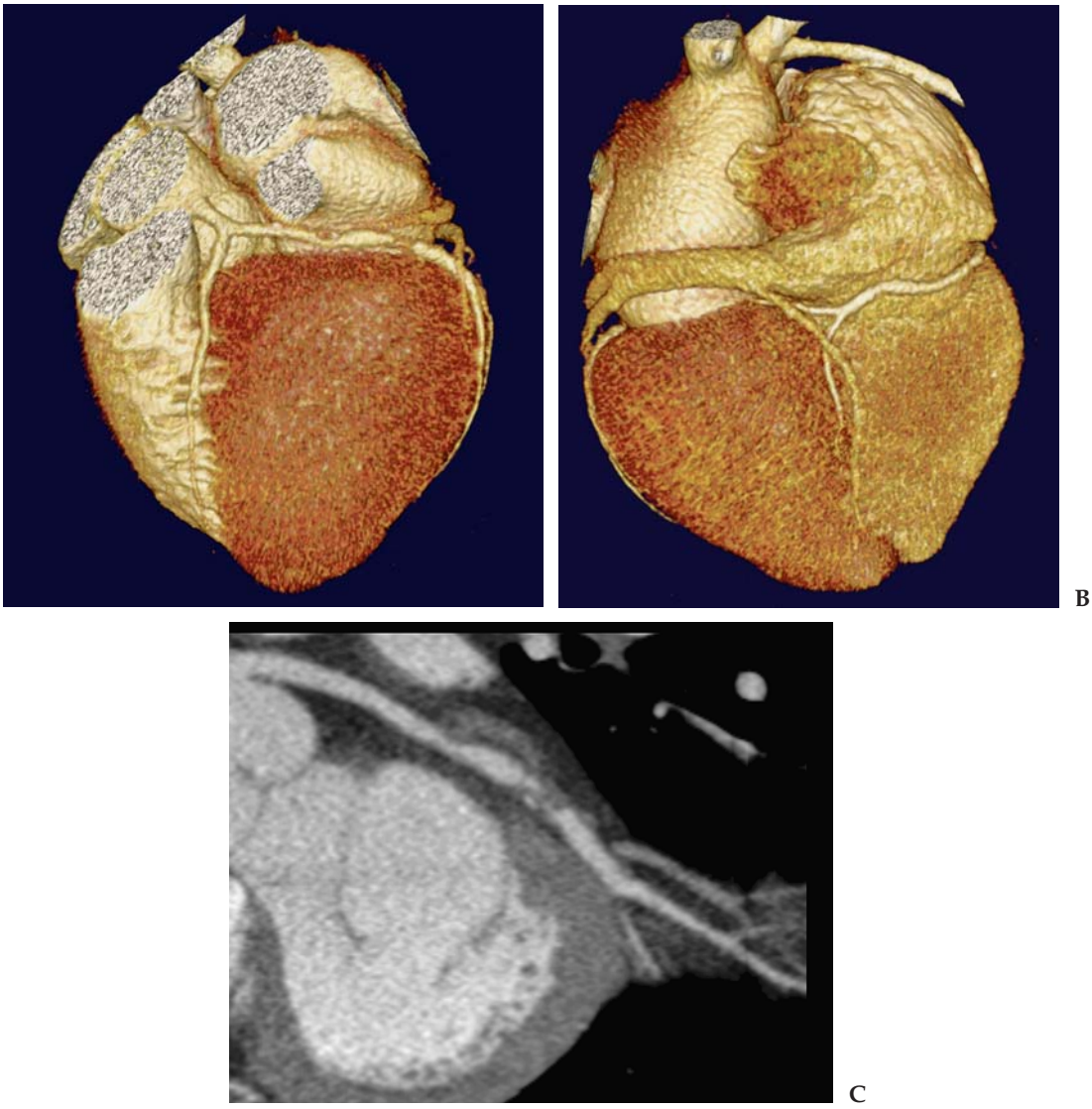

Figure 6.4. Circumflex artery stenosis. (A) Segmented volume-rendered image of the heart showing the left main, left anterior descending (LAD), and circumflex arteries. Segmentation has been performed primarily using manual sculpting from the 3D image to remove a portion of the aorta, pulmonary artery, and atrial appendage. Two areas of stenosis are present in the circumflex artery. The left main and visualized LAD appear normal. (B) Segmented volume-rendered image at the base of the heart showing the distal RCA, posterior descending artery, and coronary sinus. The diaphragm has been sculpted away to allow visualization of these structures. (C) Curved planar reconstruction of the circumflex artery generated using vessel-tracking software. There is extensive soft plaque in the vessel wall. The more distal lesion is at least a 90% stenosis. (Images courtesy of Dr. Albert de Roos.)

After reviewing the volume images, potentially stenotic segments of artery should be identified and further evaluated as needed. Thin section MPR and MIP images are often useful. Many stenoses, particularly in the renals, iliacs, and superficial femoral arteries, are best evaluated with curved planar reformations. Many workstations have automated methods to generate curved planar reconstructions through

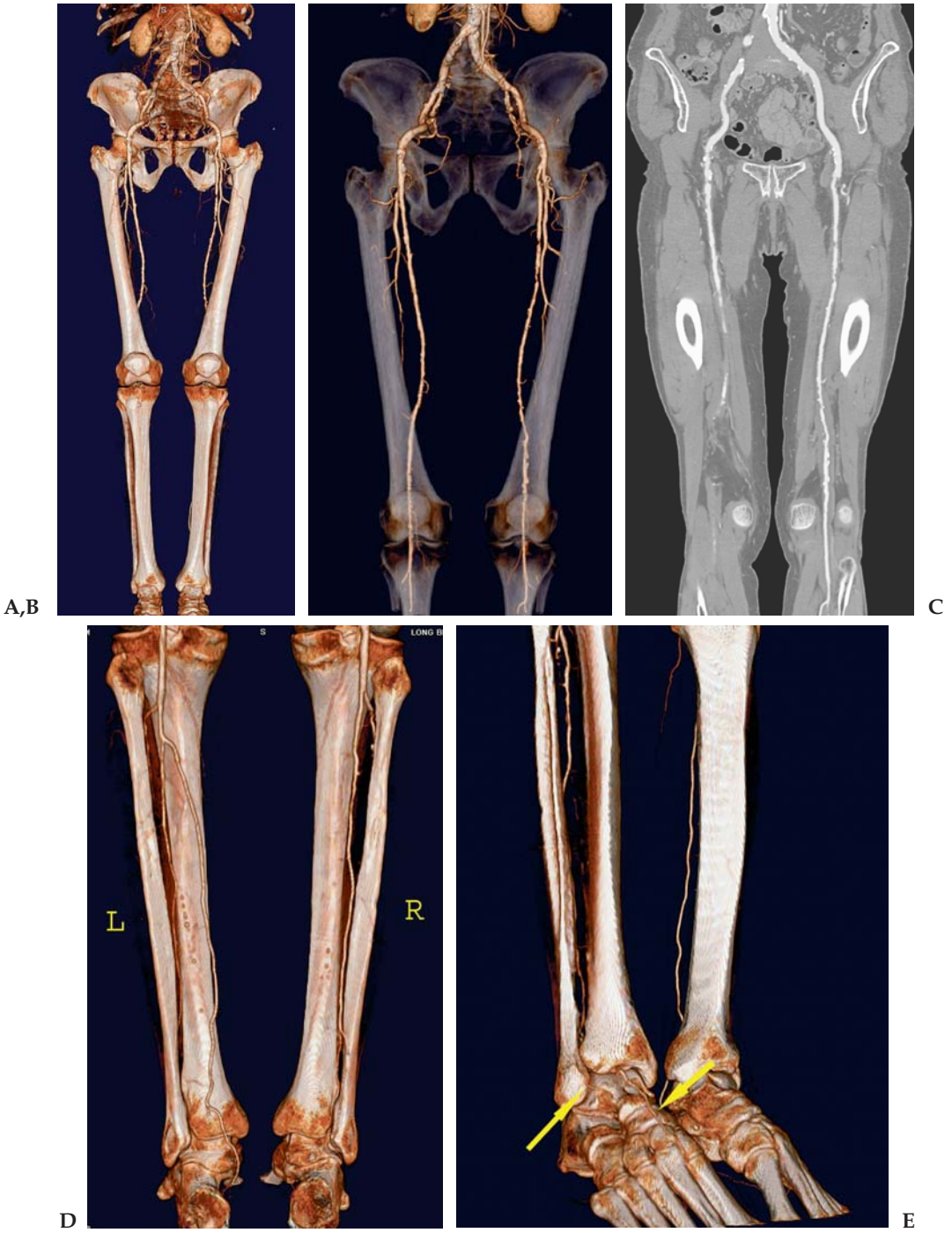

Figure 6.5. Peripheral vascular disease. (A) VR image of the full runoff. This is the starting point for the workup. (B) VR image of the pelvis and upper leg. The vessels have been isolated using automatic vessel-tracking software. A ghost image of the bones has been added as a semitransparent background. There is calcified plaque in the left common iliac artery that will need further workup. Several high-grade lesions are present in the left SFA. (C) Coronal CPR through the left iliac and SFA. There is no significant disease in the iliacs, but there are multiple high-grade lesions in the SFA and popliteal arteries. (D) Posterior VR projection of the lower legs with no segmentation. The left side shows a patent peroneal and a large patent posterior tibial artery. On the right only a peroneal artery is patent, but it occludes proximal to the ankle. (E) Oblique VR projection with no segmentation. The right anterior tibial artery is occluded but the dorsalis pedis artery (arrows) reconstitutes via collaterals from the peroneal circulation.

diseased vessels. If this is not available or does not work in a case, manual curved reconstructions can be generated.

Arteries below the knee present a unique challenge. Because of their small caliber and proximity to bone it is frequently difficult or impossible to segment the bone from the vessels without removing some or part of the artery. I use unsegmented volume images in conjunction with MIP images to best show the vessels around the foot and ankle. It is very important to correlate these images with the thin section source data, which are the most accurate for demonstrating vessel patency and stenosis.

Orthopedic MDCT

After CTA, orthopedic imaging has been the most important new growth area for advanced MDCT imaging. Extremity imaging has benefited tremendously from isotropic data acquisition. The ability to scan once and generate oblique images in any plane with no loss of resolution is key for high-quality extremity evaluation. It is no longer necessary to position patients who are already in pain into uncomfortable positions in order to obtain diagnostic images. A second major advance in orthopedic imaging is the ability by current scanners to minimize scatter artifacts from metal. This enables diagnostic scans to be performed and interpreted in patients with spinal rods, joint prostheses, and other orthopedic hardware.

The three basic postprocessing steps outlined for CTA also apply to muskuloskeletal cases, but in general these cases are more straightforward to process and interpret. Many cases do not require any segmentation, but this remains an extremely valuable tool in some cases to isolate affected bones or disarticulate joints to show pathology and allow it to be rotated in three dimensions. The most useful visualization methods for orthopedic MDCT are multiplanar reconstructions, surface-rendered images (with or without segmentation) and volume rendering.

Approach to Orthopedic CT

MPR Images

MPR images are the best way to identify fractures, fracture healing, bony lesions, and most other types of significant osseous pathology (Figure 6.6). Joint and extremity evaluation can be significantly improved by using oblique or double oblique reconstruction planes. Oblique reconstructions can be performed by the technologist at the scanner console or by the radiologist on the PACS or 3D workstation. It is a simple procedure but greatly improves diagnosis. Applying a sharpening filter to the images as they are reconstructed on the scanner can enhance bone detail on the MPR images (but this may adversely affect quality of 3D reconstructions). A similar effect can also be achieved by applying an edge enhancement postprocessing algorithm on the PACS workstation. If a bone algorithm is used on the scanner, images should generally also be reconstructed in a standard or soft

A B

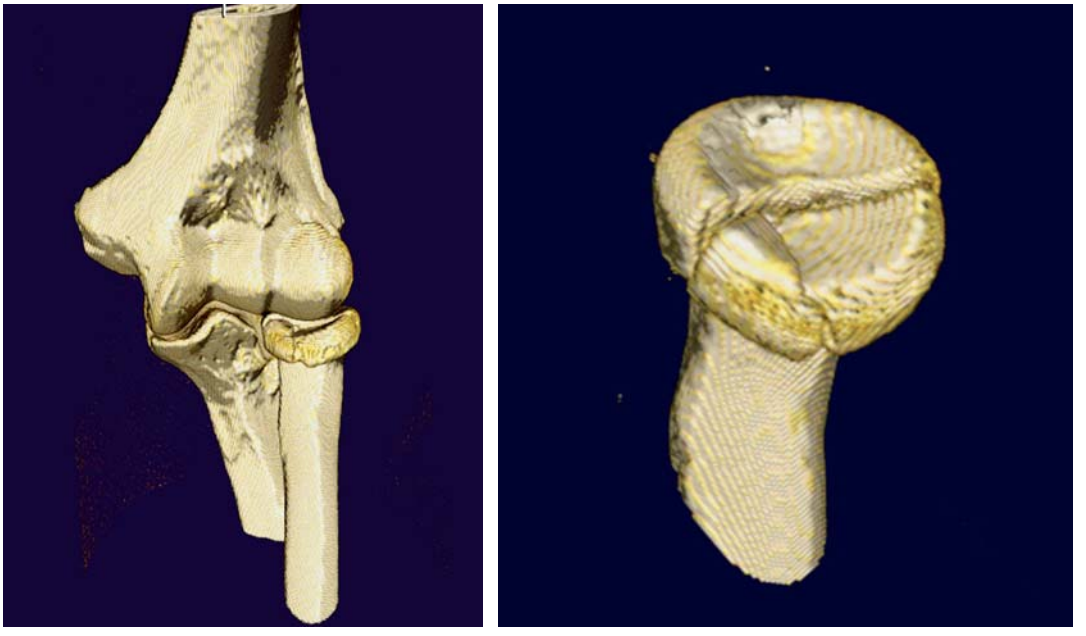

C D

Figure 6.6. Radial head fracture. (A) Double oblique coronal MPR oriented along the long axis of the radius. A comminuted intra-articular radial head fracture is present. Detail is much better appreciated on this oblique image than on a true coronal. (B) Double oblique sagittal MPR again shows the radial head fracture. (C) SR image of the elbow showing the fracture relative to the ulna and humerus. (D) SR image of the radial head. The other bones have been segmented out using a combination of automated and manual techniques. The articular surface of the radius with the depressed fragments can now be appreciated. This image is very helpful to the surgeon to plan surgical repair if indicated.

tissue algorithm that is superior for visualization of soft tissues and 3D reconstructions.

Surface-Rendered and Volume-Rendered Images

Surface rendering is generally the most useful 3D visualization technique for bone cases, but volume rendering is also useful and the two techniques are often complementary (Figure 6.7). These images excel in depicting anatomy and anatomic relationships. This is especially helpful for displaced fractures, destructive bone lesions, and anatomic variants. Lesions that involve only the marrow, without cortical involvement, are generally invisible on surface-rendered images. Also, many nondisplaced fractures are very difficult to see and are much better shown on the MPR images. VR images can be used to show both soft tissue and bone detail. For example, it is possible to use window/level and transparency settings to allow visualization of both bone and tendons or ligaments.

Surface images are also very helpful for demonstrating hardware. By adjusting window and level and opacity settings, streak artifacts can be minimized, highlighting anatomic relationships between metal and bone. By further windowing the image (or changing the threshold for the surface reconstruction) bone can be completely eliminated from the image leaving only a 3D image of the hardware, which can be rotated freely and evaluated for any sign of hardware failure. It is also possible to apply color to the hardware and restore the colorized hardware to the original image.

Segmentation

Simple segmentation techniques can greatly improve the quality of surface-shaded or volume images. In many cases a simple trimming of the data set to remove overlying soft tissues or osseous structures that limit visualization of the pathology can significantly improve demonstration of anatomy or pathology. Other cases will require more advanced techniques to remove structures in close proximity to the affected bone, i.e., disarticulating a femur to better demonstrate an acetabular fracture. This can often be accomplished with simple automatic segmentation techniques; however, some cases will require more time-consuming manual segmentation. Once isolated, the bone can be viewed on surface-rendered images as a three-dimensional object. These surface images may not be absolutely necessary for the radiologist to make a diagnosis, but they can be extremely useful to an orthopedic surgeon for treatment planning and communication with the patient.

Body Imaging

Most body cases can be adequately reviewed without use of a 3D workstation, particularly if multiplanar reconstructions are regularly viewed on a PACS workstation. Workstation review can be a tremendous problem-solving tool, however. Oblique images, volume-rendered images, MIP, and curved planar reconstructions can all be valuable tools in certain cases. These tools can be so useful that many people

A

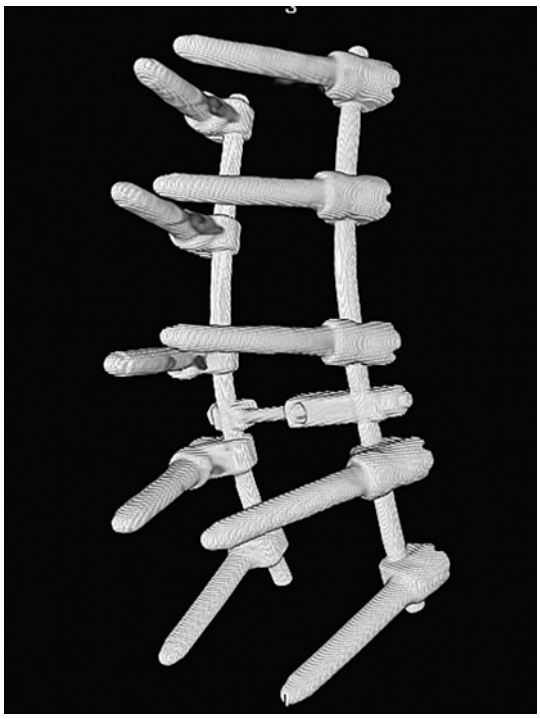

B

C

Figure 6.7. Spinal fusion. (A) Coronal MPR image in a patient who has undergone extensive laminectomy and fusion. The laminectomy, bone graft, and pedicle screws are shown on this image. (B) Surface-rendered image of the patient's spinal hardware. The bone and soft tissues have been windowed out of the image. The hardware can be evaluated for signs of failure. (C) Volume-rendered image in the same patient. The hardware has been colorized red and fused into a semitransparent volume image. The hardware, laminectomy defect, and bone graft are all well shown on this image.

choose to read all of their cases on the workstation. This solution is powerful but probably not practical for most sites. I do strongly recommend frequent use of the workstation in a wide range of cases.

It is impossible to describe all of the possible uses for the workstation in body imaging as the role will vary from case to case. One common indication is to use volume or MIP images to demonstrate vascular abnormalities that may not have been suspected (Figure 6.8). Both

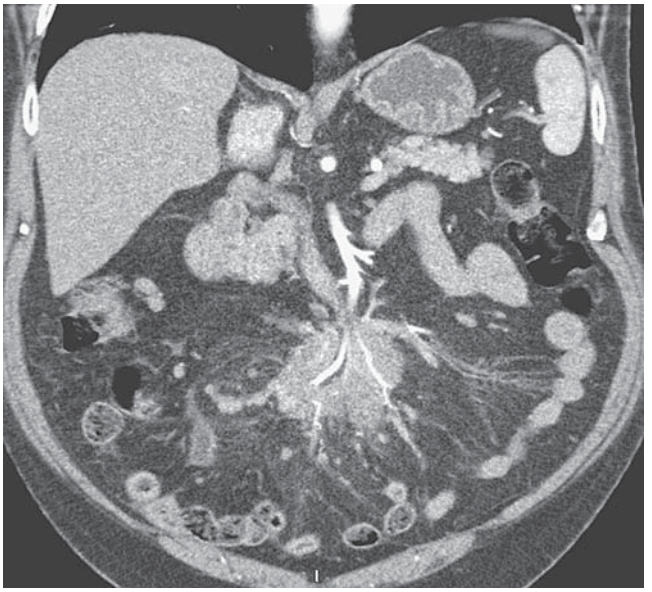

A

B

C

Figure 6.8. Mesenteric fibrosis. (A) Coronal 2-mm MPR image shows a mass in the mesentery that encases branches of the superior mesenteric artery (SMA). Edema is also present in the mesenteric fat. (B) Oblique coronal MIP (30-mm slab thickness). The branches of the SMA are well shown extending through the mass. The vessels are intact with no significant narrowing or obstruction. (C) Sagittal CPR along the SMA. There is no significant stenosis or irregularity of the vessel. Core biopsy was performed of this mass demonstrating changes compatible with mesenteric fibrosis. Follow-up study one year later showed no significant change.

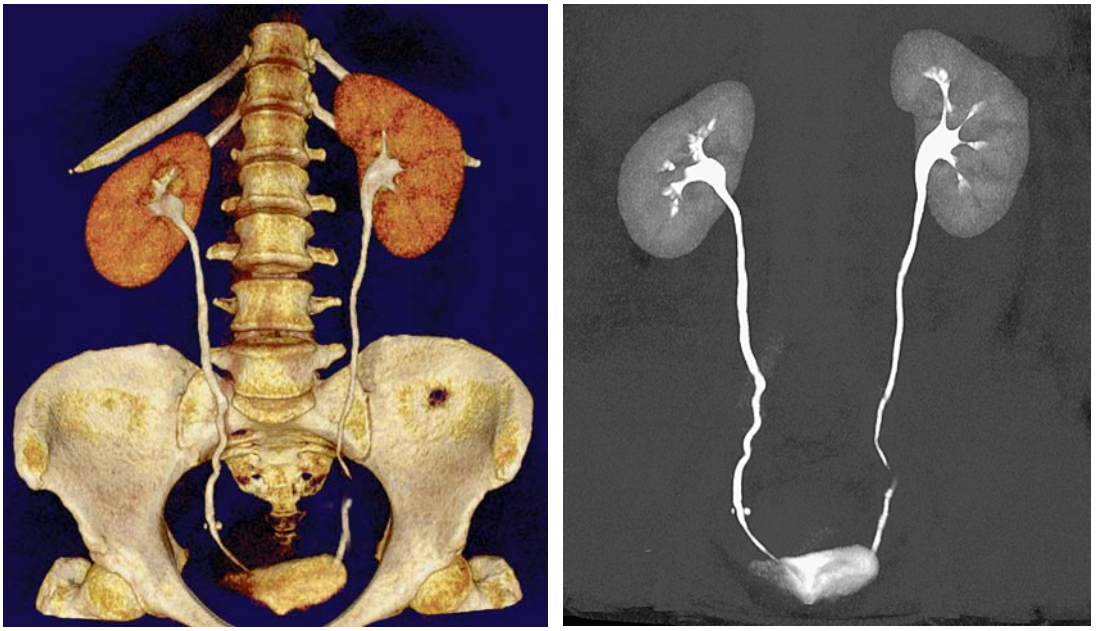

Figure 6.9. Normal CT urogram. (A) Unsegmented volume-rendered image from a CT urogram. The normal appearance of the collecting systems and ureters is shown. The apparent narrowing in the left ureter is related to peristalsis. The two high-density structures in the right pelvis adjacent to the ureter are phleboliths. (B) Coronal thick-slab MIP image from the same study. The bones have been removed using automated segmentation. Detail of the renal collecting systems is better appreciated on the MIP image.

arterial and venous abnormalities are commonly encountered and can be well shown with volume or MIP images. Surprisingly, excellent vascular images can be obtained with current scanners even when a routine non-angiographic protocol is used. MIP images are also routinely used in our CT urogram protocol to demonstrate the renal collecting systems and ureters (Figure 6.9).

Surface images are useful for documenting unsuspected bony abnormalities. A particularly helpful tool is the curved planar reformation. This is especially useful for demonstrating pancreatic pathology, but is also very helpful for abnormalities of the bile ducts and ureters. These tools have made a major impact in the area of trauma imaging. In a critically injured trauma patient, a head-to-pelvis data set can be rapidly obtained on the scanner and sent directly to the workstation for review. Using a combination of MPR, MIP, and surface or volume rendering, the soft tissues, vessels, and bones can be fully evaluated in a small fraction of the time it would take to reconstruct each individual examination and review it on the PACS.

Selected Readings

1. Alvarez-Linera J, Benito-Leon J, Escribano J, et al. Prospective evaluation of carotid artery stenosis: elliptic centric contrast-enhanced MR angiogra-

phy and spiral CT angiography compared with digital subtraction angiography. Am J Neuroradiol 2003;24:1012–1019.
2. Boiselle PM, Reynolds KF, Ernst A. Multiplanar and three-dimensional imaging of the central airways with multidetector CT. Am J Roentgenol 2002 Aug;179:301–308.
3. Catalano C, Fraioli F, Danti M, et al. MDCT of the abdominal aorta: basics, technical improvements, and clinical applications. Eur Radiol 2003 Nov;13(suppl 3):N53–N58.
4. Chen YT, Wang MS. Three-dimensional reconstruction and fusion for multi-modality spinal images. Comput Med Imaging Graph. 2004 Jan–Mar;28(1–2):21–31.
5. Choi HS, Choi BW, Choe KO, et al. Pitfalls, artifacts, and remedies in multi–detector row CT coronary angiography. Radiographics 2004;24: 787–800.
6. Chow LC, Sommer FG. Multidetector CT urography with abdominal compression and three-dimensional reconstruction. Am J Roentgenol 2001 Oct;177:849–855.
7. Coll DM, Herts BR, Davros WJ, Uzzo RG, Novick AC. Preoperative use of 3D volume rendering to demonstrate renal tumors and renal anatomy. Radiographics 2000;20:431–438.
8. Desser TS, Sommer FG, Jeffrey RB Jr. Value of curved planar reformations in MDCT of abdominal pathology. Am J Roentgenol 2004 June;182(6): 1477–1484.
9. Fishman EK. From the RSNA refresher courses: CT angiography: clinical applications in the abdomen. Radiographics 2001;21:3–16.
10. Foley WD. Special focus session: multidetector CT: abdominal visceral imaging. Radiographics 2002;22:701–719.
11. Funabashi N, Komiyama N, Komuro I. Patency of coronary artery lumen surrounded by metallic stent evaluated by three dimensional volume rendering images using ECG gated multislice computed tomography. Heart 2003;89:388.
12. Gotway MB, Dawn SK. Thoracic aorta imaging with multislice CT. Radiol Clin North Am 2003;41:521–543.
13. Harris JP, Nelson RC. Abdominal imaging with multidetector computed tomography: state of the art. J Comput Assist Tomogr 2004 Jul–Aug; 28(suppl 1):S17–S19.
14. Horton KM, Fishman EK. Volume-rendered 3D CT of the mesenteric vasculature: normal anatomy, anatomic variants, and pathologic conditions. Radiographics 2002;22:161–172.
15. Josephson SA, Bryant SO, Mak HK, Johnston SC, Dillon WP, Smith WS. Evaluation of carotid stenosis using CT angiography in the initial evaluation of stroke and TIA. Neurology 2004 Aug;63(3):457–460.
16. Katz DS, Hon M. CT angiography of the lower extremities and aortoiliac system with a multi-detector row helical CT scanner: promise of new opportunities fulfilled. Radiology 2001;221:7–10.
17. Lacomis JM, Wigginton W, et al. Multi–detector row CT of the left atrium and pulmonary veins before radio-frequency catheter ablation for atrial fibrillation. Radiographics 2003;23:S35–S48.
18. Lawler LP, Fishman EK. Multi–detector row CT of thoracic disease with emphasis on 3D volume rendering and CT angiography. Radiographics 2001;21:1257–1273.
19. Lee EY, Siegel MJ, Hildebolt CF, Gutierrez FR, Bhalla S, Fallah JH. MDCT evaluation of thoracic aortic anomalies in pediatric patients and young adults: comparison of axial, multiplanar, and 3D images. Am J Roentgenol 2004 Mar;182:777–784.

20. McTavish JD, Jinzaki M, Zou KH, et al. Multi–detector row CT urography: comparison of strategies for depicting the normal urinary collecting system. Radiology 2002;225:783–790.
21. Napoli A, Fleischmann D, Chan FP, et al. Computed tomography angiography: state-of-the-art imaging using multidetector-row technology. J Comput Assist Tomogr. 2004 Jul–Aug;28(suppl 1):S32–S45.
22. Neyman EG, Corl FS, Fishman EK. 3D-CT evaluation of metallic implants: principles, techniques, and applications. Crit Rev Comput Tomogr 2002;43(6):419–452.
23. Nino-Murcia M, Tamm EP, Charnsangavej C, Jeffrey RB Jr. Multidetector-row helical CT and advanced postprocessing techniques for the evaluation of pancreatic neoplasms. Abdom Imaging 2003;28:366–377.
24. Pannu HK, Flohr TG, Corl FM, Fishman EK. Current concepts in multi–detector row CT evaluation of the coronary arteries: principles, techniques, and anatomy. Radiographics 2003;23:111–125.
25. Pickhardt PJ, Choi JR, Hwang I, et al. CT virtual colonoscopy to screen for colorectal neoplasia in asymptomatic adults. N Engl J Med 2003;349: 2191–2200.
26. Pretorius ES, Fishman EK. Volume-rendered three-dimensional spiral CT: musculoskeletal applications. Radiographics 1999;19:1143–1160.
27. Romano M, Mainenti PP, Imbriaco M, et al. Multidetector row CT angiography of the abdominal aorta and lower extremities in patients with peripheral arterial occlusive disease: diagnostic accuracy and interobserver agreement. Eur J Radiol 2004 Jun;50(3):303–308.
28. Roos JE, Willmann JK, Weishaupt D, Lachat M, Marincek B, Hilfiker PR. Thoracic aorta: motion artifact reduction with retrospective and prospective electrocardiography-assisted multi-detector row CT. Radiology 2002; 222:271–277.
29. Rubin GD. MDCT imaging of the aorta and peripheral vessels. Eur J Radiol 2003;45(suppl 1):S42–S49.
30. Schoepf UJ, Becker CR, Ohnesorge BM, Yucel EK. CT of coronary artery disease. Radiology 2004;232:18–37.
31. Shanmuganathan K. Multi-detector row CT imaging of blunt abdominal trauma. Semin Ultrasound CT MR. 2004 Apr;25(2):180–204.
32. Siegel MJ. Multiplanar and three-dimensional multi–detector row CT of thoracic vessels and airways in the pediatric population. Radiology 2003;229:641–650.
33. Smith WS, Roberts HC, Chuang NA, et al. Safety and feasibility of a CT protocol for acute stroke: combined CT, CT angiography, and CT perfusion imaging in 53 consecutive patients. Am J Neuroradiol 2003;24:688–690.
34. Tomandl BF, Köstner NC, Schempershofe M, et al. CT angiography of intracranial aneurysms: a focus on postprocessing. Radiographics 2004;24:637–655.
35. Urban BA, Lloyd E, Ratner LE, Fishman EK. Three-dimensional volume-rendered CT angiography of the renal arteries and veins: normal anatomy, variants, and clinical applications. Radiographics 2001;21:373–386.
36. Vargas R, Nino-Murcia M, Trueblood W, Jeffrey RB Jr. MDCT in pancreatic adenocarcinoma: prediction of vascular invasion and resectability using a multiphasic technique with curved planar reformations. Am J Roentgenol 2004 Feb;182:419–425.

Chapter 7

Efficient CT Workflow

There is no one roadmap for efficient CT workflow that will succeed for all sites. Each site will need a slightly different solution based on the available equipment and the preferences of the radiologists. In the previous chapters, I have outlined how to use all of the different components involved with MDCT, from the scan acquisition parameters, to image reconstruction and review, to use of 3D workstations. While each of these components is important individually, in the end it is how they all function together that will determine if workflow is efficient and effective.

One of the most important components to efficient workflow is setting up detailed protocols and pathways for each case. Having a detailed protocol will eliminate the guesswork and minimize errors. It also saves time for both the technologist and the radiologist. If the protocol covers everything that needs to be done from start to finish, the technologist does not need to waste time figuring out what to do. The radiologist will not waste time answering unnecessary questions, and when going to review a case, can be confident that the images needed will be present and in the desired format.

Comprehensive CT Protocol

A different comprehensive protocol should be created for each examination type. Start by making a list of every basic examination type (neurology, body, MSK, CT angiography, CT perfusion) that is performed in the imaging center or hospital. Include specialized protocols such as dual phase liver, pancreas, CT urogram, CT colonoscopy etc. Each of these protocols will contain at least five different components (Table 7.1).

The first component of a comprehensive protocol contains all the parameters necessary for data acquisition, including scan mode and slice thickness, pitch, rotation speed, and dose (automatic exposure control when possible). If automatic exposure control is not available then separate protocols need to be created for adults and children of

Pancreas Protocol

Scan Parameters

Acquistion	Coverage	Scan Mode	kV	mA	AEC	Rotation Time	FOV	SliceThickness	Beam Pitch
Scan#1	Pancreas - Pre Contrast	Helical	120	400-500	Yes	0.5 sec	500mm	1 to 1.5mm	1.25

Acquistion	Coverage	Scan Mode	kV	mA	AEC	Rotation Time	FOV	SliceThickness	Beam Pitch
Scan #2	Pancreas - Pancreatic	Helical	120	400-500	Yes	0.5 sec	500mm	.5 to .75mm	1.25

Acquistion	Coverage	Scan Mode	kV	mA	AEC	Rotation Time	FOV	SliceThickness	Beam Pitch
Scan #3	Abdomen - Venous Phase	Helical	120	400-500	Yes	0.5 sec	500mm	1 to 1.5mm	1.25

Injector Values	Contrast Needed	Contrast Volume	Saline Volume	Injection Rate
	Yes	125cc	50cc	3cc/sec

Contrast Timing	Bolus Detection	Reference Location	Trigger Value (ROI)	Delay before Monitoring	Scan Delay After Trigger	Manual	Delay Scan #2	Delay Scan #3	
	Optional	Aorta	200	20 sec	15 sec	Yes (O)	40 sec	60 sec	

Reconstructions	Algorithm	Thin Axials	Recon Interval	Thick Axials	Sagittal	Coronal	PACS	Workstation
Scan #1	Standard	No		5mm			Thick Axials	No

Reconstructions	Algorithm	Thin Axials	Recon Interval	Thick Axials	Sagittal	Coronal	PACS	Workstation
Scan #2	Standard	.5 to .75mm	.5mm	2mm		2mm	Thick Axials and MPR	Thin Axials(O)

Reconstructions	Algorithm	Thin Axials	Recon Interval	Thick Axials	Sagittal	Coronal	PACS	Workstation
Scan #3	Standard	1 to 1.5mm	1mm	3mm		2mm	Thick Axials and MPR	No

different weights. If a gated study is to be performed, the type of gating and desired heart rate should be included.

The second component involves contrast. When given, the amount and concentration, injection rate, and timing must be specified. When a test bolus method or bolus triggering is used, the specifics of when and how to initiate the scan must be included, as well as the vessel to be monitored. If a split or biphasic contrast injection is to be used, this must be outlined.

The third component includes information about the body part to be scanned, including coverage needed, major landmarks to include/exclude, and whether or not multiple phases are needed. Any specialized instructions regarding the acquisition need to be included—for example, applying abdominal compression for a CT urogram or obtaining prone images for CT colonoscopy after gas insufflation.

The fourth component concerns the image reconstruction. This includes the slice thickness and spacing (overlapping reconstructions if desired), the field of view, the reconstruction filter (will images be reconstructed with more than one filter, i.e., soft tissue and bone?) and reconstruction algorithm (cone beam versus non–cone beam) to be used. If MPR or MIP images are generated directly on the scanner console, the plane and thickness of the reconstructions should be built directly into the protocol.

The fifth and final component addresses what happens to the images once generated. Specifics of which images are sent to PACS and the image archive are very important. If the case is to be sent to one or more workstations, this should also be built directly into the protocol. If filming of images is needed this must also be specified.

Although it sounds complicated, much of the above information can be built into the protocol library of most current MDCT scanners. This will help automate the process. The more information that can be built directly into the scanner protocol library the better. The information should also be kept in a protocol book next to the scanner for easy reference by the technologists. This will eliminate guesswork and minimize errors and interpretation delays caused using the wrong parameters or reconstructing the wrong data.

Efficient Image Review

Efficient workflow also requires optimizing how the images are viewed on the equipment available. This requires some knowledge of the capabilities of the network and computers that are used. Current MDCT data sets can easily reach 1000 to 2000 images and will get even bigger in the future. Networks and computers vary greatly in their ability to handle this volume of data.

For those sites that are fortunate enough to have a highly robust data network and powerful computers or workstations for image review, it is preferable to reconstruct the thinnest slice data available and send this entire data set to the review station. This gives the radiologist maximal flexibility. The data can be instantly manipulated in real time

to view either thin or thicker slices. Multiplanar reconstructions can be rapidly generated on the computer in any plane and thickness, and advanced tools such as MIP or volume rendering may be instantly available. As long as the workstation is able to load and scroll though the data in a short period of time, this is an ideal solution allowing the radiologist maximal flexibility without sacrificing efficiency. This model is clearly the future for MDCT.

Unfortunately, at this moment the vast majority of sites do not have the network and computer resources available to make submillimeter image review a viable option for routine cases. For slower networks it may take 5 minutes to 10 minutes (or even more) to transfer these large data sets from the scanner to the PACS. Many PACS workstations will take 2 minutes to 5 minutes just to fully load a large CT case into memory. Once the case is loaded, the operation of the computer may be quite slow and it could take several minutes just to scroll from one end of the data set to the other. For these sites it is crucial to decrease the number of images being sent and reviewed. If this is not done, widespread frustration with inefficiency and data overload will ensue (Figure 7.1).

By reconstructing thicker slice axial and MPR images directly on the scanner console, data sets can be reduced substantially. Depending on the specific parameters chosen, data sets for body cases and CTA can be limited to between 100 images and 300 images without significantly reducing diagnostic image quality. This is a much more manageable size for most existing computers and networks. High-quality, high-

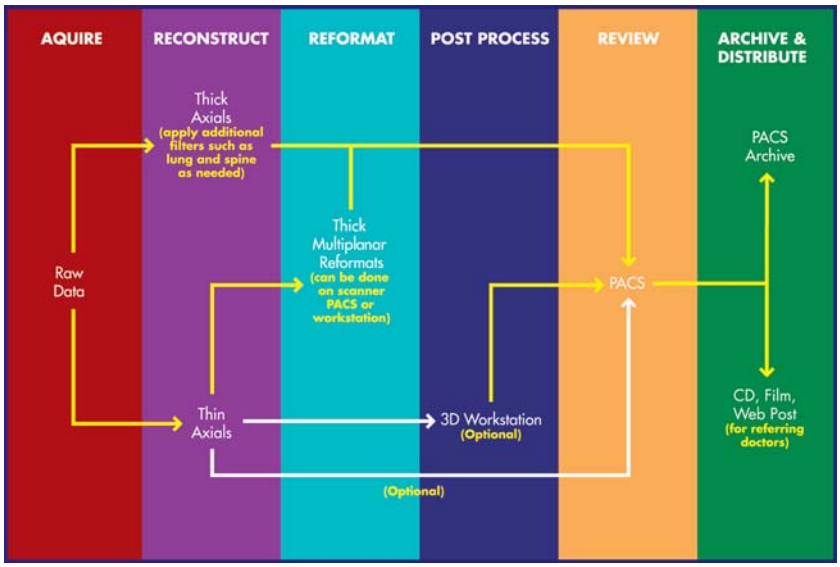

Figure 7.1. CT workflow. Flow of image data from the scanner to the PACS system and workstation and subsequently to the radiologist and referring doctors.

resolution 2-mm to 5-mm axial images with multiplanar reconstructions can be reviewed on PACS rapidly and accurately. Diagnostic accuracy will remain high without sacrificing efficiency. This approach does require frequent utilization of the 3D workstation. Cases needing volume rendering or surface rendering or MIPs should have the thin section data sent straight to the workstation for reconstruction and review. Oblique MPRs can be created either on the workstation or the scanner console by the technologist. Processed images from the workstation can then be sent back to PACS for additional review and archival. The thin submillimeter source images are not routinely reviewed but remain easily accessible when needed.

True efficiency also requires a frame shift in the minds of interpreting radiologists. For years the CT paradigm has dictated careful review of axial images with multiplanar correlation in select cases. This paradigm is obsolete in the multidetector era with volumetric data sets. Radiologists familiar with MRI can easily understand this. No experienced MRI reader would ever feel content with axial images alone. For years MRI readers have been able to review images in whichever plane best demonstrates the anatomy and pathology, and to correlate the findings with other planes. Computed tomography should now be treated exactly the same way. Many if not most examinations are better suited to primary image review in sagittal, coronal, or even oblique planes. This is fairly obvious for examinations like the spine, sinuses and hips, but can even be true for body cases. The body is much longer than it is wide and therefore 50 2-mm coronal images can be reviewed much more quickly than 200 3-mm axial images.

Making the transition from axial image–based review to a true multiplanar approach does not occur overnight. It is a gradual process that takes weeks to months to fully integrate into daily practice. The rewards are substantial, however: more efficient image review coupled with the potential for improved diagnostic accuracy.

Selected Readings

1. Jhaveri KS, Saini S, Levine LA, et al. Effect of multislice CT technology on scanner productivity. Am J Roentgenol 2001 Oct;177(4):769–772.
2. Roos JE, Desbiolles LM, Willmann JK, Weishaupt D, Marincek B, Hilfiker PR. Multidetector-row helical CT: analysis of time management and workflow. Eur Radiol 2002 Mar;12(3):680–685.
3. Rubin GD. Data explosion: the challenge of multidetector-row CT. Eur J Radiol 2000 Nov;36(2):74–80.

Part II

Volumetric Imaging Teaching File

Chapter 8

Vascular Imaging

Case 8.1: Peripheral Vascular Disease (Two Patients)

Clinical Information

Patient 1: a 70-year-old woman with surgical placement of an aortic graft, now complaining of progressive leg claudication.
Patient 2: a 61-year-old man with prior surgical bypass on the left leg, and worsening right leg claudication.

Postprocessing Techniques Used and Approach

For both patients the data set is initially segmented to remove bone and overlying soft tissues (Table 8.1 and Figures 8.1.1 and 8.1.2). Automated vessel-tracking software is utilized to isolate the vascular tree and remove bone. Additional manual editing is performed to remove fragments and remaining bone. Volume-rendered and MIP images of the aorta and runoff are taken. Curved planar reformations are also generated using automated vessel-tracking software.

Diagnosis

Patient 1: aortic graft with anastomotic pseudoaneurysm, right renal artery aneurysm, and bilateral SFA occlusions with three-vessel runoff on both sides. There is also an incidental pancreatic carcinoma.

Table 8.1. Scan Acquisition Parameters for Case 8.1, Peripheral Vascular Disease

Slice No. and Thickness	**16 × 1.0 mm**
Coverage	**Diaphragm to feet**
Helical Pitch	**1.25:1**
Rotation Speed	**0.5 sec**
Dose Parameters	**120 kVp, 200 mAs**
Contrast Dose	**125 mL Omnipaque 350**
Injection Rate	**3 mL/sec**
Bolus Timing Method	**Bolus triggering focused on the femoral artery**

A,B

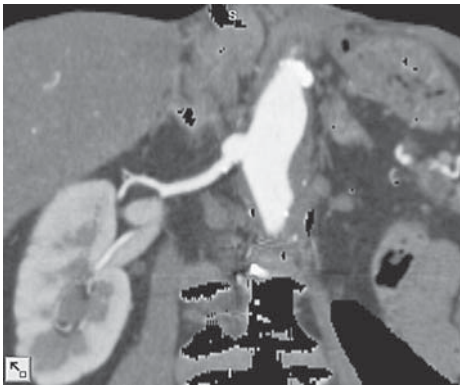

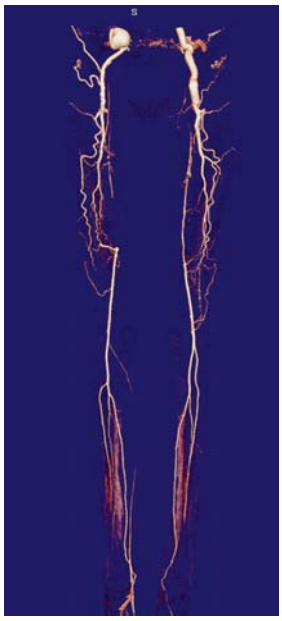

C

D

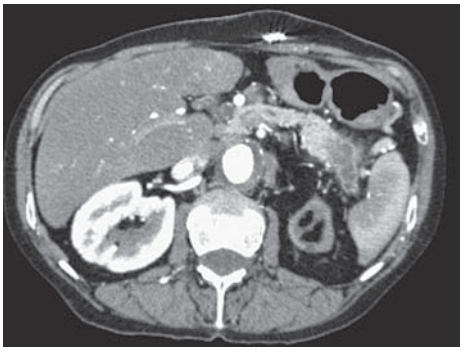

E

Figure 8.1.1. (A) Patient 1: segmented volume-rendered image of the aorta and iliac vessels. The left renal artery is occluded, and an aneurysm of the origin of the right renal artery is seen. The patient has a patent aortobifemoral graft with a proximal end-to-side anastomosis and occlusion of the native aorta. There is a large pseudoaneurysm at the distal anastomosis of the right limb of the graft. (B) Curved planar reconstruction along the right renal artery shows the proximal renal artery aneurysm. (C and D) Segmented volume-rendered and MIP images of the runoff. Both images show bilateral superficial femoral artery occlusions with distal reconstitution via collateral flow. Three-vessel runoff is present with the dominant supply from the posterior tibial arteries. Note the high origin of the left anterior tibial artery at the level of the knee joint. (E) 3-mm axial image through the pancreas. There is an incidental low-density mass in the distal body of the pancreas. This was subsequently proven to represent pancreatic cancer. Note the atrophic left kidney is related to chronic ischemia.

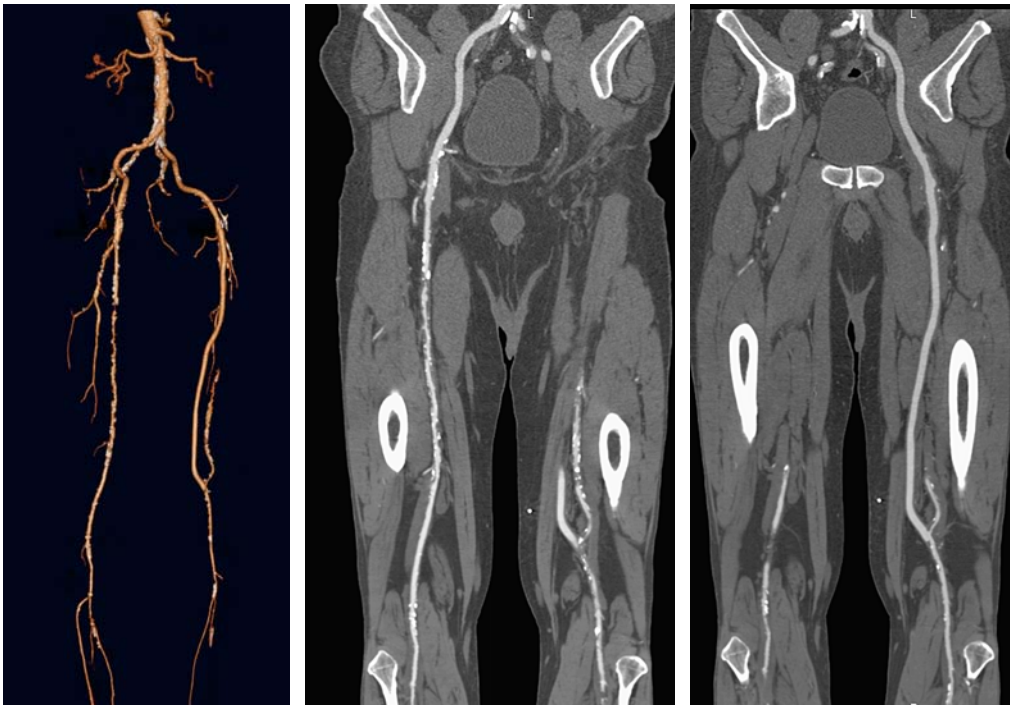

A,B C

D E

Figure 8.1.2. (A) Patient 2: segmented volume-rendered image of the runoff. The aorta and iliacs are relatively unremarkable. On the left there is a patent femoral-popliteal graft bypassing an occluded left superficial femoral artery (SFA). On the right the SFA is diffusely and severely diseased. (B and C) Curved planar reconstructions through the right SFA and left graft. The right SFA is again seen to be severely stenotic at multiple sites. The left graft is widely patent but there is moderate stenosis of the popliteal artery distal to the graft. (D and E) Segmented anterior view, and unsegmented posterior view volume-rendered images of the calf. There is extensive plaque in the tibioperoneal trunks on both sides, but three vessels are patent bilaterally.

Patient 2: severe diffuse disease of the right superficial femoral artery. Patent left femoral-popliteal graft with moderate disease in the popliteal artery below the graft. There is bilateral three-vessel runoff with significant disease in the tibioperoneal trunks.

Teaching Points

CT runoff provides the vascular surgeon with all of the information needed to properly treat both of these patients, and even some information that could not be obtained with conventional angiography. High-quality segmented volume and MIP images give the surgeon a vascular road map that is easy to understand and use for treatment planning. With a quick review of only a few images, the surgeon can plan repair of the pseudoaneurysm and assess the need for additional surgery, such as a femoral-popliteal bypass, as symptoms warrant, for patient 1. In addition, the CTA could potentially be lifesaving in this case, as an incidental pancreatic body cancer was discovered. There were no visible metastases seen, and the lesion was still at a surgically resectable stage. For patient 2 a right femoral-popliteal bypass was planned based on the CTA findings.

Peripheral arterial occlusive disease of the lower extremity is an important cause of significant morbidity in the general population, particularly in the elderly, and is frequently underdiagnosed. Intermittent claudication is the initial symptom of peripheral arterial occlusive disease of the lower extremities in most patients. This can result in significant pain and limitation of lifestyle. Several other conditions can simulate claudication caused by peripheral arterial occlusive disease, particularly disease of the spine and neurogenic disorders.

Catheter-based digital subtraction angiography (DSA) has remained the gold standard for the evaluation of peripheral ischemia, but it is an invasive and expensive procedure. The risk and cost of this procedure may be warranted for patients with severe symptoms, but it is not as clear for the many patients in whom symptoms are mild or in whom the diagnosis is in question. There is a clinical need for a noninvasive test that enables one to safely and accurately make a diagnosis, define the relevant anatomy and pathology, and effectively triage patients to an appropriate therapy option (surgery, intravascular stenting, or medical management) without needing additional imaging.

The advent of MDCT has made these goals achievable. Studies with 4-row MDCT have demonstrated excellent correlation between CTA and DSA for the diagnosis and characterization of peripheral vascular disease (PVD). The results obtainable with 16-detector and higher scanners will be even more impressive because of the higher spatial resolution possible with these scanners compared with 4-detector scanners.

Many sites now have extensive clinical experience using CTA as the primary modality to evaluate peripheral vascular disease and triage patients to the appropriate therapy. This approach is beneficial for patients who now have a rapid, noninvasive, and highly accurate screening test available. Patients can be therefore be evaluated earlier in the disease process, and interventions including medical therapy

and stent placement can be instituted while the disease is in a more readily treatable state. Patients with more advanced disease can proceed directly to surgery without needing a catheter angiogram.

Case 8.2: Aortic Occlusion With Axillary and Femoral Bypasses

Clinical Information

A 74-year-old woman with severe, long-standing PVD and prior surgical graft placement now has worsening lower extremity claudication symptoms.

Postprocessing Techniques Used and Approach

Automatic vessel-tracking software is used to isolate the vascular tree from the bones and soft tissues. Manual 3D sculpting is used to clean up remaining unwanted fragments and tissue. Vascular structures are reviewed in volume rendering and MIP images. Thin-slab MIP images are also used to show the occluded aorta (Table 8.2 and Figures 8.2.1 through 8.2.3).

Diagnosis

Chronic aortoiliac occlusion with surgical vacular reconstruction including right axillary-to-femoral bypass and femoral-femoral crossover graft. The patient's symptoms likely relate to the bilateral SFA occlusions with distal reconstitution.

Teaching Points

This case demonstrates the ability of 16-detector MDCT to cover huge distances and still maintain very high image quality. It is important to properly time the injection to insure that contrast does not run out during the study. If a very long scan is planned, either slow the injection rate slightly or increase the contrast amount in order to prolong the injection. Remember the formula injection time equals scan duration plus a delay factor. Other ways to improve coverage include shorter rotation time (0.4 sec if available) or increasing pitch to 1.5.

Table 8.2. Scan Acquisition Parameters for Case 8.2, Aortic Occlusion with Axillary and Femoral Bypasses

Slice No. and Thickness	**16 × 1.0 mm**
Coverage	**Neck to feet**
Helical Pitch	**1.5:1**
Rotation Speed	**0.5 sec**
Dose Parameters	**120 kVp, 200 mAs**
Contrast Dose	**150 mL Omnipaque 350**
Injection Rate	**3 mL/sec**
Bolus Timing Method	**Bolus triggering on the femoral artery**

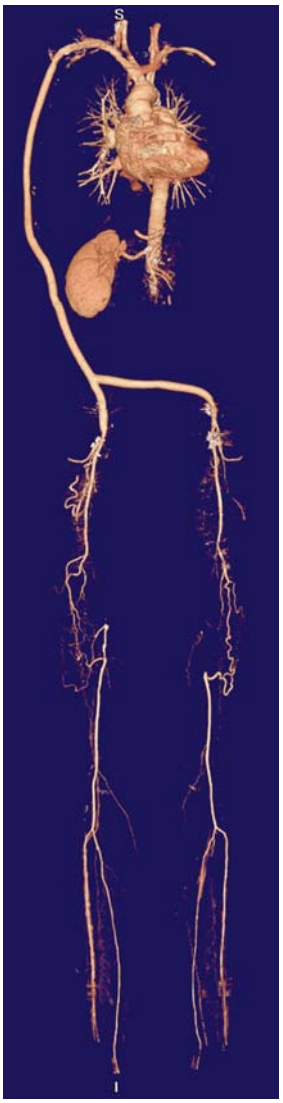

Figure 8.2.1. Segmented volume-rendered image of the entire data set. The entire vascular tree is demonstrated on one image. The aorta and both iliac arteries are occluded and are bypassed by a right axillary-to-femoral graft with a femoral-femoral crossover graft. Both SFAs are occluded and reconstitute distally via collaterals. Two-vessel runoff is present to both feet.

Figure 8.2.2. Coronal thin slab unsegmented MIP image of the aorta. The infrarenal aorta is occluded. The left kidney and left renal artery are surgically absent. The right renal artery is unremarkable.

Figure 8.2.3. Segmented VR image of the lower extremities with semitransparent background. The runoff vessels are shown with a semitransparent ghost image of the bones added back for anatomic localization.

This case also illustrates the diagnostic utility of CTA. A catheter angiogram would be more difficult in this patient with an occluded aorta. An axillary approach would be needed. Separate injections into the right subclavian artery or directly into the axillary graft and the abdominal aorta would be needed to show all the grafts and vessels. CTA provides all the necessary information with one venous injection. All grafts are clearly patent.

For the surgeon, all of the necessary information to treat the patient is demonstrated on the CTA. To improve blood flow to the legs a femoral-to-popliteal bypass graft would be needed.

Case 8.3: Aortic Dissection

Clinical Information

A 49-year-old man with acute severe chest pain. In the emergency department he is found to be hypotensive with decreased pulses.

Postprocessing Techniques Used and Approach

Multiplanar images are used to rapidly demonstrate the necessary findings and make the diagnosis in this case (Table 8.3 and Figures 8.3.1 and 8.3.2). Oblique sagittal MIP images are a quick and easy way to better show the important findings to the surgeon on just a few images.

Diagnosis

Acute Type A (Stanford) or Type II (DeBakey) aortic dissection with rupture into the mediastinum and pericardium.

Teaching Points

There are two classification systems used to describe aortic dissection, the Stanford and the DeBakey classification. For both systems the main distinguishing point is whether or not the ascending aorta is involved.

Stanford Classification:

- Type A: Accounts for 60% of cases. Involves ascending aorta.
- Type B: Accounts for 40% of cases. Only descending aorta involved.

DeBakey Classification:

- Type 1: Accounts for 50% of cases. Ascending and descending aorta involved.
- Type 2: Accounts for 10% of cases. Confined to ascending aorta.
- Type 3: Accounts for 40% of cases. Confined to descending aorta.

When an aortic dissection involves the ascending aorta it is considered a surgical emergency because of the risk of rupture into the mediastinum or pericardium and the potential for coronary artery involvement. MDCT has replaced catheter angiography as the study of choice for diagnosis of acute aortic dissection. MDCT is also generally much faster and more accessible than either transesophageal echocardiography or MRI. Care must be taken not to overcall the pulsation artifacts that can be seen in the ascending aorta in normal patients (see Figure 5.13).

In addition to being fast, accurate, and readily accessible, CT is also superior to both echocardiography and catheter angiography for identifying major complications of aortic dissection such as mediastinal or pericardial hemorrhage, extension of dissection into the coronary or

Table 8.3. Scan Acquisition Parameters for Case 8.3, Aortic Dissection

Slice No. and Thickness	**16 × 1 mm**
Coverage	**Chest through aortic bifurcation**
Helical Pitch	**1.25:1**
Rotation Speed	**0.5 sec**
Dose Parameters	**120 kVp, 200 mAs**
Contrast Dose	**125 mL Omnipaque 350**
Injection Rate	**4 mL/sec**
Bolus Timing Method	**Bolus triggering on the ascending aorta**

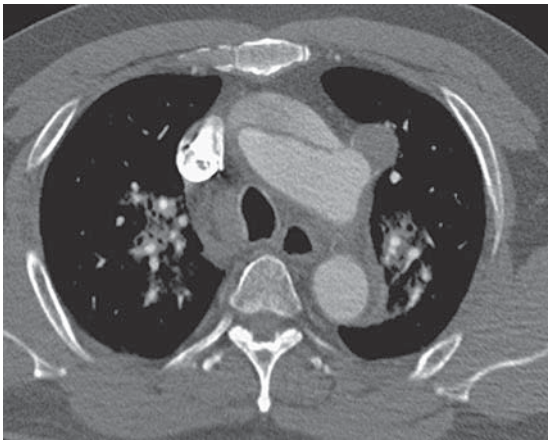

A

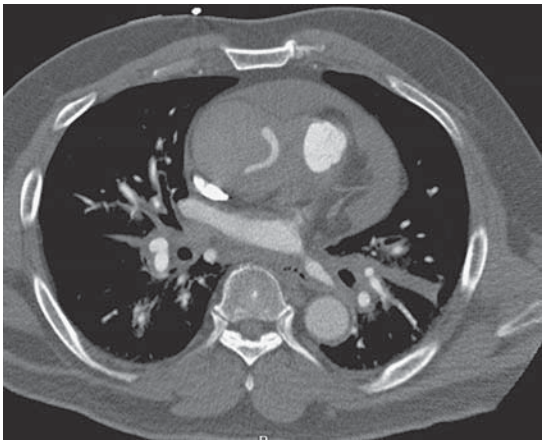

B

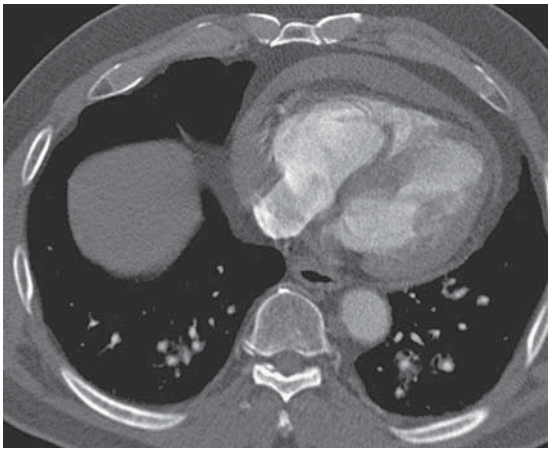

C

Figure 8.3.1. Axial 3-mm images at three levels through the chest. (A) The most superior image at the aortic arch shows an intimal flap involving the ascending aorta but not extending into the descending aorta. Hematoma is also present in the mediastinum. (B) The image at the aortic root shows extensive hematoma with a very compressed true aortic lumen. (C) The image at the level of the ventricles demonstrates moderate hemopericardium.

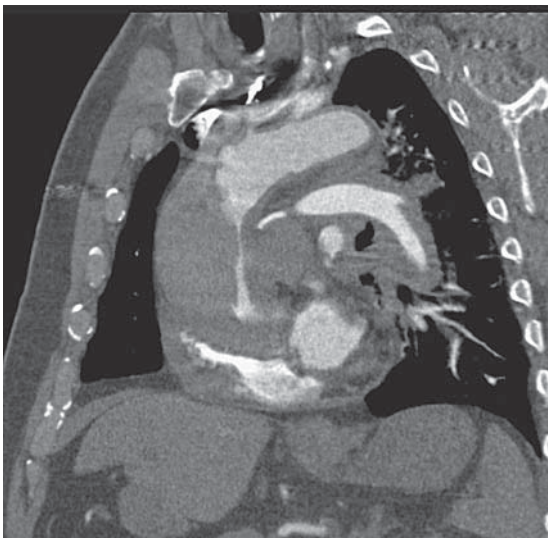

A

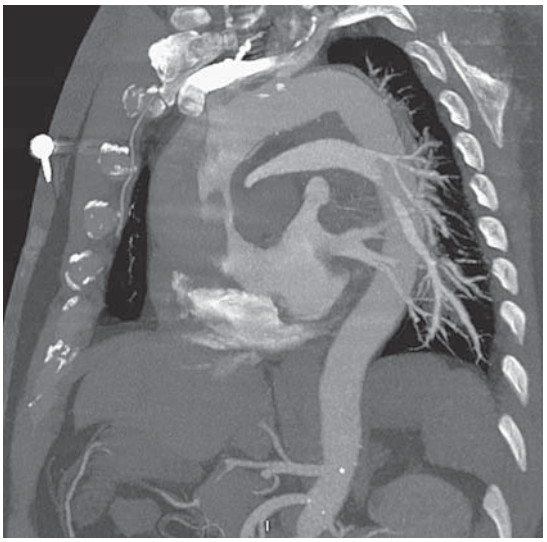

B

Figure 8.3.2. (A) Oblique sagittal MPR and (B) thin slab MIP images. The true lumen is opacified but is narrowed and compressed by thrombus in the false lumen and mediastinum. The arch and descending thoracic aorta appear intact.

great vessels, and thrombosis of vessels. CT can also allow alternate diagnoses to be made in patients with pain who do not have aortic dissection, such as pulmonary embolism, pneumonia or pneumothorax.

In this patient with an acutely leaking dissection the diagnosis was made within minutes of his arrival in the emergency department. He was taken immediately to the operating room and much valuable time was saved treating this critically ill man.

Case 8.4: Renal Artery Stenosis

Clinical Information

An 81-year-old man undergoing evaluation for bilateral lower extremity claudication. He has a long history of hypertension on medical therapy and borderline renal function.

Postprocessing Techniques Used and Approach

Automated vessel-tracking software on the workstation is used to isolate the vascular tree from the soft tissues and bones. The vessels are examined using a combination of volume rendering and thin and thick slab MIP reconstructions. Curved planar reconstructions are also used as part of the renal artery evaluation (Table 8.4 and Figures 8.4.1 through 8.4.3).

Diagnosis

Bilateral main renal artery stenosis of two renal arteries to each kidney.

Teaching Points

This case illustrates the amount of detail that can be obtained from a CT runoff. With current 16-slice and higher scanners one does not have to sacrifice resolution for speed or coverage. CTA can also provide information on collateral vessels that may not be shown on a catheter angiogram, such as the collateral to the right kidney in this case.

CTA provides an excellent roadmap prior to interventional treatment. Information is provided demonstrating the composition of the lesion (hard versus soft plaque), the location of the stenosis (ostial

Table 8.4. Scan Acquisition Parameters for Case 8.4, Renal Artery Stenosis

Slice No. and Thickness	**16 × 1.0 mm**
Coverage	**Diaphragm through feet**
Helical Pitch	**1.25:1**
Rotation Speed	**0.5 sec**
Dose Parameters	**120 kVp, 200 mAs**
Contrast Dose	**125 mL Omnipaque 350**
Injection Rate	**3 mL/sec**
Bolus Timing Method	**Bolus triggering focused on the femoral artery**

Figure 8.4.1. Segmented VR image of the entire runoff. No significant aortoiliac inflow disease is identified but there are multifocal bilateral high-grade SFA lesions present with two-vessel runoff to both feet.

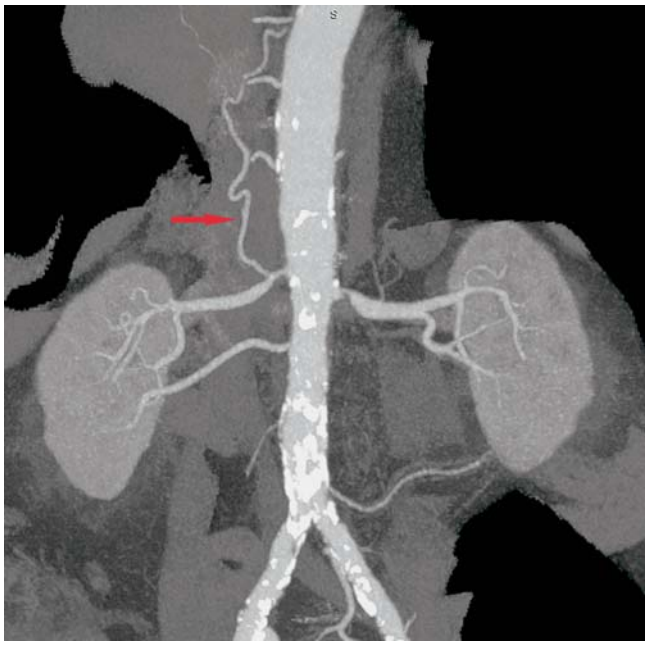

Figure 8.4.2. Thick slab segmented MIP image of the aorta and renal arteries. Removal of the spine allows the renal and aortic anatomy to be better seen on one image. There are two renal arteries to each kidney, including a very small accessory artery to the lower pole of the left kidney that arises from the distal aorta. High-grade stenotic lesions of the main renal arteries are present on both sides. In addition, note the collateral artery on the right (arrow) bypassing the renal stenosis to supply additional blood to the right kidney.

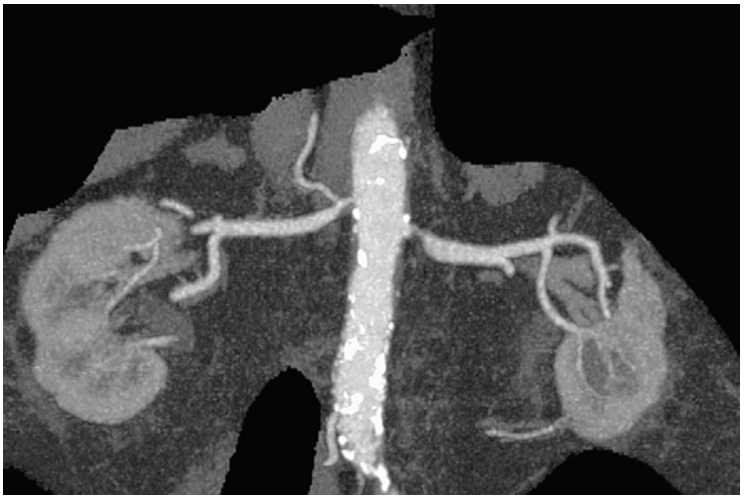

Figure 8.4.3. Curved planar reconstruction through the main renal arteries. The lesions are predominately soft plaque with some ostial calcification.

versus nonostial), and the size of the vessel involved. This allows an interventionalist to select the proper catheter, balloon, and stent prior to the start of the procedure. This can shorten the length of the procedure and insure that the proper equipment will be available when it is needed.

Noninvasive diagnosis of renal artery stenosis has been shown to be highly accurate with both CTA and MRA. MRA has several advantages, including the absence of ionizing radiation and no need for iodinated contrast. Current MDCT scanners have the main advantage of higher resolution and shorter examination times. Currently CT is also superior to MRI for plaque characterization and demonstration of calcification, and is much better for evaluating patients with indwelling stents for occlusion or restenosis.

Future studies with 16-channel or higher CT scanners will likely show some advantage in accuracy for CTA over MRA because of the higher resolution. At this time, the choice of CT or MRI as the preferred noninvasive imaging modality for potential renal artery stenosis is currently a matter of radiologist or clinician preference, ordering patterns, equipment availability, and patient factors such as renal function, allergy, and presence of stents or pacemakers.

Case 8.5: Ulnar Artery Pseudoaneurysm

Clinical Information

A 24-year-old man with a pulsatile mass on the ventral aspect of his wrist. He gives a history of repetitive work-related trauma.

Table 8.5. Scan Acquisition Parameters for Case 8.5, Ulnar Artery Pseudoaneurysm

Slice No. and Thickness	**8 × 0.5 mm**
Coverage	**Forearm to hand**
Helical Pitch	**1.5:1**
Rotation Speed	**0.5 sec**
Dose Parameters	**120 kVp, 130 mAs**
Contrast Dose	**125 mL Ultravist 370**
Injection Rate	**5 mL/sec**
Bolus Timing Method	**Bolus triggering focused on the brachial artery**

Postprocessing Techniques Used and Approach

Volume-rendered and MIP images are generated both with and without segmentation. Vessel-tracking software is used to isolate the arteries from the bones (Table 8.5 and Figures 8.5.1 and 8.5.2).

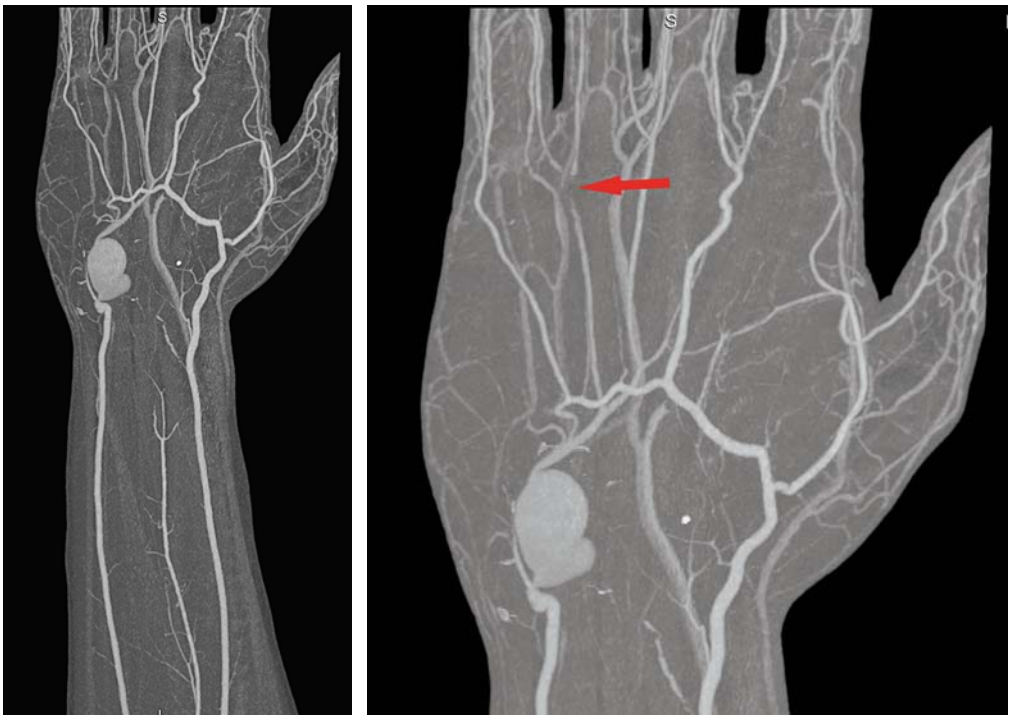

A B

Figure 8.5.1. (A and B) Segmented MIP images of the circulation to the forearm, wrist, and hand. There is a large pseudoaneurysm arising from the ulnar artery. The neck of the aneurysm is quite narrow. The radial and ulnar arteries communicate via the deep palmar arch. The superficial arch is absent. In addition, note the short segment occlusion of the palmar digital artery to the fourth finger (arrow). This is presumably related to an embolus. (Images courtesy of Dr. Ruben Sebben, Dr. Jones & Partners Medical Imaging. South Australia.)

Figure 8.5.2. Unsegmented VR image of the hand and wrist. Findings are again shown with the background of soft tissue and bony landmarks. Arrow points to the occlusion of the fourth digital artery. (Image courtesy of Dr. Ruben Sebben, Dr. Jones & Partners Medical Imaging. South Australia.)

Diagnosis

Posttraumatic pseudoaneurysm of the ulnar artery with an embolus to the palmar digital artery of the fourth finger.

Teaching Points

Pseudoaneurysms are usually caused by perforation of an artery with hematoma formation between the arterial wall and surrounding parenchyma. Flowing arterial blood creates a cavity that remains in continuity with the normal vessel and becomes lined with inflammatory cells and fibroblasts and is eventually replaced by fibrous scar tissue. In a pseudoaneurysm, only adventitia is present, whereas in a true aneurysm, all three layers of the arterial wall (intima, media, and adventitia) are present.

A pseudoaneurysm of the hand may exist as a soft tissue mass which is usually pulsatile. They are more likely to be found on the palmar side. Correct diagnosis is important because patients with pseudoaneurysms of the hand are at risk for distal embolic disease with

ischemia or gangrene of the fingers, spontaneous rupture, bone erosion and joint degeneration, or ulnar or digital nerve dysfunction.

Pseudoaneurysms of the hand may be associated with a history of a single direct trauma or, more commonly, of chronic blunt trauma as in the hypothenar or thenar hammer syndrome. Treatment can be either surgical or percutaneous embolization, depending on the location and appearance. In this patient, MDCT is used not only for diagnosis but also for treatment planning. The location and neck of the aneurysm are well demonstrated.

Case 8.6: Carotid Stenosis (Three Patients)

Clinical Information

All three patients had previously undergone carotid ultrasound, which demonstrated lesions. The patients are referred to CTA to confirm the US findings and for potential presurgical evaluation and planning.

Postprocessing Techniques Used and Approach

Complete carotid artery evaluation requires use of several different techniques (Table 8.6 and Figures 8.6.1 through 8.6.3). Thin to thicker slab MIP images are very useful to evaluate the origin of the great vessels and the vertebral arteries. Slab thickness should be adjusted to best demonstrate the vessels. For patients with mild disease at the bifurcation, oblique thin-slab MIP and volume-rendered images are generally adequate for evaluation. Patients with significant calcific plaque also require curved planar reconstructions. This can be performed manually or using automated software. Curved images should be reviewed in two planes and correlated with axial source data to provide the most accurate measurement of vessel stenosis. Volume-rendered images are also important and particularly useful to the surgeon for demonstrating the anatomy of the bifurcation and the position of the stenosis relative to landmarks in the neck. Unsegmented images are frequently adequate but if there is contrast in the jugular vein obscuring the bifurcation, consider using manual segmentation to remove the jugular vein or using automated software to isolate the carotids.

Table 8.6. Scan Acquisition Parameters for Case 8.6, Carotid Stenosis

Slice No. and Thickness	**16 × 0.5 mm**
Coverage	**Aortic arch to skull base**
Helical Pitch	**1.25:1**
Rotation Speed	**0.4 sec or 0.5 sec**
Dose Parameters	**120 kVp, 125 mAs–150 mAs**
Contrast Dose	**75 mL Omnipaque 350**
Injection Rate	**4 mL/sec**
Bolus Timing Method	**Bolus triggering on the aortic arch**

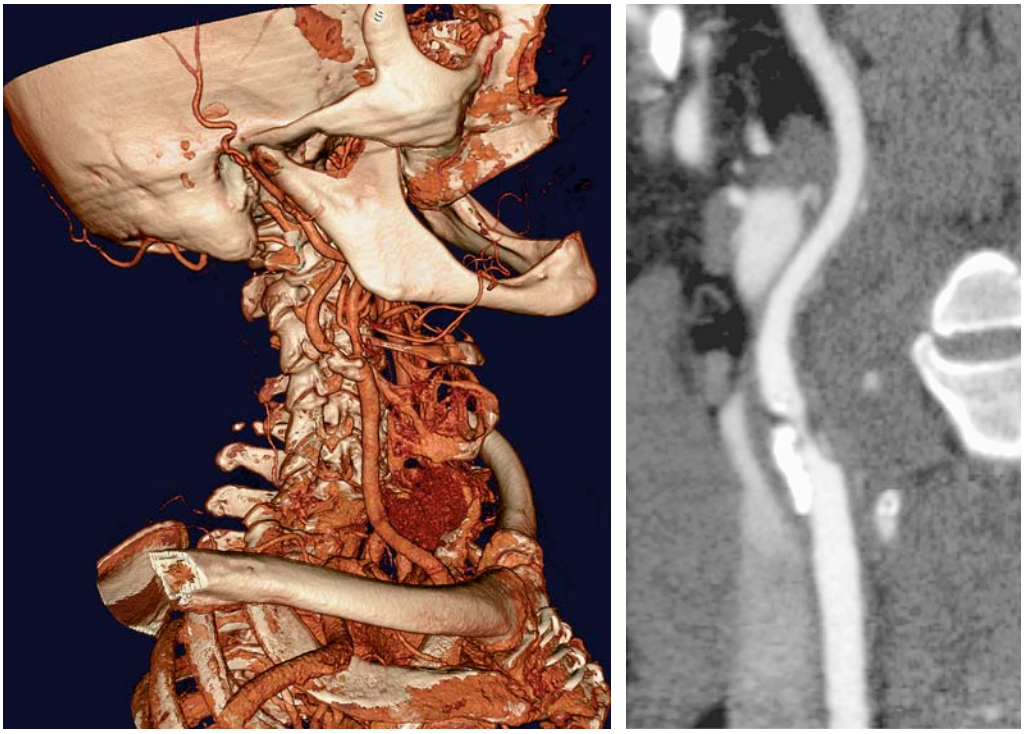

Figure 8.6.1. (A and B) Patient 1: unsegmented VR image demonstrates significant calcific plaque at the bifurcation, which limits evaluation of the stenosis. The CPR demonstrates a 90% lesion with calcific and soft plaque.

Figure 8.6.2. (A and B) Patient 2: The stenosis in this case is secondary to soft plaque and is therefore well shown with volume rendering in both a segmented and unsegmented example. Images with the bifurcation and bony landmarks are important for the surgeon.

A B

Figure 8.6.3. (A and B) Patient 3: segmented VR image obtained with automated software, and presented with a ghost background image of the osseous landmarks. This was necessary, as contrast in the jugular vein obscured the carotid artery. Both the VR and curved image show a string sign of a very critical lesion. Plaque characteristics are well seen on the curved image. Note the very small caliber ICA distal to the stenosis secondary to longstanding poor flow.

Diagnosis

Severe to critical carotid artery stenosis in three patients.

Teaching Points

Carotid artery CTA with MDCT scanners has gained rapid acceptance as a definitive modality for characterizing carotid stenosis prior to surgery. Many studies with 4-detector MDCT technology have already validated the accuracy of CTA, and I suspect that in the future additional studies using 16-detector scanners and more sophisticated workstation software will demonstrate CTA to be the single best and most accurate modality for characterizing carotid disease. CT has significant advantages over both MRA and catheter DSA. CT is currently the only method that can provide detailed 3D characterization of plaque composition and morphology. CT shows calcified, fibrous, and lipid plaque as well as acute thrombus. The higher resolution of CT compared with MRI allows for more accurate measurements.

Evaluating patients with calcified plaque has long been considered to be a major limitation of CTA of the carotids. This is true if only volume-rendered or MIP images are used for evaluation. Patients with extensive calcification should be evaluated with curved planar reconstructions. Fortunately, many workstations now have automated

vessel-tracking software that can easily generate curved reconstructions. This software has considerably shortened the processing time, but if it is not available, then manual CPRs can be performed.

Successful CTA requires attention to detail. Accurate measurements require properly oriented oblique or curved images. Careful correlation with axial or sagittal source images should also be made. Currently, measurements are made based on criteria used in the North American Symptomatic Carotid Endarterectomy Trial (NASCET). The diameter stenosis at the lesion should be measured and compared with the ICA distal to the stenosis where it appears normal. Most surgeons are still using 70% as a cutoff for surgery in asymptomatic patients, but a lower percent of stenosis is often used in symptomatic patients. These criteria were developed based on angiography which provides only a 2D representation of the stenosis. Three-dimensional imaging techniques such as multidetector CTA can allow for calculation of true cross-sectional area or volume stenosis. In the future new criteria may be developed to take advantage of this ability.

Case 8.7: Aortic Stent-Graft With Endoleak

Clinical Information

A 68-year-old man one-week status post stent-graft placement for an aortic aneurysm undergoing follow-up.

Postprocessing Techniques Used and Approach

Segmentation of the data set was performed using automatic segmentation software to isolate the vascular tree and remove overlying bone and soft tissues. Standard MIP and VR images of the vessels were reviewed after segmentation (Table 8.7 and Figures 8.7.1 through 8.7.4). Detailed images of the feeding arteries supplying the endoleak were created using manual curved planar reconstructions.

Diagnosis

Aortic stent-graft with a Type II endoleak via the inferior mesenteric artery and a right lumbar artery.

Table 8.7. Scan Acquisition Parameters for Case 8.7, Aortic Stent-graft with Endoleak

Slice No. and Thickness	**16 × 0.5 mm**
Coverage	**Diaphragm to groin** **A 3-phase study is performed (precontrast, arterial, delay)**
Helical Pitch	**1.25:1**
Rotation Speed	**0.5 sec**
Dose Parameters	**120 kVp, 200 mAs**
Contrast Dose	**100 mL Omnipaque 350**
Injection Rate	**4 mL/sec**
Bolus Timing Method	**Bolus triggering on the abdominal aorta**

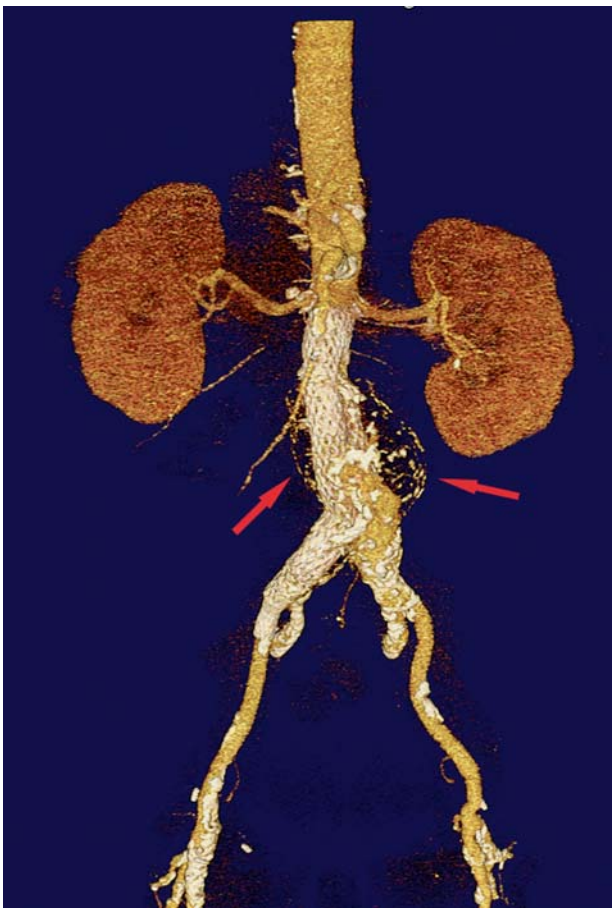

Figure 8.7.1. Three-dimensional volume reconstruction of the aorta with segmentation demonstrates a stent in the abdominal aorta just below the renal arteries. The stent extends into the common iliac arteries on both sides. The calcified wall of the native aorta is visible (arrows).

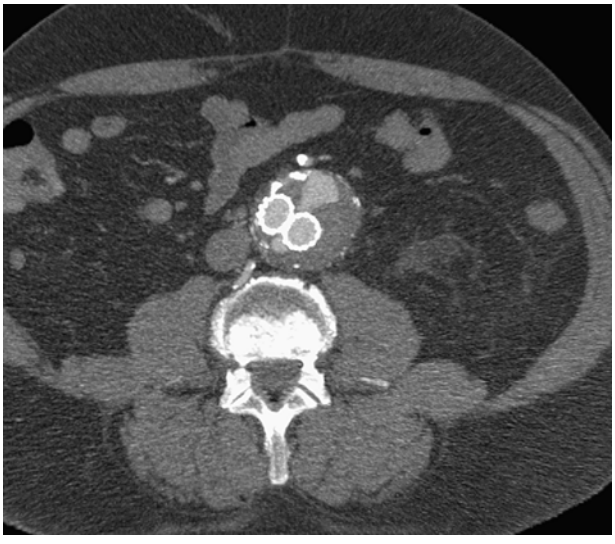

Figure 8.7.2. Axial 5-mm image from the arterial phase demonstrates extravasated contrast in the aneurysm sac. Separate anterior and posterior collections are present.

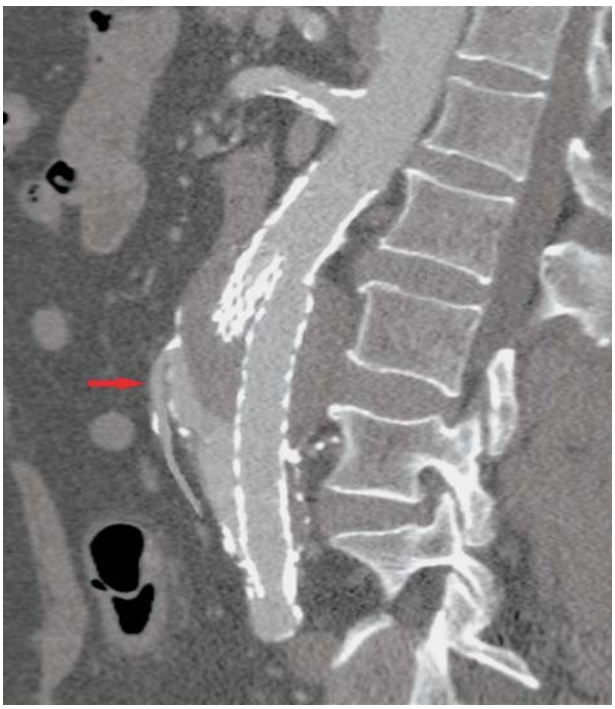

Figure 8.7.3. Sagittal curved planar reconstruction through the inferior mesenteric artery (IMA). The IMA (arrow) is clearly shown to communicate with the anterior contrast collection.

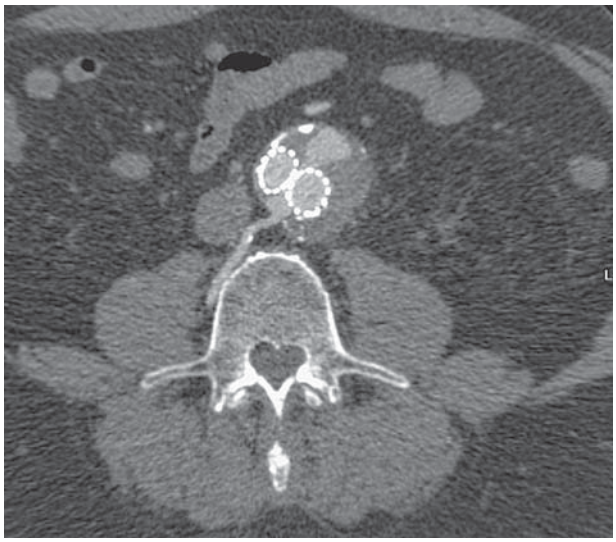

A

B

Figures 8.7.4. (A and B) Axial and sagittal curved planar reconstructions through a right lumbar artery. The posterior collection communicates with a lumbar artery on the right side.

Teaching Points

Persistent contrast enhancement outside the lumen of the stent-graft within an abdominal aortic aneurysm sac is termed an endoleak. This is the most common complication of endovascular abdominal aortic aneurysm repair (EVAR). An endoleak represents an undesirable bypass of blood around the stent-graft within the aneurysm sac. Immediately following graft placement endoleaks can be seen in 20% to 30% of patients. Many of these spontaneously close, and by six months leaks are seen in only about 10% of patients. When persistent, an endoleak is considered to represent a procedural failure because it may contribute to further enlargement and rupture of the aneurysm.

Currently endoleaks are classified into five types:

- Type 1: leaks at the proximal or distal graft attachment site.
- Type 2: branch flow leaks, usually from the inferior mesenteric artery (IMA) or lumbar arteries. These can be simple (to-and-fro flow in a vessel) or complex (flow-through with two or more patent branch vessels).
- Type 3: leaks related to a graft defect or modular separation.
- Type 4: leaks related to fabric wall porosity.
- Type 5: endotension (transmitted pressure through the graft).

CTA is the imaging modality of choice for evaluating patients following EVAR. CTA is useful for detecting and characterizing endoleaks and for following the size of the aneurysm sac. With time, the aneurysm sac should decrease in size. An increase in size, particularly when accompanied by an endoleak, is generally an indication for additional intervention. Most type I and type III endoleaks require reintervention or, less frequently, open conversion, whereas type II endoleaks are often benign because they may heal spontaneously and thus can be safely observed without treatment. For clinically important type II endoleaks, transarterial or translumbar embolization or laparoscopic clipping of the feeding vessels can be performed. Any type of endoleak associated with an enlarging aneurysm necessitates additional treatment.

CT evaluation following EVAR should be performed with a multiphasic protocol. Unenhanced CT images are acquired so that they can be compared with arterial phase images to enable identification of small perigraft leaks and differentiate such leaks from a calcified luminal thrombus or the metallic portion of the stent-graft. Delayed phase images have also been advocated to detect low-flow leaks, although these are of uncertain significance, and it is somewhat controversial as to whether these images are needed in all patients.

Postprocessing should include volume-rendered images, which are best used to demonstrate the stent-graft and its relationship to other vessels, as well as careful review of axial and multiplanar images. In this patient the diagnosis of endoleak was easily established by reviewing axial and multiplanar reconstructions. The curved planar images, however, beautifully demonstrate the feeding lumbar and IMA arteries. These images are quite useful to the interventional radiologist or surgeon for treatment planning.

Case 8.8: Mesenteric Ischemia

Clinical Information

An 87-year-old woman with severe abdominal pain, weight loss, and bloody diarrhea.

Postprocessing Techniques Used and Approach

Soft tissue structures are reviewed with standard axial and MPR images created on the scan console (Table 8.8 and Figures 8.8.1 through 8.8.4). The CTA is reviewed with VR and MIP protocols. Automated software is used to isolate the aorta and the main branches from other structures. Curved planar reconstructions are done through the superior mesenteric artery (SMA) using vessel-tracking software.

Diagnosis

Ischemic bowel of the left colon with high-grade SMA stenosis, occlusion of the IMA, and occlusion of the celiac artery with reconstitution via collaterals from the SMA.

Teaching Points

Acute mesenteric ischemia is a life-threatening condition with mortality rates that range from 59% to 93% reported in the literature. Studies have shown that early diagnosis and treatment have a substantial effect on patient outcome. MDCT is an ideal modality to evaluate any patient with suspected mesenteric ischemia. A dual-phase acquisition should be performed. An initial arterial study is done to evaluate the aorta and mesenteric arteries, and a second venous phase is done to evaluate the portal and mesenteric veins and also the appearance of the bowel and other abdominal organs.

The most common CT finding in bowel ischemia is bowel wall thickening, although it is nonspecific. The thickened bowel wall is sometimes associated with the target sign, alternating layers of high and low attenuation within the thickened bowel wall, which results from sub-

Table 8.8. Scan Acquisition Parameters for Case 8.8, Mesenteric Ischemia

Slice No. and Thickness	**16 × 1.0 mm**
Coverage	**Abdomen and pelvis**
Helical Pitch	**1.25:1**
Rotation Speed	**0.5 sec**
Dose Parameters	**120 kVp, 130 mAs**
Contrast Dose	**100 mL Omnipaque 350**
Injection Rate	**4 mL/sec**
Bolus Timing Method	**Bolus triggering on the abdominal aorta**
Additional venous phase imaging performed 60 sec from start of injection	

Figure 8.8.1. Axial 3-mm image in the lower abdomen and pelvis. Wall thickening is noted involving the left colon. The abnormality extends from the splenic flexure to the rectum with sparing of the right and transverse colons.

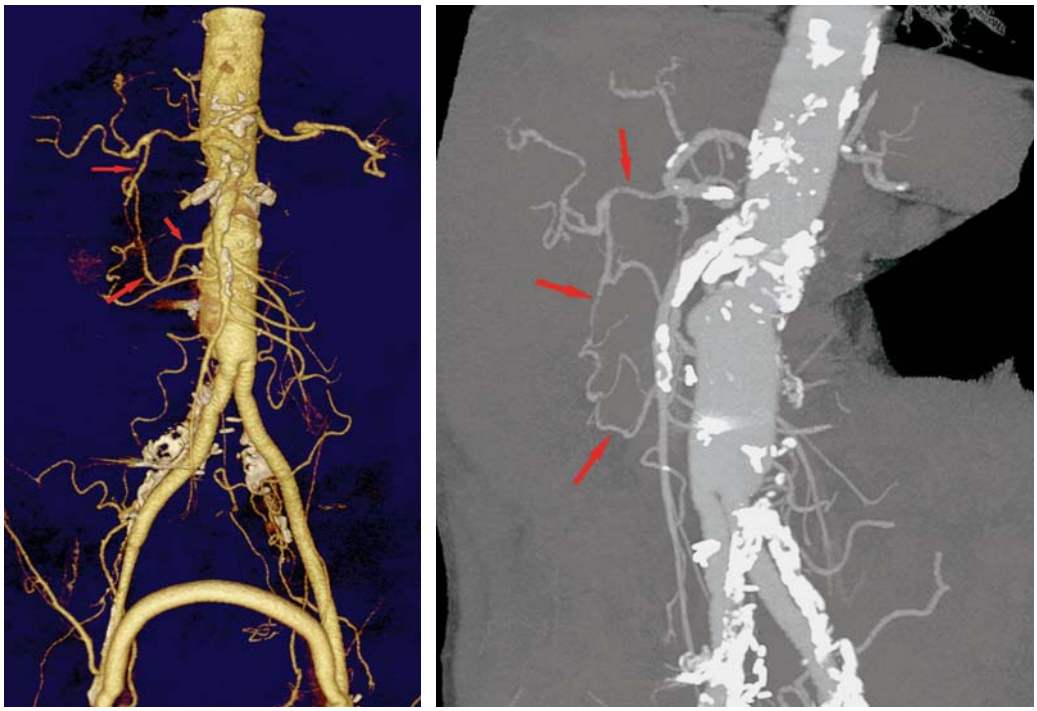

A B

Figure 8.8.2. (A and B) Segmented VR and MIP images of the aorta and branches. The patient has had prior surgery with placement of a Gore-Tex graft into the aorta with an end-to-side anastomosis. The native aorta is heavily calcified and occluded. A femoral-femoral crossover graft is also present. The IMA is completely occluded. The celiac artery is also occluded at its origin, but reconstitutes via collaterals through the pancreaticoduodenal arcade to retrograde fill the gastroduodenal artery and then the hepatic artery (arrows). The small collaterals are better seen on the MIP than the VR image.

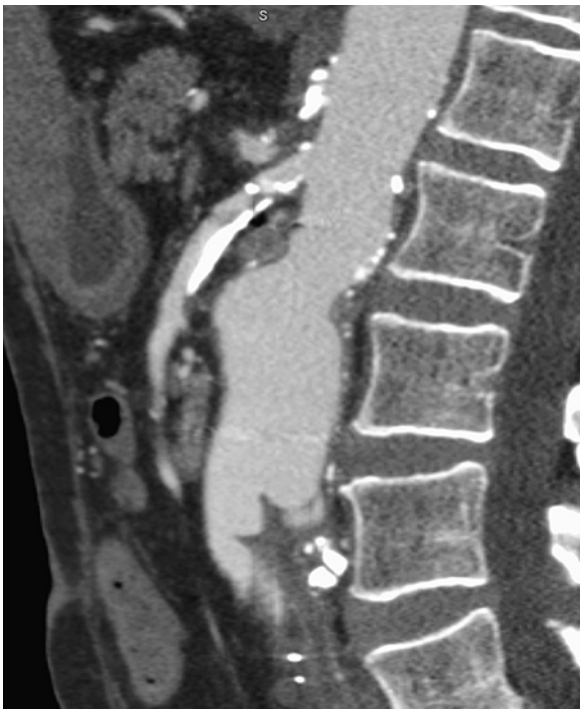

Figure 8.8.3. A CPR image through the SMA. Complex calcified and soft plaque is present resulting in over 90% stenosis.

mucosal edema or hemorrhage. The bowel wall can be either increased or decreased in enhancement. Other CT findings of bowel ischemia include the following: bowel dilatation with fluid levels, engorgement of mesenteric veins and mesenteric edema or stranding, intramural gas

Figure 8.8.4. Axial MIP image demonstrating the reconstituted hepatic and splenic arteries with celiac occlusion.

(intestinal pneumatosis), mesenteric or portal venous gas, increased enhancement of the thickened bowel wall, and ascites.

Bowel ischemia can be caused by abnormalities in either the arterial supply or venous drainage, and both arteries and veins should be carefully evaluated. Acute occlusions of the superior mesenteric artery due to thrombosis or embolization are responsible for approximately 60% to 70% of cases of acute bowel ischemia, whereas mesenteric venous thromboses account for 5% to 10% of the total, and nonocclusive conditions account for approximately 20% to 30% of cases.

MDCT is particularly well suited to diagnosis of either arterial or venous occlusions as well as proximal atherosclerotic stenosis. Peripheral embolization with occlusion of distal branches is more difficult to diagnose with CT, but current scanners are able to demonstrate even small peripheral vessels. Careful review of sliding slab MIP images can detect these more peripheral occlusions.

Case 8.9: Aortic Occlusion With Collateral Pathways

Clinical Information

A 76-year-old man with progressive leg pain and claudication.

Postprocessing Techniques Used and Approach

Automatic segmentation is used to remove the bones but leave in place the aorta and the multiple collateral vessels. Window/level and transparency functions are used to remove excess soft tissues. Images are reviewed in both MIP and VR protocols and correlated with MPR images (Table 8.9 and Figures 8.9.1 through 8.9.3).

Diagnosis

Aortic occlusion with demonstration of collateral circulation.

Teaching Points

CTA provides exquisite detail of the vascular anatomy in this patient with chronic aortic occlusion, saving him from a catheter angiogram that would require an axillary puncture. All the information needed by the surgeon to treat the patient is present on the CT. The CTA not only

Table 8.9. Scan Acquisition Parameters for Case 8.9, Aortic Occlusion with Collateral Pathways

Slice No. and Thickness	**16 × 1.0 mm**
Coverage	**Diaphragm through feet**
Helical Pitch	**1.25:1**
Rotation Speed	**0.5 sec**
Dose Parameters	**120 kVp, 200 mAs**
Contrast Dose	**125 mL Omnipaque 350**
Injection Rate	**3 mL/sec**
Bolus Timing Method	**Bolus triggering on the femoral artery**

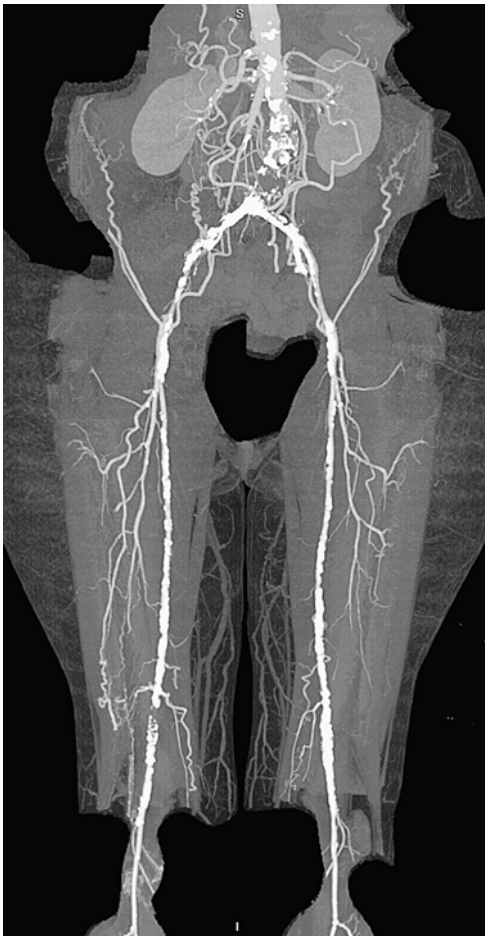

Figure 8.9.1. An MIP image of a portion of the aortogram and runoff examination. There is occlusion of the aorta and common iliac arteries bilaterally. Diffuse disease is present in the superficial femoral arteries bilaterally with a focal occlusion on the right side. Geniculate collaterals provide distal reconstitution.

Figure 8.9.2. Coronal curved planar reconstruction demonstrates the occluded aorta and common iliac arteries.

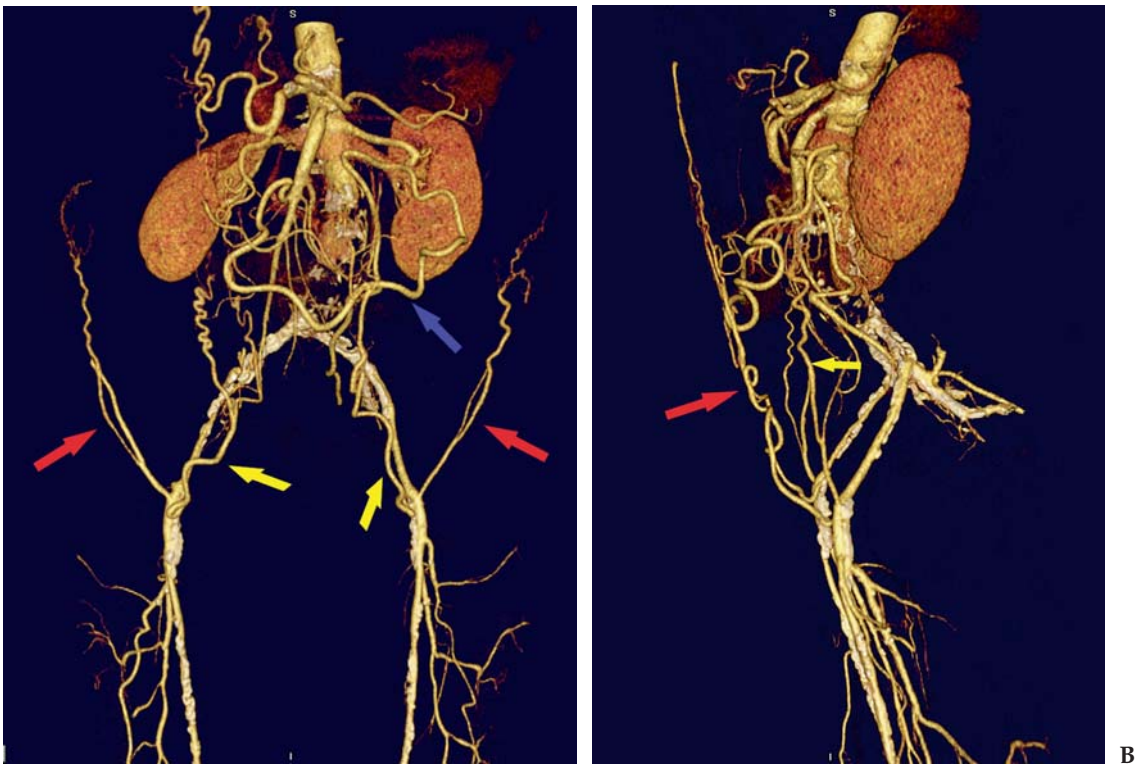

Figure 8.9.3. (A and B) Anterior-posterior and lateral volume-rendered images illustrate the collateral pathways providing circulation in this patient. The artery of Riolan (blue arrow) supplies collateral flow to the occluded interior mesenteric artery territory. The external iliac arteries are reconstituted via flow from the inferior epigastric arteries (yellow arrows) and the lateral circumflex iliac arteries (red arrows).

demonstrates the vascular occlusions of the aorta, iliacs, and IMA, but it also clearly shows the collateral circulation pathways. In this patient the IMA is occluded. Flow is maintained via an arc of Riolan arising from the SMA to the IMA territory. The occluded external iliac arteries are reconstituted via flow from the inferior epigastric and lateral circumflex iliac arteries. It would be difficult if not impossible to get all of this information from a catheter angiogram.

Case 8.10: Pulmonary Embolism

Clinical Information

A 52-year-old man arrives at the emergency room with sharp chest pain and dyspnea.

Postprocessing Techniques Used and Approach

Thin section axial and coronal images are ideal for evaluating the pulmonary arteries for embolus (Table 8.10 and Figures 8.10.1 through

Table 8.10. Scan Acquisition Parameters for Case 8.10, Pulmonary Embolism

Slice No. and Thickness	16 × 0.5 mm
Coverage	Chest
Helical Pitch	1.25:1
Rotation Speed	0.4 sec
Dose Parameters	120 kV, 200 mAs
Contrast Dose	125 mL Omnipaque 350
Injection Rate	4 mL/sec
Bolus Timing Method	Bolus triggering on the pulmonary artery

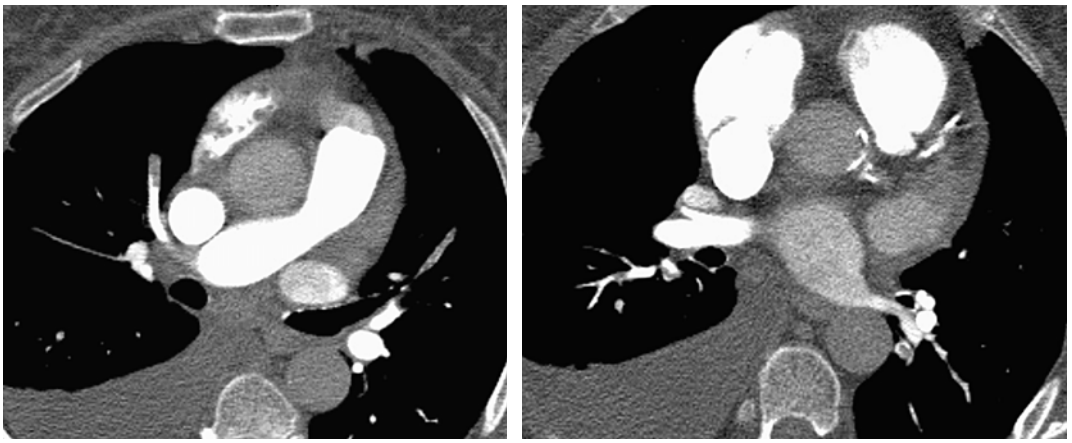

A B

Figure 8.10.1. (A and B) Axial 2-mm images through the pulmonary arteries at two different levels. Both images demonstrate bilateral pulmonary embolus to second- and third-order pulmonary arteries.

Figure 8.10.2. Coronal 2-mm image again demonstrates bilateral thrombi.

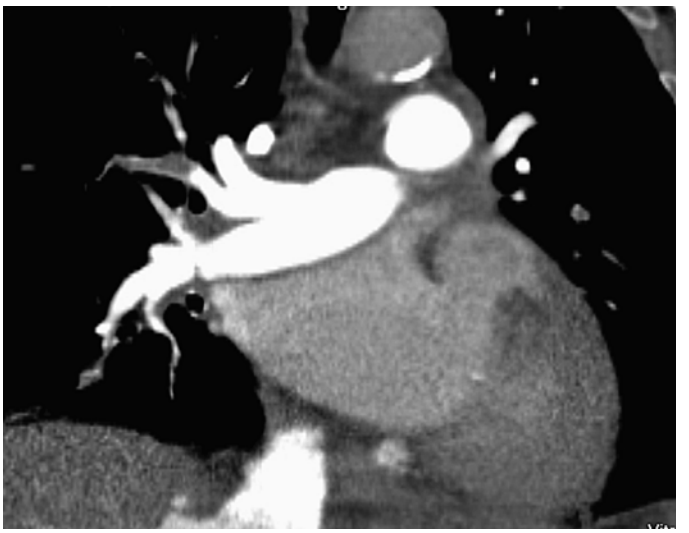

Figure 8.10.3. Curved planar reconstruction along the right upper lobe pulmonary artery better shows occlusive thrombus in a pulmonary artery branch vessel.

8.10.3). Image thickness of 1 mm to 3 mm is preferred and generally, thinner is better. Thicker slab MIP images can also be a helpful adjunct. Theses images better show vessel cutoffs in smaller, peripheral arteries and can show asymmetry from side to side better. Curved planar reconstructions are usually not needed for diagnosis, but can be useful in select cases for following a vessel and better demonstrating an intraluminal thrombus.

Diagnosis

Acute segmental and subsegmental pulmonary embolus (PE).

Teaching Points

Acute pulmonary embolus remains a very important clinical problem, and is the cause of significant morbidity and mortality. For many reasons, MDCT has rapidly become the gold standard for evaluation of suspected pulmonary embolus. An important advantage of CT over other imaging modalities is that both mediastinal and parenchymal structures can be evaluated, and thrombus can be directly visualized. Investigators have shown that up to two thirds of patients in whom there is an initial suspicion of PE actually have another diagnosis, such as aortic dissection, pneumonia, lung cancer, or pneumothorax (refer to Case 12.1). Most of these diagnoses are amenable to CT demonstration.

The accuracy of CT has been shown to be superior to that of nuclear medicine studies and equal to that of catheter angiography. Ventilation-Perfusion (VQ) scans are now rarely performed in our institution except for individuals who are unable to get iodinated contrast because of poor renal function or severe allergy.

With a high-quality CTA using thin slice thickness (1.25 mm or less) visualization of subsegmental fourth-, fifth-, and even sixth-order branches is possible in the vast majority of patients. This makes the need for catheter pulmonary angiography almost negligible. At Long Beach Memorial if a patient has an indeterminate CT (usually because of some technical or timing problem) we prefer to repeat the CTA rather than perform a catheter angiogram. Although it is still possible that small, peripheral emboli may be missed with MDCT, these emboli are not reliably diagnosed with catheter angiography, and studies have shown that they may not be clinically significant. The risk of significant embolism to patients with a negative, good quality CTA is very low.

In order to achieve high accuracy with CT, review of thin-section axial and coronal data should be routinely performed. Review of the CTA images can be performed either on PACS using 2-mm to 3-mm axial and coronal reconstructions (2 mm is preferred) or on the workstation (or PACS with similar capability) where thinner slices, multiplanar reconstructions, and MIP images can all be used in the review. Thin sections are best to directly visualize the intraluminal filling defects, but MIP images are useful to see cut off and occluded vessels which may be overlooked on thin slice data.

Selected Readings

Peripheral Vascular Disease

1. Catalano C, Fraioli F, Laghi A, et al. Infrarenal aortic and lower-extremity arterial disease: diagnostic performance of multi-detector row CT angiography. Radiology 2004 May;231(2):555–563.
2. Katz DS, Hon M. CT angiography of the lower extremities and aortoiliac system with a multi-detector row helical CT scanner: promise of new opportunities fulfilled. Radiology 2001;221:7–10.
3. Martin ML, Tay KH, Flak B, et al. Multidetector CT angiography of the aortoiliac system and lower extremities: a prospective comparison with digital subtraction angiography. Am J Roentgenol 2003 Apr;180(4): 1085–1091.
4. Napoli A, Fleischmann D, Chan FP, et al. Computed tomography angiography: state-of-the-art imaging using multidetector-row technology. J Comput Assist Tomogr 2004 Jul–Aug;28(suppl 1):S32–S45.
5. Ofer A, Nitecki SS, Linn S, et al. Multidetector CT angiography of peripheral vascular disease: a prospective comparison with intraarterial digital subtraction angiography. Am J Roentgenol 2003;180:719–724.
6. Romano M, Mainenti PP, Imbriaco M, et al. Multidetector row CT angiography of the abdominal aorta and lower extremities in patients with peripheral arterial occlusive disease: diagnostic accuracy and interobserver agreement. Eur J Radiol 2004 Jun;50(3):303–308.
7. Rubin GD. MDCT imaging of the aorta and peripheral vessels. Eur J Radiol 2003;45(suppl 1):S42–S49.
8. Willmann JK, Mayer D, Banyai M, et al. Evaluation of peripheral arterial bypass grafts with multi–detector row CT angiography: comparison with duplex US and digital subtraction angiography. Radiology 2003;229: 465–474.

Aortic Occlusion with Axillary and Femoral Bypasses

9. Catalano C, Fraioli F, Laghi A, et al. Infrarenal aortic and lower-extremity arterial disease: diagnostic performance of multi-detector row CT angiography. Radiology 2004 May;231(2):555–563.
10. Katz DS, Hon M. CT angiography of the lower extremities and aortoiliac system with a multi-detector row helical CT scanner: promise of new opportunities fulfilled. Radiology 2001;221:7–10.
11. Martin ML, Tay KH, Flak B, et al. Multidetector CT angiography of the aortoiliac system and lower extremities: a prospective comparison with digital subtraction angiography. Am J Roentgenol 2003 Apr;180(4):1085–1091.
12. Napoli A, Fleischmann D, Chan FP, et al. Computed tomography angiography: state-of-the-art imaging using multidetector-row technology. J Comput Assist Tomogr 2004 Jul–Aug;28(suppl 1):S32–S45.
13. Romano M, Mainenti PP, Imbriaco M, et al. Multidetector row CT angiography of the abdominal aorta and lower extremities in patients with peripheral arterial occlusive disease: diagnostic accuracy and interobserver agreement. Eur J Radiol 2004 Jun;50(3):303–308.
14. Rubin GD. MDCT imaging of the aorta and peripheral vessels. Eur J Radiol 2003;45(suppl 1):S42–S49.

Aortic Dissection

15. Castañer E, Andreu M, Gallardo X, Mata JM, Cabezuelo MA, Pallardó Y. CT in nontraumatic acute thoracic aortic disease: typical and atypical features and complications. Radiographics 2003;23:93–110.
16. Gavant ML, Flick P, Menke P, Gold RE. CT aortography of thoracic aortic rupture. Am J Roentgenol 1996 Apr;166:955–961.
17. Gotway MB, Dawn SK. Thoracic aorta imaging with multislice CT. Radiol Clin North Am 2003;41:521–543.
18. Roos JE, Willmann JK, Weishaupt D, et al. Thoracic aorta: motion artifact reduction with retrospective and prospective electrocardiography assisted multi-detector row CT. Radiology 2002;222:271–277.
19. Rubin GD. CT angiography of the thoracic aorta. Semin Roentgenol 2003;38:115–134.

Renal Artery Stenosis

20. Fleischmann D. Multiple detector-row CT angiography of the renal and mesenteric vessels. Eur J Radiol 2003;45(suppl 1):S79–S87.
21. Kim JK, Park SY, Kim HJ, et al. Living donor kidneys: usefulness of multidetector row CT for comprehensive evaluation. Radiology 2003;229:869–876.
22. Ofer A, Nitecki SS, Linn S, et al. Multidetector CT angiography of peripheral vascular disease: a prospective comparison with intraarterial digital subtraction angiography. Am J Roentgenol 2003;180:719–724.
23. Urban BA, Lloyd E, Ratner LE, Fishman EK. Three-dimensional volume-rendered CT angiography of the renal arteries and veins: normal anatomy, variants, and clinical applications. Radiographics 2001;21:373–386.
24. Willmann JK, Wildermuth S, Pfammatter T, et al. Aortoiliac and renal arteries: prospective intraindividual comparison of contrast-enhanced three-dimensional MR angiography and multi-detector row CT angiography. Radiology 2003;226:798–811.

Ulnar Artery Pseudoaneurysm

25. Anderson SE, Monaco DD, Buechler U, et al. Imaging features of pseudoaneurysms of the hand in children and adults. Am J Roentgenol 2003 Mar;180:659–664.
26. De Monaco D, Fritsche G, Rigoni G, Schunke S, Von Wartenburg U. Hypothenar hammer syndrome, retrospective study of nine cases. J Hand Surg [Br] 1999;24:731–734.

Carotid Stenosis

27. Alvarez-Linera J, Benito-Leon J, Escribano J, et al. Prospective evaluation of carotid artery stenosis: elliptic centric contrast-enhanced MR angiography and spiral CT angiography compared with digital subtraction angiography. Am J Neuroradiol 2003;24:1012–1019.
28. Barnett HJM, Taylor DW, Eliasziw M, et al. Benefit of carotid endarterectomy in patients with symptomatic moderate or severe stenosis. N Engl J Med 1998;339:1415–1425.
29. Hirai T, Korogi Y, Ono K, et al. Maximum stenosis of extracranial internal carotid artery: effect of luminal morphology on stenosis measurement by using CT angiography and conventional DSA. Radiology 2001;221: 802–809.
30. Josephson SA, Bryant SO, Mak HK, Johnston SC, Dillon WP, Smith WS. Evaluation of carotid stenosis using CT angiography in the initial evaluation of stroke and TIA. Neurology 2004 Aug;63(3):457–460.
31. Katano H, Kato K, Umemura A, Yamada K. Perioperative evaluation of carotid endarterectomy by 3D-CT angiography with refined reconstruction: preliminary experience of CEA without conventional angiography. Br J Neurosurg 2004 Apr;18(2):138–148.
32. Phillips CD, Bubash LA. CT angiography and MR angiography in the evaluation of extracranial carotid vascular disease. Radiol Clin North Am 2002;40:783–798.
33. Smith WS, Roberts HC, Chuang NA, et al. Safety and feasibility of a CT protocol for acute stroke: combined CT, CT angiography, and CT perfusion imaging in 53 consecutive patients. Am J Neuroradiol 2003;24:688–690.

Aortic Stent-Graft With Endoleak

34. Dattilo JB, Brewster DC, Fan CM, et al. Clinical failures of endovascular abdominal aortic aneurysm repair: incidence, causes, and management. J Vasc Surg 2002;35:1137–1144.
35. Rozenblit AM, Patlas M, Rosenbaum AT, et al. Detection of endoleaks after endovascular repair of abdominal aortic aneurysm: value of unenhanced and delayed helical CT acquisitions. Radiology 2003;227:426–433.
36. Sawhney R, Kerlan RK, Wall SD, et al. Analysis of initial CT findings after endovascular repair of abdominal aortic aneurysm. Radiology 2001;220: 157–160.
37. Tillich M, Hausegger KA, Tiesenhausen K, Tauss J, Groell R, Szolar D. Helical CT angiography of stent-grafts in abdominal aortic aneurysms: morphologic changes and complications. Radiographics 1999;19:1573–1583.
38. van Marrewijk C, Buth J, Harris PL, Norgren L, Nevelsteen A, Wyatt MG. Significance of endoleaks after endovascular repair of abdominal aortic aneurysms: the EUROSTAR experience. J Vasc Surg 2002;35:461–473.

39. White RA, Donayre CE, Walot I, Woody J, Kim N, Kopchok GE. Computed tomography assessment of abdominal aortic aneurysm morphology after endograft exclusion. J Vasc Surg 2001;33(suppl 2):S1–S10.

Mesenteric Ischemia

40. Cademartiri F, Raaijmakers RHJ, Kuiper JW, et al. Multi–detector row CT angiography in patients with abdominal angina. Radiographics 2004;24: 969–984.
41. Horton KM, Fishman EK. Multi-detector row CT of mesenteric ischemia: can it be done? Radiographics 2001;21:1463–1473.
42. Horton KM, Fishman EK. Volume-rendered 3D CT of the mesenteric vasculature: normal anatomy, anatomic variants, and pathologic conditions. Radiographics 2002;22:161–172.
43. Kirkpatrick IDC, Kroeker MA, Greenberg HM. Biphasic CT with mesenteric CT angiography in the evaluation of acute mesenteric ischemia: initial experience. Radiology 2003 229:91–98.
44. Rha SE, Ha HK, Lee SH, et al. CT and MR imaging findings of bowel ischemia from various primary causes. Radiographics 2000;20:29–42.
45. Wiesner W, Khurana B, Ji H, Ros PR. CT of acute bowel ischemia. Radiology 2003 226:635–650.
46. Zalcman M, Sy M, Donckier V, Closset J, Van Gansbeke D. Helical CT signs in the diagnosis of intestinal ischemia in small-bowel obstruction. Am J Roentgenol 2000 Dec;175:1601–1607.

Aortic Occlusion With Collateral Pathways

47. Bhalla S, Menias CO, Heiken JP. CT of acute abdominal aortic disorders. Radiol Clin North Am 2003 Nov;41(6):1153–1169.
48. Catalano C, Fraioli F, Laghi A, et al. Infrarenal aortic and lower-extremity arterial disease: diagnostic performance of multi-detector row CT angiography. Radiology 2004 May;231(2):555–563.
49. Martin ML, Tay KH, Flak B, et al. Multidetector CT angiography of the aortoiliac system and lower extremities: a prospective comparison with digital subtraction angiography. Am J Roentgenol 2003 Apr;180(4):1085–1091.
50. Napoli A, Fleischmann D, Chan FP, et al. Computed tomography angiography: state-of-the-art imaging using multidetector-row technology. J Comput Assist Tomogr 2004 Jul–Aug;28(suppl 1):S32–S45.
51. Romano M, Mainenti PP, Imbriaco M, et al. Multidetector row CT angiography of the abdominal aorta and lower extremities in patients with peripheral arterial occlusive disease: diagnostic accuracy and interobserver agreement. Eur J Radiol 2004 Jun;50(3):303–308.
52. Rubin GD. MDCT imaging of the aorta and peripheral vessels. Eur J Radiol 2003;45(suppl 1):S42–S49.

Pulmonary Embolism

53. Ghaye B, Szapiro D, Mastora I, et al. Peripheral pulmonary arteries: how far in the lung does multi-detector row spiral CT allow analysis? Radiology 2001;219:629–636.
54. Patel S, Kazerooni EA, Cascade PN. Pulmonary embolism: optimization of small pulmonary artery visualization at multi–detector row CT. Radiology 2003;227:455–460.
55. Remy-Jardin M, Tillie-Leblond I, Szapiro D, et al. CT angiography of pulmonary embolism in patients with underlying respiratory disease: impact

of multislice CT on image quality and negative predictive value. Eur Radiol 2002;12:1971–1978.
56. Schoepf UJ, Costello P. CT angiography for diagnosis of pulmonary embolism: state of the art. Radiology 2004 Feb;230(2):329–337.
57. Schoepf UJ, Goldhaber SZ, Costello P. Spiral computed tomography for acute pulmonary embolism. Circulation 2004 May;109(18):2160–2167.
58. Tillie-Leblond I, Mastora I, Radenne F, et al. Risk of pulmonary embolism after a negative spiral CT angiogram in patients with pulmonary disease: 1-year clinical follow-up study. Radiology 2002;223:461–467.

Chapter 9

Pediatric Imaging

Case 9.1: Vascular Ring

Clinical Information

A one-day-old infant with severe upper respiratory obstruction and stridor.

Postprocessing Techniques Used and Approach

The standard axial and multiplanar reconstructions were inadequate for demonstrating all of the pathology in this case (Table 9.1 and Figures 9.1.1 through 9.1.3). Oblique coronal and sagittal images were obtained along the long axis of the trachea to demonstrate the severe tracheal stenosis. Axial MIP images were made to show the complete vascular ring in one image. The double aortic arch was difficult to show on standard MIP or MPR images. Volume-rendered images best showed the double arch, but segmentation was done to remove bone and the pulmonary arteries, providing maximal detail of the aorta. Part of the segmentation required manual editing of the 3D images.

Diagnosis

Double aortic arch causing a complete vascular ring and severe tracheal and esophageal compression.

Teaching Points

This was a very small and critically ill infant with multiple abnormalities. The CT was effectively able to identify and characterize the child's abnormalities in a scan that took only a few seconds and required no anesthesia or sedation.

Different rendering techniques were used to highlight different findings. The images produced not only made possible the proper diagnosis, but also provided the surgeons with all the information they needed to operate on this child, saving valuable time and avoiding additional invasive procedures. The segmented volume images were

Table 9.1. Scan Acquisition Parameters for Case 9.1, Vascular Ring

Slice No. and Thickness	**16 × 0.5 mm**
Coverage	**Chest**
Helical Pitch	**1.25:1**
Rotation Speed	**0.5 sec**
Dose Parameters	**80 kVp, 30 mAs**
Contrast Dose	**8 mL**
Injection Rate	**Hand injection**
Bolus Timing Method	**Manual bolus trigger focused on aorta**

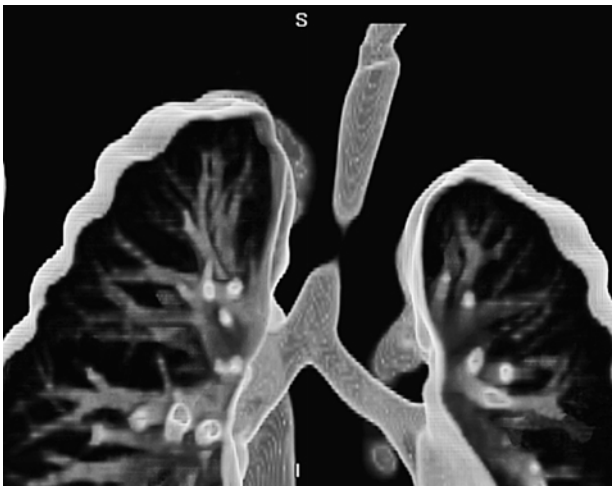

Figure 9.1.1. Thin-slab (11 mm) volume-rendered image with high transparency shows a very high grade tracheal stenosis.

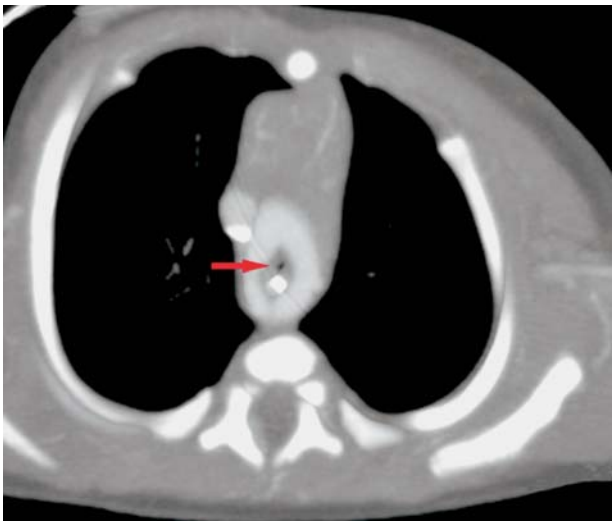

Figure 9.1.2. A 10-mm thick axial MIP image demonstrates the complete vascular ring. The trachea (red arrow) is seen as a tiny dot of air. The esophagus has a high-density nasogastric tube within it.

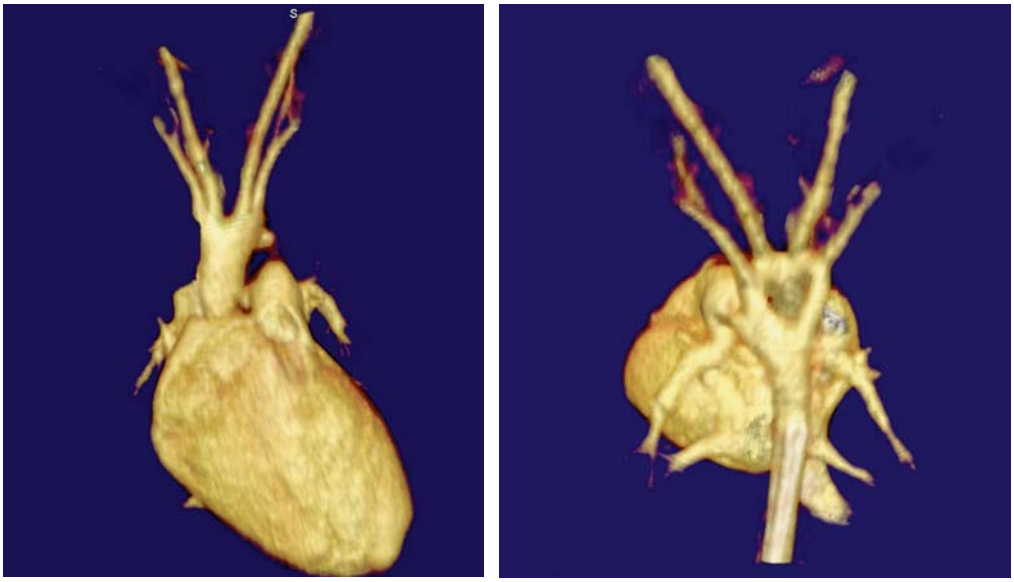

Figure 9.1.3. (A and B) Segmented volume-rendered images. A double aortic arch is present. The two arches are nearly symmetric and both give rise to a subclavian and a carotid artery.

particularly useful to the surgeons for planning the repair of this infant. At surgery the right arch was divided, leaving the carotid artery but sacrificing the subclavian artery to open the vascular ring.

Vascular anomalies are relatively common in infants and children. Many of these are asymptomatic and may not be discovered until adulthood. The anomalies that most frequently cause stridor are a double aortic arch, a right aortic arch with a left ligamentum arising from the descending aorta, and an aberrant right subclavian artery arising on the left that passes posterior to the trachea or a retroesophageal right subclavian artery.

The most common and serious complete type of vascular ring is the double aortic arch, which consists of anterior and posterior arches encircling the trachea and esophagus in a tight ring, joining distally to form a common descending aorta. The right portion and left portion of the double arch each gives rise to its own carotid and subclavian arteries. A right aortic arch with a left ligamentum arising from the descending aorta is another type of vascular ring, considerably less common than the double aortic arch. The left ligamentum arteriosum passes from the left pulmonary artery to the descending aorta or to the left subclavian artery, coursing to the left of the trachea and esophagus. The ring formed by the aorta, pulmonary artery, and ligament may compress these structures. In this anomaly, the origin of the left subclavian artery frequently is dilated (Kommerell diverticulum).

The most common aortic arch anomaly, occurring in nearly 1% of the population, is an aberrant right subclavian artery originating from an otherwise normal left aortic arch. The anomalous vessel arises from the left side of the aortic arch and crosses the mediastinum obliquely from

left to right behind the esophagus and trachea on its cephalad course. This condition rarely causes symptoms, except for occasional mild dysphagia.

Case 9.2: Skull and Orbital Fractures

Clinical Information

A nine-year-old boy who fell off his skateboard.

Postprocessing Techniques Used and Approach

Multiplanar reconstructions from the scanner, and unsegmented surface-rendered images produced on the workstation are reviewed (Table 9.2 and Figures 9.2.1 and 9.2.2).

Diagnosis

Depressed fracture of the frontal bone and superior orbital rim.

Teaching Points

This case illustrates the ability of 3D surface-rendered images to quickly and accurately display complex bony abnormalities. Although the fracture diagnosis is easily made from MPR images, the surface-rendered images are very helpful to communicate the results to the referring doctor. In this case both the neurosurgeon and ophthalmologist who operated on the patient to repair the fracture found the 3D images to be extremely helpful for surgical planning.

In many busy trauma centers, CT has replaced plain films for the diagnosis and characterization of facial and skull fractures. This is particularly true when complex fractures and multiple injuries are present. Single-slice CT has been shown previously to be far more accurate to detect facial, orbital, and skull fractures. Multidetector CT offers many additional benefits over single-slice scanners. With isotropic or near isotropic data acquisition, a single scan can generate high-quality images in any plane. Routine review of images in three planes is now possible. In addition, the data can be sent to a workstation and reviewed in volume or surface rendering. These 3D images can improve diagnostic accuracy and characterization of complex fractures. Surgeons, in particular, have found them to be very useful for operative planning.

Table 9.2. Scan Acquisition Parameters for Case 9.2, Skull and Orbital Fractures

Slice No. and Thickness	**16 × 0.5 mm**
Coverage	**Head and facial bones**
Helical Pitch	**1.25:1**
Rotation Speed	**0.5 sec**
Dose Parameters	**120 kVp, 120 mAs**
Contrast Dose	**None**

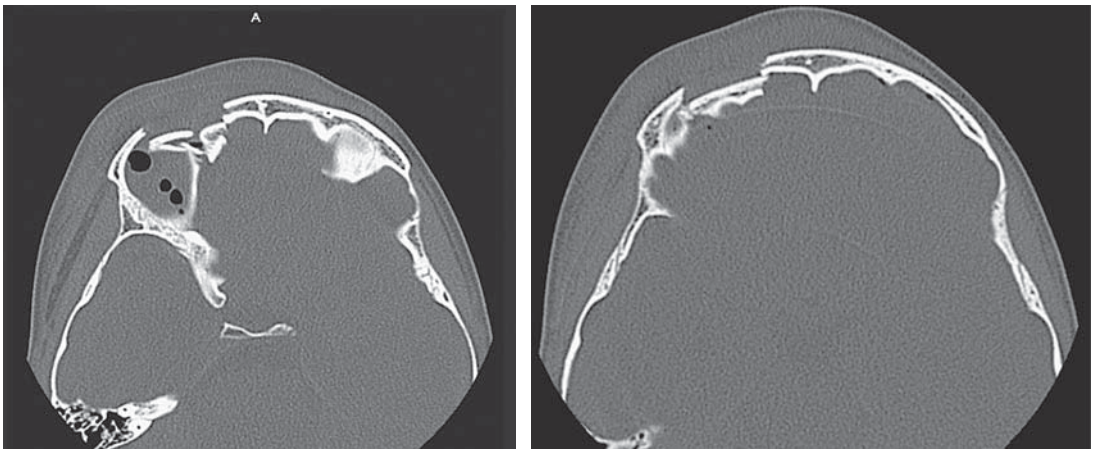

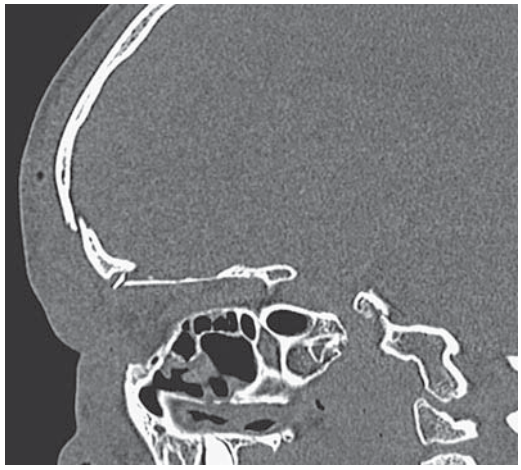

Figure 9.2.1. (A–C) Axial and sagittal 2-mm images demonstrate a comminuted fracture of the skull and superior orbital rim with depression. Orbital emphysema is present.

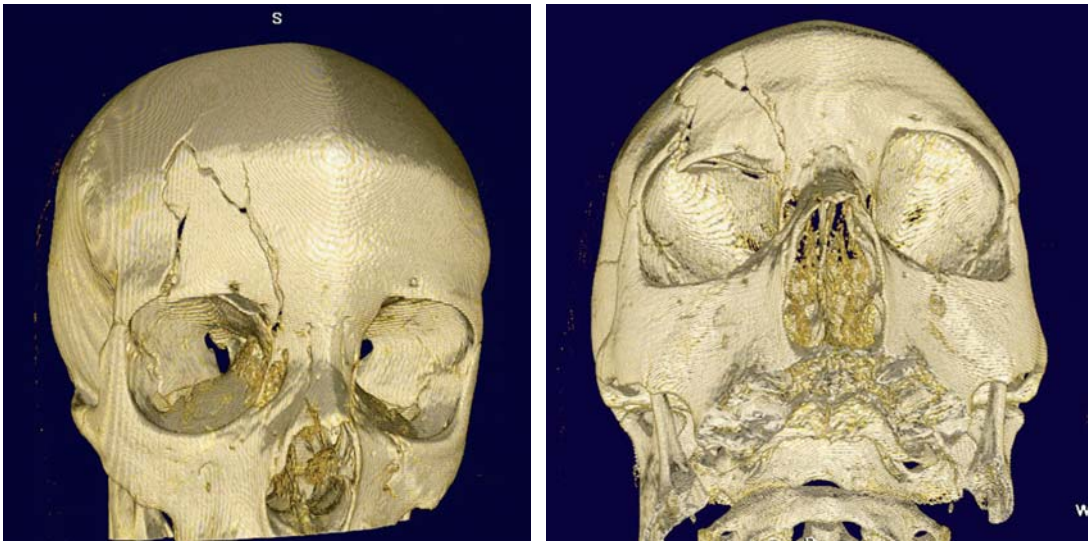

Figure 9.2.2. (A and B) Surface-rendered images of the skull in different projections. The extent and appearance of the fracture is much more easily appreciated on the 3D images compared with the MPR images. The degree of depression of the orbital rim is also better seen.

Case 9.3: Tracheal Bronchus

Clinical Information

A two-year-old boy with recurrent episodes of right upper lobe pneumonia.

Postprocessing Techniques Used and Approach

Thin-slab volume-rendered images are used to generate beautiful images of the airways (Table 9.3 and Figures 9.3.1 through 9.3.3). The slab thickness is varied to include the anatomy desired without including extraneous structures. Color, light, and transparency can be varied on the workstation to give the images the look that is desired. Many workstations have an airway preset that will give excellent images in just a few clicks. A segmented whole volume image of the right lung is also shown. The left lung has been removed with a 3D manual sculpt.

Diagnosis

Aberrant tracheal bronchus ("pig bronchus") to the right upper lobe causing recurrent pneumonia.

Teaching Points

This child had an outside CT scan on a single-detector scanner and the diagnosis was missed. The child then underwent bronchoscopy and an abnormality was noted, but the pulmonologist was unable to make a definitive diagnosis. Subsequently, the child was rescanned on the 16-slice scanner. The ability to perform superior multiplanar and 3D reconstructions in this case greatly aided diagnosis. Although a diagnosis is possible on careful review of axial images, it is much more obvious on coronal reconstructions. Once the diagnosis was made, a surgical consult was ordered, and the child subsequently underwent surgery.

Tracheal bronchus is a relatively uncommon abnormality with a reported incidence of approximately 0.1% to 2%. It is much more common on the right side and usually arises within 2 cm from the carina and is directed to the upper lobe. These aberrant bronchi are described as supernumerary when they coexist with a normal type of

Table 9.3. Scan Acquisition Parameters for Case 9.3, Tracheal Bronchus

Slice No. and Thickness	**16 × 0.5 mm**
Coverage	**Chest**
Helical Pitch	**1.5:1**
Rotation Speed	**0.5 sec**
Dose Parameters	**80 kVp, 40 mAs**
Contrast Dose	**None**

Figure 9.3.1. Coronal thin-slab volume-rendered image with high transparency. Coronal airway view of the lungs and bronchial tree demonstrates an aberrant bronchus to the right upper lobe arising from the trachea.

branching of the upper lobe bronchus. The supernumerary bronchi may end blindly; in that case, they are also called tracheal diverticula. The bronchus is described as displaced when, in addition to the aberrant bronchus, one branch of the upper lobe bronchus is missing. The displaced type is more frequent than the supernumerary type. When the entire right upper lobe bronchus is displaced on the trachea, it is also called a "pig bronchus."

Most bronchial anomalies are asymptomatic and may be discovered incidentally at chest CT or bronchoscopy. Patients may develop respi-

Figure 9.3.2. Axial view shows the abnormal bronchus arising posteriorly from the trachea, as well as pneumonia in the right upper lobe.

Figure 9.3.3. Isolated volume image of the affected lung with the aberrant bronchus.

ratory distress if drainage is impaired or if there are other associated lung abnormalities. Aberrant bronchi are often associated with recurrent infections, persistent cough, stridor, acute respiratory distress (especially in children), and hemoptysis. Bronchiectasis, atelectasis, focal emphysema (especially of the left upper lobe), and cystic lung malformations may coexist.

Case 9.4: Cavernous Hemangioma

Clinical Information

A one-year-old with a right neck and chest wall mass.

Postprocessing Techniques Used and Approach

Multiplanar reconstructions from the scanner console are reviewed. Unsegmented volume-rendered images are also reviewed on the workstation (Table 9.4 and Figures 9.4.1 and 9.4.2).

Table 9.4. Scan Acquisition Parameters for Case 9.4, Cavernous Hemangioma

Slice No. and Thickness	**16 × 0.5 mm**
Coverage	**Neck and chest**
Helical Pitch	**1.25:1**
Rotation Speed	**0.5 sec**
Dose Parameters	**80 kVp, 40 mAs**
Contrast Dose	**15 mL Omnipaque 350**
Injection Rate	**Hand injection**
Bolus Timing Method	**30-sec delay**

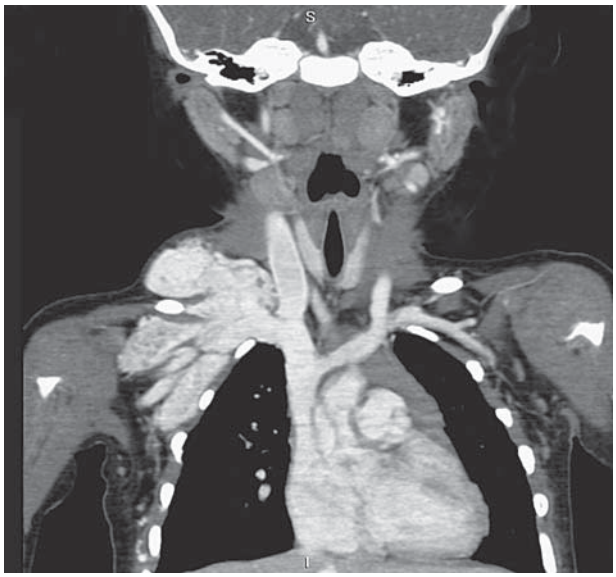

A

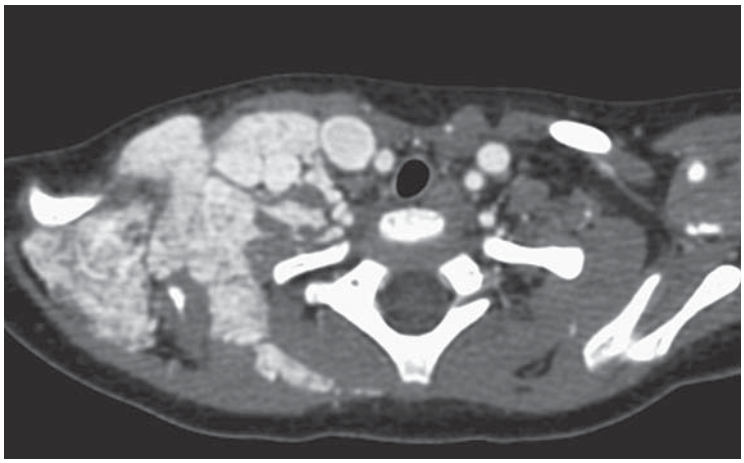

B

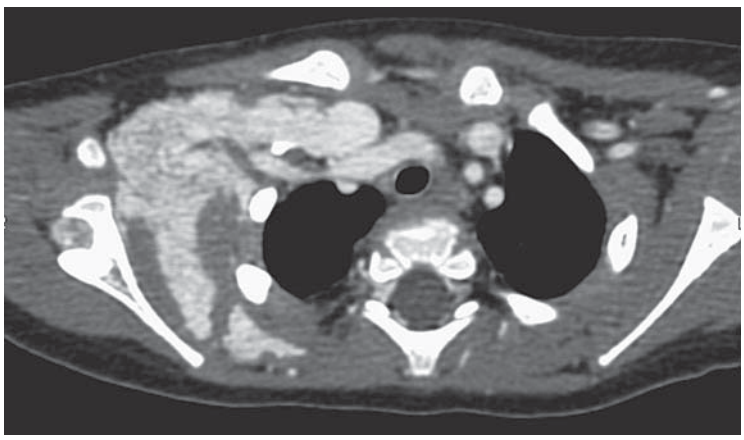

C

Figure 9.4.1. (A–C) Multiple coronal and axial images from the examination. There is an intensely enhancing mass on the right side involving the neck, supraclavicular space, shoulder, and chest wall. The mass infiltrates the subcutaneous tissues and muscle planes and encases vascular structures. The mass extends along the subclavian vessels but does not extend into the mediastinum. Multiple enlarged cervical nodes are seen on the coronal image.

Figure 9.4.2. Volume-rendered image of the neck and chest with the right clavicle removed. The relationship between the mass, vessels, and bony structures is easily seen on the volume image.

Diagnosis

Infiltrative cavernous hemangioma of the neck and chest wall.

Teaching Points

Most hemangiomas are cutaneous and are identified at physical examination and rarely require imaging to establish a diagnosis (strawberry hemangiomas). Deep soft tissue hemangiomas, however, often require imaging to establish a definitive diagnosis and to define the extent of disease and structures involved. They can arise nearly anywhere, including subcutaneous, intermuscular, intramuscular, or synovial tissues. Histologically, soft tissue hemangiomas appear as a proliferation of normal vascular elements with interspersed fatty overgrowth and can be categorized as one of five histologic subtypes: capillary, cavernous, venous, arteriovenous, or mixed.

Magnetic resonance imaging is the traditional modality for evaluation of deep soft tissue lesions such large hemangiomas. Multidetector CT with reconstructions can now rival MRI in diagnosis and characterization of lesions. A CT scan is also much faster and can often be done without sedation in pediatric patients. Multidetector CT is superb

for demonstrating the total extent of involvement and important features such as vascular encasement or involvement of bone.

Case 9.5: Pulmonary Sequestration (2 Patients)

Clinical Information

Patient 1: a seven-month-old male with a history of pneumonia. Chest x-ray shows a persistent airless consolidation in the left lower lobe. Patient 2: a two-day-old male with a lung abnormality detected on prenatal ultrasound, referred for characterization.

Postprocessing Techniques Used and Approach

Axial and coronal images are initially reviewed (Table 9.5 and Figures 9.5.1 and 9.5.2). Screening for the aberrant artery is performed with coronal thin-slab MIP technique. This identifies the aberrant artery, but because the artery has an oblique course it is difficult to show on a thin-slab MIP because of overlap with the spine. The spine is removed using automatic segmentation techniques to better show the anatomy and aberrant artery on MIP and VR images.

Diagnosis

Two cases of pulmonary sequestration. Patient 1 is an extralobar sequestration of the left lower lobe with an aberrant artery from the aorta. Patient 2 is an intralobar sequestration of the right lower lobe with an aberrant artery from the celiac artery and venous drainage to the pulmonary veins.

Teaching Points

The diagnosis of sequestration requires demonstration of an aberrant artery, which usually arises from the aorta to supply the sequestration, but can also arise from other locations. In a small infant, demonstration of this artery can be a challenge. Angiography is the traditional modality used, but is invasive and quite difficult in a small infant. Although MRA has also been used effectively, CTA offers several advantages over MRA. Being much faster, CTA can often be done

Table 9.5. Scan Acquisition Parameters for Case 9.5, Pulmonary Sequestration

Slice No. and Thickness	**16 × 0.5 mm**
Coverage	**Through chest and abdomen**
Helical Pitch	**1.25:1**
Rotation Speed	**0.4 sec**
Dose Parameters	**100 kVp, 30 mAs–40 mAs**
Contrast Dose	**10 mL–15 mL Omnipaque 350**
Injection Rate	**Hand injection**
Bolus Timing Method	**Bolus triggering on the aorta**

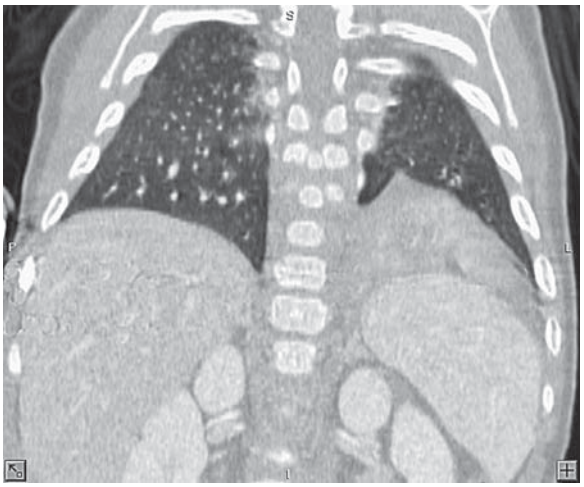

A

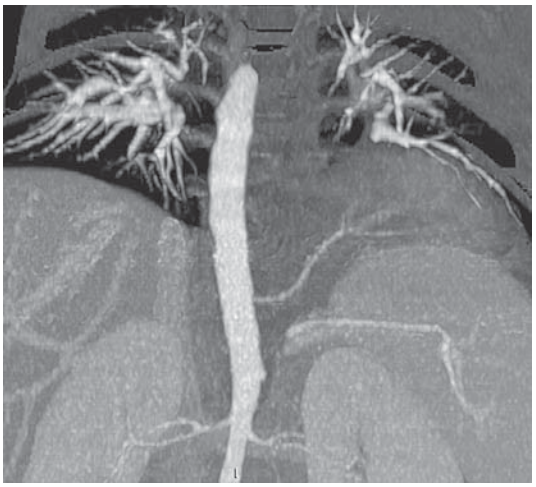

B

C

Figure 9.5.1. (A) Patient 1: Coronal 2-mm image shows a well-circumscribed airless consolidation in the left lower lobe. The appearance is characteristic of a sequestration, but diagnosis requires demonstration of systemic arterial supply. (B and C) Coronal thin slab MIP and posterior VR images. The spine has been removed to better demonstrate the aberrant artery arising from the aorta to supply the sequestration. At surgery this proved to be an extralobar sequestration.

without sedation, and it has higher resolution for demonstrating small arteries. Computed tomography also gives a much better evaluation of the lung parenchyma than MRI does.

Pulmonary sequestration is defined as a segment of lung parenchyma that is separated from the tracheobronchial tree and is supplied with blood from a systemic rather than a pulmonary artery. The blood supply usually comes from the descending thoracic aorta, but in approximately 20% of cases it can come from the upper abdominal aorta, celiac artery, or splenic artery.

Sequestrations may be either intralobar or extralobar. Intralobar sequestrations are contained within the visceral pleura of the normal

A

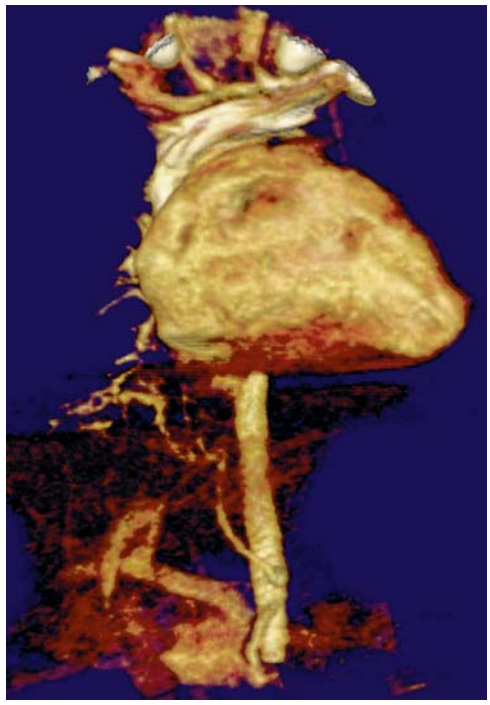

B

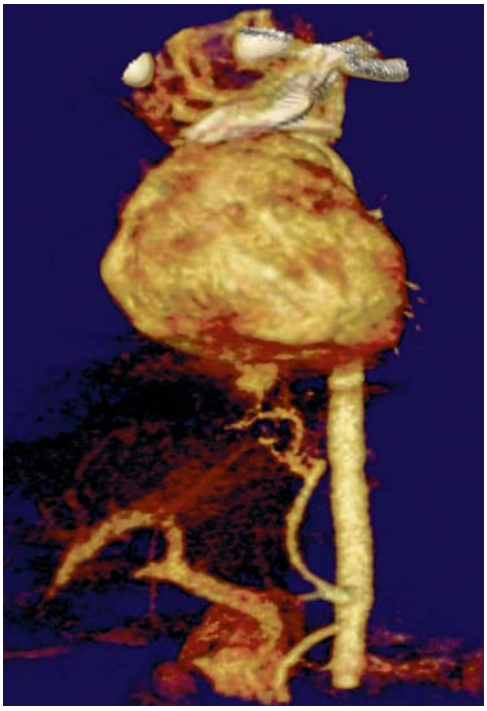

C

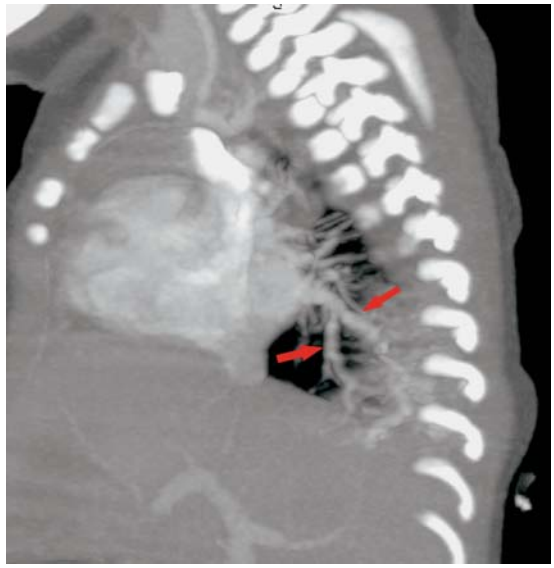

D

Figure 9.5.2. (A) Patient 2: sagittal 2-mm image in lung window through the right lung. There is a consolidation with air-filled cystic areas in the right lower lobe. (B and C) Segmented VR images with the osseous structures removed. An aberrant artery arising from the celiac artery is shown which supplies the right lower lobe sequestration. Contrast is also shown in the portal venous system. (D) Sagittal thin slab MIP image showing venous drainage from the sequestration into the pulmonary veins (arrows) confirming an intralobar sequestration.

adjacent lung and virtually always occur in the lower lobe. Intralobar sequestrations often contain air or cystic areas within them, and can contain elements of congenital cystic adenomatoid malformation (CCAM). They are more common than extralobar sequestrations by a 3:1 ratio and more likely to be asymptomatic and present later in life. In 95% of cases, venous drainage is to the pulmonary veins, resulting in a unique left-to-left shunt. Intralobar sequestrations are associated with other anomalies (usually diaphragmatic hernia) in approximately 15% of cases.

Extralobar sequestrations are surrounded by their own separate pleural lining. Unlike intralobar sequestrations, they are more likely to appear early—most occur in the first six months of life. Ninety percent of lesions occur in the left lower lobe. More than 80% drain into the right side of the heart via the azygos vein, hemiazygos vein, and inferior vena cava (IVC), resulting in a left-to-right shunt. In 65% of cases, there are associated anomalies, the most common being diaphragmatic hernia.

Case 9.6: Cherubism of the Mandible

Clinical Information

A five-year-old girl with a known diagnosis of mandibular cherubism undergoing evaluation of disease extent.

Postprocessing Techniques Used and Approach

Multiplanar reconstructions in soft tissue and bone windows generated on the scan console are reviewed (Table 9.6 and Figures 9.6.1 through 9.6.4). Surface-rendered images in various projections are reviewed on the workstation. Different threshold and window/level settings are used to emphasize either skin surface or bone.

Diagnosis

Cherubism of the mandible.

Teaching Points

Cherubism has in the past been considered to be a form of congenital, hereditary craniofacial fibrous dysplasia. Recent genetic analysis,

Table 9.6. Scan Acquisition Parameters for Case 9.6, Cherubism of the Mandible

Slice No. and Thickness	**16 × 0.5 mm**
Coverage	**Facial bones and mandible**
Helical Pitch	**0.94:1**
Rotation Speed	**0.5 sec**
Dose Parameters	**120 kVp, 80 mAs**
Contrast Dose	**None**

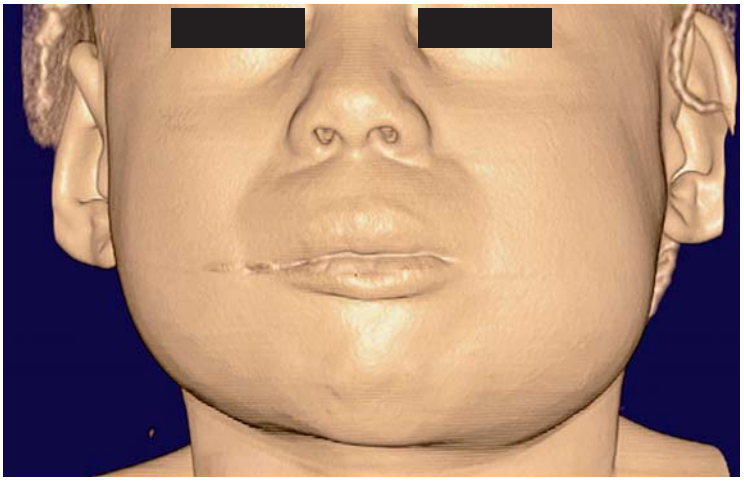

Figure 9.6.1. Skin SR image of the face. Characteristic facies with puffy cheeks mimicking an angel (cherub) is shown.

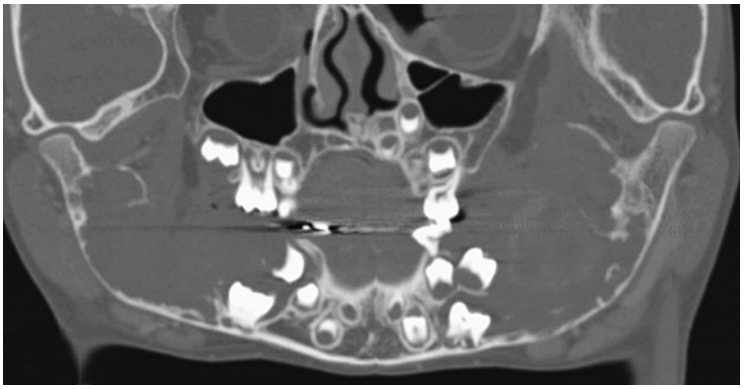

Figure 9.6.2. Coronal 2-mm image in bone window. There is extensive cystic change of the mandible on both sides. Expansion and cortical erosion is present. The TMJs are intact.

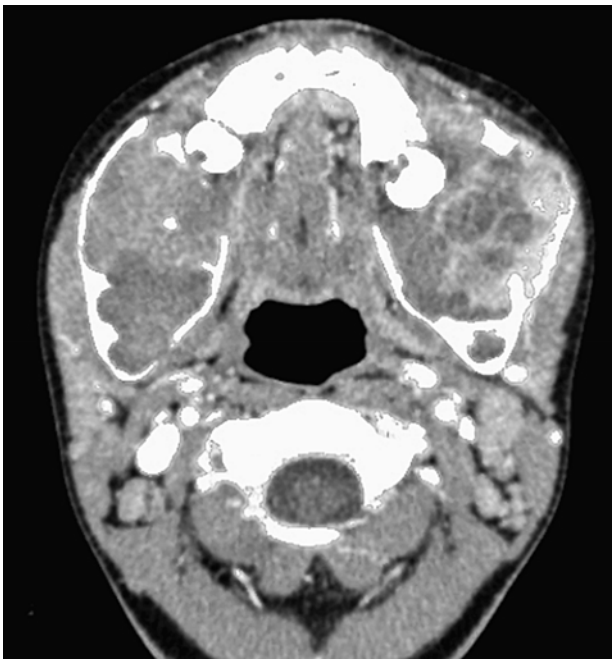

Figure 9.6.3. Axial 3-mm image with soft tissue windowing. Heterogeneous matrix with areas of hemorrhage are present within the area of lytic change.

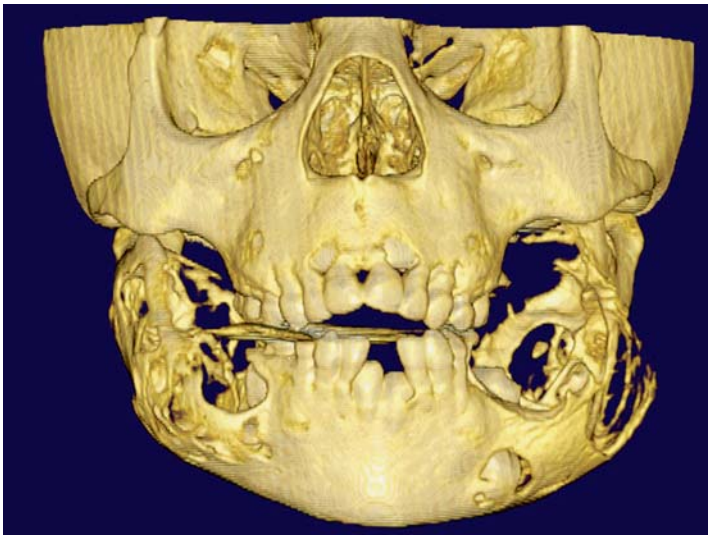

A

B

Figure 9.6.4. (A and B) Surface-rendered images of the facial bones. Expansion of mandible with cystic destruction is present, leaving areas with only lacy septations. The extent of involvement is best demonstrated on the SR images. The maxilla is relatively spared in this case.

however, has localized a mutation to a different chromosome than other types of hereditary fibrous dysplasia; therefore it is now considered to be a separate entity.

Osseous involvement in cherubism is limited to the mandible and maxilla. Almost all cases have bilateral mandibular involvement. The transmission is autosomal dominant with variable penetrance. Sporadic cases also occur however. Onset of symptoms is usually in early childhood, with boys more commonly affected than girls. Progression throughout childhood is typical, but the disease frequently regresses in adolescence or early adulthood. Children usually have a painless swelling of the jaw.

Plain films have generally been used for diagnosis and follow-up of patients. Multidetector CT, however, offers substantial advantages for evaluation of craniofacial abnormalities. Surface-rendered images are extremely helpful for demonstrating anatomy and extent of disease. The CT demonstrates expansile, cystic remodeling of bone with a mildly sclerotic matrix and internal trabeculation in most patients. Periosteal reaction is absent. Diagnosis is usually based on characteristic bilateral mandibular involvement with maxillary involvement in approximately 60% of cases.

Case 9.7: Cystic Bronchiectasis

Clinical Information

An eight-year-old boy with a history of asthma, immune deficiency, and prior respiratory infections.

Postprocessing Techniques Used and Approach

Multiplanar reconstructions performed on the scan console are reviewed (Table 9.7 and Figures 9.7.1 and 9.7.2). Thin slab volume-rendered transparent airway images are reviewed on the workstation.

Diagnosis

Cystic bronchiectasis.

Teaching Points

High resolution CT has been used for years to characterize parenchymal diseases of the lung such as pulmonary fibrosis, bronchiectasis,

Table 9.7. Scan Acquisition Parameters for Case 9.7, Cystic Bronchiectasis

Slice No. and Thickness	**16 × 0.5 mm**
Coverage	**Chest**
Helical Pitch	**1.25:1**
Rotation Speed	**0.5 sec**
Dose Parameters	**90 kVp, 70 mAs**
Contrast Dose	**None**

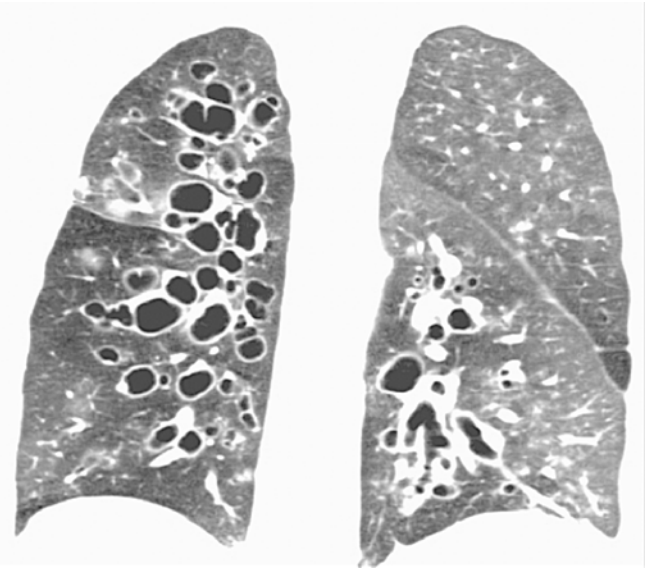

Figure 9.7.1. Coronal 2-mm MPR through the lungs. Diffuse, severe cystic bronchiectasis is present.

interstitial pneumonia, and emphysema. Prior to volumetric CT acquisition, most protocols would acquire a series of high-resolution images (1-mm thickness) at 1-cm to 2-cm increments throughout the lung. In addition, a conventional spiral study of the entire chest would be performed separately. With volumetric CT the entire lung can be scanned once, and both conventional 3-mm to 5-mm thick contiguous images

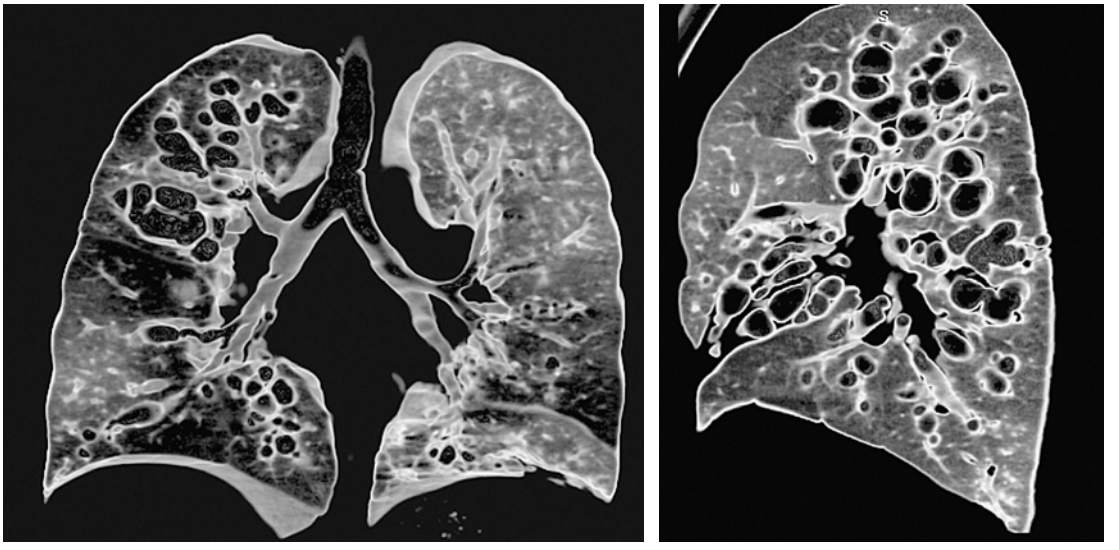

A B

Figure 9.7.2. (A and B) Coronal and sagittal thin slab volume-rendered images with transparent airway settings. The volume images dramatically show the central large airways as well as the cystic bronchiectasis in the lungs.

and 1-mm high-resolution images can be created from the same data set.

Bronchiectasis can be caused by many different conditions. Acquired bronchiectasis is most often associated with recurrent infections such as bacteria, TB, and mycobacterium avium (MAC), asthma and allergic bronchopulmonary aspergillosis, bronchial obstruction (tumor, foreign body), and immunodeficiency states. Many congenital diseases can also cause bronchiectasis, including cystic fibrosis, Kartagener's syndrome (immotile cilia and situs inversus), Williams-Campbell syndrome, and others.

High-resolution CT is used to characterize the type and distribution of bronchiectasis. The most common type is cylindrical bronchiectasis, which is the mildest form and is characterized by mildly dilated and thick-walled bronchi. Varicose bronchiectasis is like cylindrical bronchiectasis but the airways are more dilated and irregular, often with a beaded appearance. Cystic bronchiectasis is the most severe form, with markedly dilated airways that can mimic a cluster of cysts. Traction bronchiectasis is associated with lung fibrosis and distortion of lung architecture. The airways are dilated and irregular; they are similar to varicose bronchiectasis, but fibrosis is also present.

Case 9.8: Aortic Coarctation

Clinical Information

A five-year-old with asymmetric blood pressures in the arms and legs. Coarctation was diagnosed by echocardiogram. Evaluation of the aorta is needed for treatment planning.

Postprocessing Techniques Used and Approach

The coarctation is well demonstrated with thin section oblique sagittal MIP reconstructions (Table 9.8 and Figures 9.8.1 through 9.8.3). Unsegmented volume and MIP images are useful for demonstrating the collateral vessels and ribs. Volume images of the aorta are best following manual segmentation to cut away most of the heart and pulmonary outflow tract. This allows for excellent visualization of the arch anatomy, coarct, and ductus arteriosus.

Table 9.8. Scan Acquisition Parameters for Case 9.8, Aortic Coarctation

Slice No. and thickness	**16 × 0.5 mm**
Coverage	**Through chest**
Helical Pitch	**1.25:1**
Rotation Speed	**0.5 sec**
Dose Parameters	**80 kVp, 60 mAs**
Contrast Dose	**50 mL Omnipaque 350**
Injection Rate	**2 mL/sec**
Bolus Timing Method	**Bolus triggering focused on the ascending aorta**

Figure 9.8.1. Oblique sagittal thin slab MIP through the aorta. Very high grade postductal aortic coarctation is present. Almost no flow is going through the luminal stenosis (arrow).

Diagnosis

Postductal coarctation of the aorta with patent ductus arteriosus (PDA).

Teaching Points

The diagnosis of coarctation had already been made in this child by echocardiogram. A CTA examination is done to better demonstrate the anatomy prior to surgical repair. Using CTA with volume and MIP rendering provides the surgeon with all the anatomic information needed to operate on this child. Not only are the coarctation and PDA shown, but also the extensive collateral circulation. Using CTA is also an excel-

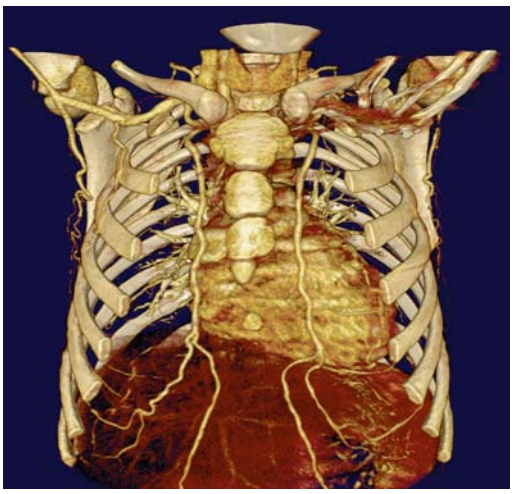

A

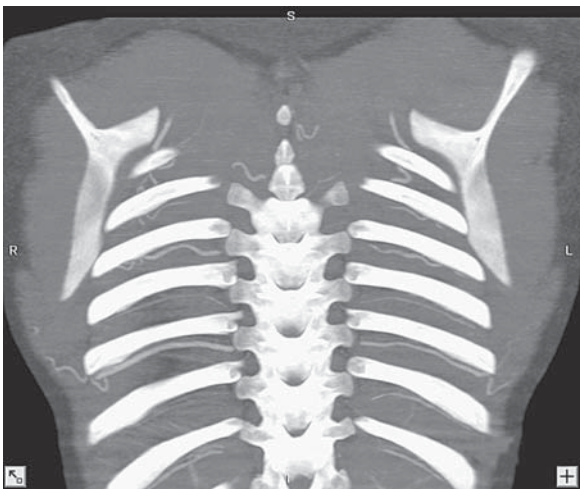

B

Figure 9.8.2. (A and B) Coronal volume-rendered and MIP images demonstrate the large internal mammary collaterals and additional collaterals arising from the subclavian and axillary arteries. There are also large intercostal collaterals, but the child has not yet developed significant rib notching.

Figure 9.8.3. Segmented volume-rendered image of the aorta. The pulmonary artery has been removed except for a small segment. The arch anatomy and coarct are well shown for surgical planning. This view also nicely shows the patent ductus arteriosus (arrow) and the large internal mammary collaterals.

lent way to follow these children after treatment and to evaluate for restenosis or other complications.

Aortic coarctation accounts for approximately 5% of congenital heart disease with males more commonly affected than females. Patent ductus arteriosus and ventricular septal defect (VSD) are commonly associated lesions. Coarctations are classified into two types, juxtaductal and postductal coarctation.

Juxtaductal coarctation occurs in infants and small children. The ductus is astride the area of coarctation and there is hypoplasia of the aortic arch and isthmus. These infants typically have dyspnea, congestive heart failure (CHF), and peripheral cyanosis, particularly when associated with left-to-right shunts (PDA, VSD). Postductal coarct occurs in older children and adults. The stenosis is distal to the ductus/ligamentum arteriosum. Older children and adults do not generally develop CHF. They have a murmur, differential blood pressure between the upper and lower limbs, hypertension, and rib notching.

Case 9.9: Craniosynostosis

Clinical Information

A one-year-old with abnormal head shape.

Table 9.9. Scan Acquisition Parameters for Case 9.9, Craniosynostosis

Slice No. and Thickness	16 × 0.5 mm
Coverage	Head
Helical Pitch	0.94:1
Rotation Speed	0.5 sec
Dose Parameters	100 kVp, 100 mAs
Contrast Dose	None

Postprocessing Techniques Used and Approach

Three-dimensional surface-rendered images are reviewed on the workstation, as well as standard multiplanar reconstructions in brain and bone windows (not shown) (Table 9.9 and Figure 9.9.1).

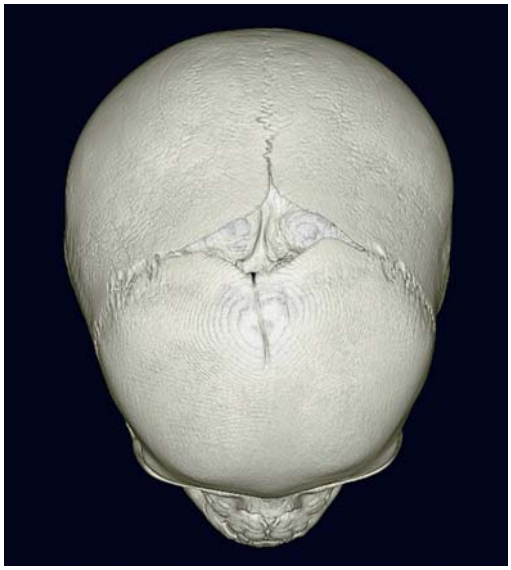

A

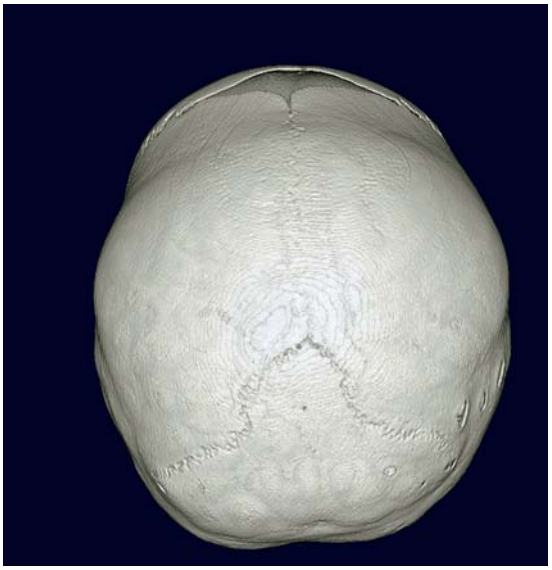

B

C

Figure 9.9.1. (A–C) Multiple SR images of the skull. The anterior fontanelle is still open. The coronal sutures are open but are not as wide as would be expected. Premature fusion of the metopic, sagittal, and lambdoidal sutures has occurred. Frontal plagiocephaly is present.

Diagnosis

Craniosynostosis of the sagittal, lambdoid, and metopic sutures. The coronal sutures are also abnormal.

Teaching Points

Craniosynostosis refers to the premature closure of one or more cranial sutures. Normal sutures do not completely fuse until the second to third decade of life, except the metopic suture, which is frequently fused by the third year of life. Craniosynostosis can be classified as primary (idiopathic) or secondary. Secondary craniosynostosis has multiple causes, including syndromes (Crouzon, Apert, etc.), hematologic abnormalities (sickle cell, thalassemia), metabolic abnormalities (rickets, hypercalcemia, hyperthyroidism), and bone dysplasias (achondroplasia, Hurler disease, etc.).

The most commonly involved suture is the sagittal suture, followed by the coronal suture. Most children with craniosynostosis will have an abnormal shape or size of the head. Premature fusion of the sutures will each result in characteristic shape abnormalities of the skull. Growth is restricted in the plane perpendicular to the suture and will preferentially occur in a plane parallel to the suture. For example, fusion of the sagittal suture produces an elongated, narrow head (scaphocephaly or dolichocephaly), whereas fusion of the coronal sutures will produce a short, wide head (brachycephaly). Lambdoidal synostosis will generally cause occipital flattening. If unilateral coronal or lambdoidal suture fusion occurs, one side of the skull will flatten out (plagiocephaly).

Diagnosis is often made with conventional skull radiographs; however, CT with 3D reconstructions has been shown to be more sensitive and provides additional diagnostic information about the skull and brain. Treatment is surgical, and early surgical intervention has been associated with an improved outcome; therefore early and accurate imaging diagnosis with CT is very important.

Case 9.10: Langerhans Cell Histiocytosis

Clinical Information

A four-year-old girl with proptosis of the left eye and blurred vision. She is also found to have multiple lytic bone lesions including involvement of the skull.

Postprocessing Techniques Used and Approach

Multiplanar reconstructions generated on the scanner console are reviewed (Table 9.10 and Figures 9.10.1 through 9.10.3). Also, MIP images of the vessels are reviewed on the workstation.

Diagnosis

Langerhans cell histiocytosis involving the orbit, sphenoid bone, and middle cranial fossa.

Table 9.10. Scan Acquisition Parameters for Case 9.10, Langerhans Cell Histiocytosis

Slice No. and Thickness	16 × 0.5 mm
Coverage	Head and neck
Helical Pitch	1.25:1
Rotation Speed	0.5 sec
Dose Parameters	120 kVp, 100 mAs
Contrast Dose	35 mL Omnipaque 350
Injection Rate	2 mL/sec
Bolus Timing Method	Scan started immediately following injection

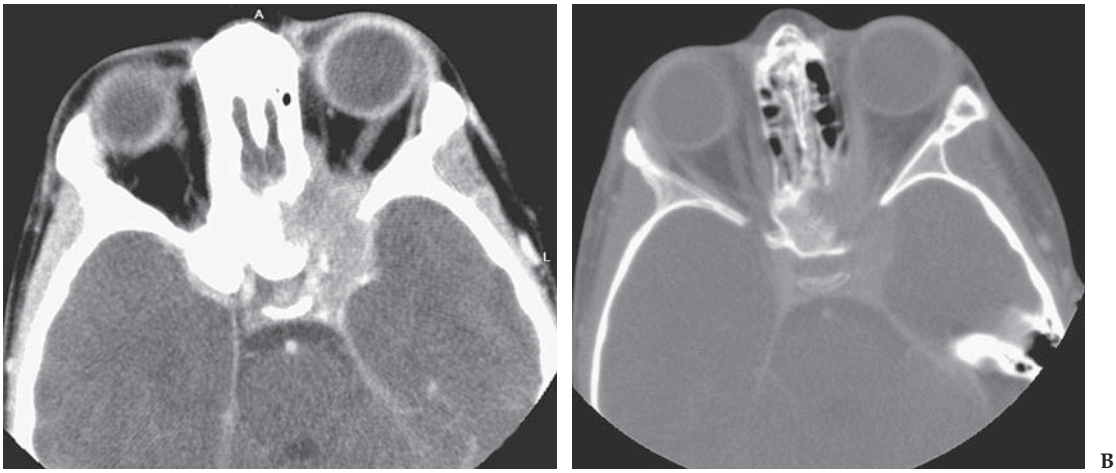

A B

Figure 9.10.1. (A and B) Axial 2-mm images in bone and soft tissue windows. There is a lytic, destructive process of the sphenoid bone at the left orbital apex with an associated soft tissue mass extending into the orbit and encasing the superior orbital vein, optic nerve, and extraocular muscles. There is also involvement of the left cavernous sinus and middle cranial fossa. Marked proptosis is present.

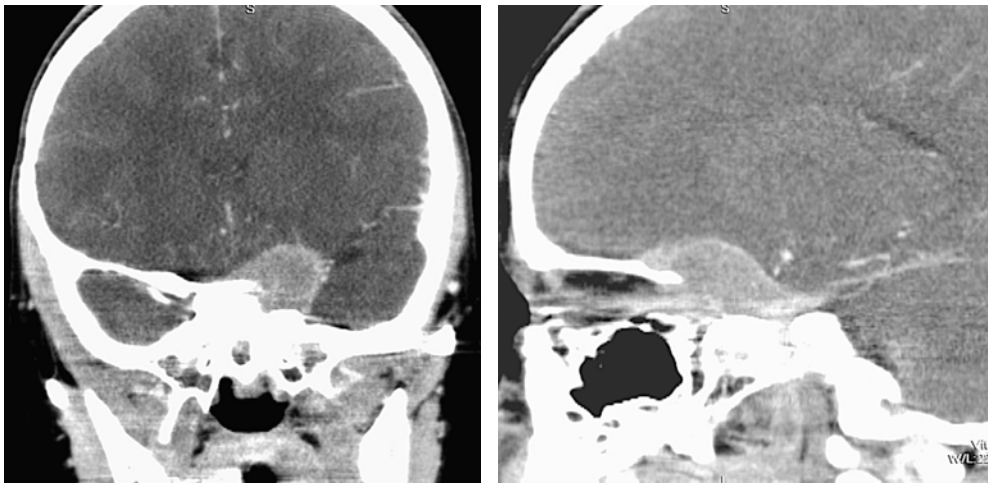

A B

Figure 9.10.2. (A and B) Coronal and sagittal MPR images again showing the extraconal soft tissue mass involving the orbit and cavernous sinus region.

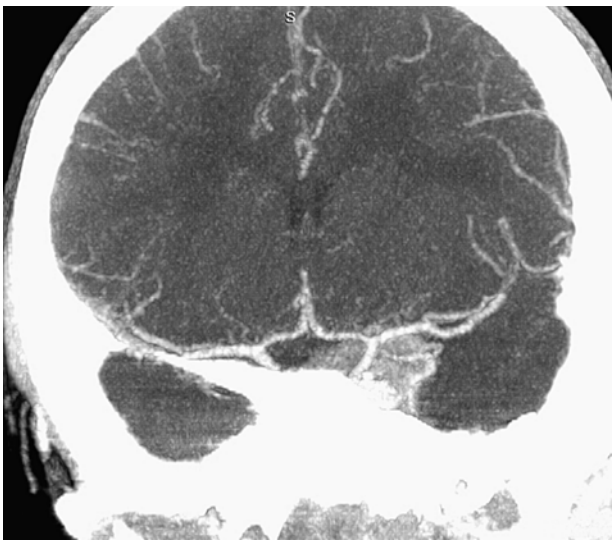

Figure 9.10.3. A MIP image demonstrating the relationship of the mass to the carotid artery and circle of Willis.

Teaching Points

Langerhans cell histiocytosis includes the disorders formerly known as histiocytosis X (eosinophilic granuloma, Hand-Schüller-Christian disease, and Letterer-Siwe disease) that express the heterogeneous clinical manifestations of the disease. The etiology and pathogenesis are still unknown. Most studies suggest that it is a reactive disease caused by abnormal immune regulation.

Bone is the organ most commonly involved. When the orbit is involved there is usually a lytic process of bone with an associated extraconal mass. Orbital involvement is part of the classic triad of Hand-Schüller-Christian disease that includes exophthalmus, diabetes insipidus, and lytic skull lesions. Involvement of the temporal bone, mandible and maxilla can also be seen, and involvement of the lungs and other organs may also occur.

This case demonstrates the ability of CT to characterize complex abnormalities in the brain with multiplanar and angiographic detail that can rival MRI, but in a fraction of the time.

Selected Readings

Vascular Ring

1. Berdon WE. Rings, sling, and other things: vascular compression of the infant trachea updated from the mid century to the millennium—the legacy of Robert E. Gross, MD, and Edward B. D. Neuchauser, MD. Radiology 2000;216:624–632.
2. Berrocal T, Madrid C, Novo S, Gutiérrez J, Arjonilla A, Gómez-León N. Congenital anomalies of the tracheobronchial tree, lung, and mediastinum: embryology, radiology, and pathology. Radiographics 2004;24:17e.
3. Ghaye B, Szapiro D, Fanchmps JM, Dondelinger RF. Congenital bronchial abnormalities revisited. Radiographics 2001;21:105–119.

4. Haramati LB, Glickstein JS, Issenberg HJ, Haramati N, Crooke GA. MR imaging and CT of vascular anomalies and connections in patients with congenital heart disease: significance in surgical planning. Radiographics 2002;22:337–349.
5. Lee EY, Siegel MJ, Hildebolt CF, Gutierrez FR, Bhalla S, Fallah JH. MDCT evaluation of thoracic aortic anomalies in pediatric patients and young adults: comparison of axial, multiplanar, and 3D images. Am J Roentgenol 2004 Mar;182:777–784.
6. Siegel MJ. Multiplanar and three-dimensional multi–detector row CT of thoracic vessels and airways in the pediatric population. Radiology 2003;229:641–650.

Skull and Orbital Fractures

7. Lee HJ, Jilani M, Frohman L, Baker S. CT of orbital trauma. Emerg Radiol 2004 Feb;10(4):168–172.
8. Philipp MO, Funovics MA, Mann FA, et al. Four-channel multidetector CT in facial fractures: do we need 2×0.5 mm collimation? Am J Roentgenol 2003 Jun;180:1707–1713.
9. Rhea JT, Rao PM, Novelline RA. Helical CT and three-dimensional CT of facial and orbital injury. Radiol Clin North Am 1999;37:489–513.
10. Turner BG, Rhea JT, Thrall JH, Small AB, Novelline RA. Trends in the use of CT and radiography in the evaluation of facial trauma, 1992–2002: implications for current costs. Am J Roentgenol 2004 Sep;183:751–754.

Tracheal Bronchus

11. Berdon WE. Rings, sling, and other things: vascular compression of the infant trachea updated from the mid century to the millennium—the legacy of Robert E. Gross, MD, and Edward B. D. Neuchauser, MD. Radiology 2000;216:624–632.
12. Berrocal T, Madrid C, Novo S, Gutiérrez J, Arjonilla A, Gómez-León N. Congenital anomalies of the tracheobronchial tree, lung, and mediastinum: embryology, radiology, and pathology. Radiographics 2004;24:17e.
13. Ghaye B, Szapiro D, Fanchmps JM, Dondelinger RF. Congenital bronchial abnormalities revisited. Radiographics 2001;21:105–119.
14. Kauczor HU, Wolcke B, Fisher B, Mildenberger P, Lorenz J, Thelen M. Three-dimensional helical CT of the tracheobronchial tree: evaluation of imaging protocols and assessment of suspected stenoses with bronchoscopic correlation. Am J Roentgenol 1996;167:419–424.
15. Siegel MJ. Multiplanar and three-dimensional multi–detector row CT of thoracic vessels and airways in the pediatric population. Radiology 2003;229:641–650.

Cavernous Hemangioma

16. Ly JQ, Sanders TG. Case 65: hemangioma of the chest wall. Radiology 2003;229:726–729.
17. Tateishi U, Gladish GW, Kusumoto M, et al. Chest wall tumors: radiologic findings and pathologic correlation: part 1. benign tumors. Radiographics 2003;23:1477–1490.

Pulmonary Sequestration

18. Berrocal T, Madrid C, Novo S, Gutiérrez J, Arjonilla A, Gómez-León N. Congenital anomalies of the tracheobronchial tree, lung, and mediastinum: embryology, radiology, and pathology. Radiographics 2004;24:17e.

19. Bratu I, Flageole H, Chen MF, Lorenzo MD, Yazbeck S, Laberge JM. The multiple facets of pulmonary sequestration. J Pediatr Surg 2001;36:784–790.
20. Do KH, Goo JM, Im JG, Kim KW, Chung JW, Park JH. Systemic arterial supply to the lungs in adults: spiral CT findings. Radiographics 2001;21:387–402.
21. Konen E, Raviv-Zilka L, Cohen RA, et al. Congenital pulmonary venolobar syndrome: spectrum of helical CT findings with emphasis on computerized reformatting. Radiographics 2003;23:1175–1184.
22. Lee EY, Siegel MJ, Hildebolt CF, Gutierrez FR, Bhalla S, Fallah JH. MDCT evaluation of thoracic aortic anomalies in pediatric patients and young adults: comparison of axial, multiplanar, and 3D images. Am J Roentgenol 2004 Mar;182:777–784.
23. Siegel MJ. Multiplanar and three-dimensional multi–detector row CT of thoracic vessels and airways in the pediatric population. Radiology 2003;229:641–650.

Cherubism of the Mandible

24. Beaman FD, Bancroft LW, Peterson JJ, Kransdorf MJ, Murphey MD, Menke DM. Imaging characteristics of cherubism. Am J Roentgenol 2004 Apr;182:1051–1054.
25. Bianchi SD, Boccardi A, Mela F, Romagnoli R. The computed tomographic appearances of cherubism. Skeletal Radiol 1987;16:6–10.
26. Cornelius EA, McClendon JL. Cherubism: hereditary fibrous dysplasia of the jaws—roentgenographic features. Am J Roentgenol 1969;106:136–143.
27. Fitzpatrick KA, Taljanovic MS, Speer DP, et al. Imaging findings of fibrous dysplasia with histopathologic and intraoperative correlation. Am J Roentgenol 2004 Jun;182:1389–1398.

Cystic Bronchiectasis

28. Boiselle PM, Reynolds KF, Ernst A. Multiplanar and three-dimensional imaging of the central airways with multidetector CT. Am J Roentgenol 2002 Aug;179:301–308.
29. Lawler LP, Fishman EK. Multi–detector row CT of thoracic disease with emphasis on 3D volume rendering and CT angiography. Radiographics 2001;21:1257–1273.
30. Ooi GC, Khong PL, Yeung MC, et al. High-resolution CT quantification of bronchiectasis: clinical and functional correlation. Radiology 2002;225: 663–672.
31. Siegel MJ. Multiplanar and three-dimensional multi–detector row CT of thoracic vessels and airways in the pediatric population. Radiology 2003; 229:641–650.
32. Webb WR, Müller NL, Naidich DP. High-Resolution CT of the Lung. 3rd ed. Philadelphia, Pa: Lippincott Williams & Wilkins; 2001.
33. Yi CA, Lee KS, Kim TS, et al. Multidetector CT of bronchiectasis: effect of radiation dose on image quality. Am J Roentgenol 2003 Aug;181:501–505.

Aortic Coarctation

34. Becker C, Soppa C, Fink U, et al. Spiral CT angiography and 3D reconstruction in patients with aortic coarctation. Eur Radiol 1997;7:1473–1477.
35. Goo HW, Park IS, Ko JK, et al. CT of congenital heart disease: normal anatomy and typical pathologic conditions. Radiographics 2003;23: 147–165.

36. Haramati LB, Glickstein JS, Issenberg HJ, Haramati N, Crooke GA. MR imaging and CT of vascular anomalies and connections in patients with congenital heart disease: significance in surgical planning. Radiographics 2002;22:337–349.
37. Lawler LP, Fishman EK. Multi–detector row CT of thoracic disease with emphasis on 3D volume rendering and CT angiography. Radiographics 2001;21:1257–1273.
38. Lee EY, Siegel MJ, Hildebolt CF, Gutierrez FR, Bhalla S, Fallah JH. MDCT evaluation of thoracic aortic anomalies in pediatric patients and young adults: comparison of axial, multiplanar, and 3D images. Am J Roentgenol 2004 Mar;182:777–784.
39. Schaffler GJ, Sorantin E, Groell R, et al. Helical CT angiography with maximum intensity projection in the assessment of aortic coarctation after surgery. Am J Roentgenol 2000 Oct;175:1041–1045.
40. Siegel MJ. Multiplanar and three-dimensional multi–detector row CT of thoracic vessels and airways in the pediatric population. Radiology 2003;229:641–650.
41. Tonkin IL. Imaging of pediatric congenital heart disease. J Thorac Imaging 2000;15:274–279.

Craniosynostosis

42. Binaghi S, Gudinchet F, Rilliet B. Three-dimensional spiral CT of craniofacial malformations in children. Pediatr Radiol 2000 Dec;30(12):856–860.
43. Parisi M, Mehdizadeh HM, Hunter JC, Finch IJ. Evaluation of craniosynostosis with three-dimensional CT imaging. Comput Assist Tomogr 1989 Nov–Dec;13(6):1006–1012.
44. Silverman FN, Slovis TL, Rozelle AA, McAlister WH. Congenital Dysplasias. In: Kuhn JP, Slovis TL, Haller JO, eds. Caffey's Pediatric Diagnostic Imaging. 10th ed. Philadelphia, PA: Mosby; 2004.
45. Vannier MW, Pilgram TK, Marsh JL, et al. Craniosynostosis: diagnostic imaging with three-dimensional CT presentation. Am J Neuroradiol 1994 Nov;15(10):1861–1869.

Langerhans Cell Histiocytosis

46. Effmann EL. Pulmonary neoplasms, tumor-like conditions and miscellaneous diseases. In: Kuhn JP, Slovis TL, Haller JO, eds. Caffey's Pediatric Diagnostic Imaging. 10th ed. Philadelphia, PA: Mosby; 2004:1147–1150.
47. Erly WK, Carmody RF, Dryden RM. Orbital histiocytosis X. Am J Neuroradiol 1995 Jun–Jul;16(6):1258–1261.
48. Fernündez-Latorre F, Menor-Serrano F, Alonso-Charterina S, Arenas-Jiménez J. Langerhans cell histiocytosis of the temporal bone in pediatric patients: imaging and follow-up. Am J Roentgenol 2000 Jan;174:217–221.

Chapter 10

Trauma Imaging

Case 10.1: Rapid Multiple Trauma Evaluation

Clinical Information

A 34-year-old man in a high-speed motor vehicle accident.

Postprocessing Techniques Used and Approach

Multiple 1-mm images through the chest, abdomen, and pelvis are reconstructed and sent immediately to the workstation (Table 10.1 and Figures 10.1.1 through 10.1.5). Multiplanar image review is performed on the workstation at 2-mm to 3-mm image thickness, documenting solid organ injury and vertebral fractures. Oblique sagittal MIP through the thoracic aorta is reviewed to evaluate for aortic injury. Coronal MIP is done in the abdomen to show abdominal aorta and renal arteries. A quick segmentation to remove the spine is performed using automatic segmentation. Finally, volume and surface images are quickly reviewed to again show vessels and bony injuries.

Diagnosis

Multiple traumatic injuries, including pneumothorax and pneumomediastinum, vertebral body and transverse process factures, multiple rib fractures, bilateral renal contusions with branch vessel occlusions, and mesenteric hematoma.

Teaching Points

In patients with significant multiple trauma, time is often of the essence. Many injuries can be life threatening and emergency surgery may be required. These patients frequently need extensive radiologic evaluation, including multiple CT examinations of the head, total spine, face, chest/abdomen, and pelvis. In the era prior to multidetector CT it would usually take 30 minutes to 60 minutes to scan the patient for all of these examinations and at least another 30 minutes to 60 minutes to reconstruct, print, and review all of the images.

Table 10.1. Scan Acquisition Parameters for Case 10.1, Rapid Multiple Trauma Evaluation

Slice No. and Thickness	16 × 1 mm
Coverage	Chest through pelvis
Helical Pitch	1.5:1
Rotation Speed	0.5 sec
Dose Parameters	120 kVp, 200 mAs
Contrast Dose	100 mL Omnipaque 350
Injection Rate	2 mL/sec
Bolus Timing Method	45-sec delay

Figure 10.1.1. Axial 3-mm image in lung window shows pneumothorax and pneumomediastinum in the chest.

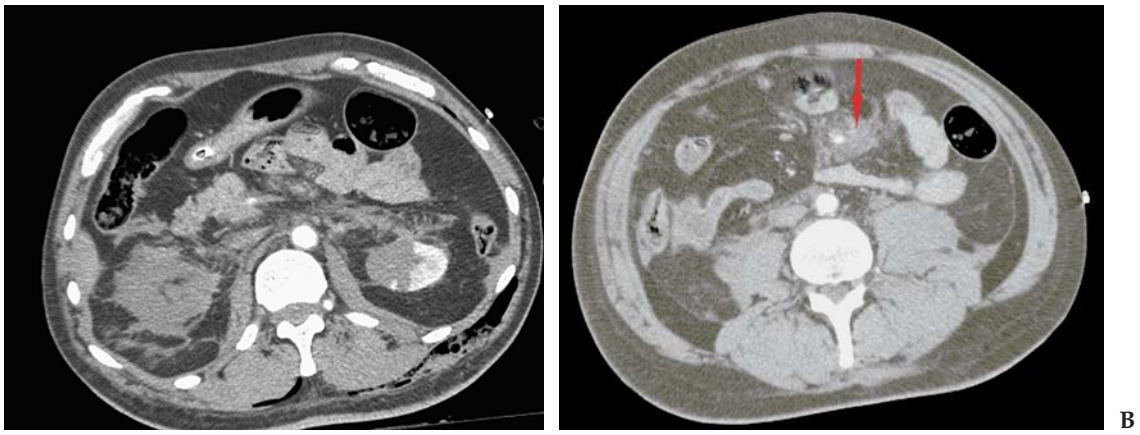

A **B**

Figure 10.1.2. (A and B) Two 3-mm axial images in the abdomen show bilateral contusions involving the kidneys with retroperitoneal hemorrhage. The more inferior image demonstrates contusion in the mesentery (arrow).

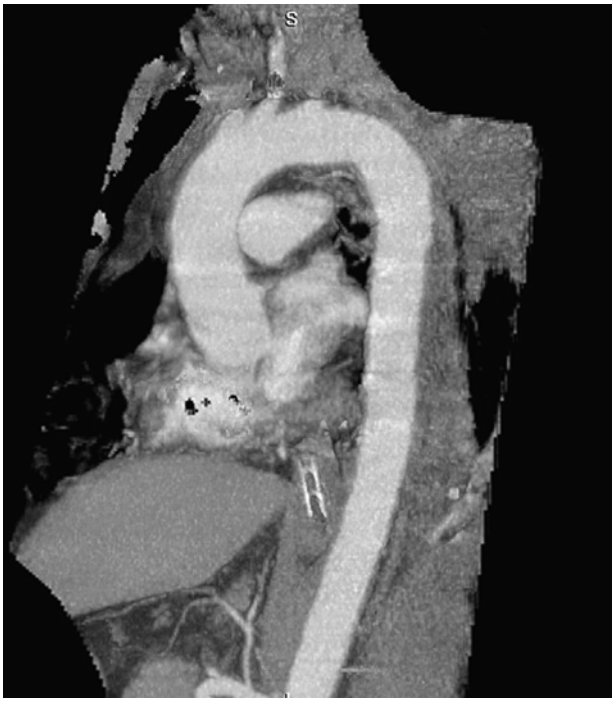

Figure 10.1.3. Oblique sagittal thin slab MIP through the thoracic aorta. There is no evidence for injury.

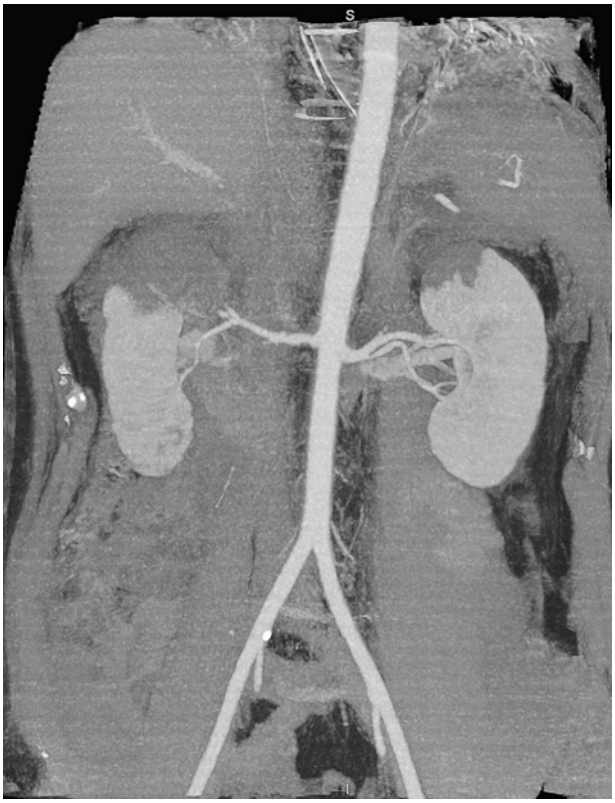

Figure 10.1.4. Coronal 20-mm slab MIP through the kidneys with the spine removed. Bilateral upper pole renal contusions are shown. The main renal arteries are intact, but there is branch vessel occlusion to the upper poles of both kidneys. No pseudoaneurysm or active extravasation is present.

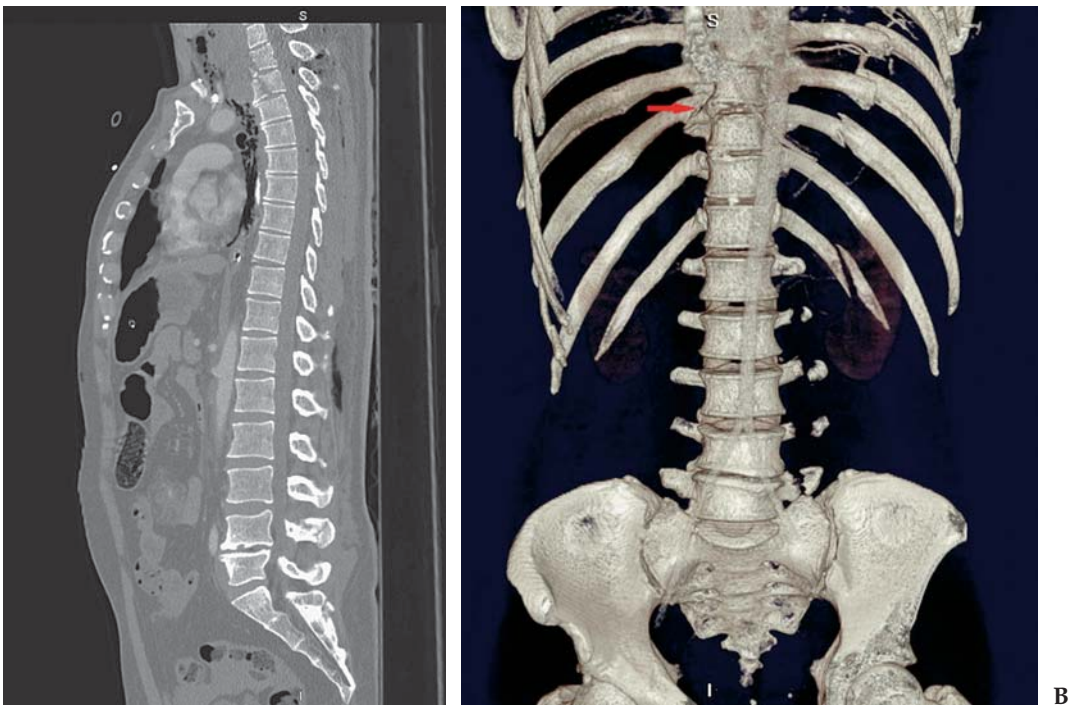

Figure 10.1.5. (A and B) Sagittal MPR of the thoracic and lumbar spine and surface-rendered image. Fractures of the bodies of T2, T3, and T10 (superior corner) are present. Surface image shows multiple fractures of the left ribs, and transverse process fractures on the left in the lumbar spine are present. The T10 vertebral body fracture is better seen on this image (arrow).

With current generation MDCT scanners the data acquisition can be performed in two runs: a noncontrast examination from the head to the shoulders covering the brain, face, and cervical spine, and a contrast-enhanced examination from the chest through the pelvis. From these two data sets complete high-resolution examinations of the head, facial bones, total spine, CTA chest and abdomen, soft tissue chest, abdomen and pelvis, and bony pelvis/hips can be reviewed in literally a matter of minutes. The patient can be scanned and the data reconstructed and sent to the workstation in approximately 15 minutes to 20 minutes. At the workstation the radiologist can rapidly review axial, multiplanar, and volume or surface images in 5 minutes to 10 minutes. The total time savings is at least 30 minutes to 90 minutes, with much more accurate diagnosis. In a severe trauma patient this can potentially be the difference between life and death.

In this patient there was no chest or abdominal injury that required immediate surgery. The renal hematomas were felt to be stable and the aorta was cleared. The spine fractures were also judged to be stable. A chest tube was placed in the trauma room and the patient was taken to the operating room emergently to evacuate a subdural brain hemorrhage (not shown) that was also present.

Table 10.2. Scan Acquisition Parameters for Case 10.2, T12 Vertebral Body Fracture

Slice No. and Thickness	**16 × 1.0 mm**
Coverage	**Chest to pelvis (1st study); thoracic and lumbar spines only (2nd study)**
Helical Pitch	**1.25:1 (1st study); 0.94:1 (2nd study)**
Rotation Speed	**0.5 sec**
Dose Parameters	**120 kVp, 200 mAs**
Contrast Dose	**100 mL Omnipaque 350 (1st study only)**

Case 10.2: T12 Vertebral Body Fracture

Clinical Information

A 21-year-old man in a rollover motor vehicle accident. The patient is paraplegic in the emergency department.

Postprocessing Techniques Used and Approach

Multiplanar reconstructions created on the scanner and unsegmented SR images are all that is needed for this case (Table 10.2 and Figures 10.2.1 through 10.2.4). Some trimming of the data set is performed when viewing the surface images to remove the ribs on the lateral view.

A B

Figure 10.2.1. (A and B) Sagittal MPR images through the lower thoracic and lumbar spine. There is a compression fracture of the T12 vertebral body with severe retrolisthesis at T11-12 interspace. Paramedian sagittal image (B) shows fracture and dislocation of the facet joint. The cord is completely transected at this level (better shown by MRI).

Figure 10.2.2. Lateral surface-rendered image of the spine. The compression fracture is again seen. The jumped facet joints are well shown on this view.

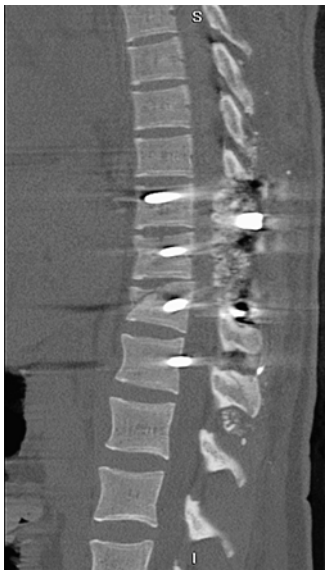

A

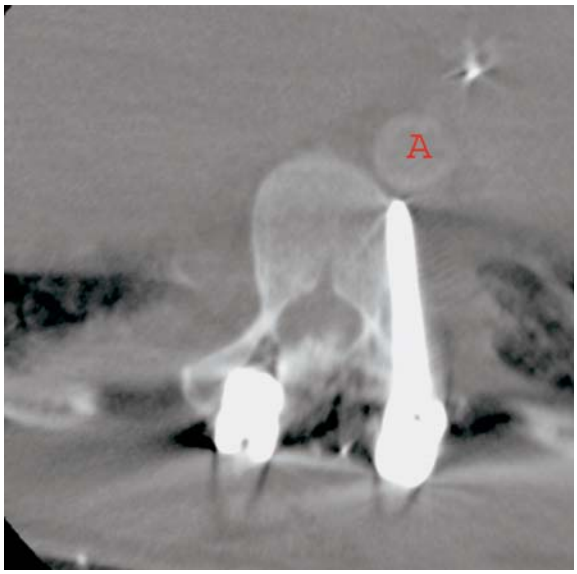

B

Figure 10.2.3. (A and B) Images following surgical repair with fusion. Sagittal image now shows near-anatomic alignment. Extensive posterior laminectomy has been performed and the posterior canal has been packed with bone graft. There is canal narrowing related to the bone graft. Axial image at the level of the T10 pedicle screw shows the left screw has extended outside the vertebral body and has come to within 1 mm of the aorta (A).

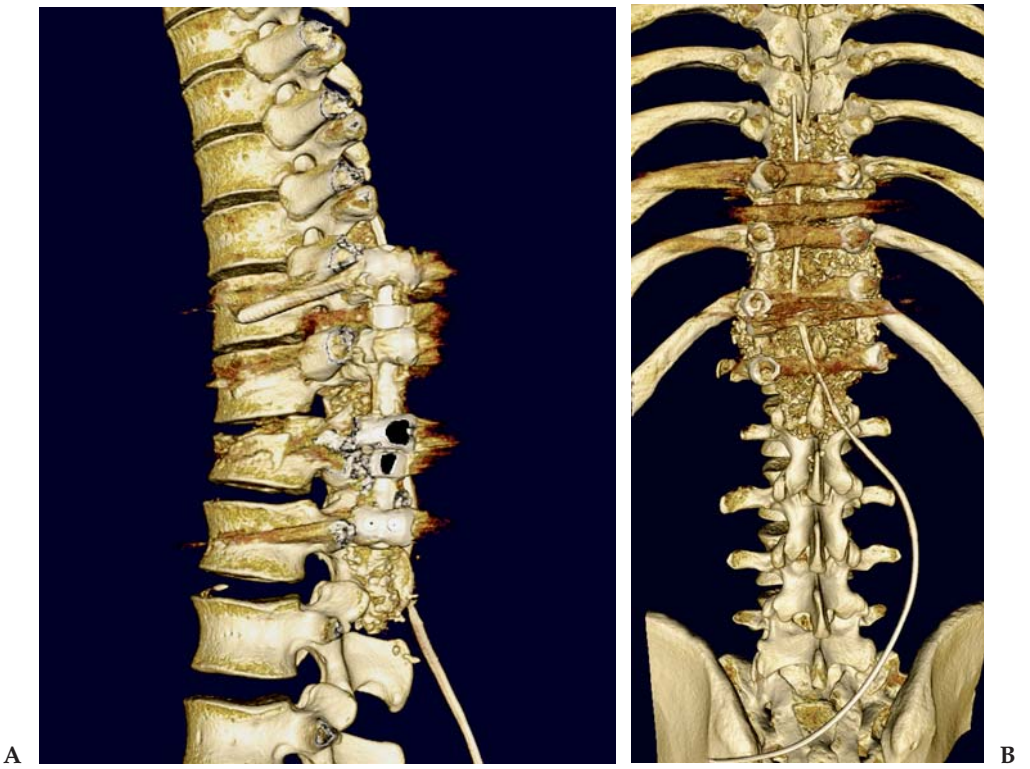

Figure 10.2.4. (A and B) Posterior and lateral SR views of the bony fusion. The lateral image demonstrates the misplaced left T10 screw outside of the vertebral body. The posterior view shows the hardware, bone graft, and the drain that was left in place.

The first study was retrospectively reconstructed from the CT study of the chest, abdomen, and pelvis. The postoperative examination was a dedicated spine study.

Diagnosis

Acute T12 vertebral body burst fracture with facet dislocation and cord transection, pre- and postoperative scans. Postoperative study complicated by a misplaced pedicle screw.

Teaching Points

In this case CT is used both for initial diagnosis and surgical planning and to evaluate the postoperative result. The initial spine examination was reconstructed from the data set of the diagnostic chest, abdomen, and pelvis CT. Following the postoperative study, the patient was taken back to the operating room to remove and replace the malpositioned screw.

Magnetic resonance imaging was superior in this case for demonstrating the extent of the spinal cord injury: however, CT was superior

for demonstrating the vertebral body and facet fractures. A CT examination is also preferred for evaluating the postsurgical result. Images provide precise visualization of the hardware, bone graft, and alignment and are nearly free of streak artifacts. Careful windowing of the images can provide information about the soft tissues, including the conus medullaris, discs, and nerve roots.

For evaluation of spine fractures CT is clearly the modality of choice. Screening for fractures can be performed with either CT or plain films. The choice of study often depends on the mechanism and index of suspicion. Any patient with significant pain and a concerning mechanism can benefit by going straight to CT. Any patient with an abnormal plain film should also go to CT. Studies have shown much higher sensitivity of CT for the detection of fractures, and characterization is also much improved.

A major benefit of MDCT in trauma patients is the availability of thin section data that can be retrospectively reconstructed to provide additional information. In a trauma patient who is undergoing CT of the chest, abdomen, and pelvis for evaluation of internal organ injury, the same data set can be used to produce high-quality images of the thoracolumbar spine and pelvis without having to rescan the patient. These images can be reviewed immediately on the PACS or a workstation in a seriously injured patient, or reconstructed and reviewed at a convenient later time on the scan console and sent to PACS.

Case 10.3: Extremity Fractures (Three Patients)

Clinical Information

Patient 1: A 12-year-old girl who injured her ankle playing soccer. Patient 2: A 36-year-old woman in a motor vehicle accident. Patient 3: A 50-year-old man who fell off his bicycle.

Postprocessing Techniques Used and Approach

In all three cases a combination of multiplanar reconstructions and surface-rendered images was used (Table 10.3 and Figures 10.3.1 through 10.3.3). For the knee fracture case the straight coronal and sagittal images from the scanner were used, but for both the elbow and ankle cases, oblique reconstructions were much more helpful. Surface-rendered images were reviewed without segmentation for all cases, but in addition, for the knee and elbow cases segmentation was performed using a manual sculpt.

Table 10.3. Scan Acquisition Parameters for Case 10.3, Extremity Fractures (Three Patients)

Slice No. and Thickness	**16 × 0.5 mm**
Coverage	**Through involved joint**
Helical Pitch	**0.94:1**
Rotation Speed	**0.5 sec to 0.75 sec**
Dose Parameters	**120 kVp, 150 mAs–180 mAs**
Contrast Dose	**None**

A

B

C

Figure 10.3.1. (A and B) Patient 1: sagittal and coronal 2-mm reconstructions through the ankle. There is a mildly displaced fracture of the distal tibia and posterior malleolus. The fracture crosses the growth plate and involves the epiphysis, which is also displaced. (C) Surface-rendered image again shows the fracture of the tibial epiphysis. The degree of displacement and alignment is better shown on the 3D view.

Figure 10.3.2. (A and B) Patient 2: sagittal and coronal 2-mm reconstructions through the knee. A comminuted and mildly depressed tibial plateau fracture is present. Multiple fragments are shown. (C and D) Segmented SR images with the femur removed. Anterior-posterior and articular surface views are shown. The intra-articular component of the fracture can now be seen.

Figure 10.3.3. (A and B) Patient 3: double oblique sagittal images oriented along the long axis of the radius. A comminuted radial head fracture with several fragments is present. (C and D) Surface-rendered image of the elbow and segmented view with the humerus removed. The orientation of the fragments is better appreciated, including a fragment insinuating between the humerus and olecranon which will limit range of motion.

Diagnosis

Patient 1: Salter-Harris type 4 fracture of the distal tibia. Patient 2: comminuted intra-articular tibial plateau fracture. Patient 3: comminuted radial head fracture.

Teaching Points

Multidetector CT has become an extremely valuable tool for orthopedic surgeons to diagnose, evaluate, and treat patients with complex

fractures. A CT examination with multiplanar and 3D imaging is the best method for evaluating bone alignment and displacement. It also shows intra-articular extension of a fracture line, and in pediatric patients it is useful for evaluating fractures that cross or involve the growth plate. Segmented images can demonstrate the articular surface of a joint, and small intra-articular fragments are easy to identify.

The CT imaging evaluation of these patients is straightforward and can usually be done rapidly. With a single isotropic acquisition, images can be reviewed in any plane, and 3D images can be generated instantly. Positioning is much less important than it was prior to MDCT. The patient can be scanned in the position that they are most comfortable in. It is also generally unnecessary to remove casts or splints. Proper anatomic alignment is obtained as a postprocessing feature. Oblique or double oblique MPRs obtained on a workstation are frequently the most helpful images for diagnosis. This allows bones to be oriented anatomically and in long axis, regardless of the position at the time of scanning. Surface-rendered and volume images are useful for demonstrating complex anatomy and pathology, and are very helpful to the orthopedic surgeons.

Case 10.4: Right Ventricular Gunshot Wound

Clinical Information

A 53-year-old man who shot himself in the upper abdomen in a suicide attempt. Patient was hemodynamically stable at time of arrival at the emergency department and was sent to CT for evaluation.

Postprocessing Techniques Used and Approach

Multiplanar reconstructions generated on the scanner console are used to make the initial diagnosis (Table 10.4 and Figures 10.4.1 through 10.4.3). Segmented VR images are also produced using automated vessel-tracking software to isolate the heart, aorta, and chest vessels.

Diagnosis

Gunshot wound to the right ventricle with extravasation of contrast and blood into the upper abdomen through a laceration of the diaphragm.

Teaching Points

The CT examination provided rapid diagnosis in this critically injured patient. The extent of injury was not initially suspected by the trauma

Table 10.4. Scan Acquisition Parameters for Case 10.4, Right Ventricular Gunshot Wound

Slice No. and Thickness	**16 × 1.0 mm**
Coverage	**Chest through pelvis**
Helical Pitch	**1.5:1**
Rotation Speed	**0.5 sec**
Dose Parameters	**120 kVp, 250 mAs**
Contrast Dose	**100 mL Omnipaque 350**
Injection Rate	**2 mL/sec**
Bolus Timing Method	**40-sec delay at lung apex**

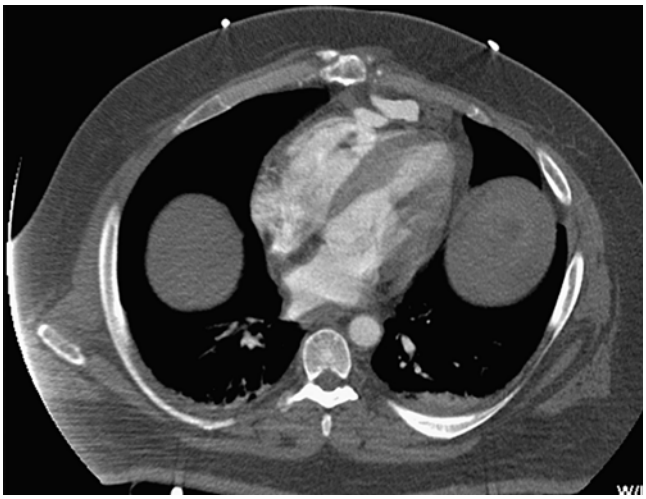

Figure 10.4.1. Axial 3-mm image through the heart shows injury to the right ventricular wall with contrast extravasation anterior to the heart. The bullet entered the chest on an oblique upward trajectory from the epigastric region.

service. The multiplanar reconstructions were all the surgeon needed to take this patient emergently to the operating room. Volume-rendered images were generated later, after the initial diagnosis had been made, but took only a few seconds to generate. The reconstructions were somewhat limited in this case related to respiratory and motion artifacts in this patient, who was unable to cooperate or hold his breath. Despite this, perfectly diagnostic images were obtained in a fast scan protocol.

Use of CT for patients with penetrating chest and abdomen trauma remains somewhat controversial. Computed tomography has been used successfully for years in patients with penetrating trauma to the back or flank, but many trauma centers do not use CT routinely for injuries to the abdomen. Traditional practice in many trauma centers includes wound exploration, diagnostic peritoneal lavage, and serial monitoring. There are questions, however, about both the sensitivity and specificity of peritoneal lavage.

Many trauma centers now incorporate the use of triple contrast CT into an algorithm for patients with penetrating torso trauma. Any

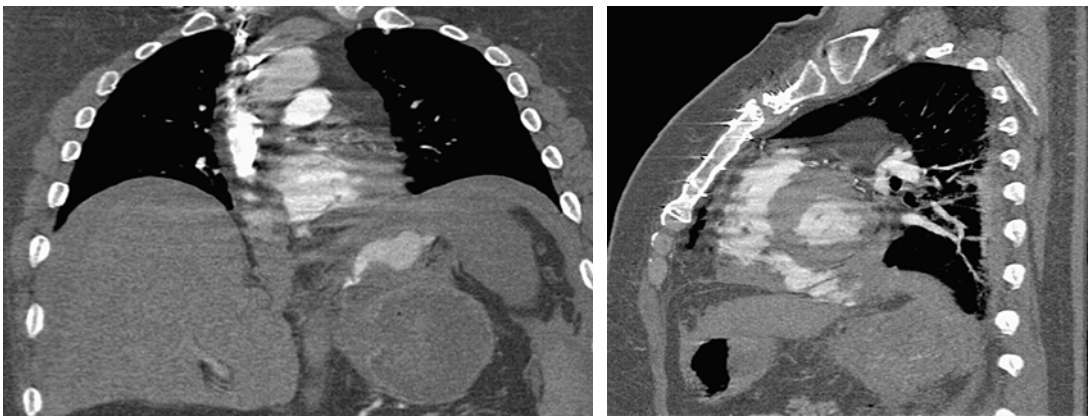

A B

Figure 10.4.2. (A and B) Coronal and sagittal reconstructions show the path of contrast and blood flow from the heart through a hole in the diaphragm and into the subphrenic space. Hemoperitoneum surrounds the liver.

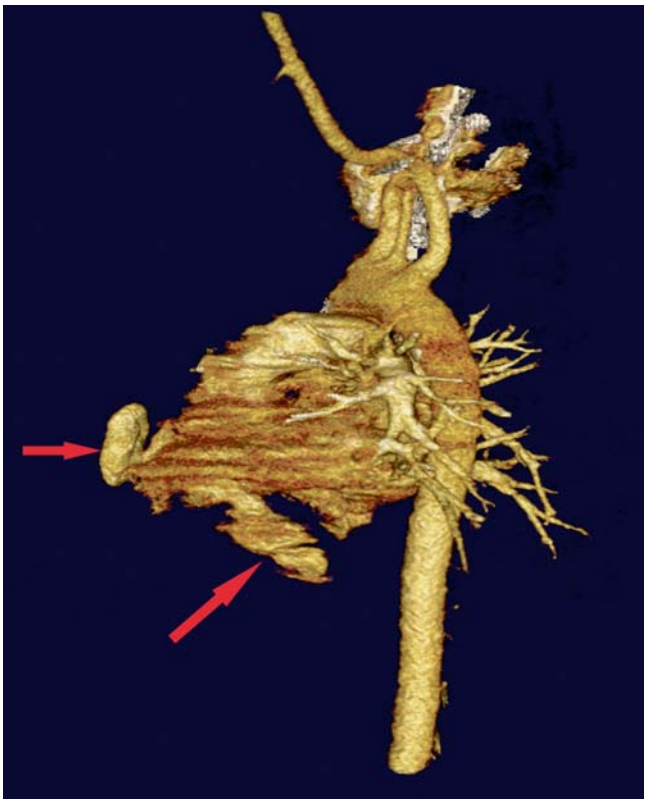

Figure 10.4.3. Segmented VR image shows the extravasated high-density contrast anterior to the heart and extending through the diaphragm into the upper abdomen (arrows).

patient who is hemodynamically unstable or has peritonitis or a clearly positive lavage should go straight to surgery. Stable patients with a negative or equivocal lavage can undergo triple contrast CT. The CT must be carefully evaluated for signs of peritoneal violation (air bubbles, fat stranding, fluid), solid organ injury, vascular injury, diaphragm injury and bowel injury. Bowel lacerations are the most commonly missed significant injuries on CT. The most sensitive CT finding of bowel injury is a wound track that extends up to the injured bowel. The most specific CT findings of bowel injury include gastrointestinal contrast material extravasation and bowel wall thickening with adjacent mesenteric injury. Depending on the CT result, the patient may still go to surgery if there is evidence for bowel injury or significant organ or vascular injury. Other patients may avoid an unnecessary laparotomy.

Case 10.5: Multiple Facial Fractures

Clinical Information

An 18-year-old man who was assaulted with a pipe.

Postprocessing Techniques Used and Approach

Multiplanar images reconstructed on the scanner console were reviewed (Table 10.5 and Figures 10.5.1 through 10.5.3). Surface-

Table 10.5. Scan Acquisition Parameters for Case 10.5, Multiple Facial Fractures

Slice No. and Thickness	16 × 0.5 mm
Coverage	Head and facial bones
Helical Pitch	1.25:1
Rotation Speed	0.5 sec
Dose Parameters	120 kVp, 150 mAs
Contrast Dose	None

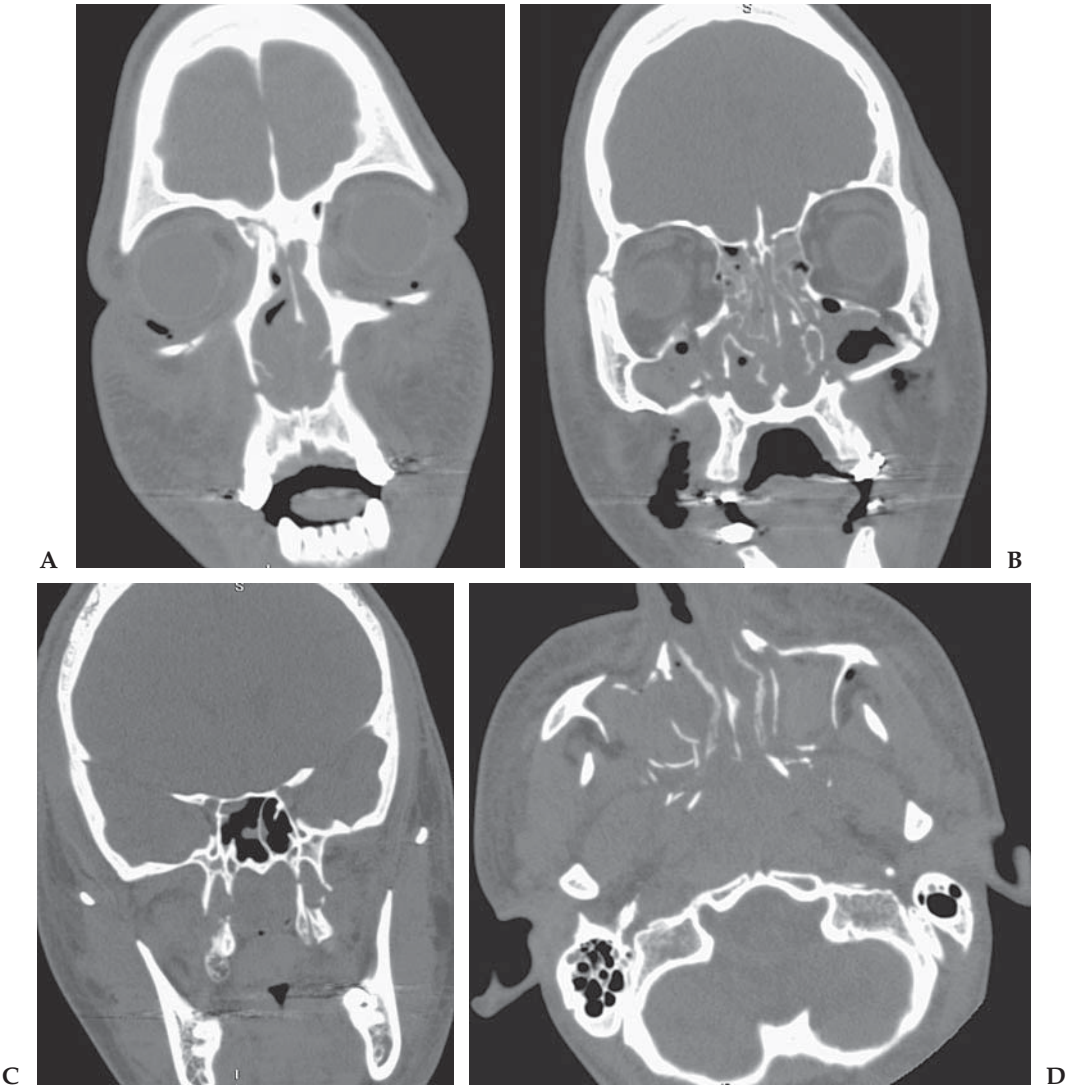

Figure 10.5.1. (A–D) Coronal 2-mm images from anterior to posterior through the facial bones and axial 2-mm image at the level of the maxillary sinuses. Multiple right-sided fractures include nasal bone; lateral, inferior, and medial orbital walls; zygomatico-frontal suture; maxilla; anterior, lateral, and medial walls; maxillary sinus; and pterygoid plate. Left-sided fractures include inferior orbital rim, maxilla, medial and lateral wall, maxillary sinus, and pterygoid plate.

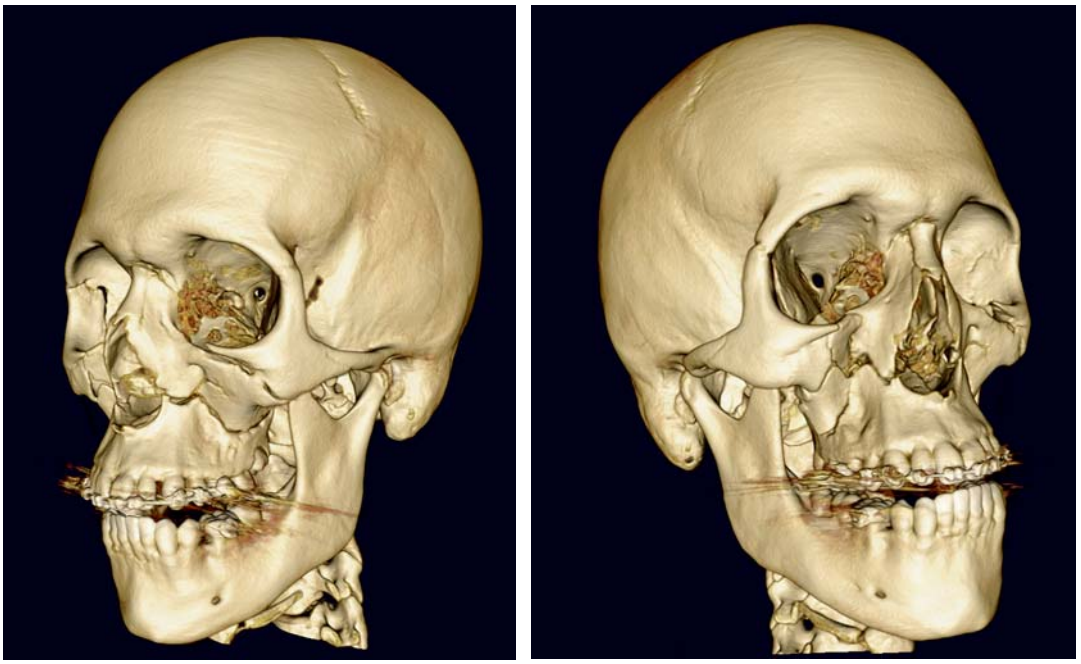

A B

Figure 10.5.2. (A and B) Surface-rendered images show the multiple fractures in three dimensions. Extent of displacement and depression is easier to appreciate on the 3D images. Some fractures are easier to identify, but other fractures cannot be seen on these views.

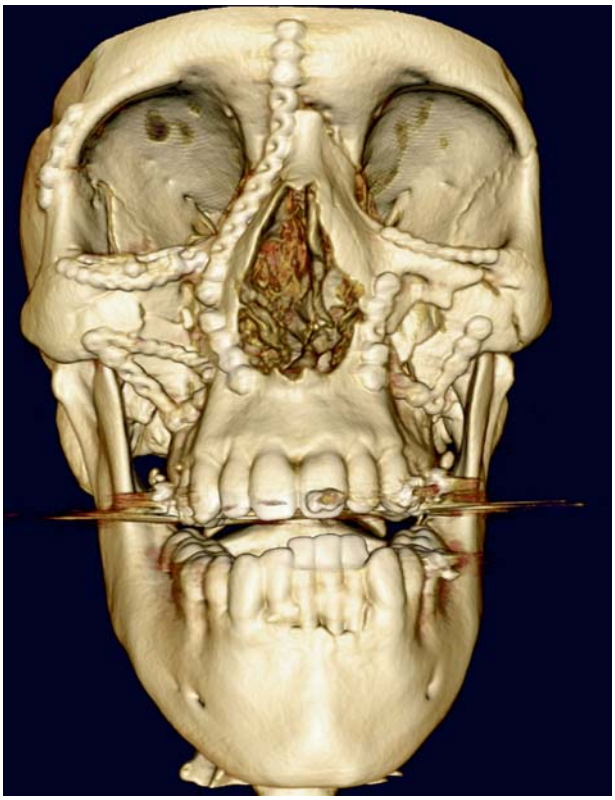

Figure 10.5.3. Surface-rendered image obtained following surgical repair, demonstrating the surgical result. Note repair of the right nasal bone and zygomatico-frontal suture, both inferior orbital rims, the maxilla bilaterally, and the anterior walls of the maxillary sinuses.

rendered images on the workstation were also reviewed. No segmentation was needed.

Diagnosis

Bilateral LeFort facial fractures. The right side is closest to a LeFort III fracture, and the left side closest to a LeFort II fracture.

Teaching Points

The use of CT to diagnose and characterize facial fractures was well established in the single-slice CT era. With MDCT this test has become easier, faster, and more clinically useful. A key advantage with multislice CT is that it is no longer necessary to try to position patients for coronal images. A single acquisition can be reconstructed into any plane. Importantly, in an acutely ill trauma patient who is already undergoing CT of the head and cervical spine, the high-resolution images of the facial bones can be obtained with no additional scanning. The same data set can be reconstructed in a smaller field of view with thin section multiplanar reconstructions through the orbits and facial bones. Since this is a volumetric data set, the same information can be used to generate high-quality 3D reconstructions on a workstation.

Optimal evaluation of facial trauma should include both multiplanar images and 3D visualization. As in other areas, these techniques are complementary, with some findings better shown on one technique over the other and vice-versa.

Case 10.6: C1 Fracture

Clinical Information

A 35-year-old woman in a motor vehicle accident with neck pain.

Postprocessing Techniques Used and Approach

Initial review was done with standard axial, sagittal, and coronal MPRs (Table 10.6 and Figures 10.6.1 through 10.6.3). Because of the complex appearance of the fracture, the data were transferred to the workstation and reviewed with a surface-rendered protocol. To better view the fracture the occiput was segmented from the C1 arch using a manual

Table 10.6. Scan Acquisition Parameters for Case 10.6, C1 Fracture

Slice No. and Thickness	**16 × 0.5 mm**
Coverage	**Cervical spine**
Helical Pitch	**0.93:1**
Rotation Speed	**0.5 sec**
Dose Parameters	**120 kV, 150 mAs**
Contrast Dose	**None**

3D sculpt. Additional editing from the 2D images was used to remove the C2 body and odontoid, isolating the C1 vertebral body.

Diagnosis

Complex horizontal cleavage fracture of C1 vertebral body.

Teaching Points

The multiplanar reconstructions in this case clearly demonstrate the presence of the cervical fracture and show which structures are involved, but it is very difficult from the MPR images alone to have a

A

B

C

Figure 10.6.1. (A–C) Axial, sagittal, and coronal MPR images show a comminuted fracture of the anterior ring of the C1 vertebral body with several small fragments present. The MPR images clearly show the fracture and the fragments, but it is difficult to appreciate the full extent of the injury.

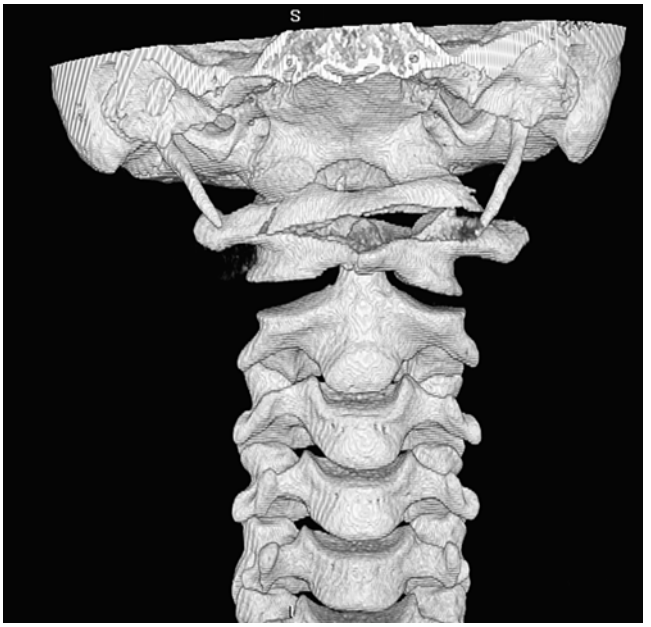

Figure 10.6.2. Three-dimensional surface-rendered view of the cervical spine. The surface image now clearly demonstrates an unusual horizontal cleavage fracture of the C1 ring, which is displaced cephalad.

full understanding of the three-dimensional anatomy. The surface-rendered images provide significant additional information and are most useful to the surgeon for planning management for this patient. The additional segmentation of the data performed in this case is not absolutely necessary; however, it takes only a few minutes and provides incredible detail of the fracture and the involved vertebral body.

Evaluation of cervical spine injuries has been under significant debate for the last few years. Many authors have advocated CT rather than plain films for initial evaluation of all patients with significant trauma. Many studies have shown that plain films can miss significant, clinically important fractures. This debate has intensified with the arrival of MDCT, which can perform examinations faster and with much higher quality. Eliminating conventional radiography for the screening of spine fractures in trauma patients affords several major advantages. In addition to improved diagnostic accuracy, there is a significant reduction in examination time required, less patient manipulation is needed, and total cost can also be reduced.

Algorithms using CT as the primary method of evaluation have been created and have been shown to save time and money when used appropriately. There is no question about the superiority of CT to identify and characterize fractures. At Long Beach Memorial we have depended on CT as the primary imaging study for the cervical spine in trauma patients for many years with great success.

Figure 10.6.3. (A and B) Three-dimensional segmented surface images of the C1 vertebral body. Manual sculpting from the 2D images demonstrates the isolated C1 body. This allows the fracture to be clearly seen and rotated into any projection.

Case 10.7: Traumatic Aortic Transection

Clinical Information

A 50-year-old woman in a high-speed deceleration motor vehicle accident.

Postprocessing Techniques Used and Approach

Rapid diagnosis is made from review of standard axial and multiplanar reconstructions (Table 10.7 and Figures 10.7.1 and 10.7.2). Images are transferred immediately to the workstation, where oblique thin-slab

Table 10.7. Scan Acquisition Parameters for Case 10.7, Traumatic Aortic Transection

Slice No. and Thickness	16 × 1 mm
Coverage	Chest to pelvis
Helical Pitch	1.5:1
Rotation Speed	0.5 sec
Dose Parameters	120 kVp, 150 mAs
Contrast Dose	125 mL Omnipaque 350
Injection Rate	3 mL/sec
Bolus Timing Method	Bolus triggering aorta

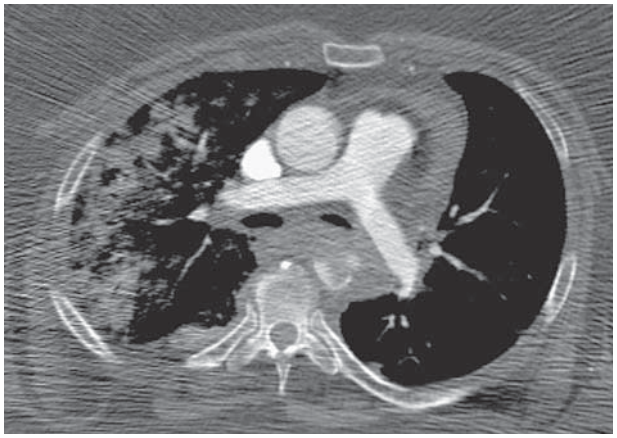

A

B

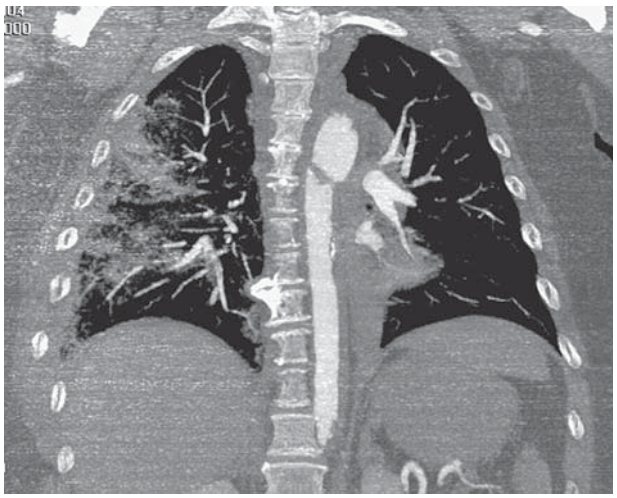

C

Figure 10.7.1. (A–C) Axial and oblique sagittal images and coronal thin slab (8 mm) MIP image through the thoracic aorta. The descending thoracic aorta has been completely transected, although continuity of the lumen is still present related to the adventitia and periaortic tissues. Adjacent hematoma is present but is relatively small given the severity of the injury. Extensive contusion is also present in the right lung.

Figure 10.7.2. Segmented volume-rendered image of the aorta. The injury starts immediately distal to the left subclavian artery origin and extends to the aortic isthmus.

MIP images are reviewed. A segmented volume-rendered image is produced by using automated software to remove the osseous structures. Manual 3D sculpting is used to remove the heart and pulmonary arteries.

Diagnosis

Traumatic transection of the thoracic aorta.

Teaching Points

Multidetector CT has replaced catheter angiography as the test of choice to diagnose acute traumatic and nontraumatic aortic pathology. The CT examination is readily available, is easy to perform, and has been shown to be highly accurate for aortic injury (99%). The diagnosis is readily made from routine axial and multiplanar reconstructions. Careful evaluation of the aorta and adjacent mediastinal fat is required. Oblique sagittal images are important for identifying small tears and pseudoaneurysms that can occur at the aortic isthmus. When the study is abnormal, volume images are very helpful for delineating the extent of injury and planning surgery or endovascular repair.

In the majority of cases (approximately 80%) traumatic injury results in rupture of all three layers of the aortic wall (intima, media and adventitia). This usually results in exsanguination and death at the point of trauma. In the remaining patients the injury will involve either the intima or both the intima and media but will leave the adventitia intact enough to prevent immediate exsanguination. If these patients

are treated promptly, they have a chance for survival. A CT examination in these patients will demonstrate mediastinal hemorrhage and injury to the aorta. Formation of false or pseudoaneurysms is typical. If only the intima is involved, the appearance may be identical to a nontraumatic dissection.

Approximately 90% of blunt traumatic aortic injuries occur at the anteromedial aspect of the aortic isthmus distal to the origin of the left subclavian artery. This appears to be related to a combination of traction, torsion, and hydrostatic forces created by differential deceleration of thoracic structures that occurs in this location. The second most common site of injury is at the aortic root, which may result in aortic valve tears, cardiac contusions or ruptures, coronary artery tears, and/or hemopericardium with cardiac tamponade.

Treatment of acute traumatic injury has traditionally required open surgical repair. However, many sites do not have extensive experience and success treating these patients with endovascular stent-graft repair, particularly in high-risk patients.

Selected Readings

Rapid Multiple Trauma Evaluation

1. Novelline RA, Rhea JT, Rao PM, Stuk JL. Helical CT in emergency radiology. Radiology 1999;213:321–339.
2. Shanmuganathan K. Multi-detector row CT imaging of blunt abdominal trauma. Semin Ultrasound CT MR 2004 Apr;25(2):180–204.
3. Titton RL, Gervais DA, Boland GW, Mueller PR. Renal trauma: radiologic evaluation and percutaneous treatment of nonvascular injuries. Am J Roentgenol 2002 Jun;178:1507–1511.
4. Wintermark M, Mouhsine E, Theumann N, et al. Thoracolumbar spine fractures in patients who have sustained severe trauma: depiction with multi–detector row CT. Radiology 2003;227:681–689.

T12 Vertebral Body Fracture

5. Begemann PG, Kemper J, Gatzka C, Stork A, Nolte-Ernsting C, Adam G. Value of multiplanar reformations (MPR) in multidetector CT (MDCT) of acute vertebral fractures: do we still have to read the transverse images? J Comput Assist Tomogr 2004 Jul–Aug;28(4):572–580.
6. Novelline RA, Rhea JT, Rao PM, Stuk JL. Helical CT in emergency radiology. Radiology 1999;213:321–339.
7. Rock C, Linsenmater UH, Pilgram H, et al. Diagnosis of thoracic and lumbar spine fractures in trauma patients: are plain film radiographs still necessary? Can thoracic and abdominal spiral CT replace them? Radiology 2001;221(P):434.
8. Wintermark M, Mouhsine E, Theumann N, et al. Thoracolumbar spine fractures in patients who have sustained severe trauma: depiction with multi–detector row CT. Radiology 2003;227:681–689.

Extremity Fractures

9. Buckwalter KA, Farber JM. Application of multidetector CT in skeletal trauma. Semin Musculoskelet Radiol 2004 Jun;8(2):147–156.

10. Buckwalter KA, Rydberg J, Kopecky KK, Crow K, Yang EL. Musculoskeletal imaging with multislice CT. Am J Roentgenol 2001 Apr;176:979–986.
11. Novelline RA, Rhea JT, Rao PM, Stuk JL. Helical CT in emergency radiology. Radiology 1999;213:321–339.
12. Pretorius ES, Fishman EK. Volume-rendered three-dimensional spiral CT: musculoskeletal applications. Radiographics 1999;19:1143–1160.

Right Ventricular Gunshot Wound

13. Grossman MD, May AK, Schwab CW, et al. Determining anatomic injury with computed tomography in selected torso gunshot wounds. J Trauma 1998;45:446–456.
14. Múnera F, Morales C, Soto JA, et al. Gunshot wounds of abdomen: evaluation of stable patients with triple-contrast helical CT. Radiology 2004;231:399–405.
15. Shanmuganathan K, Mirvis SE, Chiu WC, Killeen KL, Hogan GJF, Scalea TM. Penetrating torso trauma: triple-contrast helical CT in peritoneal violation and organ injury—a prospective study in 200 patients. Radiology 2004;231:775–784.
16. Shanmuganthan K, Scalea TM. Imaging of penetrating trauma of the torso and chest. In: Mirvis SE, Shanmuganathan K, eds. Imaging in Trauma and Critical Care. 2nd ed. Philadelphia, PA: Saunders; 2003:633–696.

Multiple Facial Fractures

17. Holmgren EP, Dierks EJ, Homer LD, Potter BE. Facial computed tomography use in trauma patients who require a head computed tomogram. J Oral Maxillofac Surg 2004 Aug;62(8):913–918.
18. Lee HJ, Jilani M, Frohman L, Baker S. CT of orbital trauma. Emerg Radiol 2004 Feb;10(4):168–172.
19. Philipp MO, Funovics MA, Mann FA, et al. Four-channel multidetector CT in facial fractures: do we need 2×0.5 mm collimation? Am J Roentgenol 2003 Jun;180:1707–1713.
20. Rhea JT, Rao PM, Novelline RA. Helical CT and three-dimensional CT of facial and orbital injury. Radiol Clin North Am 1999;37:489–513.
21. Turner BG, Rhea JT, Thrall JH, Small AB, Novelline RA. Trends in the use of CT and radiography in the evaluation of facial trauma, 1992–2002: implications for current costs. Am J Roentgenol 2004 Sep;183:751–754.

C1 Fracture

22. Barba CA, Taggert J, Morgan AS, et al. A new cervical spine clearance protocol using computed tomography. J Trauma 2001;51:652–657.
23. Berlin L. CT versus radiography for initial evaluation of cervical spine trauma: what is the standard of care? Am J Roentgenol 2003 Apr;180:911–915.
24. Blackmore CC, Mann FA, Wilson AJ. Helical CT in the primary trauma evaluation of the cervical spine: an evidence-based approach. Skeletal Radiol 2000;29:632–639.
25. Brandt MM, Wahl WL, Yeom K, Kazerooni E, Wang SC. Computed tomographic scanning reduces cost and time of complete spine evaluation. J Trauma 2004 May;56(5):1022–1026.
26. Crim JR, Moore K, Brodke D. Clearance of the cervical spine in multitrauma patients: the role of advanced imaging. Semin Ultrasound CT MR 2001;22:283–305.

27. Daffner RH. Helical CT of the cervical spine for trauma patients: a time study. Am J Roentgenol 2001 Sep;177:677–679.

Traumatic Aortic Transection

28. Alkadhi H, Wildermuth S, Desbiolles L, et al. Vascular emergencies of the thorax after blunt and iatrogenic trauma: multi-detector row CT and three-dimensional imaging. Radiographics 2004 Sep;24(5):1239–1255.
29. Gavant ML. Helical CT grading of traumatic aortic injuries: impact on clinical guidelines for medical and surgical management. Radiol Clin North Am 1999;37:553–574.
30. Macura KJ, Corl FM, Fishman EK, Bluemke DA. Pathogenesis in acute aortic syndromes: aortic aneurysm leak and rupture and traumatic aortic transection. Am J Roentgenol 2003;181:303–307.
31. Marty-Ane CH, Berthet JP, Branchereau P, Mary H, Alric P. Endovascular repair for acute traumatic rupture of the thoracic aorta. Ann Thorac Surg 2003 Jun;75(6):1803–1807.
32. Parker MS, Matheson TL, Rao AV, et al. Making the transition: the role of helical CT in the evaluation of potentially acute thoracic aortic injuries. Am J Roentgenol 2001;176:1267–1272.

Chapter 11

Body Imaging

Case 11.1: Lung Cancer

Clinical Information

A 69-year-old woman with cough and shortness of breath. She is found to be markedly hypoxemic and is referred to CT to rule out acute pulmonary embolus.

Postprocessing Techniques Used and Approach

Simple multiplanar axial and coronal images supply excellent detail to evaluate the mass and pulmonary arteries (Table 11.1 and Figures 11.1.1 and 11.1.2). Oblique coronal plane is also used to demonstrate along the long axis of the left pulmonary artery. Thick-slab (50 mm) unsegmented MIP images are used to show the peripheral pulmonary arteries.

Diagnosis

Lung cancer with encasement and compression of the left pulmonary artery causing marked oligemia to the left lung.

Teaching Points

Combining multiplanar reconstructions with thin- and thick-slab MIP images is a powerful and quick way to evaluate the chest and pulmonary vasculature. These images are created and interpreted quite easily and add a tremendous amount of information to the examination.

In this patient, CT explains the cause of the hypoxia in this woman suspected to have acute pulmonary embolism, and is able to make an alternate diagnosis of lung cancer with pulmonary artery compression. One of the important additional benefits of using MDCT over VQ scanning and catheter angiography for the diagnosis of pulmonary emboli is the ability of CT to make alternate diagnoses, such as in this case.

Table 11.1. Scan Acquisition Parameters for Case 11.1, Lung Cancer

Slice No. and Thickness	**16 × 0.5 mm**
Coverage	**Chest**
Helical Pitch	**1.25:1**
Rotation Speed	**0.5 sec**
Dose Parameters	**120 kVp, 200 mAs**
Contrast Dose	**125 mL Omnipaque 350**
Injection Rate	**4 mL/sec**
Bolus Timing Method	**Bolus triggering on the pulmonary artery**

Computed tomography remains a very important test for evaluating and following patients with known or suspected lung cancer. The higher resolution and multiplanar imaging of MDCT will clearly improve staging accuracy compared with single-slice scanners. Involvement of the mediastinum, main bronchus or trachea, vascular encasement, heart, and chest wall should all be improved with MDCT.

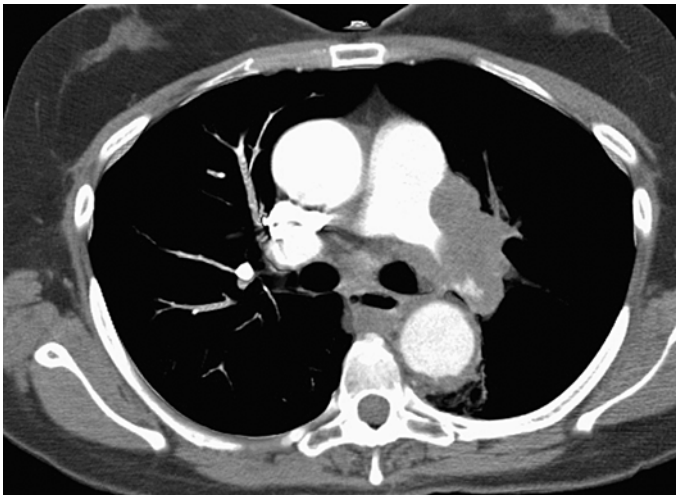

A

B

Figure 11.1.1. (A and B) Axial 3-mm and oblique coronal image along the left pulmonary artery. There is a large left hilar mass that completely encases and compresses the left main pulmonary artery. Certain slices can make the mass appear intraluminal, but by visualizing the abnormality in different planes it is clearly shown to be entirely extrinsic.

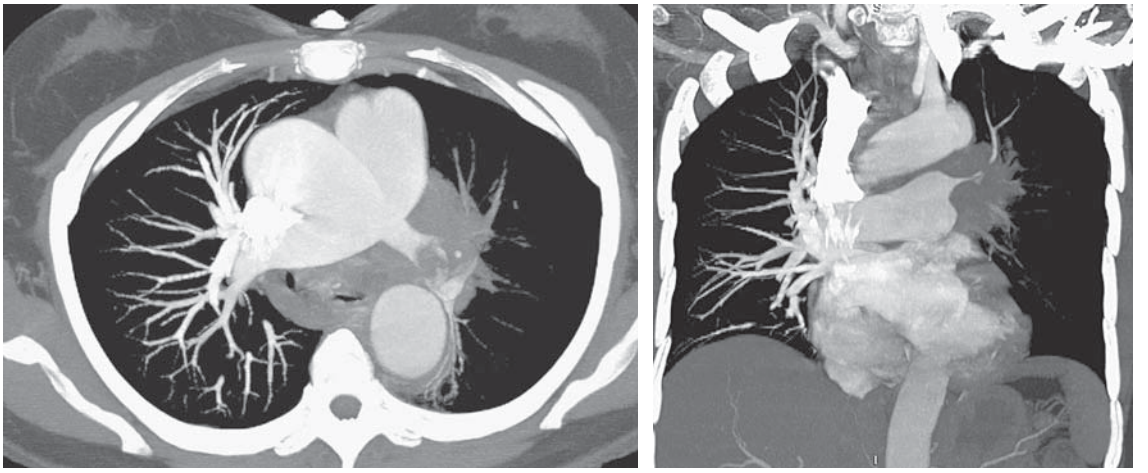

A B

Figure 11.1.2. (A and B) Axial and coronal thick slab MIP images. The marked asymmetry of the pulmonary circulation is demonstrated. The tumor has caused severe pulmonary artery compression with only a few central pulmonary artery branches seen on the left.

In addition, identification of small lymph nodes is easier with the higher resolution images. Most studies currently looking at lung cancer staging are focused on the combination of PET and CT. These studies have clearly shown that PET/CT has a staging accuracy that exceeds either modality alone, and should be considered the gold standard for preoperative staging at this time.

Case 11.2: Renal Cell Carcinoma

Clinical Information

A 55-year-old man with abdominal pain.

Postprocessing Techniques Used and Approach

The primary review of the case was performed with standard 3-mm axial and coronal images (Table 11.2 and Figures 11.2.1 through 11.2.4). In order to better evaluate the left renal vein, curved planar reconstructions were performed on the workstation. Although this was not

Table 11.2. Scan Acquisition Parameters for Case 11.2, Renal Cell Carcinoma

Slice No. and Thickness	**16 × 0.1 mm**
Coverage	**Abdomen and pelvis**
Helical Pitch	**1.25:1**
Rotation Speed	**0.5 sec**
Dose Parameters	**120 kVp, 200 mAs**
Contrast Dose	**100 mL Omnipaque 350**
Injection Rate	**2 mL/sec**
Bolus Timing Method	**70-sec delay**

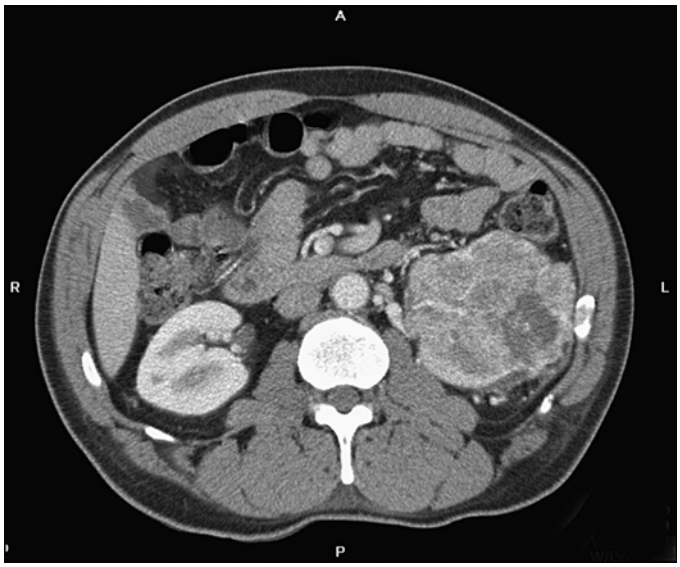

Figure 11.2.1. A 3-mm axial image shows a large, heterogeneous solid mass with areas of necrosis in the left kidney. Appearance is typical for renal cell carcinoma. Infiltration of the perinephric fat is present, suggesting that the lesion is at least a T3 tumor.

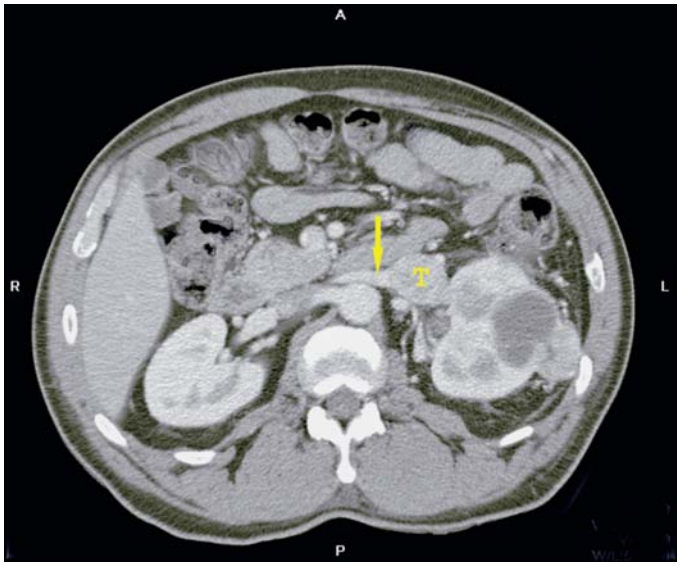

Figure 11.2.2. Axial image at the level of the left renal vein. There is apparent tumor invasion (T) into the left renal vein (arrow). This would make the tumor a T3b lesion.

Figure 11.2.3. Coronal curved planar reconstruction along the left renal vein. The renal and left gonadal veins are well shown. The tumor is causing extrinsic compression on the renal vein but does not actually invade it.

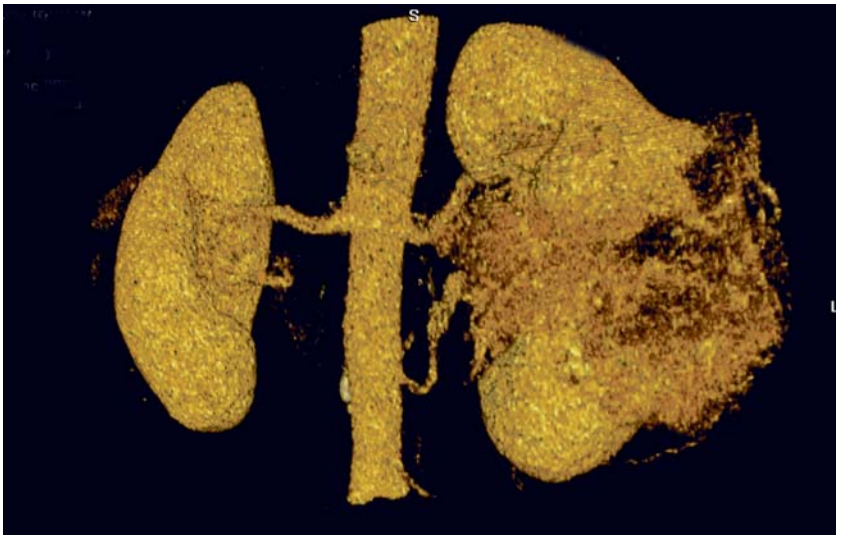

Figure 11.2.4. Segmented volume-rendered image through the aorta. Two renal arteries are present to the left kidney with a single renal artery noted on the right.

an arterial study, a volume-rendered image with the bone removed was done to show the arterial supply to the kidneys.

Diagnosis

Renal cell carcinoma stage T3a, N0, M0.

Teaching Points

This case was done with a routine protocol in a patient with abdominal pain. The history of hematuria was not available at the time of the study. Initial review of the axial images diagnosed a renal cell carcinoma which was thought likely to be stage T3b with left renal vein invasion. However, the coronal images were equivocal for renal vein invasion; therefore, a curved reformation was done along the left renal vein. The curved image clearly showed the tumor to extrinsically compress the vein without invading it (confirmed by surgery). This changed the stage to a T3a lesion, which has a different prognosis and surgical approach. In addition, volume-rendered images showing the arterial anatomy were generated even though this was not a CTA. These images clearly showed two left renal arteries and provided the surgeon with all the information necessary to operate on this patient.

Surgical treatment of renal cell carcinoma is highly dependent on the stage of the tumor at presentation. Small lesions that are confined to the kidney can frequently be removed laparoscopically, and patients may be candidates for partial nephrectomy. For larger tumors a key point of distinction involves invasion of perinephric fat. If the fat is invaded (T3a lesion), then an open radical nephrectomy should be per-

formed, but if the fat is not invaded (T2 lesion), then a conservative nephrectomy can be done (possibly laparoscopic).

The evaluation of the renal vein and inferior vena cava for tumor thrombus is crucial for treatment planning. If tumor thrombus spreads into the inferior vena cava, the exact extent of the thrombus is essential for planning the correct surgical approach. An abdominal incision is performed if the thrombus is infrahepatic (T3b), whereas a thoracoabdominal incision is needed if the thrombus extends above the diaphragm (T3c).

Complete evaluation should also look for enlarged lymph nodes, invasion of the adrenal glands or other structures, and distant metastasis to the liver or lung. The diagnosis of malignancy with regard to lymph node involvement is still based on size criteria only. With 10 mm as the limiting size for normal nodes, 4% of lymph nodes have a false-negative finding because micrometastases cannot be identified. Furthermore, false-positive findings can be between 3% and 43%, according to different studies, because nodal enlargement may be caused by reactive hyperplasia. The reported accuracy of conventional CT in diagnosing lymph node involvement is between 83% and 88%.

Case 11.3: CT Colonography

Clinical Information

A 56-year-old woman undergoing screening for colon polyps.

Postprocessing Techniques Used and Approach

A combination approach of multiplanar 2D image review, 3D volume-rendered correlation, and endoluminal fly-through imaging is used to evaluate the colon in this patient (Table 11.3 and Figures 11.3.1 and 11.3.2).

Diagnosis

A 9-mm adenomatous polyp in the transverse colon.

Teaching Points

Colorectal cancer is the second leading cause of cancer-related deaths in the United States, accounting for nearly 60,000 deaths each year.

Table 11.3. Scan Acquisition Parameters for Case 11.3, CT Colonography

Slice No. and Thickness	**16 × 1.0 mm**
Coverage	**Abdomen and pelvis, supine and prone**
Helical Pitch	**1.25:1**
Rotation Speed	**0.5 sec**
Dose Parameters	**120 kVp, 130 mAs**
Contrast Dose	**None. Air insufflation performed**

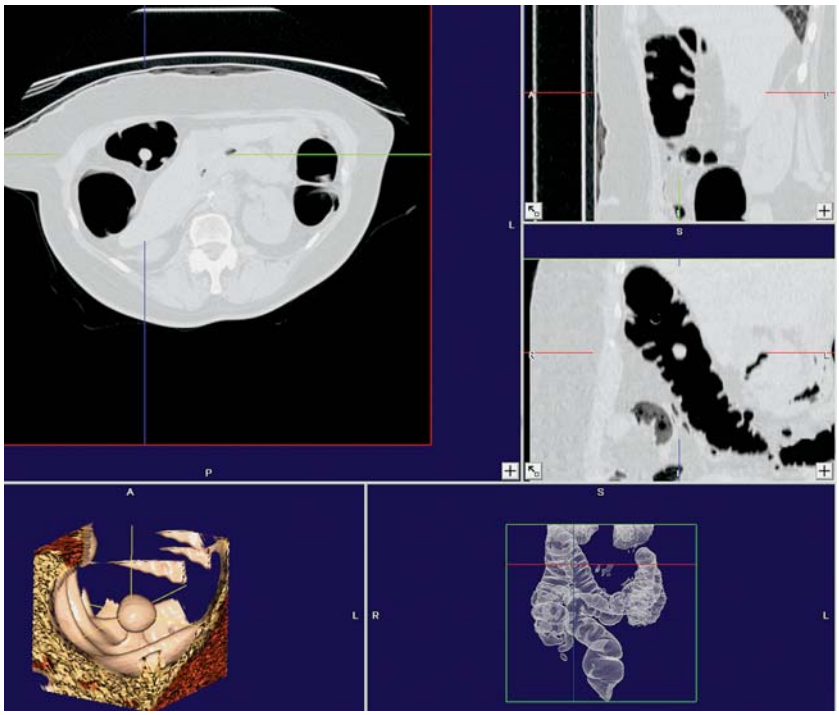

A

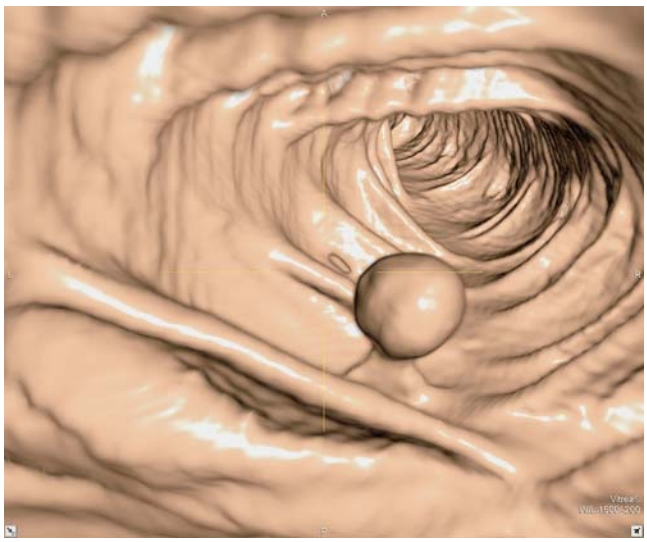

B

Figure 11.3.1. (A and B) Workstation navigation screen from the prone data set demonstrates three plane 2D projections correlated to a volume-rendered image of the colon and a 3D endoluminal view of the selected area. The polyp is shown on both 2D and 3D images and can be evaluated and measured on-screen. Anatomic localization is made to the transverse colon. Endoluminal fly-through spot image shows a pedunculated polyp on a stalk on the prone image.

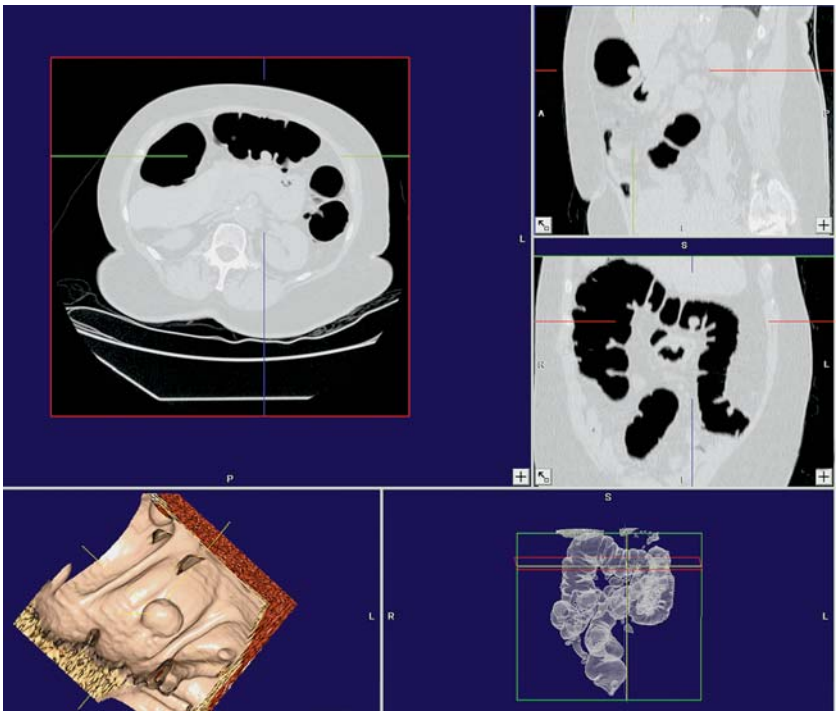

A

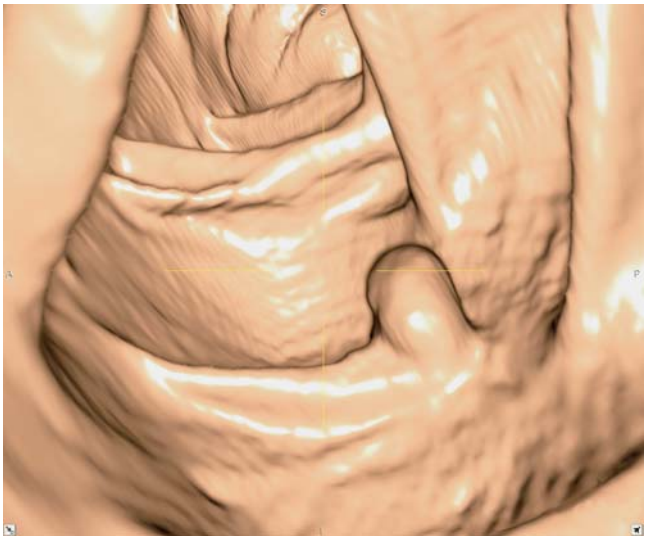

B

Figure 11.3.2. (A and B) Similar images from the supine data set again show the polyp in the transverse colon. On this image the pedunculated nature of the polyp cannot be appreciated since the lesion arises from the posterior wall of the colon and is dependent in this position.

Most colorectal cancers are believed to arise within benign adenomatous polyps that develop slowly over the course of many years. This long lead time between adenomatous polyp and cancer affords a significant window during which screening can occur and polyps can be removed before they become malignant. Current guidelines recom-

mend the screening of adults who are at average risk for colorectal cancer starting at age 50 and even younger for patients at higher risk. Unfortunately, approximately half the average-risk population of the United States does not follow these guidelines and are not screened by any method for this largely preventable disease.

Optical colonoscopy (OC) is currently the gold standard for screening, detection, and removal of polyps. Unfortunately, the procedure is invasive, expensive, and somewhat limited in availability. It is hoped that a less invasive test such as CT colonoscopy (CTC) could take over much of the burden for screening patients and leave OC primarily to treat lesions and evaluate questionable cases.

Numerous studies in the literature have looked at the accuracy of CTC compared with OC for evaluation of polyps of different sizes and in different populations. Results of these studies have varied dramatically, as have scanning and image interpretation techniques. The best studies have shown accuracy for CT that equals or even surpasses OC; other studies have shown substantially worse results. While it is still too early in the experience with CTC to predict whether it will ultimately replace OC as the screening test of choice, there are some generalizations that can be made regarding patient preparation, scan technique, and image interpretation techniques.

Patient preparation remains very important. Currently, a cleansing prep is needed which can be combined with a dose of Gastrografin for the purpose of tagging any residual stool. In the future it may be possible to perform a study using only stool tagging without cleansing, but this technique is not proven. Patients should be scanned on an MDCT scanner with very low dose technique and thin collimation. Both supine and prone scans should be obtained.

The optimal way to review CTC images remains highly controversial. The most successful study of CTC (Pickhart et al.) relied on primary endoluminal fly-through imaging in the forward and reverse directions on both supine and prone images. Other investigators advocate a combined 2D/3D image review with endoluminal fly-through of any suspicious area. Workstation manufacturers are all diligently working to improve and automate current software, and the field is changing rapidly. For CTC to become truly successful and widely performed around the country automated software and computed-aided diagnosis (CAD) will be very important.

Case 11.4: Pancreatic Cancer

Clinical Information

A 69-year-old man with abdominal pain.

Postprocessing Techniques Used and Approach

Axial and multiplanar images are initially reviewed. On the workstation, axial and sagittal thin slab MIP images and curved reconstructions through the superior mesenteric artery (SMA), celiac artery, and pan-

Table 11.4. Scan Acquisition Parameters for Case 11.4, Pancreatic Cancer

Slice No. and Thickness	**16 × 1 mm**
Coverage	**Abdomen**
Helical Pitch	**1.25:1**
Rotation Speed	**0.5 sec**
Dose Parameters	**120 kVp, 150 mAs**
Contrast Dose	**125 mL Omnipaque 350**
Injection Rate	**3 mL/sec**
Bolus Timing Method	**40-sec delay**

creas are produced (Table 11.4 and Figures 11.4.1 through 11.4.3). Volume-rendered images using segmentation to remove the spine are also reviewed.

Diagnosis

Pancreatic adenocarcinoma with vascular invasion of the celiac and superior mesenteric arteries.

Teaching Points

Pancreatic carcinoma is the fourth leading cause of cancer-related deaths in the United States. The prognosis is generally dismal, with an overall 5-year survival rate of only 4.1%. Currently, the only available curative therapy is surgical removal, which usually requires pancreaticoduodenectomy (Whipple procedure). Unfortunately, the majority of patients (78%–95%) have advanced disease and are not eligible for surgery.

Accurate preoperative staging for patients with pancreatic cancer is very important for identifying appropriate surgical candidates. The surgery itself carries significant morbidity and mortality and should be

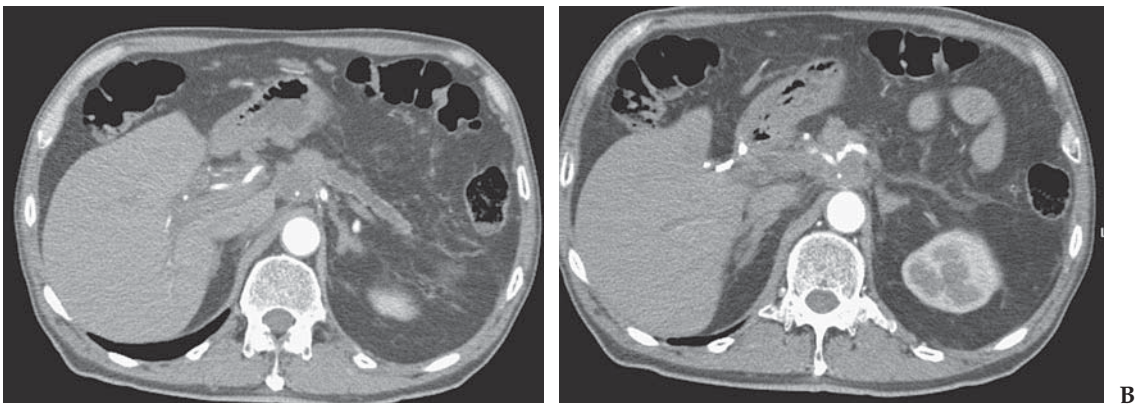

A B

Figure 11.4.1. (A and B) Axial 2-mm images through the pancreas and celiac axis. There is a mass in the pancreatic head with marked atrophy of the pancreatic body and dilatation of the pancreatic duct. Tumor encasement of the celiac branches is shown. (Courtesy of Dr. Stanley Laucks, Alpha Advanced CT, York, PA.)

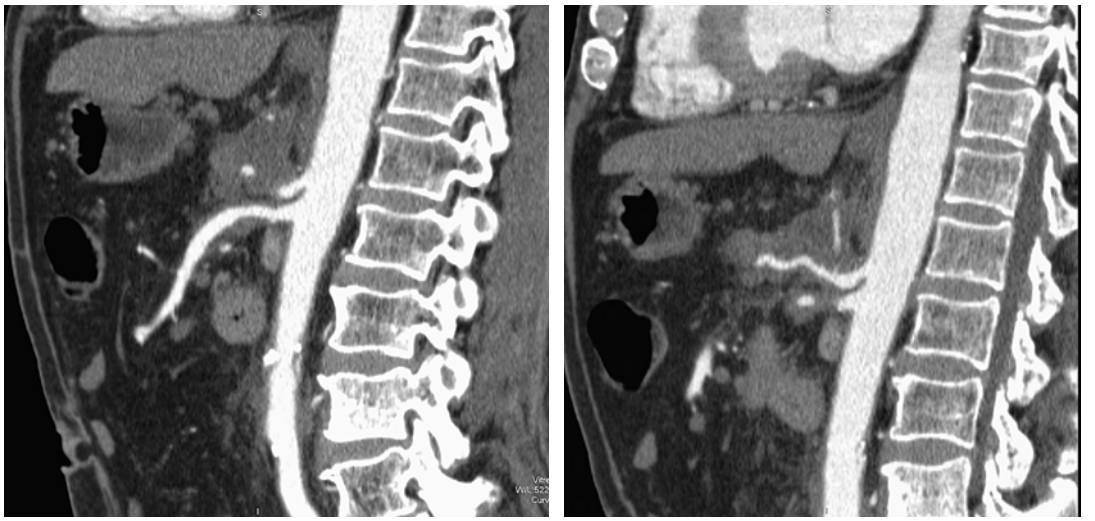

A B

Figure 11.4.2. (A and B) Curved sagittal images through the SMA and celiac arteries. The curved images show the circumferential encasement of the vessels by tumor. Mild narrowing and irregularity is also present. (Courtesy of Dr. Stanley Laucks, Alpha Advanced CT, York, PA.)

Figure 11.4.3. Additional vascular evaluation with segmented volume-rendered image. Note the irregular narrowing of both the celiac and SMA vessels. (Courtesy of Dr. Stanley Laucks, Alpha Advanced CT, York, PA.)

avoided if complete resection is not possible. Findings that preclude surgery include liver, lymph node, and peritoneal metastasis, as well as vascular invasion. Unfortunately, imaging studies, including MDCT, are relatively insensitive to micrometastasis to liver, nodes, and peritoneum. Multidetector CT has been shown, however, to be accurate for the diagnosis of vascular encasement when thin sections and a dual phase protocol are used.

The CT scans of patients with pancreatic cancer must be carefully scrutinized for signs of vascular invasion. This assessment is greatly improved by reviewing not only axial but also multiplanar and curved reconstructions. Curved planar reconstructions along the course of the pancreatic duct, celiac artery, SMA, and superior mesenteric vein (SMV) can improve diagnostic accuracy. Criteria for vacular invasion includes tumor encasement of any of the major peripancreatic vessels that exceeds one half of the circumference of the vessel. Encasement of less than one half of the circumference is indeterminate but can still be associated with unresectability of the tumor. Invasion of the SMV may not exclude patients for surgery at some centers and is surgeon dependent.

In this patient, gross vascular invasion was present, and he was clearly not a surgical candidate. Curved planar and MIP images were used to demonstrate the irregularity of the invaded vessels. Three-dimensional volume-rendered images can also be created. These images are particularly useful if the patient is a surgical candidate and resection of the pancreas is planned.

Case 11.5: Small Bowel Obstruction (Three Patients)

Clinical Information

All three patients arrived at the emergency room with abdominal pain and vomiting. Patient 1 had a known history of Crohn's disease, but the other two patients had no relevant past medical history. None of the patients had prior surgery.

Postprocessing Techniques Used and Approach

Multiplanar reconstructions are produced on the scan console (Table 11.5 and Figures 11.5.1 through 11.5.3).

Table 11.5. Scan Acquisition Parameters for Case 11.5, Small Bowel Obstruction

Slice No. and Thickness	**16 × 1.0 mm**
Coverage	**Abdomen and pelvis**
Helical Pitch	**1.25:1**
Rotation Speed	**0.5 sec**
Dose Parameters	**120 kVp, 150 mAs–200 mAs**
Contrast Dose	**100 mL Omnipaque 350**
Injection Rate	**2 mL/sec**
Bolus Timing Method	**70-sec delay**

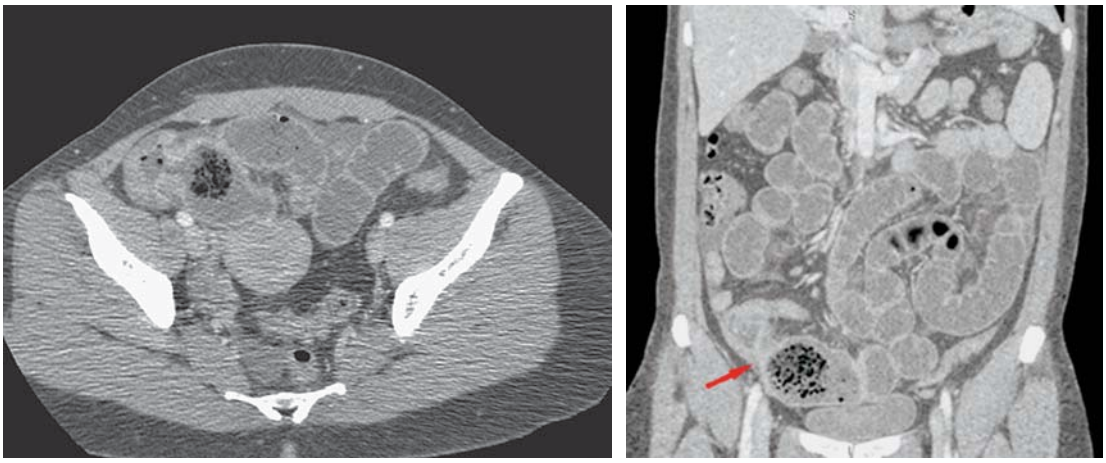

A B

Figure 11.5.1. (A and B) Patient 1: axial and coronal images through the abdomen. Multiple dilated, fluid-filled loops of small bowel are present. In the right lower quadrant there is a focal segment of abnormal ileum with narrowing of the lumen and wall thickening (arrow). There is also increased contrast enhancement secondary to acute inflammation. Note the small bowel feces sign immediately proximal to the point of obstruction and the decompressed small bowel immediately distal to the inflamed segment.

Diagnosis

Patient 1: inflammatory stricture of the ileum secondary to Crohn's disease causing small bowel obstruction (SBO). Patient 2: lymphoma of the ileum with SBO. Patient 3: incarcerated periumbilical hernia with SBO.

A B

Figure 11.5.2. (A and B) Patient 2: axial and coronal images through the abdomen. There are dilated loops of fluid-filled small bowel which end abruptly in a mass in the ileum (arrow) in the right lower quadrant. The point of obstruction is difficult to identify on the axial images but is easily seen on the coronal views.

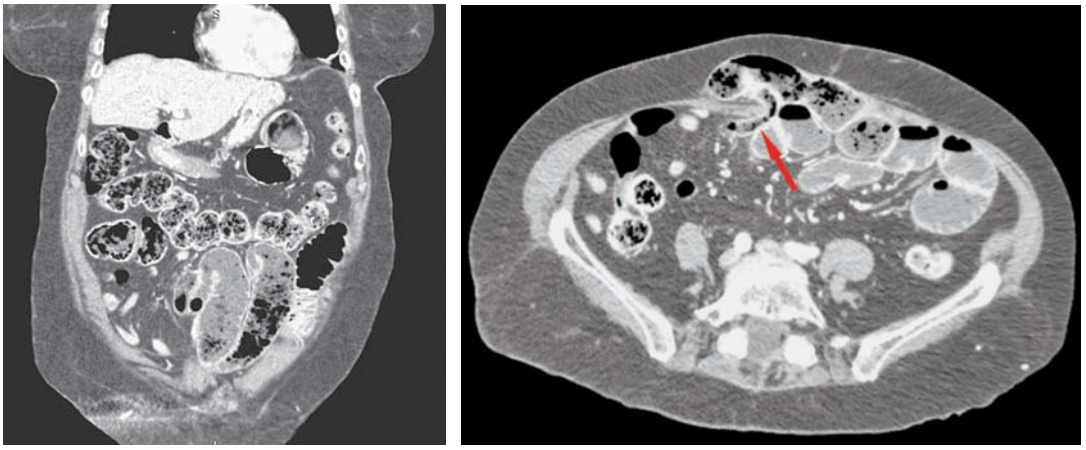

A B

Figure 11.5.3. (A and B) Patient 3: axial and coronal images through the abdomen. Coronal images again show dilated loops of small bowel in the left lower quadrant with the small bowel feces sign (stool is also present in the transverse colon above these loops). Axial image shows the incarcerated periumbilical hernia with the dilated, feces-containing loops of small bowel. Note the collapsed segment exiting from the hernia (arrow) and additional collapsed loops in the right lower quadrant.

Teaching Points

Many studies have demonstrated the superiority of CT in revealing the site, level, and cause of small bowel obstruction (SBO), and in demonstrating threatening signs of bowel ischemia. Computed tomography has proved useful in characterizing small bowel obstruction from many different etiologies, including extrinsic causes (adhesions, closed loop, strangulation, hernia, extrinsic masses and adjacent inflammatory processes), intrinsic causes (adenocarcinoma, Crohn's disease, tuberculosis, radiation enteropathy, intramural hemorrhage, intussusception), intraluminal causes (e.g., bezoars, gallstones), or intestinal malrotation. A CT examination is now widely utilized as the first-line diagnostic test for known or suspected bowel obstruction.

Much of this success has been achieved with axial images alone. The ability of current scanners to instantly produce high-quality multiplanar reconstructions has made the diagnosis significantly easier and faster. Coronal images are particularly well suited to help identify the site and etiology of the bowel obstruction. In many cases the findings are present on the axial images but are much more difficult to identify, whereas the key findings are much easier to perceive on coronal images. An experienced radiologist reviewing axial and multiplanar reconstructions can usually identify the level, and frequently the cause, of obstruction.

A CT scan for SBO should be performed with IV contrast whenever possible. Contrast administration may help show abnormal enhancement of bowel segments, intrinsic or extrinsic masses, and peritoneal abscess or inflammation. Oral contrast is not needed for patients with significant obstruction. The bowel in these patients is generally fluid

filled, and this provides excellent CT contrast. For patients with mild or partial obstruction, oral water-soluble contrast can be helpful.

A CT diagnosis of SBO depends on identification of dilated proximal bowel and collapsed distal bowel. In general, small bowel with a caliber greater than 2.5 cm is considered dilated. Identification of a transition zone between dilated and nondilated bowel is very important and will confirm both the diagnosis and location of obstruction. The "small bowel feces" sign is demonstrated as gas bubbles mixed with particulate matter in dilated small bowel loops proximal to an obstruction. This sign is not always present, but it is a reliable indicator of small bowel obstruction when seen, and can often help pinpoint the precise site of obstruction. In contrast, when no transition zone is present, and there is distension of the entire small bowel without colonic collapse, the most probable diagnosis is an adynamic ileus.

Case 11.6: Tracheal Carcinoma

Clinical Information

A 39-year-old woman with hemoptysis.

Postprocessing Techniques Used and Approach

Standard multiplanar reconstructions are reviewed (Table 11.6 and Figures 11.6.1 through 11.6.3). In addition, an endoluminal virtual bronchoscopy is performed on the workstation to demonstrate the tracheal mass and show bronchial anatomy.

Diagnosis

Tracheal carcinoma with mediastinal adenopathy and pulmonary hemorrhage.

Teaching Points

Routine CT images are adequate for evaluating many airway abnormalities, but they do have several limitations. Axial images have a limited ability to detect airway stenosis and will often underestimate the craniocaudal extent of airway disease. They also have difficulty displaying complex 3D relationships of the airways, particularly airways that are oriented obliquely to the axial plane.

Table 11.6. Scan Acquisition Parameters for Case 11.6, Tracheal Carcinoma

Slice No. and Thickness	**16 × 0.5 mm**
Coverage	**Chest**
Helical Pitch	**1.25:1**
Rotation Speed	**0.5 sec**
Dose Parameters	**120 kV, 200 mAs**
Contrast Dose	**None**

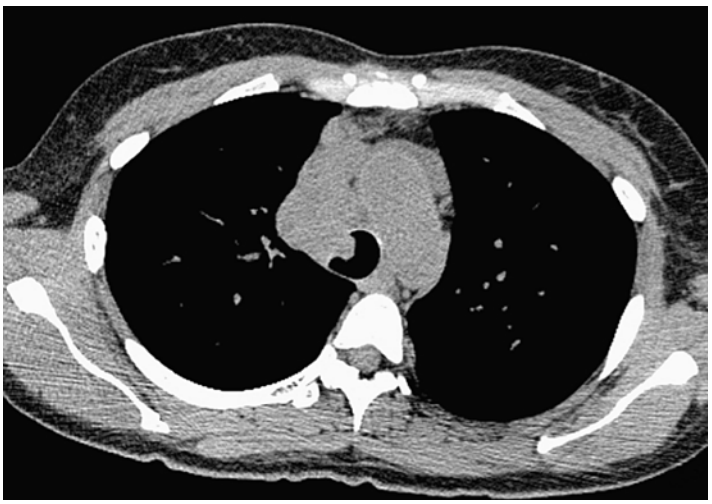

Figure 11.6.1. Axial 3-mm image through the mediastinum. There is paratracheal adenopathy present. A polypoid mass is projecting into the lumen of the trachea.

Multiplanar and 3D reconstructions offer many benefits for the evaluation of the trachea and central airways. They provide a more anatomically relevant display of complex structures such as the airways. The visual accessibility of these images allows for improved diagnostic confidence of interpretation as well as for improved planning for bronchoscopy and surgery. It also allows for better communication among radiologists and referring doctors.

The MPR image review was very helpful in this case to identify the tracheal mass. The coronal images were also useful for planning bron-

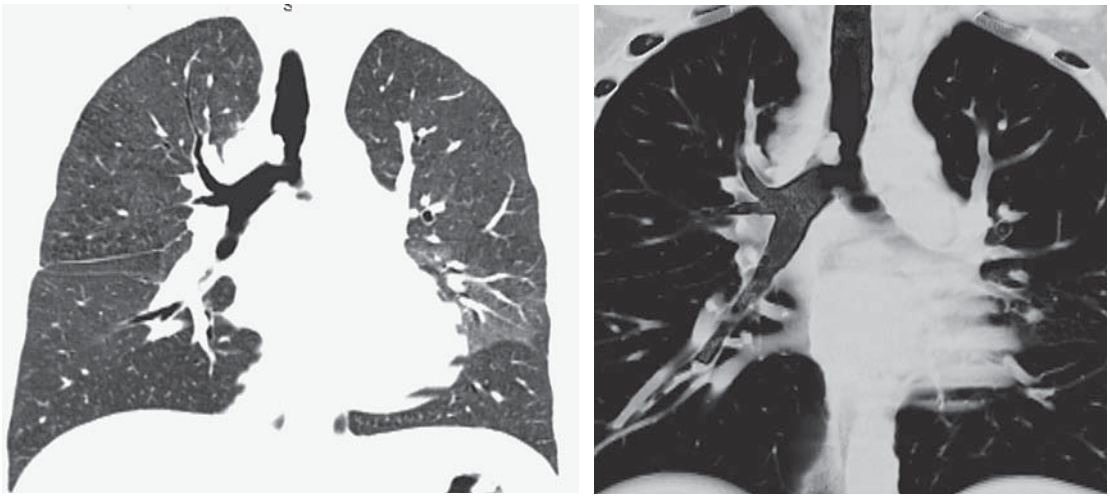

A

Figure 11.6.2. (A and B) Coronal MPR in lung window and 10-mm thick 3D volume-rendered image. The tracheal mass is much better shown on the coronal and volume reconstructions. In addition, the lung window image demonstrates ground glass opacity in the left lower lobe representing aspirated blood.

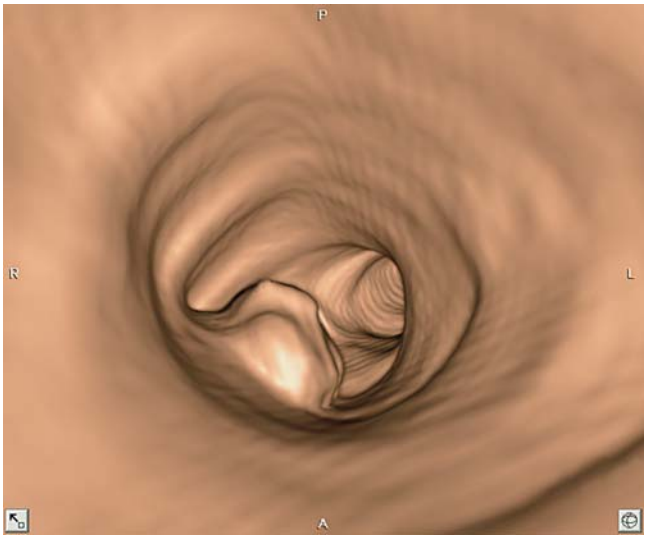

Figure 11.6.3. Spot image from an endoluminal virtual bronchoscopy examination. The polypoid tracheal mass is well shown with the carina and left main bronchus in the background.

choscopy and subsequently radiation therapy. The virtual bronchoscopy examination performed here generated amazing images but was not necessary for diagnosis or treatment planning. In other cases it can be useful to demonstrate plaque-like mass lesions or show bronchial anatomy.

Tracheal cancer is uncommon. Squamous cell carcinoma is the most common subtype, with adenoid cystic carcinoma the second most common type.

Case 11.7: Ureteral Stricture

Clinical Information

A 48-year-old woman with a history of multiple urinary tract stones. She has had indwelling stents in her right ureter on multiple occasions for stone disease and obstruction during lithotripsy treatment. She now has increasing flank pain on the right side and right hydronephrosis by ultrasound.

Postprocessing Techniques Used and Approach

Multiplanar reconstructions are performed on the scan console. Maximum intensity projection images and curved planar reconstructions through the right ureter are performed on the workstation (Table 11.7 and Figures 11.7.1 through 11.7.3).

Diagnosis

Inflammatory stricture of the right ureter related to stone disease and prior stent placement.

Table 11.7. Scan Acquisition Parameters for Case 11.7, Ureteral Stricture

Slice No. and Thickness	**16 × 1.0 mm**
Coverage	**Abdomen and pelvis**
Helical Pitch	**1.25:1**
Rotation Speed	**0.5 sec**
Dose Parameters	**120 kVp, 200 mAs**
Contrast Dose	**100 mL Omnipaque 350**
Injection Rate	**2 mL sec**
Bolus Timing Method	**Initial postcontrast scan at 70 sec, delayed phase scan at 5 min (compression study not done secondary to known hydronephrosis)**

Figure 11.7.1. Axial 3-mm image from a delayed phase of a complete CT urogram study. Marked right hydronephrosis and hydroureter is present. The left side is normal.

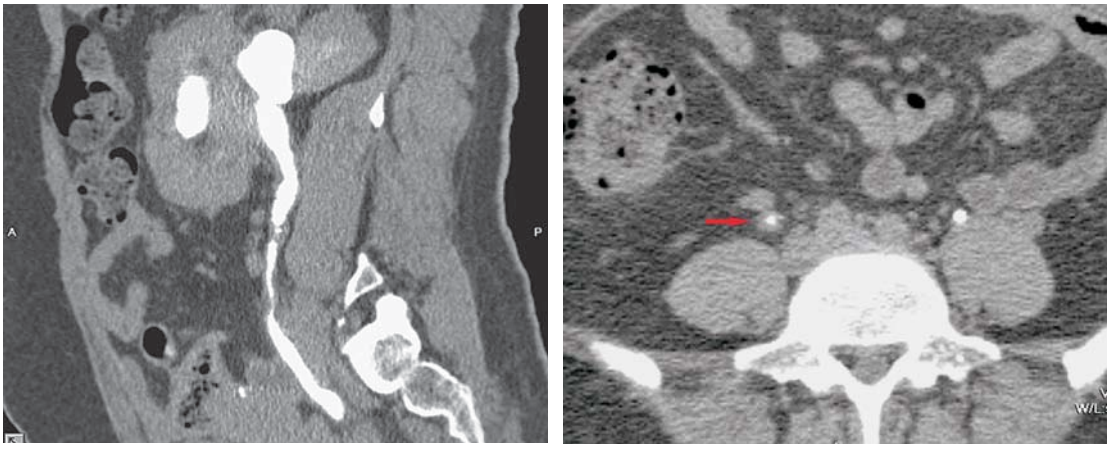

A B

Figure 11.7.2. (A and B) Axial 2-mm image through the mid right ureter and sagittal curved planar reconstruction through the ureter. There is significant irregular wall thickening of the ureter over a long segment with resultant narrowing of the ureter and partial obstruction (arrow).

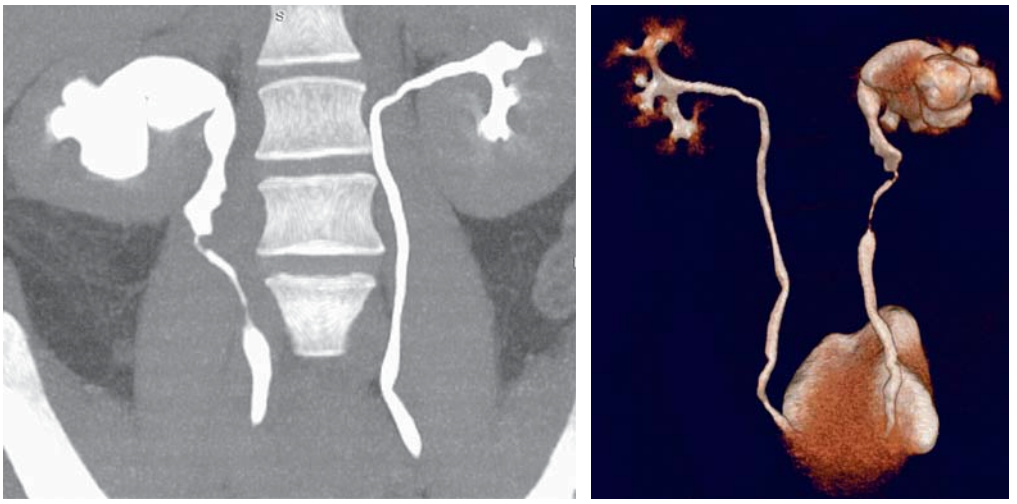

Figure 11.7.3. (A and B) Thick slab MIP image and posterior volume-rendered images of the ureters. The 3D images best show the position and length of the ureteral stricture as well as the degree of hydronephrosis and remaining urinary tract anatomy. The left side is normal.

Teaching Points

Noncontrast CT has clearly been established as the test of choice for evaluating patients with acute flank pain for the presence of urinary tract calculi. In addition, for patients undergoing evaluation for flank pain who do not have urinary tract disease, CT will frequently demonstrate the true cause of the patient's symptoms. A large variety of unsuspected pathology may be discovered, including examples such as diverticulitis, colitis, pancreatitis, appendicitis, abdominal aortic aneurysm, pelvic masses, hernias, bowel obstruction, and abdominal tumors.

Contrast-enhanced CT urography (CTU) has gained rapid acceptance as the study of choice for the evaluation of urinary tract pathology and hematuria. The CTU scan has been shown to successfully depict anatomic variants, stone disease, inflammatory processes, and benign and malignant neoplasms. It is an excellent modality for the evaluation of prospective renal donors. The sensitivity and specificity of CT far exceeds that of excretory urography (IVU) in virtually every area with the possible exception of small transitional cell tumors of the urothelium. Further study with MDCT will likely show that CT is at least as good as IVU for the diagnosis of transitional cell carcinoma (TCC), and is far superior at demonstrating stone disease, renal cell carcinoma, and other benign and malignant conditions.

Technique is very important for good quality CTU. I use a modified version of the protocol described by the Stanford group (Chow et al.). This protocol uses a split contrast injection and abdominal compression to distend the collecting system and requires only two scans

instead of three, minimizing radiation exposure. The first scan is a noncontrast study from the kidneys to the bladder. Second, 50 mL of IV contrast is injected, followed by a saline flush, and compression is applied to the abdomen with an abdominal binder (same as for traditional IVU). After waiting at least 3 min to 4 min, an additional 75 mL of contrast is injected at 1.5 mL/sec, followed by a 50-mL saline flush. The abdomen is scanned at a 70-sec delay with compression still on. Following this scan the compression is released after an additional 3-min to 4-min delay from the start of the second injection. The mid abdomen and pelvis are scanned immediately post release of compression. Coronal MPR and MIP reconstructions are generated from the postcontrast images.

Case 11.8: Polysplenia

Clinical Information

A 35-year-old woman who is imaged for abdominal pain.

Postprocessing Techniques Used and Approach

Routine axial and coronal images and MIP images are reviewed on the workstation. Coronal curved planar reconstruction is also done to better show the azygous continuation of the IVC (Table 11.8 and Figures 11.8.1 through 11.8.3).

Diagnosis

Polysplenia with situs ambiguous, and interruption of the IVC with azygous continuation.

Teaching Points

Polysplenia (left isomerism) or bilateral left-sidedness, was an incidental finding in this woman who was imaged for abdominal pain. Although the study was done with a routine protocol, all the major findings were demonstrated, including situs ambiguous (left heart and midline, transverse liver, right polysplenia, and right-sided stomach), multiple splenules, and IVC interruption with azygous continuation.

Table 11.8. Scan Acquisition Parameters for Case 11.8, Polysplenia

Slice No. and Thickness	**16 × 1.0 mm**
Coverage	**Abdomen and pelvis**
Helical Pitch	**1.25:1**
Rotation Speed	**0.5 sec**
Dose Parameters	**120 kVp, 110 mAs**
Contrast Dose	**100 mL Omnipaque 350**
Injection Rate	**2 mL/sec**
Bolus Timing Method	**Routine 70-sec delay**

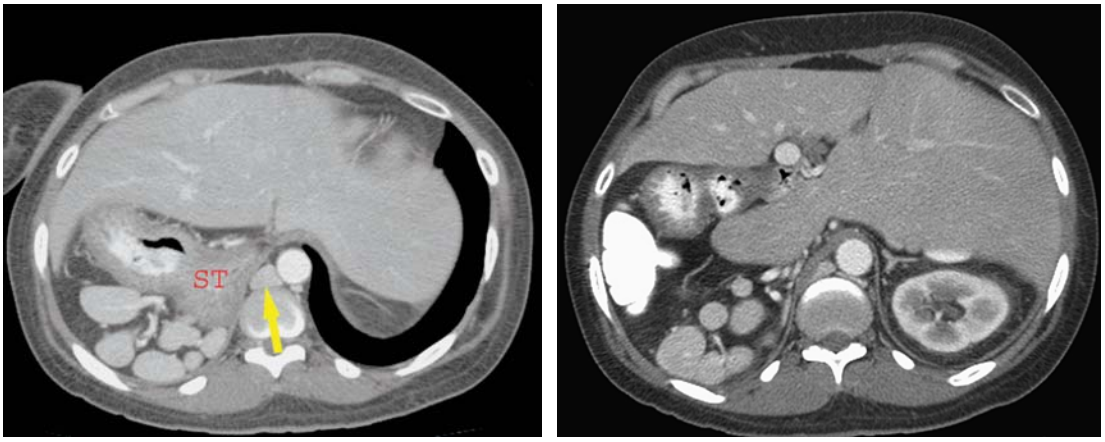

A B

Figure 11.8.1. (A and B) Axial 3-mm images show multiple splenules in the right upper quadrant. The stomach (ST) is on the right, and the liver is transverse and predominately on the left with mirror image morphology of the normal liver. The IVC is absent at these levels and there is a large azygous vein (arrow).

Polysplenia is a heterogeneous entity associated with situs ambiguous and an abnormal arrangement of the solid organs and bowel, as well as the presence of multiple spleens. Multiple other anomalies can be associated with polysplenia. The liver is usually midline, and there is frequently truncation or partial atresia of the pancreas. Gastrointestinal abnormalities include abnormalities of the stomach and bowel rotation. The stomach can be either left or right sided, and the small

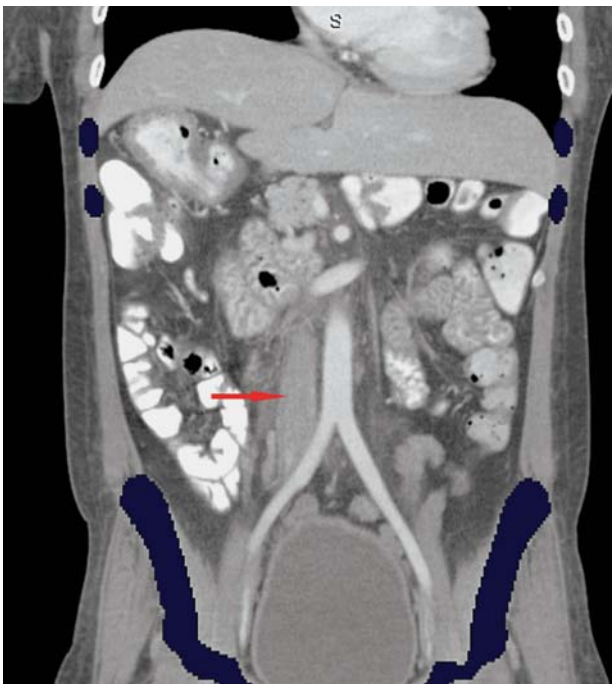

Figure 11.8.2. Coronal 3-mm image demonstrates the IVC in the lower abdomen (arrow), and the transverse liver. The heart is left-sided.

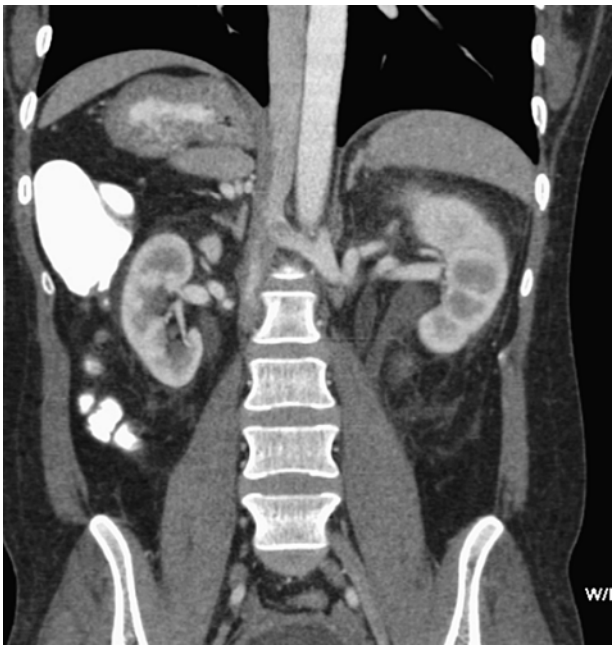

Figure 11.8.3. Coronal CPR along the azygous vein showing the left renal vein draining into the azygous vein.

bowel is predominantly right sided, with the colon predominantly left sided in most patients. Volvulus is a rare potential complication. Chest and cardiac abnormalities include hyparterial bronchi, double SVC, congenital heart disease (atrial septal defect, ventricular septal defect, double outlet right ventricle), and partial anomalous venous return. Congenital heart disease, when present, is mild in most patients.

Various imaging studies, including MRI, US, nuclear medicine (NM), and venography have been advocated for evaluation of the multiple anomalies. I believe that current MDCT offers the best evaluation of the multiple anomalies in a single test. Both soft tissue and vascular lesions can be easily demonstrated in a single examination.

Case 11.9: Gastric Cancer

Clinical Information

A 60-year-old man arrives at the emergency room with acute onset of severe abdominal pain. Peritonitis is suspected on physical examination.

Postprocessing Techniques Used and Approach

Only routine multiplanar images are generated on the scan console, with no additional processing (Table 11.9 and Figures 11.9.1 through 11.9.3).

Diagnosis

Perforated gastric cancer with peritoneal metastasis.

Table 11.9. Scan Acquisition Parameters for Case 11.9, Gastric Cancer

Slice No. and Thickness	16 × 1.0 mm
Coverage	Abdomen and pelvis
Helical Pitch	1.25:1
Rotation Speed	0.5 sec
Dose Parameters	120 kVp, 145 mAs
Contrast Dose	100 mL Omnipaque 350
Injection Rate	2 mL/sec
Bolus Timing Method	70-sec delay

Figure 11.9.1. A 3-mm axial image through the stomach. There is a large amount of free intraperitoneal air present. There is also a mass present in the body of the stomach. Also notice the infiltration of the fat anterior to the stomach and a small amount of fluid in Morison's pouch. Initial review of the axial images does not clearly show the site of perforation.

Figure 11.9.2. Coronal 2-mm image shows a peritoneal mass lateral to the splenic flexure of the colon (arrow).

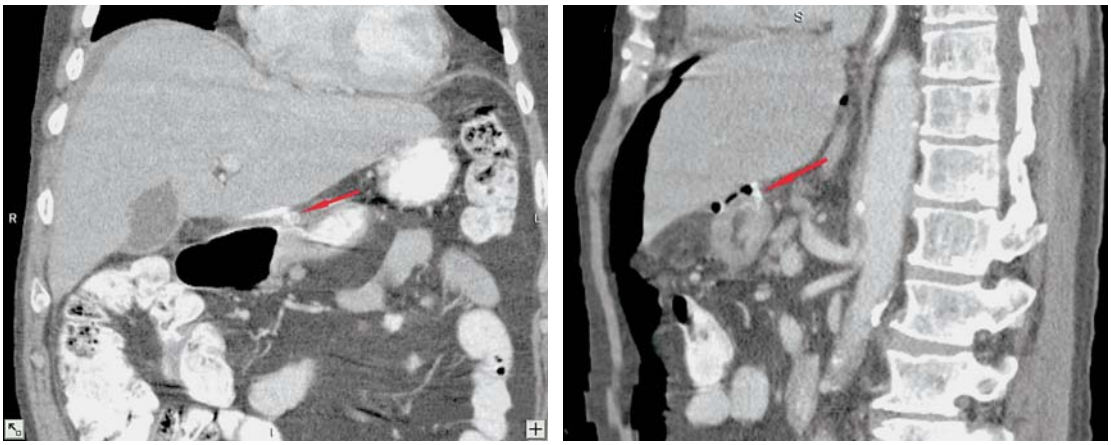

Figure 11.9.3. (A and B) Coronal and sagittal 2-mm reformations focused on the stomach. Both the coronal and sagittal images demonstrate a linear tract of oral contrast leaking through a small perforation in the wall of the stomach (arrows). This very small leak was much better seen on the coronal and sagittal images than on the axial images.

Teaching Points

This case illustrates the benefit of routine multiplanar image review. Coronal image review allowed for rapid identification of the major findings in this case, including the gastric mass, the site of perforation with a small collection of extravasated oral contrast, and the peritoneal metastatic disease. Although these findings are present on the axial images, they are more difficult to perceive and therefore are more easily missed. No additional postprocessing was needed on this case. Multiplanar reconstructions can be created routinely on the scanner console or PACS workstation.

Multidetector CT can be an excellent modality for evaluation of gastric pathology. Proper distention of the stomach is very important if gastric pathology is suspected. Water is the preferred oral contrast agent and carbon dioxide granules can also be given immediately prior to the scan. On occasion it can be helpful to obtain both supine and prone, or decubitus, images.

Gastric cancer has a peak prevalence between 50 years and 70 years of age and remains a deadly disease, with overall 5-year survival rates of less than 20%. However, early gastric cancers are curable lesions, with 5-year survival rates of more than 90%. It is important to identify evidence for transmural tumor invasion (T3 lesion) which significantly reduces prognosis. In transmural extension, the serosal contour becomes blurred, and strand-like areas of increased attenuation may be seen extending into the perigastric fat. Metastatic spread to lymph nodes is commonly found in gastric carcinoma, seen in approximately 74% to 88% of patients. Additional common sites of metastasis include the peritoneum, omentum, lung, liver, adrenal glands, and ovaries.

Table 11.10. Scan Acquisition Parameters for Case 11.10, Pancreatitis With Splenic Vein Thrombosis

Slice No. and Thickness	**16 × 1.0 mm**
Coverage	**Abdomen and pelvis**
Helical Pitch	**1.25:1**
Rotation Speed	**0.5 sec**
Dose Parameters	**120 kVp, 100 mAs**
Contrast Dose	**100 mL/sec Omnipaque 350**
Injection Rate	**2 mL/sec**
Bolus Timing Method	**70-sec delay**

Case 11.10: Pancreatitis With Splenic Vein Thrombosis

Clinical Information

A 53-year-old woman arrives at the emergency department with severe abdominal pain, vomiting and anorexia. Routine abdominal CT is performed.

Postprocessing Techniques Used and Approach

Standard multiplanar review of the case provided much information (Table 11.10 and Figures 11.10.1 through 11.10.4). Curved planar reformations through the pancreas were used to better demonstrate the irregular pancreatic duct dilatation. Coronal MIP images with a 20-mm slab were used to confirm the diagnosis of splenic vein thrombosis. The volume images better show the many collateral vessels that are present. Segmentation was not absolutely needed in this case, but a very quick automatic bone removal was done to better show the anatomy, particularly all the collateral vessels.

Diagnosis

Acute pancreatitis with multiple pseudocyst formation and splenic vein thrombosis.

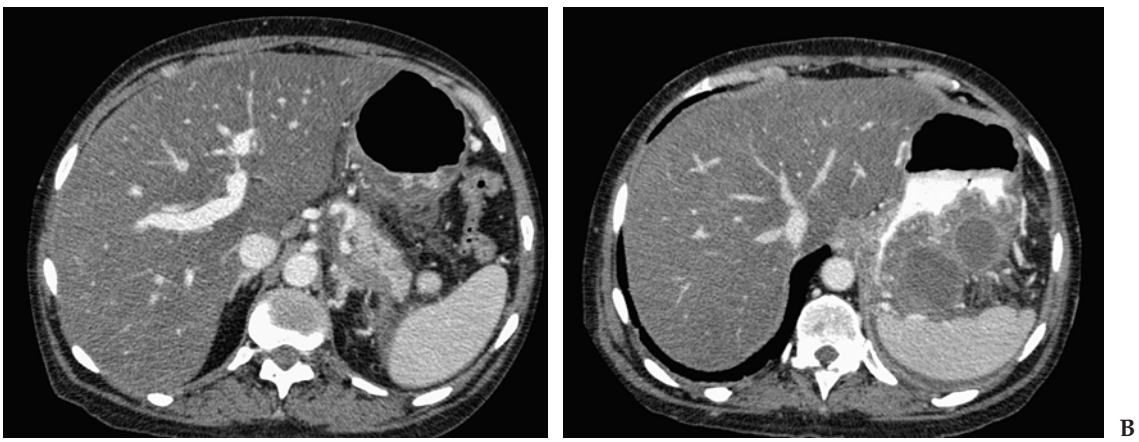

A B

Figure 11.10.1. (A and B) Axial 3-mm images demonstrate acute pancreatitis with peripancreatic inflammatory changes. Two pseudocysts are present in the lesser sac involving the greater curvature of the stomach.

Figure 11.10.2. Coronal curved planar reformation. Irregular dilatation of the pancreatic duct related to pancreatitis is best seen on the curved reconstruction. Pseudocyst in the lesser sac is again shown, and an additional small pseudocyst in the pancreatic head is present.

Teaching Points

The diagnosis of acute pancreatitis with pseudocyst formation could be made easily from the standard axial and coronal images. Splenic vein thrombosis is more difficult to appreciate on the axial images but was suggested by the coronal reconstructions. This suspicion prompted further review on the workstation. Maximum intensity projection images were done which clearly demonstrated the thrombosed splenic vein. This is also very well shown on volume-rendered images, but in addition, the multiple collateral vessels are more easily appreciated, particularly after a quick automated segmentation to remove the spine.

Splenic vein thrombosis is a known but somewhat rare complication of pancreatitis. In this case the diagnosis may have been missed if axial images alone were reviewed. This case demonstrates several different benefits of postprocessing for abdominal imaging. The volume and

Figure 11.10.3. A 20-mm thick MIP image through the mesenteric venous confluence. Occlusion of the splenic vein is present with patent portal and superior mesenteric veins. Review of the entire volume is needed to confidently diagnose splenic vein thrombosis.

A B

Figure 11.10.4. (A and B) Unsegmented and segmented volume-rendered images demonstrate the absent (occluded) splenic vein. In addition, there are multiple gastric and perisplenic collateral veins seen. A large perisplenic collateral is noted to enter the SMV. The segmented image allows better visualization of the collateral veins.

MIP images are used to better show the major abdominal veins, whereas curved planar reconstructions are done to evaluate the pancreas and demonstrate ductal dilatation.

Case 11.11: Crossed-Fused Renal Ectopia With Ureteropelvic Junction Obstruction

Clinical Information

A 16-year-old girl with known hydronephrosis and renal ectopia diagnosed by ultrasound and retrograde pyelogram. She is referred for CTA to evaluate the kidney and look at the arterial anatomy.

Postprocessing Techniques Used and Approach

Because of the complex anatomy, the kidney is best evaluated using curved planar and volume-rendered reconstructions (Table 11.11 and Figures 11.11.1 through 11.11.5). Automated segmentation is used to

Table 11.11. Scan Acquisition Parameters for Case 11.11, Crossed-Fused Renal Ectopia with Ureteropelvic Junction Obstruction

Slice No. and Thickness	**16 × 0.5 mm**
Coverage	**Abdomen and pelvis**
Helical Pitch	**1.25:1**
Rotation Speed	**0.5 sec**
Dose Parameters	**120 kVp, 150 mAs**
Contrast Dose	**75 mL**
Injection Rate	**4 mL/sec**
Bolus Timing Method	**Bolus triggering on the aorta**

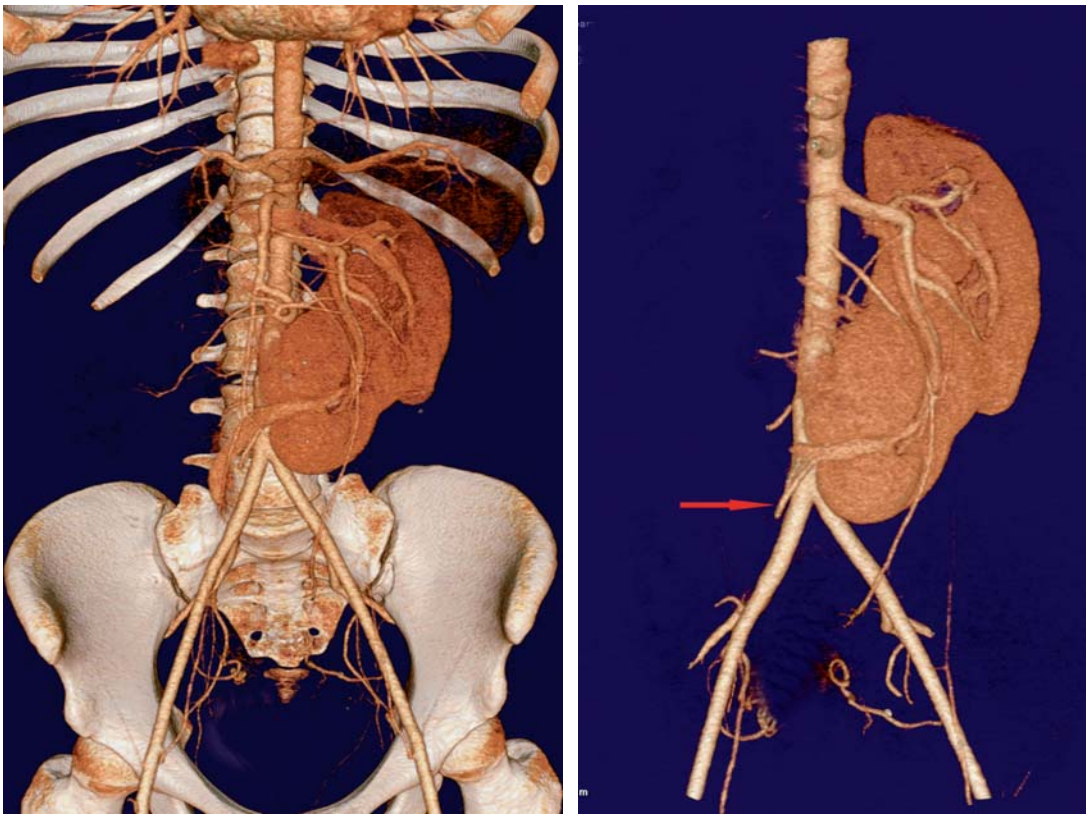

A B

Figure 11.11.1. (A and B) Volume-rendered images with and without segmentation. The segmented image has the osseous structures and renal veins removed to better show the arterial anatomy. The left (orthotopic) kidney is in the left renal fossa but malrotated. The right (ectopic) kidney is crossed to the left side and fused to the inferior pole of the left kidney. The unsegmented image demonstrates the renal veins. The segmented image shows the dominant left renal artery and the smaller right renal artery that initially extends to the right then makes a hairpin turn to cross over to the left (arrow). The inferior mesenteric artery (IMA) is draped over the kidney.

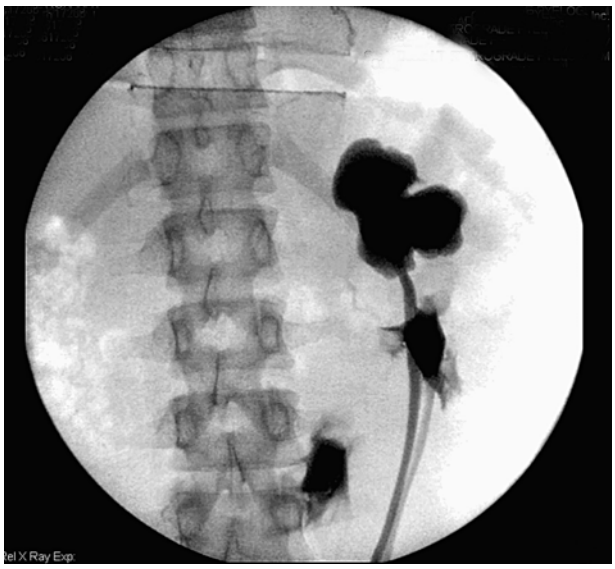

Figure 11.11.2. Spot image from a retrograde study of the ureters. The left kidney is duplicated with a UPJ obstruction of the upper pole moiety. The right (ectopic) ureter originated from the right trigone in the bladder.

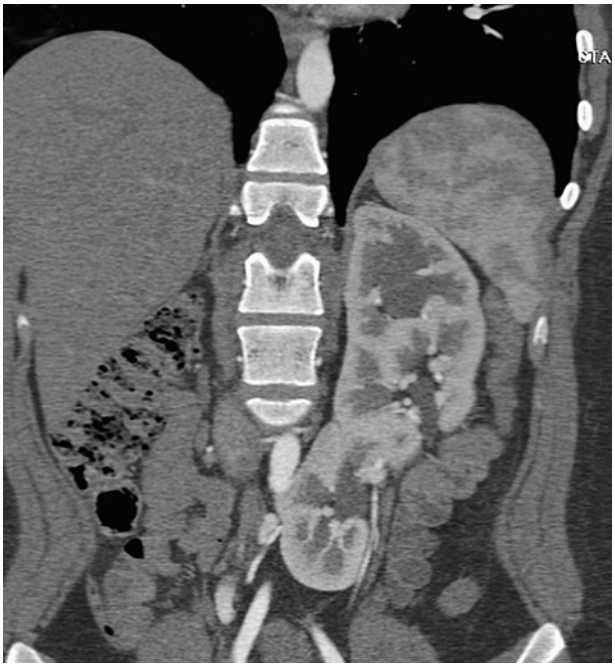

Figure 11.11.3. Curved planar reconstruction of the fused kidney. Curved image allows visualization of the entire kidney on one picture. Hydronephrosis of the upper pole is seen.

remove the osseous structures. Manual sculpting from the 3D images is performed to remove the SMA and celiac arteries and the renal veins. This is done to better show the renal arteries on the volume-rendered images.

Diagnosis

Crossed-fused renal ectopia. The left orthotopic kidney has a duplicated collecting system with a ureteropelvic junction (UPJ) obstruction of the upper pole moiety secondary to a crossing vessel.

Figure 11.11.4. Axial thin-slab MIP image. A branch of the left renal artery crosses immediately anterior to the dilated upper pole renal pelvis contributing to the UPJ obstruction.

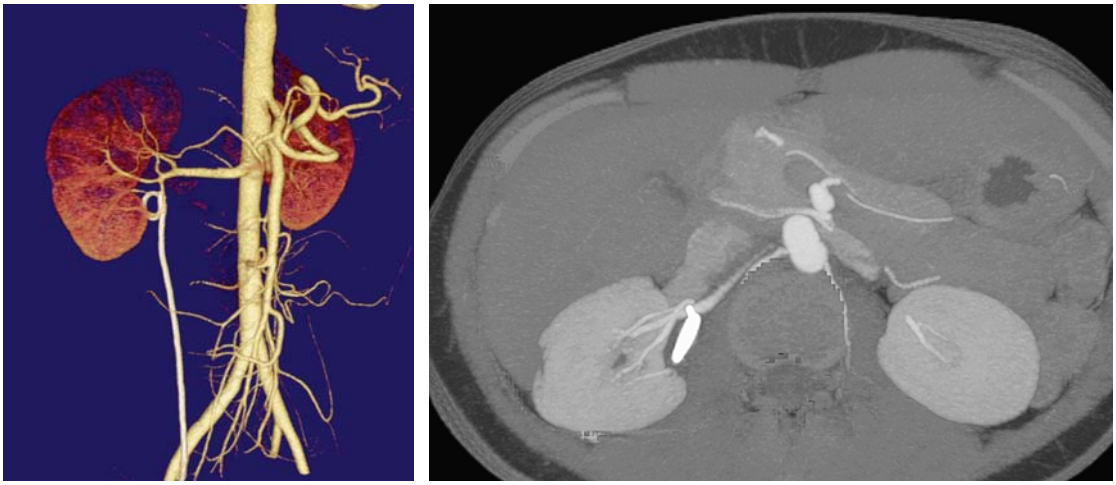

A B

Figure 11.11.5. (A and B) Volume-rendered and axial MIP images in a different patient with UPJ obstruction and a segmental lower pole crossing artery. A stent is present in the collecting system which is decompressed.

Teaching Points

Volumetric CT is an excellent test for evaluating congenital anomalies of the kidneys. Arterial and venous information can be easily obtained with a multiphase study, and correlated with high-quality imaging of the kidney and collecting systems. Crossed-fused ectopia is an uncommon anomaly; however, UPJ obstruction is quite common.

Extrinsic ureteropelvic junction obstruction due to anterior crossing segmental renal vessels is present in more than 50% of patients in adulthood. A CT scan is used in these patients to identify a crossing vessel that may be the cause of the obstruction. Endoscopic treatment of UPJ obstruction has a success rate that approaches 90%. These results drop to 40% in the presence of crossing vessels. Unrecognized crossing vessels can also result in significant hemorrhage during endopyelotomy.

Foreknowledge of a crossing vessel will likely change the surgical approach. Patients without crossing vessels may undergo primary endopyelotomy (endoscopic procedure), whereas patients with a crossing anterior vessel are better treated with laparoscopic dismembered pyeloplasty. In this procedure the ureter is dismembered and transposed anterior to the crossing vascular structures, where it is anastomosed to the renal pelvis.

In this patient a laparoscopic dismembered pyeloplasty was planned to treat the patient's UPJ obstruction. It was extremely helpful to the urologist to have precise knowledge of the vascular anatomy prior to the procedure. Multidetector CT is particularly well suited for this evaluation.

Selected Readings

Lung Cancer

1. Cerfolio RJ, Ojha B, Bryant AS, Raghuveer V, Mountz JM, Bartolucci AA. The accuracy of integrated PET-CT compared with dedicated PET alone for the staging of patients with nonsmall cell lung cancer. Ann Thorac Surg 2004 Sep;78(3):1017–1023.
2. Chern MS, Wu MH, Chang CY. CT and MRI for staging of locally advanced non-small cell lung cancer. Lung Cancer 2003 Dec;42(suppl 2):S5–S8.
3. Costello P. Thoracic helical CT. Radiographics 1994 Jul;14(4):913–918.
4. Lardinois D, Weder W, Hany TF, et al. Staging of non-small-cell lung cancer with integrated positron-emission tomography and computed tomography. N Engl J Med 2003 Jun;348(25):2487–2488.
5. Lawler LP, Fishman EK. Multi–detector row CT of thoracic disease with emphasis on 3D volume rendering and CT angiography. Radiographics 2001;21:1257–1273.
6. Schoepf UJ, Costello P. CT angiography for diagnosis of pulmonary embolism: state of the art. Radiology 2004 Feb;230(2):329–337.
7. Verschakelen JA, De Wever W, Bogaert J. Role of computed tomography in lung cancer staging. Curr Opin Pulm Med 2004 Jul;10(4):248–255.

Renal Cell Carcinoma

8. Catalano C, Fraioli F, Laghi A, et al. High-resolution multidetector CT in the preoperative evaluation of patients with renal cell carcinoma. Am J Roentgenol 2003;180:1271–1277.
9. Coll DM, Herts BR, Davros WJ, Uzzo RG, Novick AC. Preoperative use of 3D volume rendering to demonstrate renal tumors and renal anatomy. Radiographics 2000;20:431–438. Radiographics 2000;20:431–438.
10. Desser TS, Sommer FG, Jeffrey RB Jr. Value of curved planar reformations in MDCT of abdominal pathology. Am J Roentgenol 2004 June;182(6): 1477–1484.
11. Joffe SA, Servaes S, Okon S, Horowitz M. Multi–detector row CT urography in the evaluation of hematuria. Radiographics 2003;23:1441–1455.
12. Sheth S, Scatarige JC, Horton KM, Corl FM, Fishman EK. Current concepts in the diagnosis and management of renal cell carcinoma: role of multidetector CT and three-dimensional CT. Radiographics 2001;21[suppl]: 237S–254S.
13. Tunaci A, Yekeler E. Multidetector row CT of the kidneys. Eur J Radiol 2004 Oct;52(1):56–66.
14. Urban BA, Lloyd E. Ratner LE, Fishman EK. Three-dimensional volume-rendered CT angiography of the renal arteries and veins: normal anatomy, variants, and clinical applications. Radiographics 2001;21:373–386.

CT Colonography

15. Cotton PB, Durkalski VL, Pineau BC, et al. Computed tomographic colonography (virtual colonoscopy): a multicenter comparison with standard colonoscopy for detection of colorectal neoplasia. JAMA 2004;291:1713–1719.
16. Gluecker TM, Johnson CD, Harmsen WS, et al. Colorectal cancer screening with CT colonography, colonoscopy, and double-contrast barium enema

examination: prospective assessment of patient perceptions and preferences. Radiology 2003;227:378–384.
17. Macari M, Bini EJ, Xue X, et al. Colorectal neoplasms: prospective comparison of thin-section low-dose multi-detector row CT colonography and conventional colonoscopy for detection. Radiology 2002;224:383–392.
18. Pickhardt PJ, Choi JR, Hwang I, et al. CT virtual colonoscopy to screen for colorectal neoplasia in asymptomatic adults. N Engl J Med 2003;349: 2191–2200.
19. van Gelder RE, Venema HW, Florie J, et al. CT colonography: feasibility of substantial dose reduction—comparison of medium to very low doses in identical patients. Radiology 2004;232:611–620.
20. Yee J, Akerkar GA, Hung RK, Steinauer-Gebauer AM, Wall SD, McQuaid KR. Colorectal neoplasia: performance characteristics of CT colonography for detection in 300 patients. Radiology 2001;219:685–692.

Pancreatic Cancer

21. Catalano C, Laghi A, Fraioli F, et al. Pancreatic carcinoma: the role of high-resolution multislice spiral CT in the diagnosis and assessment of resectability. Eur Radiol 2003;13:149–156.
22. Foley WD. Special focus session: multidetector CT: abdominal visceral imaging. Radiographics 2002;22:701–719.
23. Horton KM, Fishman EK. Multidetector CT angiography of pancreatic carcinoma: part I, evaluation of arterial involvement. Am J Roentgenol 2002 Apr;178:827–831.
24. McNulty NJ, Francis IR, Platt JF, Cohan RH, Korobkin M, Gebremariam A. Multidetector-row helical CT of the pancreas: effect of contrast-enhanced multiphasic imaging on enhancement of the pancreas, peripancreatic vasculature, and pancreatic adenocarcinoma. Radiology 2001;220: 97–102.
25. Nino-Murcia M, Jeffrey RB Jr, Beaulieu CF, Li KC, Rubin GD. Multidetector CT of the pancreas and bile duct system: value of curved planar reformations. Am J Roentgenol 2001;176:689–693.
26. Valls C, Andía E, Sanchez A, Fabregat J, Pozuelo O, Quintero JC, et al. Dual-phase helical CT of pancreatic adenocarcinoma: assessment of resectability before surgery. Am J Roentgenol 2002 Apr;178:821–826.
27. Vargas R, Nino-Murcia M, Trueblood W, and Jeffrey RB Jr. MDCT in pancreatic adenocarcinoma: prediction of vascular invasion and resectability using a multiphasic technique with curved planar reformations. Am J Roentgenol 2004 Feb;182:419–425.

Small Bowel Obstruction

28. Boudiaf M, Soyer P, Terem C, et al. CT evaluation of small bowel obstruction. Radiographics 2001;21:613–624.
29. Caoili EM, Paulson EK. CT of small-bowel obstruction: another perspective using multiplanar reformations. Am J Roentgenol 2000 Apr;174: 993–998.
30. Furukawa A, Yamasaki M, Furuichi K, et al. Helical CT in the diagnosis of small bowel obstruction. Radiographics 2001;21:341–355.
31. Lazarus DE, Slywotsky C, Bennett GL, Megibow AJ, Macari M. Frequency and relevance of the "small-bowel feces" sign on CT in patients

with small-bowel obstruction. Am J Roentgenol 2004 Nov;183:1361–1366.
32. Obuz F, Terzi C, Sokmen S, Yilmaz E, Yildiz D, Fuzun M. The efficacy of helical CT in the diagnosis of small bowel obstruction. Eur J Radiol 2003 Dec;48(3):299–304.

Tracheal Carcinoma

33. Boiselle PM, Reynolds KF, Ernst A. Multiplanar and three-dimensional imaging of the central airways with multidetector CT. Am J Roentgenol 2002 Aug;179:301–308.
34. Boiselle PM. Multislice helical CT of the central airways. Radiol Clin North Am 2003 May;41(3):561–574.
35. Ferretti GR, Bricault I, Coulomb M. Helical CT with multiplanar and three-dimensional reconstruction of nonneoplastic abnormalities of the trachea. J Comput Assist Tomogr 2001 May–Jun;25(3):400–406.
36. Revel MP, Fournier LS, Hennebicque AS, et al. Can CT replace bronchoscopy in the detection of the site and cause of bleeding in patients with large or massive hemoptysis? Am J Roentgenol 2002 Nov;179:1217–1224.
37. Zeiberg AS, Silverman PM, Sessions RB, Troost TR, Davros WJ, Zeman RK. Helical (spiral) CT of the upper airway with three-dimensional imaging: technique and clinical assessment. Am J Roentgenol 1996 Feb;166(2): 293–299.

Ureteral Stricture

38. Caoili EM, Cohan RH, Ellis JH, Korobkin M, Platt JF, Francis IR. Experience with multidetector CT urography (MDCTU) in 370 patients [abstract]. Am J Roentgenol 2003;180(suppl):71.
39. Chow LC, Sommer FG. Multidetector CT urography with abdominal compression and three-dimensional reconstruction. Am J Roentgenol 2001 Oct;177:849–855.
40. Joffe SA, Servaes S, Okon S, Horowitz M. Multi–detector row CT urography in the evaluation of hematuria. Radiographics 2003;23:1441–1455.
41. Kawashima A, Vrtiska TJ, LeRoy AJ, Hartman RP, McCollough CH, King BF Jr. CT urography. Radiographics 2004 Oct;24(suppl 1):S35–S54;discussion:S55–S58.
42. McTavish JD, Jinzaki M, Zou KH, et al. Multi–detector row CT urography: comparison of strategies for depicting the normal urinary collecting system. Radiology 2002;225:783–790.
43. Rydberg J, Kopecky KK, Tann M, et al. Evaluation of prospective living renal donors for laparoscopic nephrectomy with multisection CT: the marriage of minimally invasive imaging with minimally invasive surgery. Radiographics 2001;21:S223–S236.
44. Sheth S, Fishman EK. Multi-detector row CT of the kidneys and urinary tract: techniques and applications in the diagnosis of benign diseases. Radiographics 2004 Mar;24(2):e20.

Polysplenia

45. Applegate KE, Goske MJ, Pierce G, Murphy D. Situs revisited: imaging of the heterotaxy syndrome. Radiographics 1999 Jul–Aug;19(4):837–852; discussion:853–854.

46. Bass JE, Redwine MD, Kramer LA, Huynh PT, Harris JH Jr. Spectrum of congenital anomalies of the inferior vena cava: cross-sectional imaging findings. Radiographics 2000;20:639–652.
47. Fulcher AS, Turner MA. Abdominal manifestations of situs anomalies in adults. Radiographics 2002;22:1439–1456.
48. Hernanz-Schulman M, Ambrosino MM, Genieser NB. Pictorial essay. Current evaluation of the patient with abnormal visceroatrial situs. Am J Roentgenol 1990;Apr;154(4):797–802.

Gastric Cancer

49. Ba-Ssalamah A, Prokop M, Uffmann M, Pokieser P, Teleky B, Lechner G. Dedicated multidetector CT of the stomach: spectrum of diseases. Radiographics 2003;23:625–644.
50. Habermann CR, Weiss F, Riecken R, et al. Preoperative staging of gastric adenocarcinoma: comparison of helical CT and endoscopic US. Radiology 2004;Feb;230(2):465–471.
51. Harris JP, Nelson RC. Abdominal imaging with multidetector computed tomography: state of the art. J Comput Assist Tomogr 2004 Jul–Aug; 28(suppl 1):S17–S19.
52. Insko EK, Levine MS, Birnbaum BA, Jacobs J. Benign and malignant lesions of the stomach: evaluation of CT criteria for differentiation. Radiology 2003 Jul;228(1):166–171.
53. Macari M, Balthazar EJ. CT of bowel wall thickening: significance and pitfalls of interpretation. Am J Roentgenol 2001;176:1105–1116.

Pancreatitis With Splenic Vein Thrombosis

54. Balthazar EJ. Staging of acute pancreatitis. Radiol Clin North Am 2002 Dec;40(6):1199–1209.
55. Desser TS, Sommer FG, Jeffrey RB Jr. Value of curved planar reformations in MDCT of abdominal pathology. Am J Roentgenol 2004 June;182(6): 1477–1484.
56. Harris JP, Nelson RC. Abdominal imaging with multidetector computed tomography: state of the art. J Comput Assist Tomogr 2004 Jul–Aug; 28(suppl 1):S17–S19.
57. Nino-Murcia M, Jeffrey RB Jr, Beaulieu CF, Li KC, Rubin GD. Multidetector CT of the pancreas and bile duct system: value of curved planar reformations. Am J Roentgenol 2001;176:689–693.
58. Vargas R, Nino-Murcia M, Trueblood W, and Jeffrey RB Jr. MDCT in pancreatic adenocarcinoma: prediction of vascular invasion and resectability using a multiphasic technique with curved planar reformations. Am J Roentgenol 2004 Feb;182:419–425.

Crossed-Fused Renal Ectopia With Ureteropelvic Junction Obstruction

59. Coll DM, Herts BR, Davros WJ, Uzzo RG, Novick AC. Preoperative use of 3D volume rendering to demonstrate renal tumors and renal anatomy. Radiographics 2000;20:431–438.
60. Foley WD. Renal MDCT. Eur J Radiol 2003 Mar;45(suppl 1):S73–S78.
61. Herts BR. Helical CT and CT angiography for the identification of crossing vessels at the ureteropelvic junction. Urol Clin North Am 1998 May;25(2):259–269.

62. Khaira HS, Platt JF, Cohan RH, Wolf JS, Faerber GJ. Helical computed tomography for identification of crossing vessels in ureteropelvic junction obstruction—comparison with operative findings. Urology 2003 Jul; 62(1):35–39.
63. Rabah D, Soderdahl DW, McAdams PD, et al. Ureteropelvic junction obstruction: does CT angiography allow better selection of therapeutic modalities and better patient outcome? J Endourol 2004 Jun;18(5):427–430.
64. Tunaci A, Yekeler E. Multidetector row CT of the kidneys. Eur J Radiol 2004 Oct;52(1):56–66.

Chapter 12

Cardiac Imaging

Case 12.1: Coronary Calcium Screening

Clinical Information

A 59-year-old man with a history of hypertension and increased cholesterol level undergoing screening for coronary calcium.

Postprocessing Techniques Used and Approach

Axial data set is reconstructed at 3 mm and evaluated on the workstation (Table 12.1 and Figures 12.1.1 and 12.1.2). Foci of calcification in the coronary arteries are identified and circled to assign them to the appropriate artery. The computer performs automatic measurement of calcium score, and an automated but personalized report is generated (Table 12.2).

Diagnosis

Extensive coronary calcification.

Teaching Points

Coronary artery disease (CAD) remains the leading cause of death in the Western world. Unfortunately, death may be the initial event for patients with CAD. Screening for CAD is therefore of significant importance. Coronary calcium scoring has been used and researched for many years now. It started with electron beam CT (EBCT) but is now most often performed with MDCT scanners. With MDCT, patients are scanned with prospective ECG triggering using a partial scanner rotation to achieve improved temporal resolution. Reconstructions are relatively thick (2 mm to 3 mm) depending on the scanner, and are not suitable for 3D reconstruction.

The equivalence of calcium measurements obtained with MDCT and EBCT has been investigated. Most studies have shown good correlation between the two techniques. It has been argued that databases developed with EBCT studies on age- and sex-based calcium-score

Table 12.1. Scan Acquisition Parameters for Case 12.1, Coronary Calcium Screening

Slice No. and Thickness	**16 × 1.0 mm**
Coverage	**Heart**
Helical Pitch	**Axial sequence with prospective gating**
Rotation Speed	**0.32 sec (partial scan)**
Dose Parameters	**120 kVp, 160 mAs**
Contrast Dose	**None**

percentiles and risk profiles should not be applied to calcium scores obtained with MDCT scanners. This assertion is hard to justify given the close correlation of MDCT and EBCT for measuring the same physical entity—calcified tissue in the wall of the coronary arteries.

A

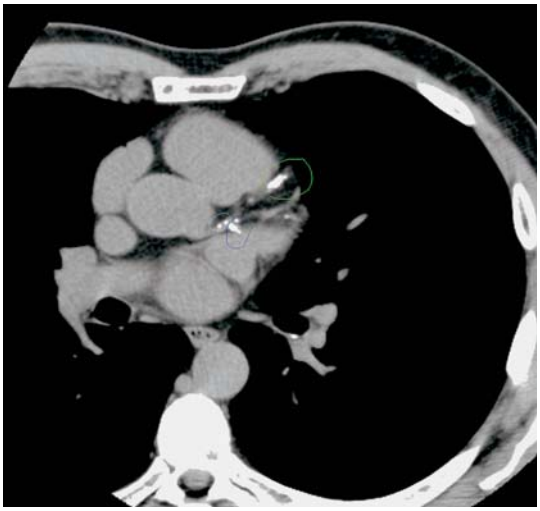

B

C

Figure 12.1.1. (A–C) Axial prospective gated images from a calcium scoring study. Calcific plaque is circled and assigned to the appropriate coronary artery. A sample of the extensive calcification in this patient is shown on these three images. Left main = turquoise, LAD = green, circumflex = blue, RCA = red.

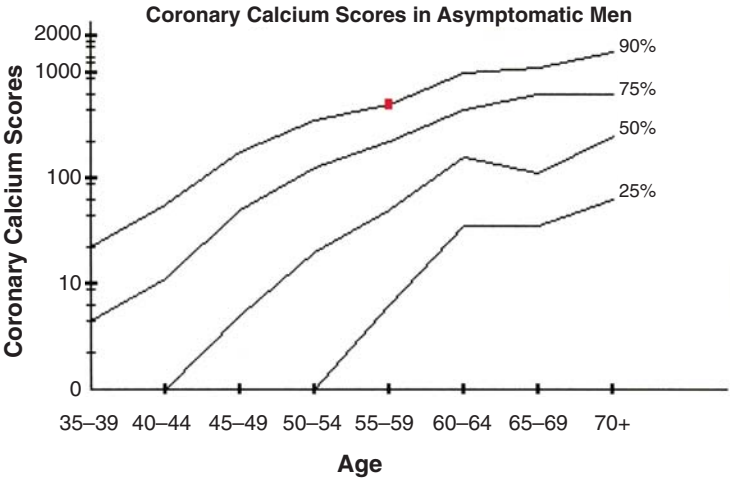

Figure 12.1.2. Curve demonstrating the patient's total calcium score plotted against age- and sex-matched controls.

One problem that is well recognized, however, is the significant interscan, interobserver, and intraobserver variability associated with calcium scoring. This limits the utility of the test to follow patients and assess responses to therapy. Some sites will routinely perform two acquisitions back-to-back on a patient and average the score to try to limit this variability.

The identification of coronary arterial calcification signifies the presence of atherosclerosis. Computed tomography is a very effective test to detect calcification and, therefore, coronary atherosclerosis. Currently, there is a lack of good prospective data to clearly show the utility of coronary calcium as a screening tool, but many studies are in progress. Current consensus from the American College of Cardiology/American Heart Association is summarized as follows:

1. A negative CT test makes the presence of atherosclerotic plaque, including unstable plaque, very unlikely.

Table 12.2. Summary Report of the Calcium Score by Artery With Total Score Using Both the Agatston and Volume Measurement Techniques

Region	Volume (mm^3)	Calcium Score (Agatston)
Left Main	37	21
Right Coronary Artery	159	172
Left Anterior Descending	152	187
Circumflex	72	83
Posterior Descending Artery	0	0
Total	420	463

2. A negative test is highly unlikely in the presence of significant luminal obstructive disease.
3. Negative tests occur in the majority of patients who have angiographically normal coronary arteries.
4. A negative test may be consistent with a low risk of a cardiovascular event in the next 2 years to 5 years.
5. A positive CT confirms the presence of coronary atherosclerotic plaque.
6. The greater the amount of calcium, the greater the likelihood of occlusive CAD, but there is not a one-to-one relationship, and findings may not be site specific.
7. The total amount of calcium correlates best with the total amount of atherosclerotic plaque, although the true "plaque burden" is underestimated.
8. A high calcium score may be consistent with moderate-to-high risk of a cardiovascular event within the next two years to five years.

A major criticism of calcium scoring has been that it does not show soft plaque, which is potentially more dangerous. Currently it is possible to perform a comprehensive cardiac examination combining coronary calcium scoring with coronary CTA. The combination of these two tests will show soft and hard plaque, measure stenosis, and quantify calcium burden. As 16-, 32-, and 64-detector scanners proliferate, this test will become widely available and may change how patients are screened.

Case 12.2: Coronary Artery CTA (Four Patients)

Clinical Information

Scans from four different currently asymptomatic patients aged from 53 years to 69 years who underwent screening for coronary artery disease.

Postprocessing Techniques Used and Approach

Images are reconstructed at multiple phases of the R-R interval using retrospective gating (Table 12.3 and Figures 12.2.1 through 12.2.4). The

Table 12.3. Scan Acquisition Parameters for Case 12.2, Coronary Artery CTA

Slice No. and Thickness	**16 × 0.5 mm**
Coverage	**Heart**
Helical Pitch	**0.25:1–0.3:1 (retrospective gating)**
Rotation Speed	**0.4 sec or 0.5 sec**
Dose Parameters	**120 kVp–135 kVp, 84 mAs–121 mAs**
Contrast Dose	**125 mL Omnipaque 350**
Injection Rate	**4 mL/sec**
Bolus Timing Method	**Bolus triggering on the ascending aorta**

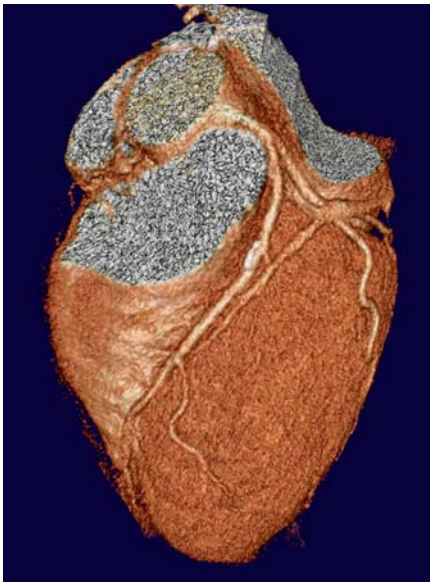

A

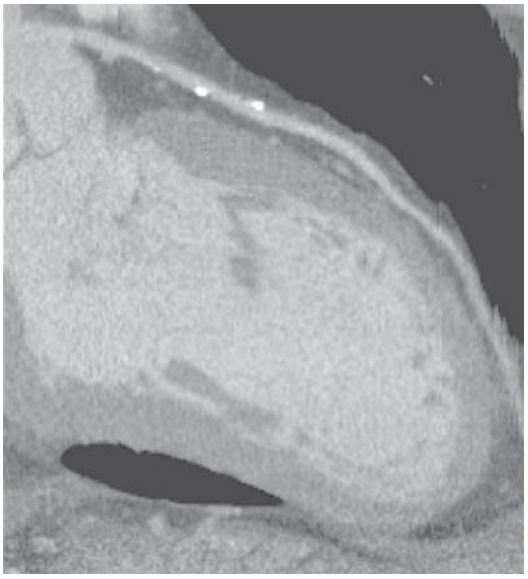

B

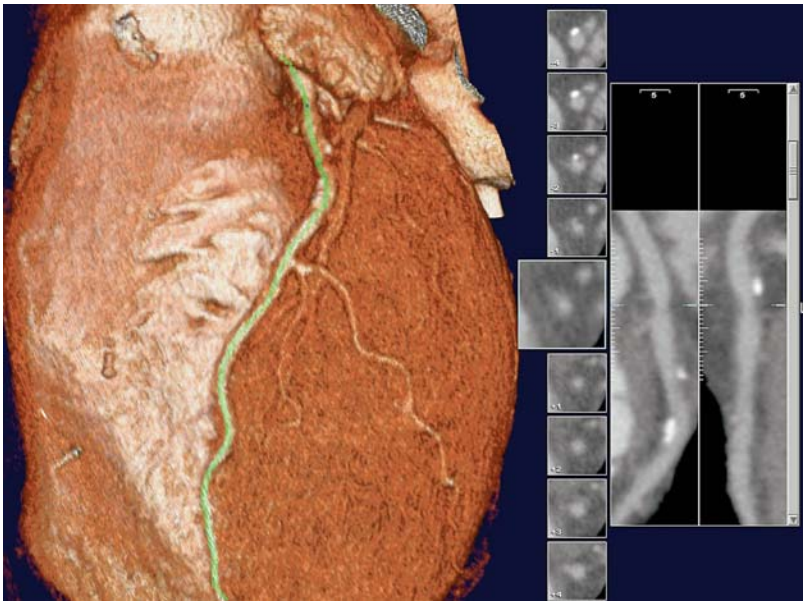

A

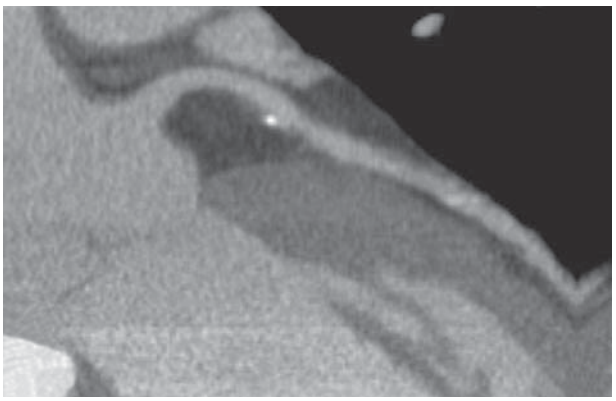

B

Figure 12.2.2. (A and B) Patient 2: Vessel-tracking software is used to generate a centerline path through the LAD and produce curved reconstructions with additional short axis views. Standard CPR is also shown. The proximal LAD contains multiple foci of both soft and calcified plaque. Luminal narrowing of approximately 30% is present.

Figure 12.2.3. (A–C) Patient 3: Volume-rendered image of the LAD demonstrates dense calcified plaque, which essentially obscures the underlying vessel. Curved planar reconstructions shows extensive soft and calcific plaque, which appears to cause stenosis of greater than 90% in areas. Axial 0.5-mm image shows that there is some motion artifact, which can magnify the calcium blooming artifact and cause overestimation of vessel stenosis. Catheter angiogram in this patient showed the luminal narrowing in the LAD was no more than 50% to 60%.

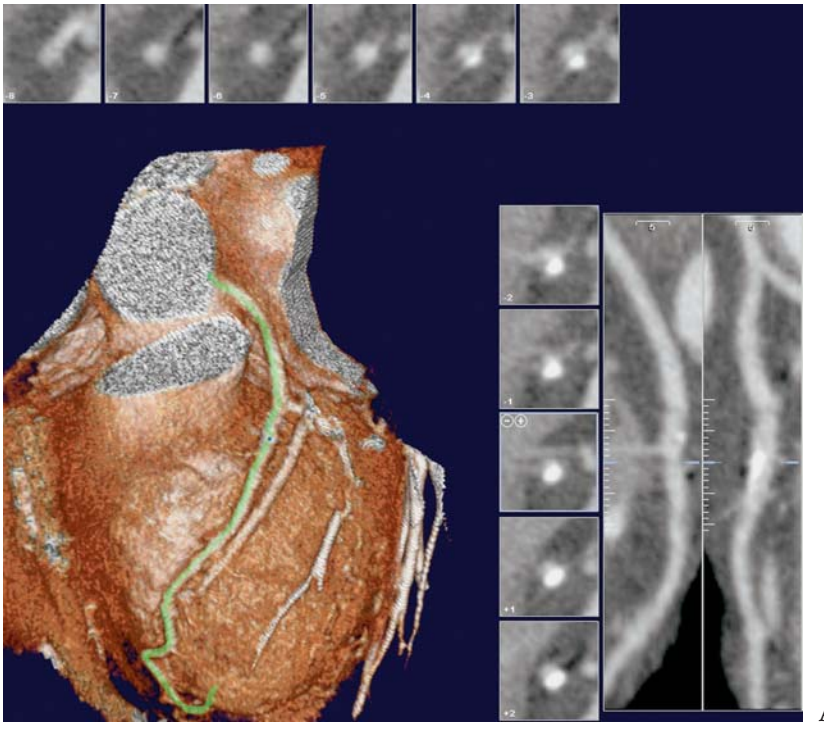

A

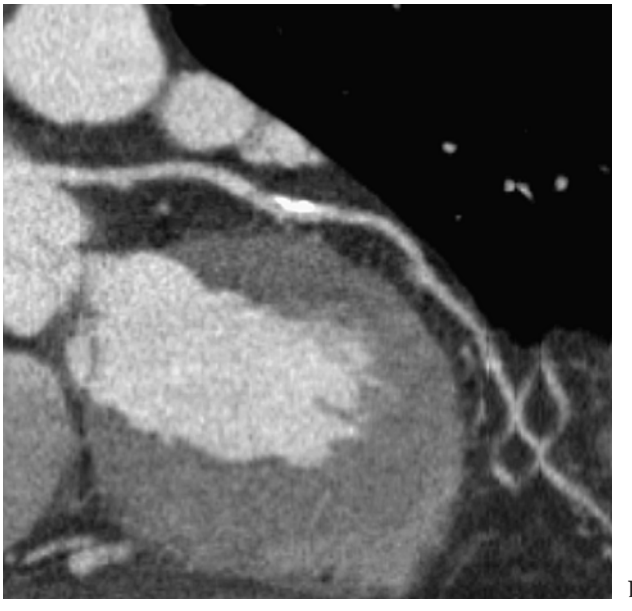

B

Figure 12.2.4. (A and B) Patient 4: vessel-tracking view and CPR through the LAD. There is an eccentric calcified plaque, which causes a stenosis of approximately 70%. This is best measured on the axial short axis views. Findings were confirmed by cardiac catheterization.

best quality data set with the least motion is selected for evaluation. For the left anterior descending (LAD) and circumflex arteries this is generally in diastole at 70% or 80% R-R interval. For the right coronary artery (RCA) this is more variable, between 40% and 70% R-R interval. Volume-rendered images are reviewed to demonstrate the morphology of the involved arteries. Manual segmentation is performed from the 3D images to remove the diaphragm and overlying vascular structures that limit visualization of the vessels. Curved planar reconstructions are generated using automated software to visualize the vessel lumen and plaque deposits.

Diagnosis

Patient 1: mild calcific plaque without significant stenosis. Patient 2: moderate soft and calcific plaque with areas of luminal narrowing measuring less than 40%. Patient 3: dense calcified plaque present. Stenosis on CT was estimated at 90%, however a catheter angiogram was performed, which showed no lesion greater than 50% to 60%. Patient 4: 70% stenosis of the LAD secondary to an eccentric calcified plaque. This was confirmed by angiogram.

Teaching Points

Coronary artery disease remains the leading cause of death and disability in the Western world for both men and women. The financial cost of the disease is staggering. Although many patients have symptoms of ischemia or myocardial infarction, for many other patients their first event results in sudden death. Currently catheter coronary angiography is the gold standard for diagnosis of CAD. This test is expensive and invasive, however, and clearly not suitable for screening patients. It is performed frequently as a second-line test for diagnostic and therapeutic purposes. However, only one third of all conventional coronary angiographic examinations in the United States are performed in conjunction with an interventional procedure, while the rest are performed only for diagnostic purposes. Many of these examinations could be avoided if an accurate and noninvasive test were available.

Coronary artery CTA is a very exciting and rapidly progressing field. The initial research with 4-slice scanners yielded results that were less than ideal. These scanners were limited by long acquisition times (breath holds of more than 30 sec) and low spatial resolution. Early results with 16-detector scanners have been more promising. For stenosis of 50% or greater, detection accuracy has been shown to approach 90%. A normal CTA examination has also been found to have a very high negative predictive value of a normal coronary CTA (97% with 16-detector scanners). This high negative predictive value demonstrates the utility of a noninvasive CTA as a reliable test to exclude CAD in the large population of patients with equivocal clinical presentation and findings. Many of these patients will end up with a costly workup that may include cardiac catheterization.

Another very exciting aspect of coronary CTA is the potential ability to perform plaque characterization. Currently, the only other diagnostic test that has this ability is intravascular ultrasound. Studies have shown that the plaque composition is tied to its risk of rupture and sudden death or severe ischemia. Lipid-rich noncalcified plaques are most prone to spontaneous rupture and are known as "vulnerable plaque." Calcified and fibrous plaques are more stable and chronic and less likely to rupture. Excessive vessel calcification currently is a limitation of coronary CTA. The blooming effect of the calcium may cause overestimation of stenosis, particularly if motion is present. For this reason many sites will screen patients first with a coronary calcium study, and if extensive calcium is present, will forego the CTA.

The obvious benefit of accurate noninvasive identification of vulnerable plaque is that cardiologists can intervene preemptively before an acute coronary event, either by invasive means such as angioplasty and stenting, or by pharmacologic means such as statin therapy. This is an area that will require additional research in the future.

The future holds considerable promise for cardiac CTA, particularly with 64-detector scanners. These scanners can decrease acquisition time to less than 10 sec with spatial resolution of 0.5 mm to 0.625 mm. The shorter breath hold improves patient cooperation and decreases heart rate variability that occurs frequently in longer breath holds. This produces a better quality data set. The main problem for cardiac CTA is temporal resolution. Additional improvements in gantry rotation time will be difficult because of the very high g-forces involved. Therefore, improved temporal resolution will primarily require software improvements using adaptive segmented reconstruction or other new techniques.

Case 12.3: Bypass Graft Evaluation

Clinical Information

A 70-year-old man with prior two-vessel bypass, undergoing evaluation for bypass graft patency.

Postprocessing Techniques Used and Approach

Images are reconstructed using retrospective gating at 10% R-R intervals from 10% to 90% (Table 12.4 and Figures 12.3.1 and 12.3.2). Volume-rendered images are reviewed to demonstrate the morphology of the grafts. Some manual segmentation is performed from the 3D images to remove overlying vascular structures that limit visualization of the grafts. Curved planar reconstructions are generated using automated software.

Diagnosis

Patent left internal mammary artery (IMA) to left anterior descending artery graft and patent saphenous vein graft to the RCA.

Table 12.4. Scan Acquisition Parameters for Case 12.3, Bypass Graft Evaluation

Slice No. and Thickness	**16 × 1.0 mm**
Coverage	**Lung apex through heart**
Helical Pitch	**0.25:1 (retrospective gating)**
Rotation Speed	**0.4 sec**
Dose Parameters	**135 kVp, 96 mAs**
Contrast Dose	**125 mL Omnipaque 350**
Injection Rate	**4 mL/sec**
Bolus Timing Method	**Bolus triggering on the ascending aorta**

Teaching Points

Coronary artery bypass surgery with use of either venous or internal mammary artery bypass grafts is an established treatment for symptomatic multivessel coronary artery disease. One of the most important variables that determines the successful clinical outcome of coronary artery bypass graft placement is the short- and long-term patency rate of the grafts. For venous coronary artery bypass grafts, an occlusion rate of 12% to 20% has been reported within the first year after surgery.

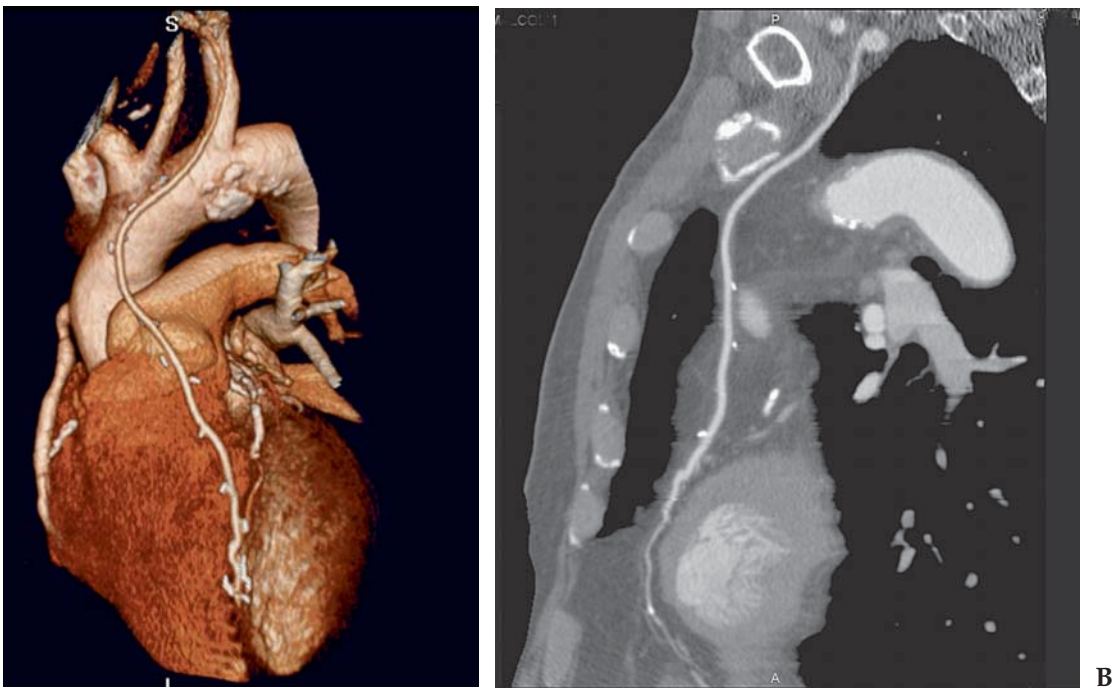

A B

Figure 12.3.1. (A and B) Volume-rendered image demonstrates the left internal mammary artery (LIMA) graft extending from the left subclavian artery to the LAD. The CPR demonstrates patency of the graft without significant stenosis and patency of the LAD distal to the anastomosis. (Courtesy of Dr. Ruben Sebben, Dr. Jones & Partners Medical Imaging, South Australia.)

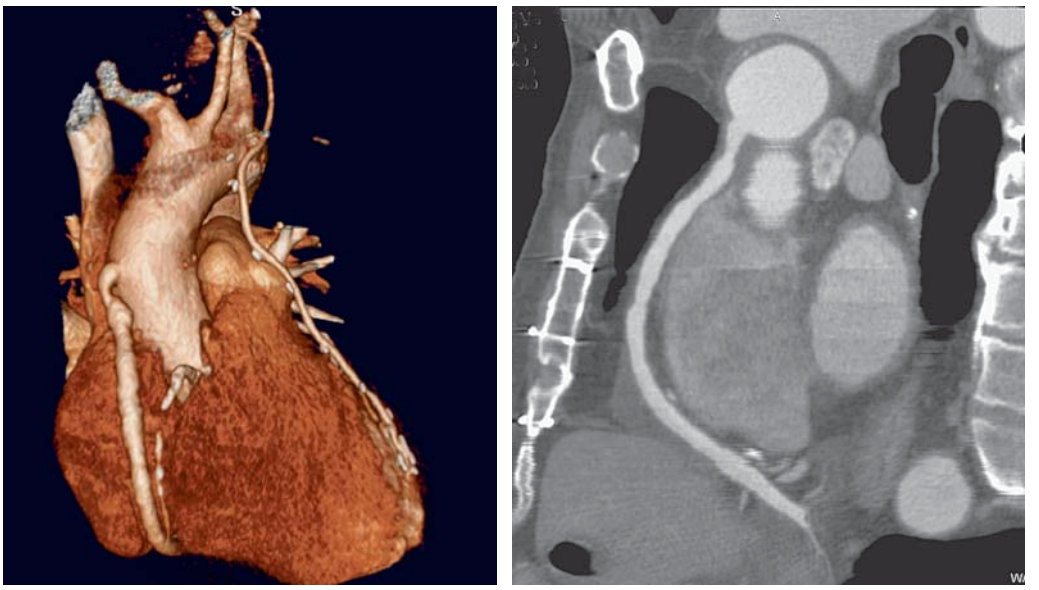

Figure 12.3.2. (A and B) Volume-rendered and curved images show patency of the right coronary artery saphenous vein graft. (Courtesy of Dr. Ruben Sebben, Dr. Jones & Partners Medical Imaging, South Australia.)

After 5 years postsurgery, the occlusion rate is 4% per year. For IMA bypass grafts, the occlusion rate is approximately 10% after 10 years postimplantation.

Currently cardiac catheterization remains the standard procedure to evaluate bypass grafts for patency and stenosis. However, because of the invasive nature of that examination it is generally not performed for evaluation of grafts unless patients are significantly symptomatic. Multidetector CT now offers a noninvasive test to accurately determine graft patency and morphology. Computed tomography can be used for surveillance of grafts following surgery, and it is also very helpful to a cardiac surgeon for demonstrating the precise location of the bypass grafts prior to a redo coronary bypass operation.

One significant danger of reoperation is injury to an existing graft that can occur during the sternotomy. There is a reported injury rate of 5.3% to patent left internal mammary artery (LIMA) grafts during re-operative bypass procedures, and the risk for right internal mammary artery (RIMA) grafts is even higher. Computed tomography can demonstrate grafts in unusual locations and warn the surgeon of a bypass graft immediately adjacent or adhesed to the sternum. Other graft complications, such as formation of a pseudoaneurysm, can also be detected.

Table 12.5. Scan Acquisition Parameters for Case 12.4, Aberrant Right Coronary Artery

Slice No. and Thickness	**16 × 0.5 mm**
Coverage	**Through heart**
Helical Pitch	**0.25:1 (retrospective gating)**
Rotation Speed	**0.5 sec**
Dose Parameters	**135 kVp, 180 mAs**
Contrast Dose	**150 mL Omnipaque 350**
Injection Rate	**4 mL/sec**
Bolus Timing Method	**Bolus triggering on the ascending aorta**

Case 12.4: Aberrant Right Coronary Artery

Clinical Information

A 40-year-old weight lifter who notices chest pain during strenuous workouts.

Postprocessing Techniques Used and Approach

Images are reconstructed using retrospective gating at 10% R-R intervals from 10% to 90% (Table 12.5 and Figures 12.4.1 through 12.4.3). Volume-rendered images of the heart are used to show the coronary artery anatomy. Segmentation to remove the pulmonary artery is performed manually from 2D images. Coronal curved reformations are also generated with automated software.

Diagnosis

Aberrant origin of the right coronary artery, which arises on the left above the left coronary artery. The vessel then courses to the right between the aorta and pulmonary artery.

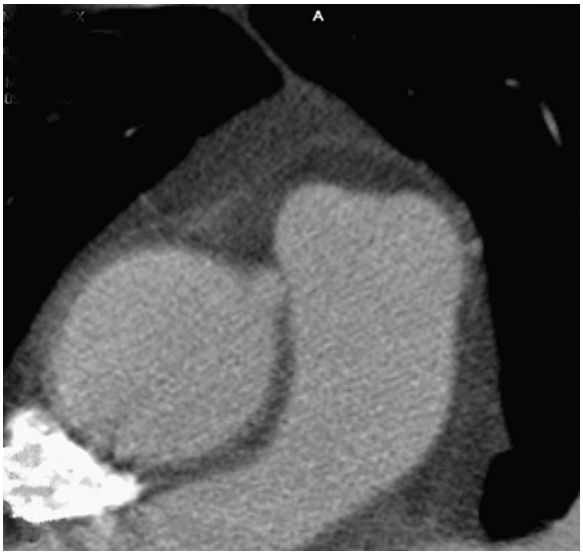

Figure 12.4.1. Axial image demonstrating the origin of the right coronary artery from the left side of the aorta adjacent to the main pulmonary artery.

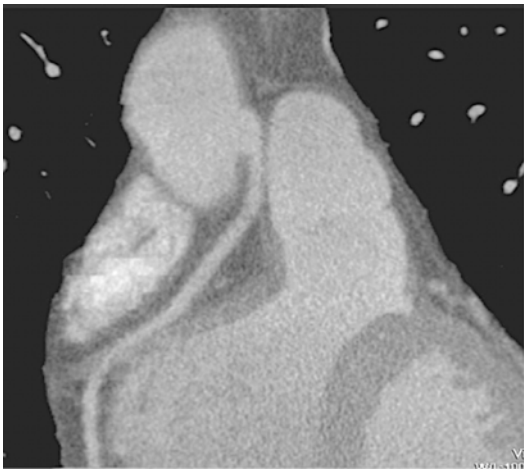

A

B

Figure 12.4.2. (A and B) Coronal curved planar reconstruction and VR image through the heart. The path of the RCA (arrows), which arises from the left side of the aorta and passes between the aorta and the main pulmonary artery before entering the atrioventricular groove, is clearly shown.

Teaching Points

Coronary artery anomalies are relatively common and have been reported in up to 2% of the population. Many anomalies are benign; however, certain anomalies can result in myocardial ischemia and death.

Coronary anomalies include abnormalities of coronary origin and are highly variable. Typical anomalies include origin of a coronary artery from the pulmonary trunk, left or right ventricle, or high on the aorta or great vessels. Another common anomaly is origination of the

Figure 12.4.3. Segmented VR image with the pulmonary artery cut away. The relationship between the origin of the right and left main coronary arteries is now seen.

coronary ostium from the opposite, facing coronary sinus, and cases of single coronary artery. Other patients may have abnormalities related to abnormal course, termination, or structure of the coronary artery. Examples include myocardial bridges, coronary fistulas, and congenital stenosis or atresia of a coronary artery.

In this patient with an aberrant right coronary artery that arises on the left above the normal coronary cusp and has an abnormal course, the main symptom was exercise-induced chest pain. Ischemia may result from compression of the coronary artery between the aorta and the pulmonary trunk. This can occur during periods of exercise when these vessels undergo vasodilatation.

In this case CTA provided excellent documentation of the origin and course of the aberrant coronary artery. The origin of the RCA in this case was relatively high, well above the left coronary cusp. Had the origin been lower, near the left cusp, the ischemia would likely be worse. In cases of significant compression, treatment is surgical. Either surgical reimplantation of the aberrant artery or bypass can be performed.

Case 12.5: Pulmonary Vein Evaluation

Clinical Information

A 67-year-old woman with atrial fibrillation undergoing evaluation for radiofrequency ablation.

Table 12.6. Scan Acquisition Parameters for Case 12.5, Pulmonary Vein Evaluation

Slice No. and Thickness	**16 × 0.5 mm**
Coverage	**Chest**
Helical Pitch	**0.25:1 (cardiac gated study)**
Rotation Speed	**0.4 sec**
Dose Parameters	**120 kVp, 250 mAs**
Contrast Dose	**125 mL Omnipaque 350**
Injection Rate	**4 mL/sec**
Bolus Timing Method	**Bolus triggering on ascending aorta**

Postprocessing Techniques Used and Approach

The examination was performed as a retrospective cardiac gated study with reconstruction of images at 80% of the R-R interval (Table 12.6 and Figures 12.5.1 through 12.5.4). Processing is performed on the workstation. Initial volume-rendered views of the atrium and pulmonary veins are obtained after manual segmentation to remove the spine and descending thoracic aorta. Coronal and axial thin- and thick-slab MIP images are reviewed to identify and measure the pulmonary veins and

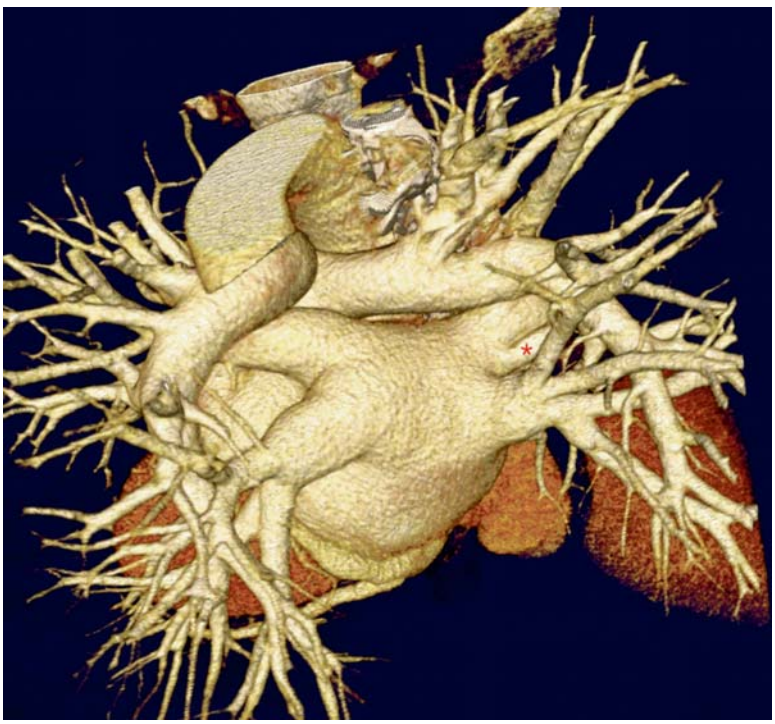

Figure 12.5.1. Volume-rendered image of the left atrium and pulmonary veins. The aorta and spine have been removed. Note the accessory pulmonary vein to the right middle lobe (*).

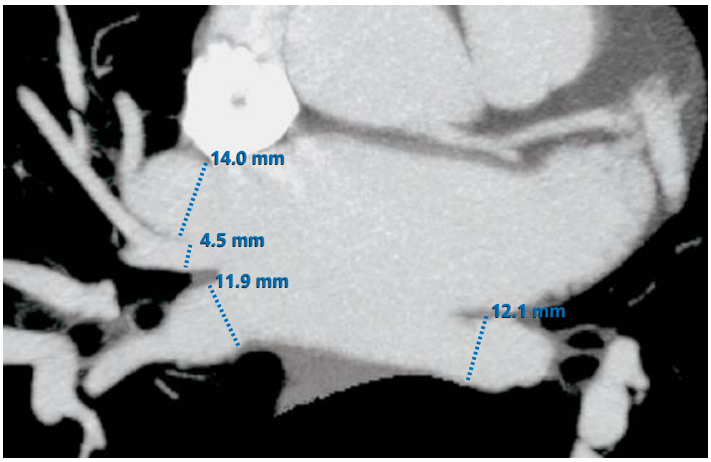

Figure 12.5.2. Axial MIP image demonstrating measurement of the right upper, middle, and lower veins, and the left lower vein. The atrial appendage is shown, but the left upper vein is not included on this image.

left atrium. Finally, endoluminal fly-through imaging is performed within the left atrium to visualize the pulmonary vein ostia. Three-dimensional markers arrows can be place on the 2D images to facilitate identification of the veins on the endoluminal images.

Diagnosis

Pulmonary vein mapping prior to radiofrequency ablation.

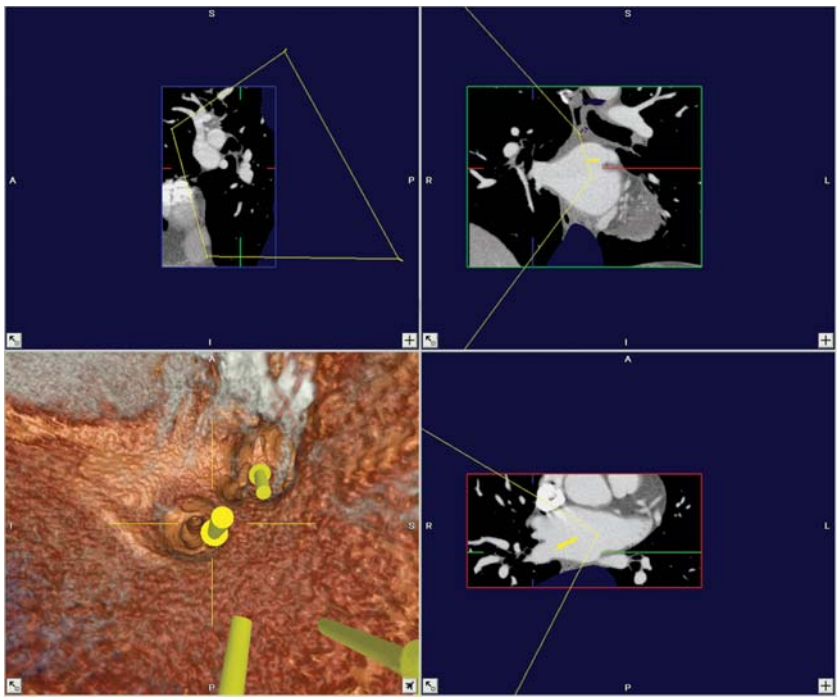

Figure 12.5.3. Navigation view showing localization of the right-sided pulmonary veins. The 3D marker arrows are seen.

Figure 12.5.4. Magnified view of the right pulmonary veins. The right, middle, and upper lobe veins have a conjoined origin.

Teaching Points

Atrial fibrillation (AF) is an important clinical problem with significant potential morbidity, particularly cerebrovascular accidents. Many patients can be adequately treated with medical therapy; however, some patients are refractory to medical management. Atrial fibrillation occurs when multiple ectopic electrical foci fire independently of the sinoatrial (SA) node. Instead of receiving one electrical signal, the atrioventricular (AV) node is bombarded by up to 300 discharges per minute.

The muscular sleeves of the pulmonary veins are a major source of ectopic electrical foci. Recently, it has been discovered that paroxysms of atrial fibrillation are initiated by trains of spontaneous activity originating from the pulmonary veins in 90% to 96% of patients, with almost half arising in the left superior pulmonary vein. Cardiologists are now performing radiofrequency catheter ablation (RFCA) to suppress these ectopic foci. The RFCA works by electrically isolating the conduction pathways through ablation of the distal pulmonary veins and posterior left atrium.

During RFCA, radiofrequency energy is preferably applied at the venoatrial junction of all the pulmonary veins to avoid stenoses and eliminate ostial remnants that may contribute to recurrent atrial fibrillation. Therefore, advance knowledge of how many pulmonary veins are present, and their ostial locations, is important to ensure that all the ostia are ablated. It is difficult and time-consuming to locate the ostia with conventional angiography at the time of ablation.

Since successful RFCA depends in part on good preprocedural mapping, MDCT can be used to evaluate the left atrium and pul-

monary veins. Evaluation should include discussion of size, number and location of pulmonary veins, description of anatomic variants, and the presence of ostial branches. Left atrial volume can also be measured, and thrombi in the atrium or atrial appendage must be excluded. Anatomy of the pulmonary veins is highly variable, with variations reported in 30% to 40%, including accessory veins (usually on the right) and conjoined veins (usually on the left). The distance from the ostium to the first major branch is also important.

Computed tomography of the atrium and pulmonary veins can be performed with either gated or nongated technique. Gating is generally preferred, as it will minimize motion artifacts, but in patients with very irregular heart rates it may not be possible and it is not suggested for ill patients who cannot hold their breath for the entire study. Also, gated studies increase radiation exposure.

Workstation evaluation should include segmentation with volume rendering to show the atrium and pulmonary veins; thin and thick slab MIP images to show anatomy, measure size of the venous ostia, and look for thrombi; and endoluminal images to demonstrate ostial branches and provide a map for the electrophysiologist.

Case 12.6: Atrial Myxoma

Clinical Information

A 57-year-old woman with a history of chest pain and dyspnea undergoing evaluation to rule out pulmonary embolus.

Postprocessing Techniques Used and Approach

Multiplanar axial, sagittal, and coronal images are reviewed (Table 12.7 and Figure 12.6.1).

Diagnosis

Myxoma of the left atrium.

Teaching Points

Although this was not a gated cardiac study, excellent visualization of the atria and ventricles is obtained routinely on nongated CTAs. The

Table 12.7. Scan Acquisition Parameters for Case 12.6, Atrial Myxoma

Slice No. and Thickness	**16 × 1.0 mm**
Coverage	**Through chest**
Helical Pitch	**1.25:1**
Rotation Speed	**0.5 sec**
Dose Parameters	**120 kVp, 200 mAs**
Contrast Dose	**125 mL Omnipaque 350**
Injection Rate	**3 mL/sec**
Bolus Timing Method	**Sure start on pulmonary artery**

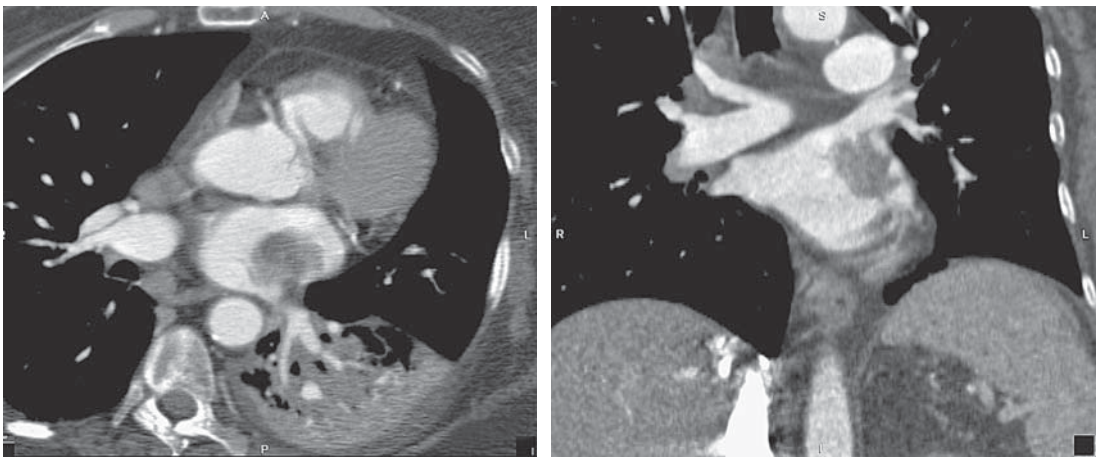

A B

Figure 12.6.1. (A and B) Axial and coronal 2-mm images focused on the heart show a polypoid mass with a stalk arising from the left atrium. Appearance is consistent with a left atrial myxoma.

atrial tumor was an unsuspected finding in this patient but was likely the cause of her symptoms.

Cardiac myxoma is a benign neoplasm that accounts for approximately one half of all primary cardiac tumors. Myxoma typically manifests as a polypoid, intracavitary atrial mass that arises from the interatrial septum. Left atrial involvement is four times more common than right atrial involvement, but myxoma may originate in any cardiac chamber. Most affected patients have at least one feature of a classically described triad that includes cardiac obstructive symptoms, constitutional symptoms, and embolic events.

Presenting complaints relate to tumor location, which predicts obstructive sequelae and influences embolic sites (pulmonary or systemic). Left atrial myxomas commonly cause mitral valve obstruction. Affected patients may have dyspnea and orthopnea from pulmonary venous hypertension. The pedunculated and prolapsing nature of these tumors allows for positional and intermittent mitral valve obstruction. Of patients in a large series with left atrial myxomas, 60% had symptoms related to mitral valve obstruction. Right atrial myxomas may obstruct the tricuspid valve and cause symptoms of right-sided heart failure, peripheral edema, passive hepatic congestion, and syncope. In this series, only 9% of patients with right atrial myxomas had signs and symptoms of tricuspid valve obstruction.

Constitutional symptoms of fever, malaise, weight loss, anemia, and elevated sedimentation rate have been reported and may be related to an autoimmune reaction initiated by the tumor. These symptoms can be seen in 25% to 30% of patients. Cardiac arrhythmias, atrial fibrillation, and atrial flutter reportedly occur in approximately 20% of patients with cardiac myxoma. Embolic phenomena are reported in approximately 35% of left-sided and 10% of right-sided myxomas.

Table 12.8. Scan Acquisition Parameters for Case 12.7, Coronary Stent Evaluation

Slice No. and Thickness	**16 × 0.5 mm**
Coverage	**Heart**
Helical Pitch	**0.25:1 (retrospective gating)**
Rotation Speed	**0.4 sec**
Dose Parameters	**135 kVp, 98 mAs–114 mAs**
Contrast Dose	**125 mL Omnipaque 350**
Injection Rate	**4 mL/sec**
Bolus Timing Method	**Bolus triggering on the ascending aorta**

Case 12.7: Coronary Stent Evaluation (Two Patients)

Clinical Information

Two patients undergoing evaluation of coronary stents for patency.

Postprocessing Techniques Used and Approach

Images are reconstructed at multiple phases of the R-R interval using retrospective gating (Table 12.8 and Figures 12.7.1 and 12.7.2). The best quality data set with the least motion is selected for evaluation. For the circumflex artery this was 80% R-R interval, and for the RCA, 50% R-R interval. Volume-rendered images are reviewed to demonstrate the morphology of the involved arteries and show the location of the stent. Manual segmentation is performed from the 3D images to remove the diaphragm and overlying vascular structures that limit visualization of the vessels. Curved planar reconstructions are generated using automated software to visualize the lumen inside the stent.

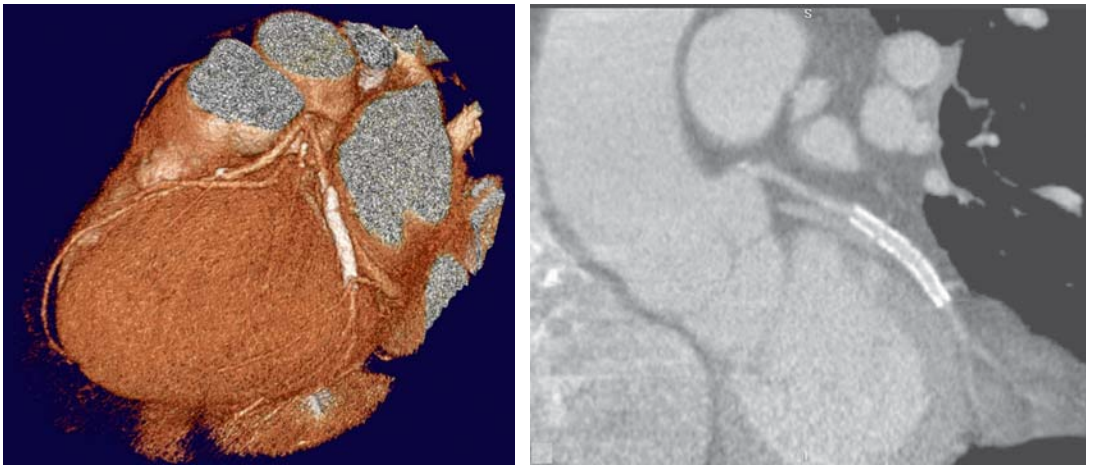

A B

Figure 12.7.1. (A and B) Patient 1: three-dimensional volume-rendered and curved planar reconstructions of a stent in the circumflex coronary artery. Stent patency is confirmed.

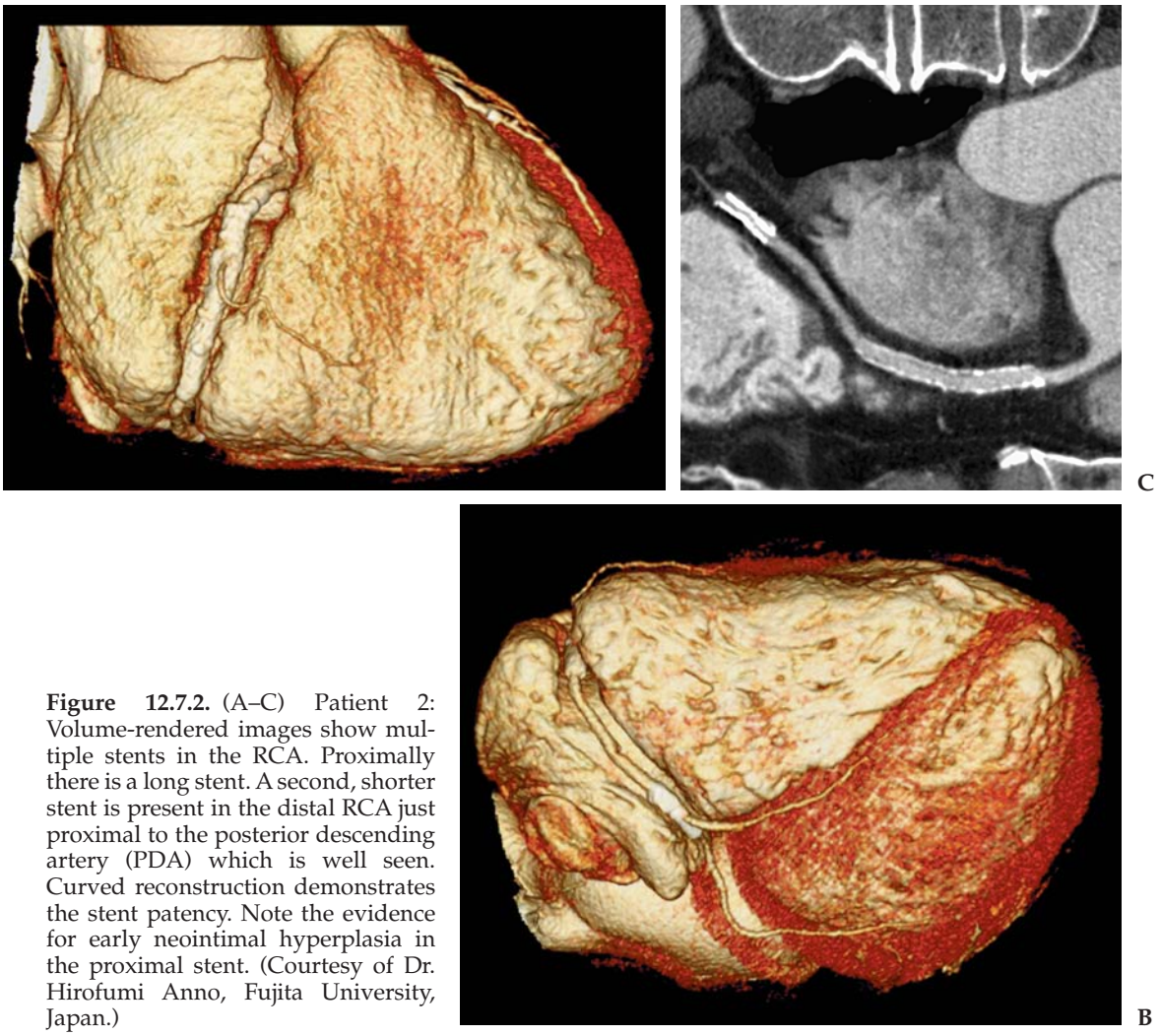

Figure 12.7.2. (A–C) Patient 2: Volume-rendered images show multiple stents in the RCA. Proximally there is a long stent. A second, shorter stent is present in the distal RCA just proximal to the posterior descending artery (PDA) which is well seen. Curved reconstruction demonstrates the stent patency. Note the evidence for early neointimal hyperplasia in the proximal stent. (Courtesy of Dr. Hirofumi Anno, Fujita University, Japan.)

Diagnosis

Patient 1: patent stent in the circumflex artery. Patient 2: patent stents in the right coronary artery.

Teaching Points

Coronary artery stent placement has become the accepted standard of practice for the percutaneous treatment of coronary artery stenosis in both acute and chronic coronary artery disease. Coronary artery stent placement reduces early complications of percutaneous transluminal coronary angioplasty (PTCA), as well as restenosis rates, and thus improves the safety and efficacy of angioplasty. Although patency rates are much better for stented vessels compared with vessels treated by PTCA alone, neointimal hyperplasia remains a significant problem and

can lead to vessel occlusion. This risk has led to the routine use of invasive and costly coronary angiography for surveillance of stent patency and stenosis. There is therefore a clinical need for a less expensive and noninvasive test that can successfully evaluate coronary stents.

Early studies with 4-detector MDCT had mixed result for the evaluation of stents, but more recent studies with 16-detector scanners have shown good results for CT stent evaluation. Hong et al. was able to adequately evaluate 20 stents out of 26 stents in 19 patients. In 5 patients, 6 stents could not be adequately evaluated because of too much motion or gating failure.

One major difficulty of CT stent evaluation is partial volume averaging associated with the metal struts of the stent. These struts will also accentuate motion streak artifacts if present. It is therefore very important to use the highest spatial resolution possible (0.5 mm to 0.625 mm) for data acquisition. Multiple cardiac phases must also be reconstructed and carefully reviewed for the phase with the least motion for each involved artery. It has also been shown that reconstructing the images with a sharp kernel rather than a soft tissue kernel will improve visualization of the stent lumen, although the images will be noisier.

Selected Readings

Coronary Calcium Screening

1. Callister TQ, et al. Coronary artery calcium scores on electron beam computed tomography. JACC 1999;33(suppl):415A.
2. Carr JJ, et al. Evaluation of subsecond gated helical CT for quantification of coronary artery calcium and comparison with electron beam CT. Am J Roentgenol 2000;174:915–921.
3. Mayo Clinic Proceedings. Findings based on EBCT data. March 1999, Vol. 74.
4. Nieman K, Oudkerk M, Rensing BJ, et al. Coronary angiography with multi-slice computed tomography. Lancet 2001;357:599–603.
5. O'Malley PG, Taylor AJ, Gibbons RV, et al. Rationale and design of the Prospective Army Coronary Calcium (PACC) study: utility of electron beam computed tomography as a screening test for coronary artery disease and as an intervention for risk factor modification among young, asymptomatic, active-duty United States Army personnel. Am Heart J 1999;137:932–941.
6. O'Rourke R, Brundage B, Froelicher V, et al. American College of Cardiology/American Heart Association Expert Consensus document on electron-beam computed tomography for the diagnosis and prognosis of coronary artery disease. Circulation 2000;102:126–140.
7. Schoepf UJ, Becker CR, Ohnesorge BM, Yucel EK. CT of coronary artery disease. Radiology 2004;232:18–37.

Coronary Artery CTA

8. Achenbach S, Giesler T, Ropers D, et al. Detection of coronary artery stenoses by contrast-enhanced, retrospectively electrocardiographically-gated, multislice spiral computed tomography. Circulation 2001;103: 2535–2538.

9. Becker CR, Knez A, Ohnesorge B, Schoepf UJ, Reiser MF. Imaging of noncalcified coronary plaques using helical CT with retrospective ECG gating. Am J Roentgenol 2000;175:423–424.
10. Choi HS, Choi BW, Choe KO, et al. Pitfalls, artifacts, and remedies in multidetector row CT coronary angiography. Radiographics 2004;24:787–800.
11. Desjardins B, Kazerooni EA. ECG-gated cardiac CT. Am J Roentgenol 2004 Apr;182:993–1010.
12. Kopp A, Kuttner A, Heuschmid M, Schroder S, Ohnesorge B, Claussen C. Multidetector-row CT cardiac imaging with 4 and 16 slices for coronary CTA and imaging of atherosclerotic plaques. Eur Radiol 2002;12:S17–S24.
13. Nieman K, Cademartiri F, Lemos PA, Raaijmakers R, Pattynama PM, de Feyter PJ. Reliable noninvasive coronary angiography with fast submillimeter multislice spiral computed tomography. Circulation 2002;106: 2051–2054.
14. Pannu HK, Flohr TG, Corl FM, Fishman EK. Current concepts in multi–detector row CT evaluation of the coronary arteries: principles, techniques, and anatomy. Radiographics 2003;23:111–125.
15. Schoenhagen P, Halliburton SS, Stillman AE, et al. Noninvasive imaging of coronary arteries: current and future role of multi–detector row CT. Radiology 2004;232:7–17.
16. Schoepf UJ, Becker CR, Ohnesorge BM, Yucel EK. CT of coronary artery disease. Radiology 2004;232:18–37.

Bypass Graft Evaluation

17. Desjardins B, Kazerooni EA. ECG-gated cardiac CT. Am J Roentgenol 2004 Apr;182:993–1010.
18. Ha J, Cho S, Shim W, et al. Noninvasive evaluation of coronary artery bypass graft patency using three-dimensional angiography obtained with contrast-enhanced electron beam CT. Am J Roentgenol 1999;172:1055–1059.
19. Lu B, Dai RP, Jing BL, et al. Evaluation of coronary artery bypass graft patency using three-dimensional reconstruction and flow study on electron beam tomography. J Comput Assist Tomogr 2000;24:663–670.
20. Pannu HK, Flohr TG, Corl FM, Fishman EK. Current concepts in multi–detector row CT evaluation of the coronary arteries: principles, techniques, and anatomy. Radiographics 2003;23:111–125.
21. Ropers D, Ulzheimer S, Wenkel E, et al. Investigation of aortocoronary artery bypass grafts by multislice spiral computed tomography with electrocardiographic-gated image reconstruction. Am J Cardiol 2001;88: 792–795.
22. Schoepf UJ, Becker CR, Ohnesorge BM, Yucel EK. CT of coronary artery disease. Radiology 2004;232:18–37.
23. Willmann JK, Weishaupt D, Kobza R, Verdun FR, et al. Coronary artery bypass grafts: ECG-gated multi–detector row CT angiography—influence of image reconstruction interval on graft visibility. Radiology 2004;232: 568–577.

Aberrant Right Coronary Artery

24. Angelini P, Velasco JA, Flamm S. Coronary anomalies: incidence, pathophysiology, and clinical relevance. Circulation 2002;105:2449–2454.
25. Dirksen M, Bax J, Blom N, et al. Detection of malignant right coronary artery anomaly by multi-slice CT coronary angiography. Eur Radiol 2002;12:S177–S180.

26. McConnell MV, Ganz P, Selwyn AP. Identification of anomalous coronary arteries and their anatomic course by magnetic resonance coronary angiography. Circulation 1995 Dec;92(11):3158–3162.
27. Ropers D, Moshage W, Daniel WG. Visualization of coronary artery anomalies and their anatomic course by contrast-enhanced electron beam tomography and three-dimensional reconstruction. Am J Cardiol 2001 Jan;87(2):193–197.
28. Ropers D, Gehling G, Pohle K, et al. Anomalous course of the left main or left anterior descending coronary artery originating from the right sinus of valsalva: identification of four common variations by electron beam tomography. Circulation 2002;105:e42–e43.

Pulmonary Vein Evaluation

29. Cronin P, Sneider MB, Kazerooni EA, et al. MDCT of the left atrium and pulmonary veins in planning radiofrequency ablation for atrial fibrillation: a how-to guide. Am J Roentgenol 2004 Sep;183:767–778.
30. Lacomis JM, Wigginton W, et al. Multi–detector row CT of the left atrium and pulmonary veins before radio-frequency catheter ablation for atrial fibrillation. Radiographics 2003;23:S35–S48.
31. Lin WS, Prakash VS, Tai CT, et al. Pulmonary vein morphology in patients with paroxysmal atrial fibrillation initiated by ectopic beats originating from the pulmonary veins: implications for catheter ablation. Circulation 2000;101:1274–1281.
32. Scharf C, Sneider M, Case I, et al. Anatomy of the pulmonary veins in patients with atrial fibrillation and effects of segmental ostial ablation analyzed by computed tomography. J Cardiovasc Electrophysiol 2003;14: 150–155.
33. Yang M, Akbari H, Redd GP, Higgins CB. Identification of pulmonary vein stenosis after radiofrequency ablation for atrial fibrillation using MRI. J Comput Assist Tomogr 2001;25:34–35.

Atrial Myxoma

34. Burke AP, Virmani R. Cardiac myxoma: a clinicopathologic study. Am J Clin Pathol 1993;100:671–680.
35. Grebenc ML, Rosado-de-Christenson ML, Green CE, Burke AP, Galvin JR. From the archives of the AFIP: cardiac myxoma: imaging features in 83 patients. Radiographics 2002;22:673–689.
36. Gotway MB, Nagai BK, Reddy GP, Patel RA, Higgins CB, Webb WR. Incidentally detected cardiovascular abnormalities on helical CT pulmonary angiography: spectrum of findings. Am J Roentgenol 2001 Feb;176:421–427.
37. Reynen K. Cardiac myxomas. N Engl J Med 1995;333:1610–1617.

Coronary Stent Evaluation

38. Funabashi N, Komiyama N, Komuro I. Patency of coronary artery lumen surrounded by metallic stent evaluated by three dimensional volume rendering images using ECG gated multislice computed tomography. Heart 2003;89:388.
39. Hong C, Chrysant GS, Woodard PK, Bae KT. Coronary artery stent patency assessed with in-stent contrast enhancement measured at multi-detector row CT angiography: initial experience. Radiology 2004 Oct;233(1): 286–291.

40. Maintz D, Juergens KU, Wichter T, Grude M, Heindel W, Fischbach R. Imaging of coronary artery stents using multislice computed tomography: in vitro evaluation. Eur Radiol 2003;13:830–835.
41. Maintz D, Grude M, Fallenberg EM, Heindel W, Fischbach R. Assessment of coronary arterial stents by multislice-CT angiography. Acta Radiol 2003 Nov;44(6):597–603.
42. Nieman K, Cademartiri F, Raaijmakers R, Pattynama P, De Feyter P. Non-invasive angiographic evaluation of coronary stents with multi-slice spiral computed tomography. Herz 2003;28:136–142.
43. Pump H, Mohlenkamp S, Sehnert CA, et al. Coronary arterial stent patency: assessment with electron-beam CT. Radiology 2000;214:447–452.

Chapter 13

Orthopedic Imaging

Case 13.1: Knee Arthrogram

Clinical Information

A 55-year-old man with knee pain and a pacemaker which precludes MRI evaluation.

Postprocessing Techniques Used and Approach

Multiplanar reconstructions, including oblique reconstructions, are viewed on the 3D workstation (Table 13.1 and Figures 13.1.1 through 13.1.3).

Diagnosis

Tear of the posterior horn of the medial meniscus with associated chondromalacia of the femoral and patellar cartilages.

Teaching Points

In patients who are unable to undergo MRI, noninvasive diagnosis of internal derangement of the joints is very difficult. Conventional arthrography is often very limited, particularly for the knee. Many patients will therefore either forgo imaging evaluation or be referred directly to arthroscopy.

Multidetector CT arthrography now offers an excellent means of diagnosing internal derangement in patients who are unable to have MRI. The procedure is simple and highly effective. Dilute iodinated contrast is injected into the joint under fluoroscopic guidance, and the patient is scanned with an isotropic acquisition. Processing is minimal, with multiplanar reconstructions adequate for most findings, although it is often helpful to review oblique reconstructions on the workstation.

Studies have shown that MDCT arthrography is highly accurate for the diagnosis of meniscal tears, assessment of unstable meniscal tears, and identification of complete anterior cruciate ligament (ACL) and posterior cruciate ligament (PCL) tears. Sensitivity and specificity

Table 13.1. Scan Acquisition Parameters for Case 13.1, Knee Arthrogram

Slice No. and Thickness	**16 × 0.5 mm**
Coverage	**Through knee**
Helical Pitch	**0.94 : 1**
Rotation Speed	**0.5 sec**
Dose Parameters	**120 kVp, 175 mAs**
Contrast Dose	**20 mL intraarticular contrast mixed 50/50 with saline**

Figure 13.1.1. Sagittal reconstruction through the medial meniscus shows a tear of the inferior surface of the posterior horn of the meniscus (arrow).

A B

Figure 13.1.2. (A and B) Coronal and sagittal reconstructions though the menisci and cartilage. There are focal defects in the medial femoral cartilage and patellar cartilages (arrows).

Figure 13.1.3. Oblique sagittal reconstruction through an intact anterior cruciate ligament (ACL).

values are well over 90%. Results obtained have shown CT arthrography to perform as well as MRI for these abnormalities, but the current experience is much smaller than exists for MRI. Computed tomographic arthrography also excels at demonstration of osseous injury, osteophyte formation, and cartilage injury. Some findings that can be identified with MRI are difficult to diagnose with MDCT arthrography, including partial ACL tears, collateral ligament injury, bone contusion without fracture, and muscle or soft tissue injury.

Case 13.2: Scaphoid Fracture Nonunion

Clinical Information

An 18-year-old man who had previously undergone surgical repair of a scaphoid fracture. He is now referred to evaluate healing and position of the pin.

Postprocessing Techniques Used and Approach

Double oblique MPRs are reviewed on the workstation (Table 13.2 and Figures 13.2.1 through 13.2.3). The images are oriented along the long axis of the pin on both the oblique sagittal and oblique coronal planes. Surface-rendered images are also used to demonstrate anatomy of the wrist.

Diagnosis

Nonunion of a scaphoid fracture following surgical pinning with avascular necrosis in the proximal pole of the scaphoid.

Table 13.2. Scan Acquisition Parameters for Case 13.2, Scaphoid Fracture Nonunion

Slice No. and Thickness	**16 × 0.5 mm**
Coverage	**Wrist**
Helical Pitch	**0.94:1**
Rotation Speed	**0.75 sec**
Dose Parameters	**135 kVp, 210 mAs**
Contrast Dose	**None**

Teaching Points

This case illustrates the advantages of using CT to follow up and evaluate patients with complex injuries. Computed tomography is superior to plain film evaluation for demonstrating degree of healing, nonunion, and complications such as avascular necrosis. In the past, most patients with metal in place would undergo conventional tomograms for the assessment of surgical result and complications. Multidetector CT can provide much more information in a fraction of the time it takes to perform tomograms. Magnetic resonance imaging can also be used but is often limited by artifacts from the metal. Oblique MPR images are generally most useful for demonstrating healing and bone complications such as cystic areas, erosions, and sclerosis. Surface-rendered images are useful for demonstrating anatomy and alignment.

Figure 13.2.1. Surface-rendered image of the wrist. Scaphoid fracture with three main fragments is present. Note the hardware cannot be seen on the surface image.

Figure 13.2.2. (A and B) Double oblique coronal and sagittal images oriented along the pin. The relationship of the pin to the bony fragments is shown. The fracture is clearly unfused, and no significant bony union or osseous bridging is seen.

Computed tomography is also very useful for the initial diagnosis of wrist fractures. Compared to conventional radiographs, MDCT has been shown to reveal many additional occult fractures, mainly in small carpal bones. In addition, cases of suspected questionable fractures of the scaphoid or other carpal bones can be ruled out by CT. Multidetector CT examinations are not dependent on the careful positioning of the wrist in the CT gantry. Oblique views can be generated after

Figure 13.2.3. Coronal oblique image ventral to the pin. The nonunion is demonstrated, but there is also sclerosis seen in the proximal fragment consistent with avascular necrosis.

the study to produce images in the proper anatomic planes. Three-dimensional reformatted images are very helpful in cases of complex trauma with multiple fractures and/or carpal dislocations.

Case 13.3: Hemophilic Arthropathy

Clinical Information

A 40-year-old man with hemophilia B (factor IX deficiency) and worsening pain and limitation of motion in the right ankle.

Postprocessing Techniques Used and Approach

Oblique multiplanar reconstructions performed on the workstation and surface-rendered images without segmentation are reviewed (Table 13.3 and Figure 13.3.1 and 13.3.2).

Diagnosis

Severe hemophilic arthropathy of the right ankle.

Teaching Points

Computed tomography is not commonly used to image arthritis in most practices, but it can be a very helpful adjunctive imaging modality. Computed tomography excels in demonstrating complications of arthritis, including osteophytes, osseous loose bodies, joint narrowing, erosions, subchondral cysts, effusions, lytic areas, osteochondral defects, and occult fractures. In conjunction with arthrography it can also demonstrate cartilage loss, noncalcified loose bodies, and meniscal and ligament injury.

This case illustrates the advantages of CT in this patient with hemophilia. Some of the findings shown were clearly visible on plain film radiography, but the extent of geode formation and erosive disease was significantly underestimated. Computed tomography also better demonstrates the inflammatory synovitis.

Hemophilic arthropathy is caused by repetitive bleeding into the joints. The inflammatory response elicited by the blood leads to synovitis, erosion, and subchondral cyst formation. Eventually, superimposed osteoarthritis occurs as the cartilage is eaten away. Repetitive hemorrhage into the bones can result in an osseous pseudotumor,

Table 13.3. Scan Acquisition Parameters for Case 13.3, Hemophilic Arthropathy

Slice No. and Thickness	**16 × 0.5 mm**
Coverage	**Both lower legs and ankles**
Helical Pitch	**0.94:1**
Rotation Speed	**0.5 sec**
Dose Parameters	**120 kVp, 85 mAs**
Contrast Dose	**None**

Figure 13.3.1. (A–C) Multiple oblique coronal and sagittal 2-mm MPRs through the ankle. Severe subchondral cyst formation with large erosions is present within the distal tibia, talus, and calcaneus. Marked superimposed osteoarthritis is noted within the subtalar joint with joint narrowing, sclerosis, and osteophyte formation. In addition, note the hypertrophied synovium with high density from hemosiderin staining (arrows).

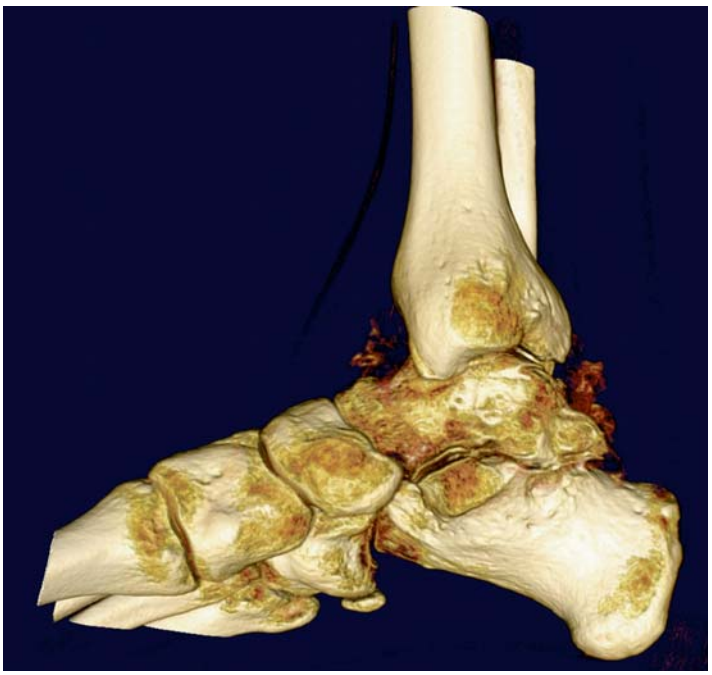

Figure 13.3.2. Surface-rendered image. The subtalar narrowing is seen, but most of the osseous findings are unapparent on the surface image. The high-density synovial hypertrophy is seen, however.

another significant complication of hemophilia. The bones most frequently implicated, in order of descending frequency, are the femur, pelvis, tibia, and small bones of the hand.

Case 13.4: Aneurysmal Bone Cyst of the Mandible

Clinical Information

A 15-year-old boy with a rapidly growing mass in the left mandible.

Postprocessing Techniques Used and Approach

Curved reconstructions are performed through the mandible to generate a CT Panorex type view of the mandible (Table 13.4 and Figures 13.4.1 through 13.4.3). This allows the entire mandible to be shown on one image. Surface-rendered images are used to show the bony

Table 13.4. Scan Acquisition Parameters for Case 13.4, Aneurysmal Bone Cyst of the Mandible

Slice No. and Thickness	**16 × 0.5 mm**
Coverage	**Face and mandible**
Helical Pitch	**1.25:1**
Rotation Speed	**0.5 sec**
Dose Parameters	**120 kVp, 150 mAs**
Contrast Dose	**None**

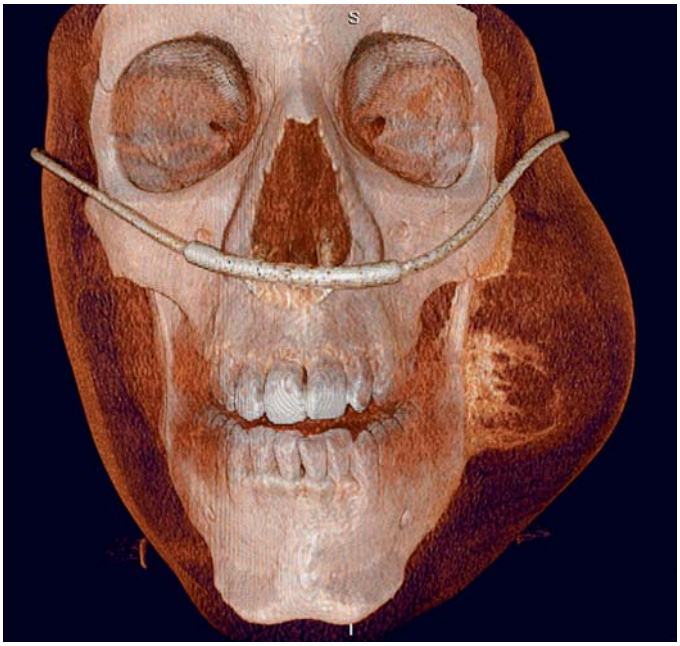

Figure 13.4.1. Three-dimensional soft tissue volume-rendered image demonstrates a large soft tissue mass arising from the left mandible.

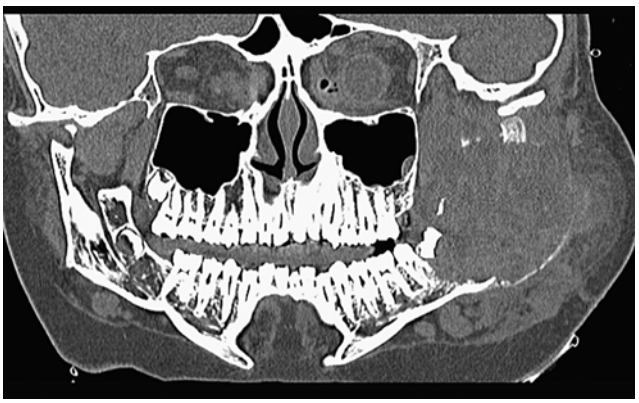

A

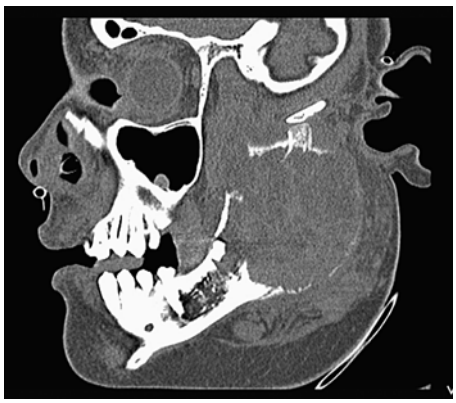

B

Figure 13.4.2. (A and B) Coronal and sagittal curved planar reformatted images through the mandible show a large expansile, lytic tumor of the mandible with a very thin cortical rim that is destroyed in some regions. The matrix is heterogeneous with areas of hemorrhage and fluid levels.

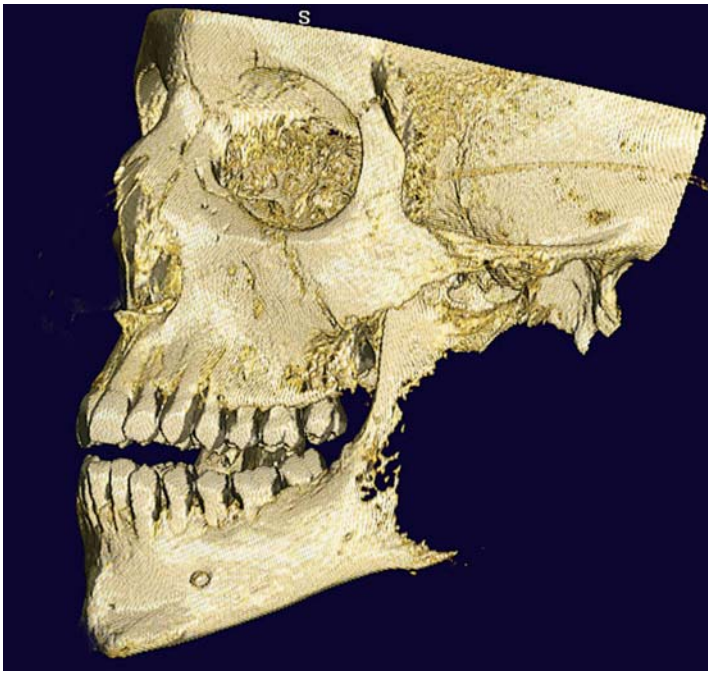

Figure 13.4.3. Surface-rendered view highlights the destruction of the mandibular body and ramus.

destruction in three dimensions. Volume rendering was also used to highlight the soft tissue mass.

Diagnosis

Aneurysmal bone cyst of the mandible.

Teaching Points

A CT examination was the first imaging test in this patient to suggest that this lesion could possibly be an aneurysmal bone cyst. An MRI had suggested an aggressive sarcoma. The CT was also instrumental in the surgical removal and reconstruction planned for this patient. Initial biopsy result in this patient was eventually diagnosed as an aneurysmal bone cyst. However, because of the aggressive appearance on imaging, there was concern that the lesion could be arising from a preexisting, possibly malignant lesion, which was not shown on the biopsy.

Aneurysmal bone cysts are benign expansile lesions that can be classified as primary (65%) or secondary (35%). Secondary aneurysmal bone cysts can arise from preexisting benign or malignant lesions. Most (80%) show the radiographic characteristics of the preexisting tumor. Many of these "blowout" lesions destroy most of the underlying process, allowing a missed diagnosis of malignancy at histologic examination. To prevent misdiagnosis, it is essential that the radiologist report any atypical and malignant features. The most common preexisting lesion is a giant cell tumor, which accounts for 19% to 39%

of cases in which the preceding lesion is found. Other common precursor lesions include osteoblastoma, angioma, and chondroblastoma. Less common lesions include fibrous dysplasia, nonossifying fibroma, chondromyxoid fibroma, solitary bone cyst, fibrous histiocytoma, eosinophilic granuloma, and even osteosarcoma.

The vast majority (approximately 80%) of patients with aneurysmal bone cyst are less than 20 years old. More than half of all such lesions occur in long bones, with approximately 12% to 30% of cases occurring in the spine. The pelvis accounts for approximately half of all flat bone lesions. Involvement of the mandible, maxilla, and temporal bone occurs but is relatively uncommon.

Case 13.5: Congenital Scoliosis

Clinical Information

A 12-year-old girl with congenital scoliosis. Study is performed for preoperative planning.

Postprocessing Techniques Used and Approach

In addition to standard multiplanar reconstructions, curved reconstructions are performed in both sagittal and coronal planes to better demonstrate and follow the spinal curvature (Table 13.5 and Figures 13.5.1 through 13.5.3). Three-dimensional surface-rendered images are also reviewed. The ribs are removed using a 3D sculpt so that they do not obscure the spine as the image is rotated.

Diagnosis

Congenital kyphoscoliosis related to T12 hemivertebra.

Teaching Points

Patients with congenital vertebral anomalies frequently are afflicted with kyphoscoliosis, with the curvatures often being severe and progressive. Conventional radiographic imaging for these disorders is often difficult to interpret because of the patient's small size, the complexity of the disorder, vertebral deformities that are not in the plane of the radiographs, and the presence of superimposed structures. It is

Table 13.5. Scan Acquisition Parameters for Case 13.5, Congenital Scoliosis

Slice No. and Thickness	**16 × 0.75 mm**
Coverage	**Thoracic and lumbar spine**
Helical Pitch	**0.94:1**
Rotation Speed	**0.75 sec**
Dose Parameters	**120 kVp, 130 mAs**
Contrast Dose	**None**

A

B

C

Figure 13.5.1. (A–C) Surface-rendered images in three projections with the ribs segmented out. Marked kyphoscoliosis is present. The cause of the scoliosis is shown to be a right T12 hemivertebra. Posterior view also demonstrates fusion of the posterior elements of the hemivertebra with those of L1, and spina bifida occulta of the S1 body.

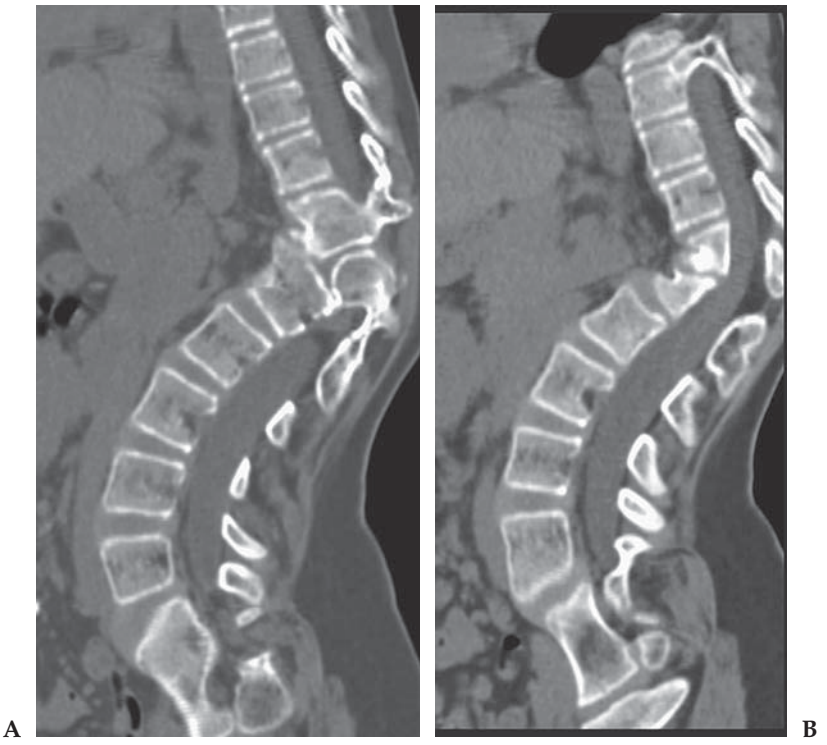

Figure 13.5.2. (A and B) Curved sagittal reconstructions. The first reconstruction (A) is right parasagittal and includes the hemivertebra, while the second (B) is left parasagittal and does not include the abnormal vertebral body. The vertebral alignment and kyphosis is much easier to appreciate on the curved images compared with conventional sagittal images. On the straight sagittal images the vertebral bodies constantly move in and out of the plane and it is impossible to see more than two or three vertebra on the same image.

Figure 13.5.3. Curved coronal reconstruction out of the plane of the hemivertebra. The spinal curvature is much easier to see on the curved image. Note the marked sclerosis and degenerative change at the T11–L1 articulation.

often difficult for both the radiologist and orthopedists to formulate an accurate 3D image of the pathology from radiographic studies. Spinal fusion almost always is the treatment of choice in such patients. Accurate preoperative characterization of the scoliosis and anomalies is essential for successful surgery.

Multiplanar reformatted and 3D MDCT imaging offers many potential advantages for defining congenital spine anomalies, including visualization of the deformity in any plane, from any angle, and with the overlying structures subtracted. Computed tomography has also been shown to be more accurate in characterizing the nature of the abnormality, and to be able to find additional abnormalities that were not detected by radiographs. A combination of 3D surface images and curved planar reconstructions are most useful for evaluation of the spine when severe kyphoscoliosis is present. The CPRs allow the spine to be viewed on one or two images rather that constantly following the spine in and out of plane on multiple images. The 3D reconstructions are valuable in defining failures of formation such as spina bifida, as well as showing the spinal curvature and alignment.

Computed tomography and MRI are often used as complementary tests for evaluation of congenital spine disorders. Magnetic resonance imaging excels in demonstrating the cord and spinal canal, whereas CT is superior for showing the vertebral bodies and for 3D reconstruction of the spine. Computed tomography also plays a major role in following these patients after spinal fusion to look at alignment and placement of hardware, and in evaluating the fusion and spinal canal.

Case 13.6: Brodie Abscess

Clinical Information

A 22-year-old man with several months of knee pain but no systemic symptoms or fever. Plain film showed a lytic lesion of the tibial metaphysis.

Postprocessing Techniques Used and Approach

Multiplanar reconstructions are used for initial review (Table 13.6 and Figures 13.6.1 and 13.6.2). Curved planar reconstructions were also

Table 13.6. Scan Acquisition Parameters for Case 13.6, Brodie Abscess

Slice No. and Thickness	**16 × 0.5 mm**
Coverage	**Knee and upper calf**
Helical Pitch	**1.25:1**
Rotation Speed	**0.75 sec**
Dose Parameters	**120 kVp, 150 mAs**
Contrast Dose	**None**

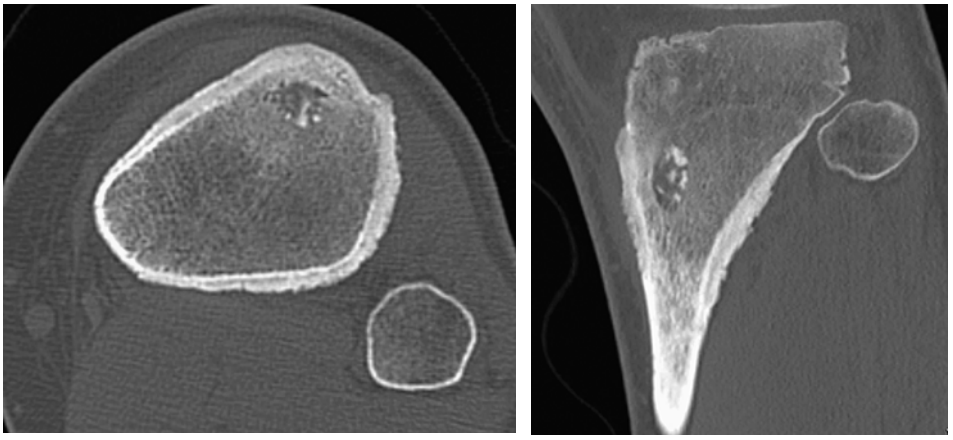

Figure 13.6.1. (A and B) Axial and sagittal 2-mm images through the proximal tibia. There is a lytic lesion in the metaphysis with a minimally sclerotic rim and small foci of sequestered bone centrally. Thick periosteal reaction is present.

used to better demonstrate the tract communicating from the abscess to the cortex. Surface-rendered images were also reviewed but were not very helpful in this case.

Diagnosis

Subacute osteomyelitis of the tibial metaphysis (Brodie abscess).

Teaching Points

Brodie abscess is a form of subacute osteomyelitis. It is characterized by mild-to-moderate dull pain, intermittent symptoms, and insidious

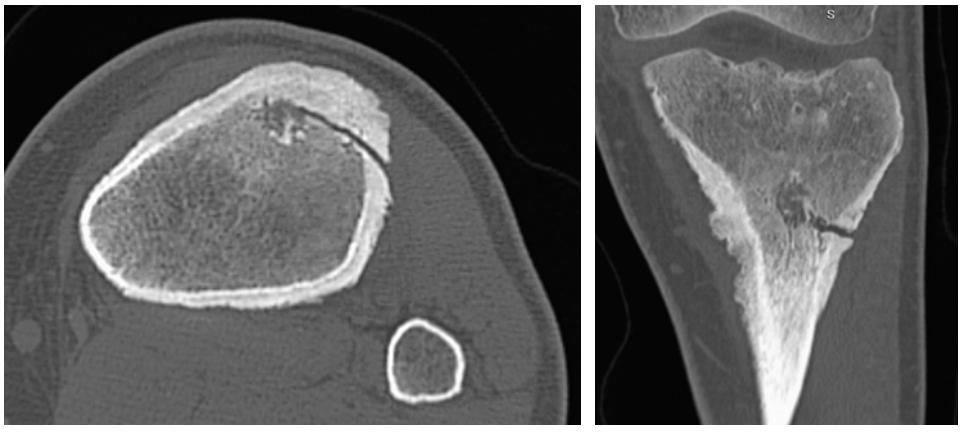

Figure 13.6.2. (A and B) Axial and coronal curved planar reconstructions. The curved reconstructions are done along the length of the fistula tract to better show the communication between the abscess and the bone cortex.

onset. Frequently there is a long delay between the onset of pain and diagnosis. The course is generally marked by few or no constitutional symptoms. Subacute osteomyelitis may mimic various benign and malignant conditions, resulting in delayed diagnosis and treatment. The causative organism usually is coagulase-positive *Staphylococcus* (30%–60%) but also can be other gram-positive and gram-negative organisms. Lesions are most often metaphyseal but also occur in the epiphysis and diaphysis. The tibia is the most common site, but a variety of bones can be involved.

The classic radiologic finding is a lytic lesion with a sclerotic border. Lesions can be well circumscribed or appear aggressive. Cortical hyperostosis may be present and mimic osteoid osteoma. Onionskin type periosteal reaction can also be seen. Other helpful findings include the presence of a sequestrum or a fistula to the cortex or growth plate.

Computed tomography can be very useful in these patients to better characterize the lesion and look for important ancillary findings. In this case the sequestration and cortical fistula were much better seen on the CT than on plain films. The CPRs were very useful to document the communication between the abscess and the bony cortex.

Case 13.7: Radial Fracture Nonunion

Clinical Information

A 41-year-old man status post internal fixation of a radial fracture undergoing evaluation for healing and pseudoarthrosis secondary to persistent pain at the fracture site.

Postprocessing Techniques Used and Approach

Oblique multiplanar reconstructions are reviewed on the workstation interactively. Surface-rendered images are also reviewed. No segmentation was needed (Table 13.7 and Figures 13.7.1 and 13.7.2).

Diagnosis

Nonunion of a mid radial shaft fracture post internal fixation.

Teaching Points

One of the great advantages of current MDCT scanners is the availability of reconstruction algorithms that minimize artifacts from metal.

Table 13.7. Scan Acquisition Parameters for Case 13.7, Radial Fracture Nonunion

Slice No. and Thickness	**16 × 0.5 mm**
Coverage	**Elbow to wrist**
Helical Pitch	**0.94:1**
Rotation Speed	**1.0 sec**
Dose Parameters	**120 kVp, 250 mAs**
Contrast Dose	**None**

With previous generation scanners it was almost impossible to scan patients with significant hardware or joint prostheses present and still obtain useful diagnostic information about the adjacent bone. Proper scan technique is important to minimize metal artifacts. Higher kV settings (135 kV as opposed to standard 120 kV), longer rotation time (1 sec), and special reconstruction filters designed for metal artifact reduction can make a significant difference in image quality and artifacts, although there is an increase in radiation dose to the patient.

With current MDCT scanners, we routinely scan patients with hardware in place to look for degree of healing or fusion, hardware failure, malpositioned screws, impingement on adjacent structures, or abnormalities of the underlying bone such as refracture, lytic destruction, or infection. Review of these cases on the workstation is very helpful. Interactive windowing to minimize streak artifact and use of oblique reconstructions are very helpful. Surface-rendered images are also an excellent way to demonstrate anatomy with minimal artifacts.

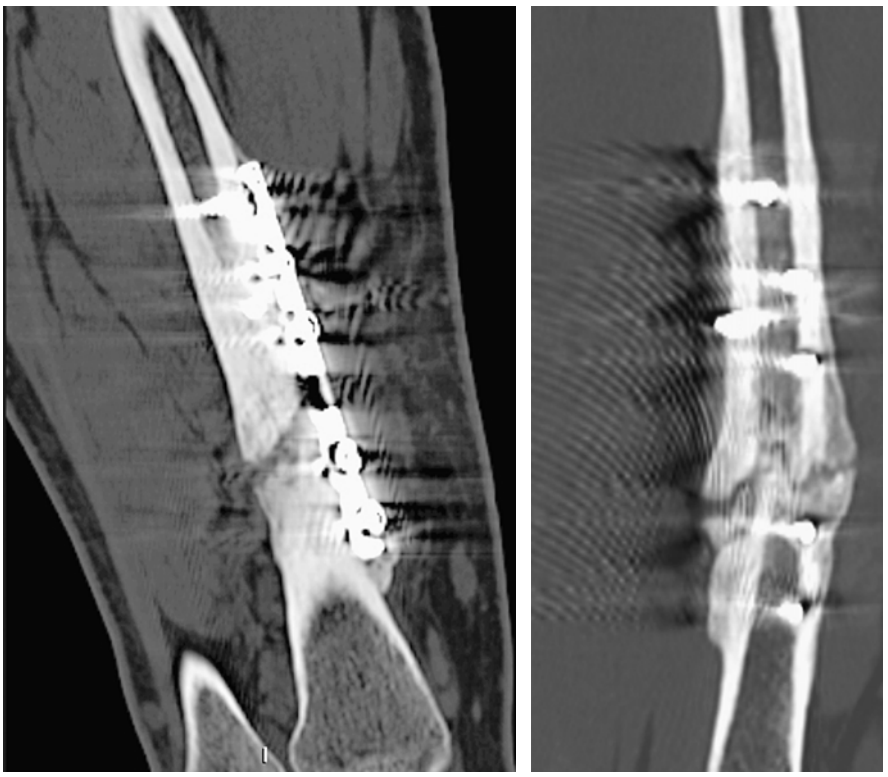

A B

Figure 13.7.1. (A and B) Oblique coronal and sagittal images oriented along the long axis of the radius. There are artifacts from the metal plate; however, excellent bone detail is still present, clearly showing nonunion of the fracture despite sclerosis and thick callus.

Figure 13.7.2. Surface-rendered image of the forearm. Window/level function is used to minimize streak artifact without obscuring bone detail. The nonunion is well seen with minimal artifacts.

Case 13.8: Osteochondroma of the Hand

Clinical Information

A 23-month-old boy with swelling and reduced mobility of his second metacarpal-phalangeal (MCP) joint. A palpable hard mass is present.

Postprocessing Techniques Used and Approach

Surface-rendered images of the hand and wrist are viewed in multiple projections (Table 13.8 and Figures 13.8.1 through 13.8.3). Oblique sagittal and coronal MPRs of the second digit are also performed. Segmentation using a 3D sculpt from the surface image is done to isolate the affected second metacarpal so it can be viewed from any angle.

Diagnosis

Osteochondroma of the second metacarpal of the hand.

Table 13.8. Scan Acquisition Parameters for Case 13.8, Osteochondroma of the Hand

Slice No. and Thickness	16 × 0.5 mm
Coverage	Hand and wrist
Helical Pitch	0.94:1
Rotation Speed	0.5 sec
Dose Parameters	100 kVp, 50 mAs
Contrast Dose	None

Teaching Points

This child had a painless lump and limited motion at the second MCP joint. Computed tomography is used in this case to confirm the diagnosis of osteochondroma by demonstrating contiguity of the cortex and medullary space of the bony growth with the metacarpal. The CT scan is also used for surgical planning. Excision of the osteochondroma to improve mobility was planned. The superior spatial resolution of MDCT combined with 3D imaging makes this the ideal test to characterize the lesion.

Osteochondromas are the most common benign tumors or tumorlike lesions of bone. Osteochondromas are developmental lesions rather

Figure 13.8.1. Surface-rendered image of the hand and wrist. Osteochondroma formation is present, involving the second metacarpal arising from the metaphysis and partially covering the epiphyseal ossification center.

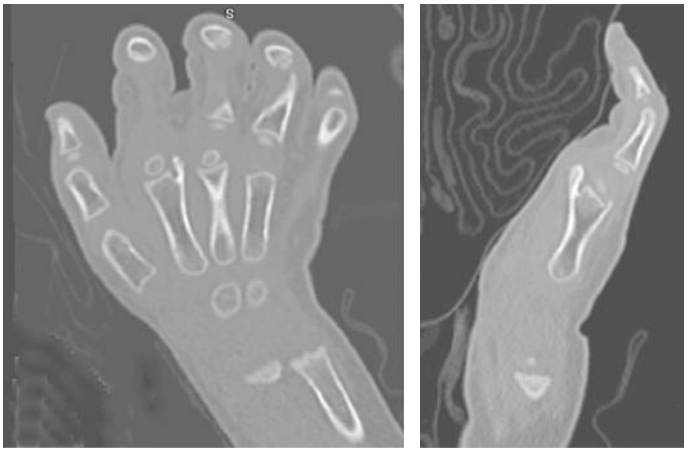

A B

Figure 13.8.2. (A and B) Double oblique coronal and sagittal images show the osteochondroma arising at the metaphysis. Contiguity of the cortical and medullary space of the lesion and the metacarpal shaft is shown.

A B

Figure 13.8.3. (A and B) Segmented SR images of the isolated second metacarpal again showing the abnormality.

than true neoplasms and are often referred to as an osteocartilaginous exostosis or simply exostosis. Any bone that develops from preformed cartilage (enchondral ossification) may develop an osteochondroma. The long bones of the lower extremity are most frequently affected. As with other bone tumors, osteochondromas occur most often about the knee (40% of cases). The femur (usually distal) is the single most frequently affected bone (30% of cases). Tibial osteochondromas account for 15% to 20% of cases and most commonly occur in a proximal location. The humerus is also a frequent site of osteochondromas. Other more unusual locations of osteochondroma include small bones of the hands and feet, scapula, pelvis, and spine. Long bone lesions frequently affect the metaphysis, with the diaphysis being a rare location.

The radiographic appearance of osteochondromas is frequently characteristic. The lesion is composed of cortical and medullary bone with an overlying hyaline cartilage cap. In all cases there must be continuity of this lesion with the underlying native bone cortex and medullary canal. Osteochondromas may be solitary or multiple, with the latter associated with the syndrome hereditary multiple exostoses. Complications are commonly associated with these exophytic masses and include cosmetic and osseous deformity, fracture, vascular compromise, neurologic sequelae, overlying bursa formation, and malignant transformation.

The vast majority of solitary osteochondromas are asymptomatic and, if detected, are found incidentally. Symptomatic lesions usually occur in younger patients, with 75% to 80% of such cases being discovered before the age of 20 years. The most common symptom related to osteochondroma is a nontender, painless cosmetic deformity related to the slowly enlarging exophytic mass. Additional complications that cause symptoms include osseous deformity, fracture, vascular compromise, neurologic sequelae, overlying bursa formation, and malignant transformation. Surgical intervention for these lesions may be necessary. Excision, even incomplete resection, may result in a reduction of symptoms.

Case 13.9: Posterior Labral Tear of the Shoulder

Clinical Information

An 83-year-old woman with a prior traumatic humeral neck fracture and posterior dislocation of the shoulder. She is evaluated for persistent shoulder pain and limited mobility.

Postprocessing Techniques Used and Approach

Multiplanar images are reconstructed on the scan console. Oblique MPRs are also reviewed on the workstation (Table 13.9 and Figures 13.9.1 and 13.9.2).

Diagnosis

Posterior labral tear with posterior/inferior glenoid rim fracture (reverse Bankart lesion) and healed fracture of the humeral head.

Table 13.9. Scan Acquisition Parameters for Case 13.9, Posterior Labral Tear of the Shoulder

Slice No. and Thickness	**16 × 0.5 mm**
Coverage	**Through shoulder**
Helical Pitch	**0.94:1**
Rotation Speed	**0.75 sec**
Dose Parameters	**120 kVp, 210 mAs**
Contrast Dose	**15 mL intraarticular contrast and 20 mL intraarticular air**

Figure 13.9.1. Oblique coronal MPR image. Deformity of the humeral head from the prior fracture is present. Coronal view shows posterior/inferior glenoid rim fracture and absence of inferior labrum.

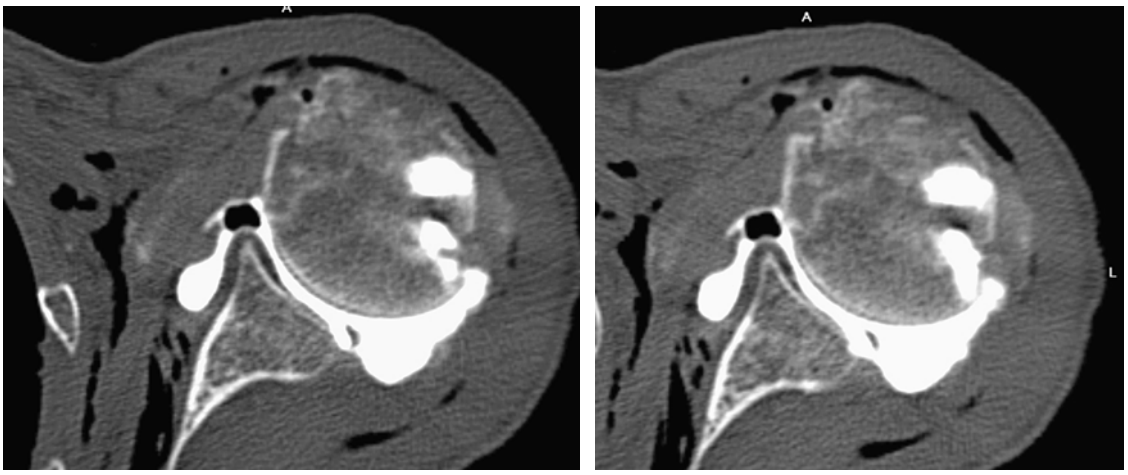

A B

Figure 13.9.2. (A and B) Axial 2-mm images at the level of the inferior glenoid. Tear and displacement of the posterior labrum are shown, as is the glenoid fracture.

Teaching Points

Reverse Bankart injuries are associated with posterior shoulder dislocations. Typical findings include posterior labral tear, posterior glenoid rim fracture, and reverse Hill-Sachs lesion of the anterior humeral head. Computed tomographic arthrography is an excellent way to visualize these abnormalities, particularly in patients who are unable to undergo MRI. In this patient intraarticular contrast followed by air was injected into the joint. The majority of the air leaked out of the joint through a capsular defect. I now prefer to inject contrast diluted 50/50 with saline rather than a mixed contrast/air injection for CT arthrography.

Selected Readings

Knee Arthrogram

1. Farber JM. CT arthrography and postoperative musculoskeletal imaging with multichannel computed tomography. Semin Musculoskelet Radiol 2004 Jun;8(2):157–166.
2. Lee W, Kim HS, Kim SJ, et al. CT arthrography and virtual arthroscopy in the diagnosis of the anterior cruciate ligament and meniscal abnormalities of the knee joint. Korean J Radiol 2004 Jan–Mar;5(1):47–54.
3. Mutschler C, Vande Berg BC, Lecouvet FE, et al. Postoperative meniscus: assessment at dual-detector row spiral CT arthrography of the knee. Radiology 2003 Sep;228(3):635–641.
4. Vande Berg BC, Lecouvet FE, Poilvache P, et al. Dual-detector spiral CT arthrography of the knee: accuracy for detection of meniscal abnormalities and unstable meniscal tears. Radiology 2000;216:851–857.
5. Vande Berg BC, Lecouvet FE, Poilvache P, Dubuc JE, Maldague B, Malghem J. Anterior cruciate ligament tears and associated meniscal lesions: assessment at dual-detector spiral CT arthrography. Radiology 2002;223: 403–409.

Scaphoid Fracture Nonunion

6. Farber JM. Imaging of the wrist with multichannel CT. Semin Musculoskelet Radiol 2004 Jun;8(2):167–173.
7. Kiuru MJ, Haapamaki VV, Koivikko MP, Koskinen SK. Wrist injuries: diagnosis with multidetector CT. Emerg Radiol 2004 Feb;10(4):182–185.
8. Neyman EG, Corl FS, Fishman EK. 3D-CT evaluation of metallic implants: principles, techniques, and applications. Crit Rev Comput Tomogr 2002; 43(6):419–452.
9. Trumble T, Nyland W. Scaphoid nonunions. Pitfalls and pearls. Hand Clin 2001 Nov;17(4):611–624.

Hemophilic Arthropathy

10. Hermann G, Gilbert MS, Abdelwahab IF. Hemophilia: evaluation of musculoskeletal involvement with CT, sonography and MR imaging. Am J Roentgenol 1992;158:119–123.
11. Kerr R. Imaging of musculoskeletal complications of hemophilia. Semin Musculoskelet Radiol 2003 Jun;7(2):127–136.

12. Park SJ, Ryu KN. Hemophilic pseudotumor involving the musculoskeletal system: spectrum of radiologic findings. Am J Roentgenol 2004 Jul;183:55–61.
13. Stafford JM, James TT, Allen AM, Dixon LR. Hemophilic pseudotumor: radiologic-pathologic correlation. Radiographics 2003;23:852–856.

Aneurysmal Bone Cyst of the Mandible

14. Asaumi J, Konouchi H, Hisatomi M, et al. MR features of aneurysmal bone cyst of the mandible and characteristics distinguishing it from other lesions. Eur J Radiol 2003 Feb;45(2):108–112.
15. DelBalso AM. Lesions of the jaws. Semin Ultrasound CT MR 1995 Dec;16(6):487–512.
16. Kransdorf MJ, Sweet DE. Aneurysmal bone cyst: concept, controversy, clinical presentation, and imaging. Am J Roentgenol 1995 Mar;164:573–580.
17. Weber AL, Bui C, Kaneda T. Malignant tumors of the mandible and maxilla. Neuroimaging Clin N Am 2003 Aug;13(3):509–524.
18. Yoshiura K, Weber AL, Runnels S, Scrivani SJ. Cystic lesions of the mandible and maxilla. Neuroimaging Clin N Am 2003 Aug;13(3):485–494.

Congenital Scoliosis

19. Bush CH, Kalen V. Three-dimensional computed tomography in the assessment of congenital scoliosis. Skeletal Radiol 1999 Nov;28(11):632–637.
20. Kamimura M, Kinoshita T, Itoh H, et al. Preoperative CT examination for accurate and safe anterior spinal instrumentation surgery with endoscopic approach. J Spinal Disord Tech 2002 Feb;15(1):47–51.
21. Newton PO, Hahn GW, Fricka KB, Wenger DR. Utility of three-dimensional and multiplanar reformatted computed tomography for evaluation of pediatric congenital spine abnormalities. Spine 2002 Apr;27(8):844–850.
22. Sucato DJ, Kassab F, Dempsey M. Analysis of screw placement relative to the aorta and spinal canal following anterior instrumentation for thoracic idiopathic scoliosis. Spine 2004 Mar;29(5):554–559.

Brodie Abscess

23. Miller WB Jr, Murphy WA, Gilula LA. Brodie abscess: reappraisal. Radiology 1979 Jul;132(1):15–23.
24. Rasool MN. Primary subacute haematogenous osteomyelitis in children. J Bone Joint Surg Br 2001 Jan;83(1):93–98.

Radial Fracture Nonunion

25. Buckwalter KA, Rydberg J, Kopecky KK, Crow K, Yang EL. Musculoskeletal imaging with multislice CT. Am J Roentgenol 2001 Apr;176:979–986.
26. Buckwalter KA, Farber JM. Application of multidetector CT in skeletal trauma. Semin Musculoskelet Radiol 2004 Jun;8(2):147–156.
27. Farber JM. CT arthrography and postoperative musculoskeletal imaging with multichannel computed tomography. Semin Musculoskelet Radiol 2004 Jun;8(2):157–166.
28. Horton KM. CT imaging of patients with metallic hardware. Crit Rev Comput Tomogr 2003;44(6):305–313.
29. Link TM, Berning W, Scherf S, et al. CT of metal implants: reduction of artifacts using an extended CT scale technique. Comput Assist Tomogr 2000 Jan–Feb;24(1):165–172.

30. Neyman EG, Corl FS, Fishman EK. 3D-CT evaluation of metallic implants: principles, techniques, and applications. Crit Rev Comput Tomogr 2002; 43(6):419–452.

Osteochondroma of the Hand

31. Karasick D, Schweitzer ME, Eschelman DJ. Symptomatic osteochondromas: imaging features. Am J Roentgenol 1997;168:1507–1512.
32. Kobayashi H, Kotoura Y, Hosono M, et al. 3D-spiral CT of multiple exostoses. Comput Med Imaging Graph 1995;19:419–422.
33. Murphey MD, Choi JJ, Kransdorf MJ, Flemming DJ, Gannon FH. Imaging of osteochondroma: variants and complications with radiologic-pathologic correlation. Radiographics 2000 Sep–Oct;20(5):1407–1434.

Posterior Labral Tear of the Shoulder

34. Bresler F, Blum A, Braun M, et al. Assessment of the superior labrum of the shoulder joint with CT-arthrography and MR-arthrography: correlation with anatomical dissection. Surg Radiol Anat 1998;19:57–62.
35. Maeseneer MD, Roy FR, Lenchik L, et al. CT and MR arthrography of the normal and pathologic anterosuperior labrum and labral-bicipital complex. Radiographics 2000;20:67–81.
36. Stoller DW, Tirman PF, Bredella MA, et al. Diagnostic Imaging: Orthopedics. Salt Lake City, Utah: Amirsys; 2004.

Chapter 14

Neuroimaging

Case 14.1: Cerebral Aneurysms (Three Patients)

Clinical Information

Patient 1: a 59-year-old woman with acute left temporal parenchymal and subarachnoid hemorrhage (SAH). Patient 2: an 87-year-old man with an abnormal vertebral and basilar arteries detected on noncontrast CT examination. Patient 3: a 56-year-old woman with headache and SAH.

Postprocessing Techniques Used and Approach

A combination of MIP and volume images are used to evaluate the circle of Willis (COW) (Table 14.1 and Figures 14.1.1 through 14.1.3). Sliding thin-slab MIPs are reviewed initially. Slice thickness is varied interactively. Thicker slabs show the anatomy better, but thinner slabs show more detail, such as the size of the aneurysm neck. Volume images are produced after manual segmentation. Contours are drawn around the arteries on 2D axial images and interpolated into the entire volume. Extraneous small veins are removed either by a 3D sculpt or by changing window/level settings to take advantage of the denser enhancement in the arteries. Unsegmented volume images can also be reviewed, but it is often more difficult to visualize the aneurysms and their necks because there is less freedom of rotation related to overlapping vessels.

Diagnosis

Patient 1: aneurysms of the left supraclinoid internal carotid artery (ICA), basilar artery, and proximal left anterior cerebral artery (ACA). Patient 2: fusiform aneurysm of the left vertebral and basilar artery. Patient 3: bilateral middle cerebral artery (MCA) trifurcation aneurysms and aneurysm of the right pericallosal artery.

Table 14.1. Scan Acquisition Parameters for Case 14.1, Cerebral Aneurysms

Slice No. and Thickness	16 × 0.5 mm
Coverage	Skull base though brain
Helical Pitch	1.25:1
Rotation Speed	0.75 sec
Dose Parameters	135 kVp, 195 mAs
Contrast Dose	75 mL Omnipaque 350
Injection Rate	3 mL/sec
Bolus Timing Method	Bolus triggering on the carotid artery

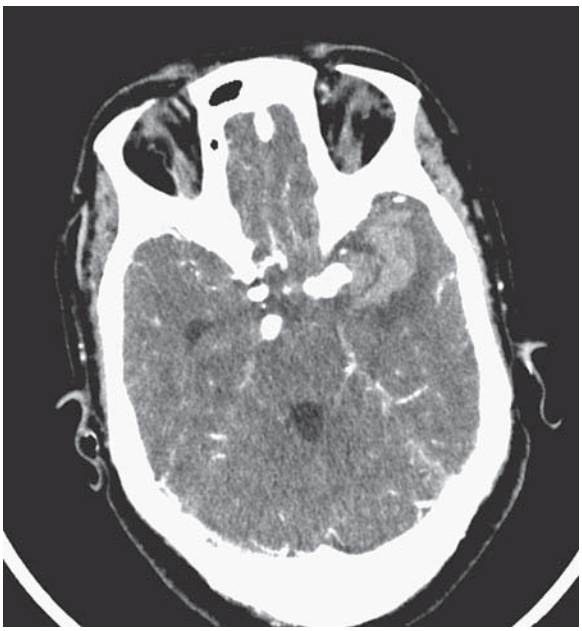

A

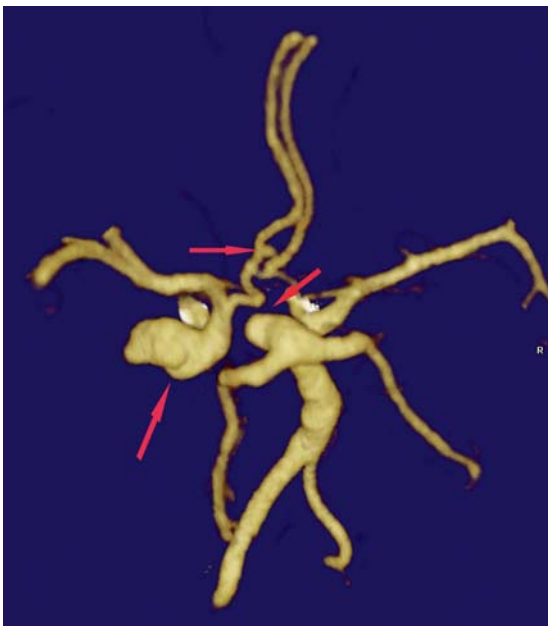

B

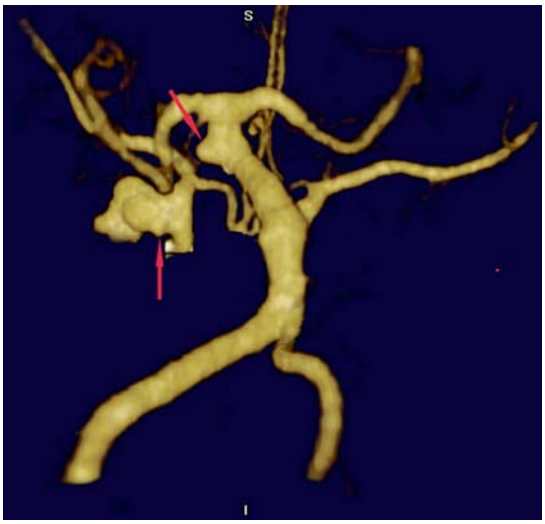

C

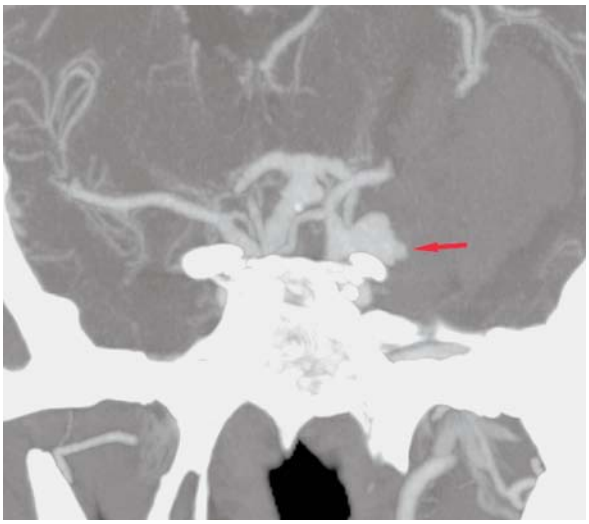

D

Figure 14.1.1. (A) Patient 1: Axial 3-mm image from the CTA study demonstrates an enhancing aneurysm arising from the left ICA with acute hemorrhage in the adjacent temporal lobe with surrounding edema. (B and C) Three-dimensional segmented volume image of the COW in two different projections. Three aneurysms are shown (arrows). There is a large, irregular aneurysm arising from the left supraclinoid ICA. This is the aneurysm that acutely bled. The second aneurysm arises from the basilar artery just proximal to the superior cerebellar artery and measures 4 mm. This aneurysm also projects to the left. The third aneurysm measures only 2 mm and arises from the left anterior cerebral artery just distal to the ACOM. (D) Coronal thin slab MIP image demonstrates the ICA and basilar aneurysms. Also note the small "teat" (arrow) projecting from the large aneurysm. This corresponds to the site of rupture.

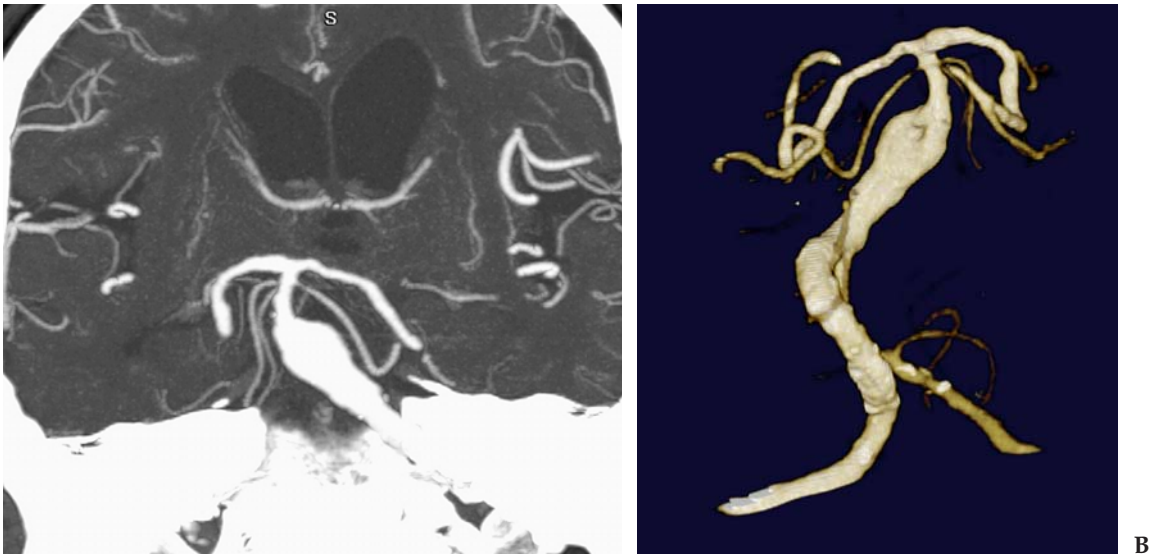

A B

Figure 14.1.2. (A) Patient 2: coronal thin-slab MIP through the posterior fossa. There is fusiform aneurysmal dilatation of the vertebral and proximal basilar arteries. (B) Segmented VR image of the vertebrobasilar system. The fusiform dilatation is well shown on the volume image.

Teaching Points

Currently, catheter angiography is considered the gold standard for the diagnosis and evaluation of intracranial aneurysms. Our experience with 16-slice CTA suggests that this may not always be the case in the future. We have found CTA to be extremely sensitive and specific in the diagnosis of aneurysms, and have found several aneurysms with

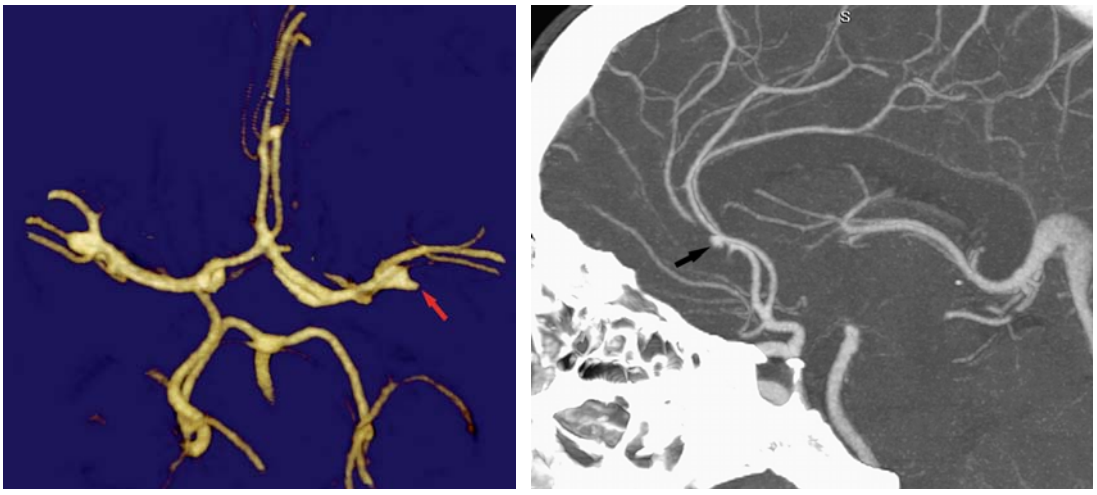

A B

Figure 14.1.3. (A) Patient 3: segmented VR image of the COW. Bilateral MCA trifurcation aneurysms are present. The right-sided aneurysm has a teat sign (arrow) and is the site of rupture. There is also a 2-mm right pericallosal aneurysm. (B) Sagittal thin-slab MIP showing the pericallosal aneurysm (arrow).

CTA that were overlooked initially on the catheter angiogram (including the left ACA aneurysm in Patient 3).

Besides detection of aneurysms, CTA offers many additional benefits. With catheter angiography the radiologist is limited to a certain number of views. In some cases the ideal view to demonstrate the aneurysm neck cannot be obtained. This is not a problem with CTA. Three-dimensional data sets allow the images to be interactively rotated on a 3D workstation to optimally demonstrate the pathology. Source image data can also be reviewed to measure the aneurysm and precisely define the aneurysm neck.

Computed tomographic angiography, MRA, and catheter angiography are often complementary. Computed tomographic angiography excels at demonstrating aneurysms arising at the circle of Willis, but it has more trouble with lesions occurring in the carotid canal, at the ophthalmic artery origin, and sometimes from the posterior-inferior cerebellar artery. These areas are difficult to visualize on volume-rendered images and should be carefully scrutinized on thin slab MIPs and source images. In patients with SAH, we perform CTA as the initial diagnostic test. If the CTA does not demonstrate the source of hemorrhage, we always proceed with a catheter angiogram.

Our neurosurgeons have found CTA be an extremely valuable tool prior to aneurysm surgery. They not only see the aneurysm, but also can see its relationship to the surrounding brain and bony landmarks. They can use the 3D workstation to plan a virtual surgery. The surgeon can orient the head exactly as he will in the operating room and plan the best approach to the aneurysm prior to the craniotomy.

The precise incidence of intracranial berry aneurysms is unknown. In the past, most berry aneurysms were thought to be congenital in origin, arising from focal defects in the media and gradually developing over a period of years as arterial pressure first weakens and subsequently balloons out the vessel wall. Recent studies, however, suggest most intracranial aneurysms probably result from hemodynamically induced degenerative vascular injury. Less common causes of saccular aneurysms include trauma, infection, tumor, drug abuse (cocaine), and high-flow states associated with arteriovenous malformations (AVMs) or fistulae. Some associated conditions include: anomalous vessels, coarctation of the aorta, polycystic kidney disease, fibromuscular dysplasia (FMD), connective tissue disorders (e.g., Marfan, Ehlers-Danlos), and high-flow states (e.g., vascular malformations, fistulae).

Intracranial aneurysms are multiple in 15% to 20% of all cases. A strong female predilection is observed with multiple aneurysms. Aneurysms typically become symptomatic in people aged 40 years to 60 years, and are uncommon in pediatric patients unless associated with trauma, infection, or AVMs.

Aneurysms commonly arise at the bifurcations of major arteries. Most saccular aneurysms arise on the circle of Willis or the middle cerebral artery bifurcation. Common locations are the anterior communicating artery (ACOM) (30%–35%), the internal carotid artery at the posterior communicating artery origin (30%–35%), and the MCA bifur-

cation (20%). Approximately 15% of all intracranial aneurysms arise from the posterior (vertebrobasilar) circulation.

The risk of aneurysm rupture is difficult to determine precisely but is estimated at 1% to 2% per year, cumulative, for asymptomatic lesions that have not yet ruptured. Ruptured aneurysms that are not operated on have a very high risk of rebleeding after the initial hemorrhage has occurred. The risk is estimated at 20% to 50% in the first 2 weeks, and such rebleeding carries a mortality rate of nearly 85%.

Case 14.2: Carotid Thrombus

Clinical Information

A 50-year-old man with sudden onset of right-sided weakness. Stat MRI was performed which showed several small embolic type infarcts in the left MCA territory on diffusion-weighted images. Following this, carotid CTA was done to look for occlusive disease of the carotid bifurcations.

Postprocessing Techniques Used and Approach

The images demonstrating the carotid artery with thrombus are oblique MPRs created on the workstation (Table 14.2 and Figures 14.2.1 through 14.2.4). Segmented VR images are also created using vessel-tracking software to better show the occluded external carotid artery (ECA) and narrowed ICA. Had the vessels been more tortuous, curved reconstructions would have been used instead of the oblique MPRs.

Diagnosis

Acute hemorrhage into a preexisting carotid plaque with free-floating thrombus extending into the internal carotid artery and occluding the origin of the external carotid artery. This resulted in microembolism to the left cerebral hemisphere.

Teaching Points

The CTA provided a rapid, noninvasive diagnosis in this case that was potentially lifesaving. Catheter angiography may have been dangerous in this patient given the unstable appearance of the thrombus in the

Table 14.2. Scan Acquisition Parameters for Case 14.2, Carotid Thrombus

Slice No. and Thickness	**16 × 0.5 mm**
Coverage	**Aortic arch to skull base**
Helical Pitch	**1.25:1**
Rotation Speed	**0.5 sec**
Dose Parameters	**120 kVp, 125 mAs**
Contrast Dose	**75 mL Omnipaque 350**
Injection Rate	**4 mL/sec**
Bolus Timing Method	**Bolus triggering focused on the aortic arch**

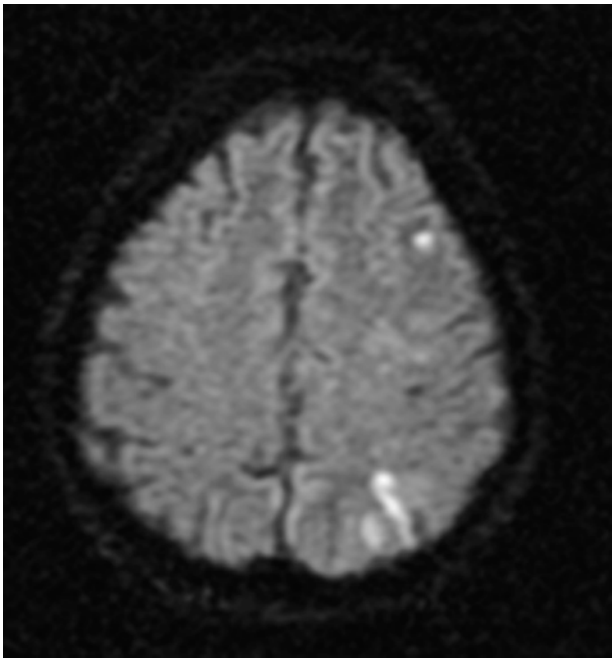

Figure 14.2.1. Diffusion MRI demonstrates several small acute infarcts in the left MCA territory. Distribution is suggestive of embolic disease.

carotid artery. The CTA was performed emergently and clearly showed the diagnosis. Based on the CTA findings the patient was felt to be at very high risk for additional embolic events. He was taken emergently to surgery based on the CTA findings, and the thrombus was removed. The surgeon was able to remove the entire thrombus en bloc, leaving a nearly normal underlying artery. A potentially catastrophic stroke was thereby averted in this 50-year-old man.

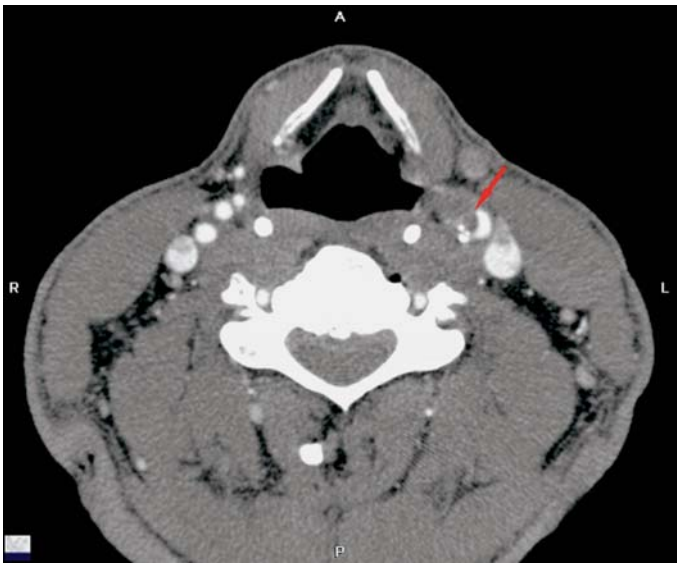

Figure 14.2.2. Axial source image demonstrating thrombus occluding the origin of the left external carotid artery and extending into the origin of the internal carotid artery (arrow).

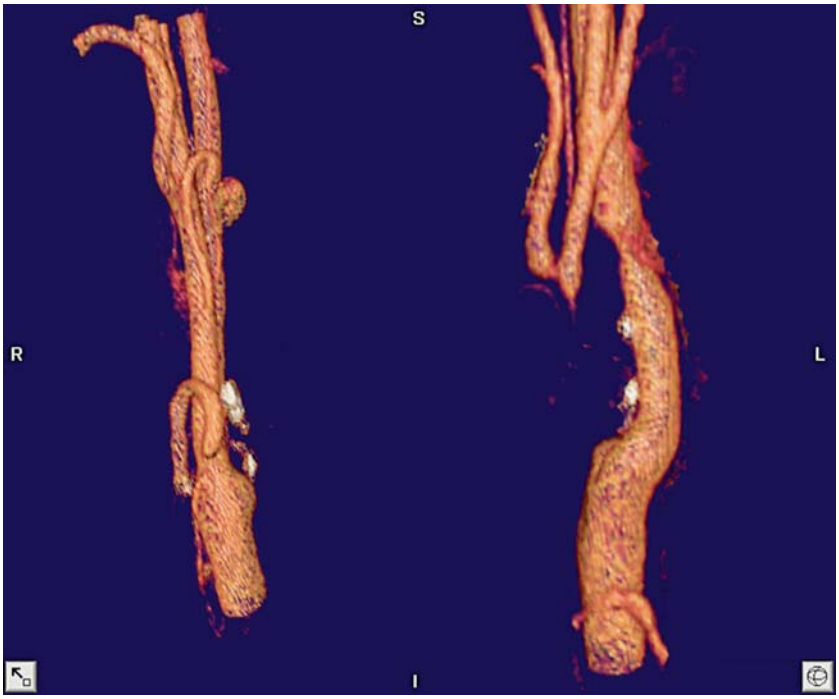

Figure 14.2.3. Three-dimensional volume image demonstrating occlusion of the origin of the left external carotid artery with smooth narrowing at the origin of the internal carotid artery.

A

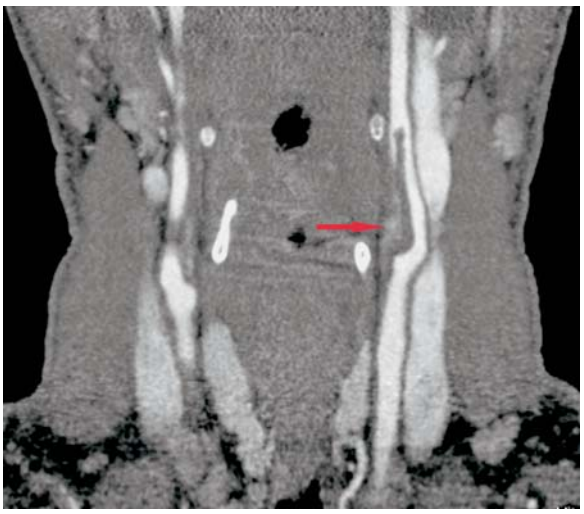

B

Figure 14.2.4. (A and B) Sagittal and coronal oblique MPR images of the left carotid bifurcation. Thrombus is demonstrated occluding the origin of the external carotid, with a tongue of thrombus seen extending up the internal carotid artery. High density is present within the thrombus (arrows) consistent with acute hemorrhage.

Many stroke centers are now using MDCT as part of a comprehensive emergent stroke evaluation protocol. This approach starts with a noncontrast CT of the brain to look for hemorrhage, followed by a CT perfusion examination of the brain, and finally a CT angiogram from the aortic arch through the circle of Willis. The major advantage of a comprehensive CT stroke protocol is that CT is much more readily available and easier to access compared with MRI for emergency room patients in most hospitals. The disadvantages include incomplete visualization of the entire brain on perfusion with current scanners (inferior to MRI diffusion/perfusion evaluation) and the postprocessing time needed to evaluate the brain perfusion and CT angiogram. Improvements in software and next generation scanners will hopefully limit or eliminate these disadvantages.

Case 14.3: Sphenoidal Encephalocele

Clinical Information

A 6-year-old boy with two episodes of meningitis.

Postprocessing Techniques Used and Approach

Only standard axial, sagittal, and coronal reconstructions were used (Table 14.3 and Figures 14.3.1 and 14.3.2).

Diagnosis

Transsphenoidal meningoencephalocele containing the pituitary gland and the optic chiasm.

Teaching Points

With current MDCT scanners, high-resolution brain imaging is a simple and effective tool. In this child an important clinical diagnosis was made in a scan that took only a few seconds and required no sedation. As long as brain scans are performed with a helical protocol using collimation of 1 mm or less, very high quality multiplanar reconstructions can be performed and reviewed on a routine or as needed basis.

Cephaloceles result from herniation of intracranial contents through a defect in the skull with a persistent connection to the subarachnoid space. If they contain only meninges and cerebrospinal fluid (CSF) they

Table 14.3. Scan Acquisition Parameters for Case 14.3, Sphenoidal Encephalocele

Slice No. and Thickness	**16 × 0.5 mm**
Coverage	**Brain and skull base**
Helical Pitch	**0.94:1**
Rotation Speed	**0.5 sec**
Dose Parameters	**120 kVp, 125 mAs**
Contrast Dose	**None**

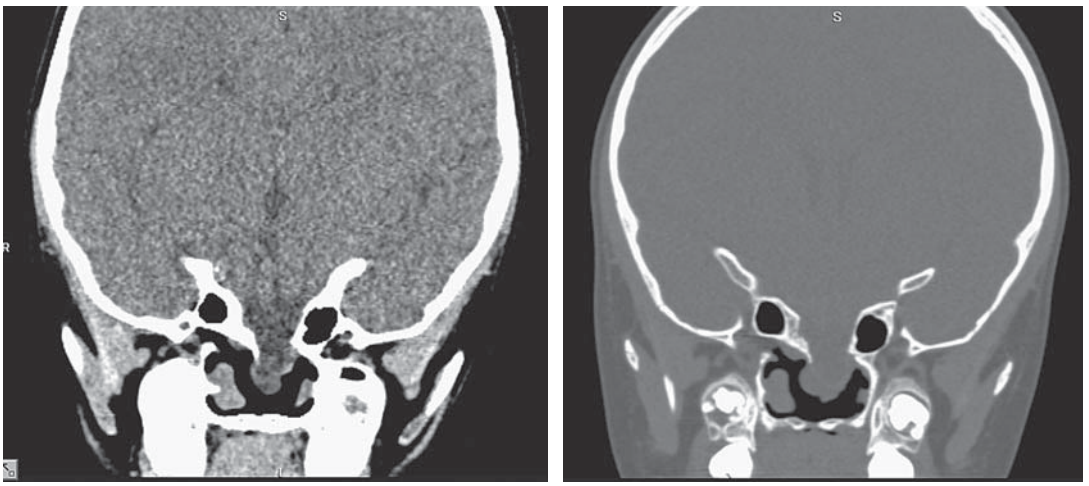

Figure 14.3.1. (A and B) High-resolution 0.5-mm coronal images in soft tissue and bone window. There is a left parasagittal defect in the sphenoid bone with herniation of meninges and CSF into the sphenoid sinus.

are termed meningoceles, but if they also contain brain they are termed meningoencephaloceles. They occur in one of every 4,000 live births and have no sex predilection. The nomenclature used for encephaloceles is based on the origin of their roof and floor; thus, for example, the roof and floor of frontonasal encephaloceles are the frontal and nasal bones, respectively. Cephaloceles are also classified according to location as either occipital (75% of cases), sincipital (15%), or basal

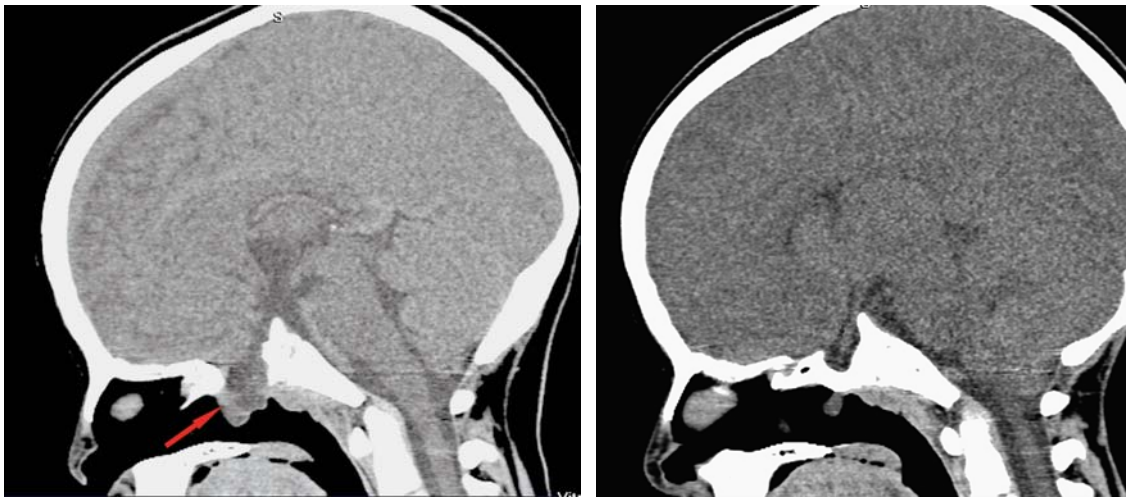

Figure 14.3.2. (A and B) Sagittal 0.5-mm images again show the bone defect and encephalocele. The pituitary tissue is shown at the bottom of the encephalocele (arrow). Paramidline image shows the optic chiasm partially extending into the sac.

(10%). Sincipital cephaloceles involve the midface (anterior skull) and occur about the dorsum of the nose, the orbits, and the forehead. They are typically either frontonasal (40%–60% of cases) or nasoethmoidal (30%), with the remaining 10% being a combination of the two. Basal cephaloceles involve the sphenoid or ethmoid bone and may relate to either persistence of the craniopharyngeal canal—which may create an osseous defect—or failure of the ossification centers within the sphenoid bone. A major difference between basal and sincipital cephaloceles is that sincipital lesions are always externally visible and basal lesions are not. Transsphenoidal encephaloceles typically extend through the floor of the sella turcica and contain the pituitary gland, hypothalamus, anterior recess of the third ventricle, and the optic apparatus.

Cephaloceles have a high prevalence of associated intracranial anomalies, including intracranial cysts, callosal agenesis, interhemispheric lipomas, facial clefts, and schizencephaly. Younger siblings of affected patients are at a 6% risk for a congenital central nervous system abnormality.

The clinical manifestation of encephaloceles is variable and may consist of an obvious mass, nasal stuffiness, rhinorrhea, a broad nasal root, or hypertelorism. Depending on the size of the intracranial connection, encephaloceles may be pulsatile or change in size during crying, the Valsalva maneuver, or jugular compression. Biopsy is contraindicated in encephaloceles due to the potential for cerebrospinal fluid leaks, seizures, or meningitis.

Encephaloceles are treated with complete surgical resection as soon as possible to prevent cerebrospinal fluid leakage, meningitis, or increase in mass size. The surgical approach initially involves addressing intracranial involvement and repairing the dura mater. The extracranial portion of the lesion may be resected simultaneously or at a later time. Resection of the extracranial portion does not lead to an increased risk of neurologic deficit due to the abnormal function of the herniated brain tissue.

Case 14.4: Arachnoiditis

Clinical Information

A 61-year-old man with a history of a traumatic fracture of L3. He has previously undergone laminectomy with spinal fusion. He now has recurrent back pain, leg weakness, and paresthesias.

Postprocessing Techniques Used and Approach

Standard coronal, sagittal, and axial reconstructions provide most of the necessary information (Table 14.4 and Figures 14.4.1 through 14.4.4). Oblique reconstructions can also be useful for evaluating disc spaces or hardware in the long axis. The case is also reviewed with surface rendering on the workstation. This is useful to show the bony fusion and laminectomy. The isolated metal images are created using

Table 14.4. Scan Acquisition Parameters for Case 14.4, Arachnoiditis

Slice No. and Thickness	**16 × 0.5 mm**
Coverage	**Lower thoracic and lumbar spines**
Helical Pitch	**0.94:1**
Rotation Speed	**1 sec**
Dose Parameters	**135 kVp, 340 mAs**
Contrast Dose	**10 mL Isovue 200 m, intrathecal**

an SR protocol and using window/level controls to remove bone and soft tissue until only the metal remains.

Diagnosis

Arachnoiditis following spinal fusion.

Teaching Points

The imaging of the postoperative spine has long been a very challenging and difficult area. Magnetic resonance imaging with gadolinium is effective in many patients, but the presence of fusion hardware causes significant susceptibility to artifacts which can render the study limited in the region of the hardware. Until recently CT had a similar problem. Beam-hardening artifacts at the level of the metal would typically make those slices uninterpretable. Most current MDCT scanners have

Figure 14.4.1. Sagittal MPR image demonstrates a fracture of the L3 vertebral body. The patient has had a previous laminectomy with fusion from L2 to L4.

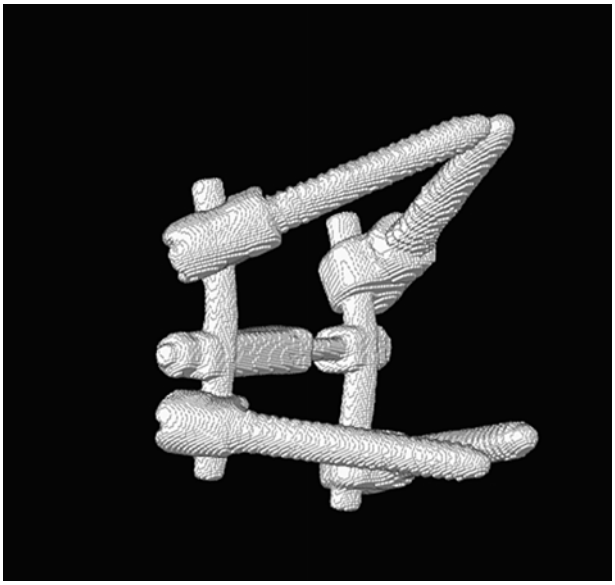

Figure 14.4.2. Isolated SR image of the spinal hardware. Other structures have been windowed out.

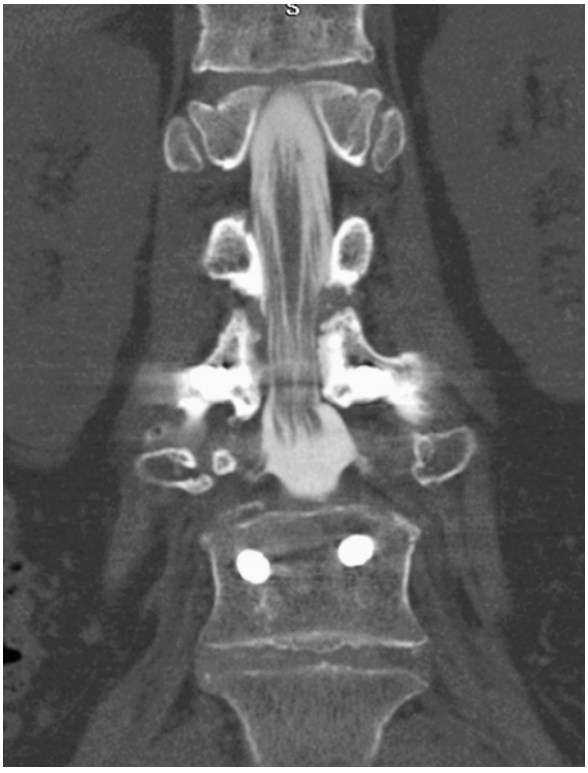

Figure 14.4.3. Coronal MPR image through the conus. Exquisite detail of the nerve roots of the cauda equina is evident. The roots appear normal at this level.

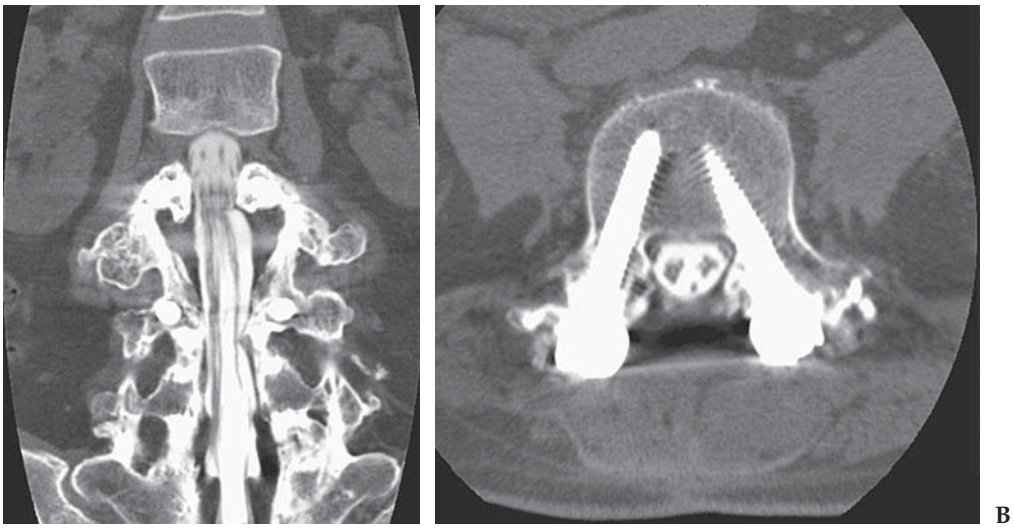

Figure 14.4.4. (A and B) Coronal and axial images at the level of the fusion. There is thickening and clumping of the nerve roots present consistent with arachnoiditis. Note the almost complete lack of artifacts on the axial image at the level of the bilateral pedicle screws.

reconstruction algorithms that significantly reduce this limitation. Suppression of the typical beam-hardening artifacts allows very high quality and fully diagnostic images to be obtained even when metal is present. In addition, the metal itself can be evaluated for complications such as screw fractures or loosening.

Recurrent back pain in a patient with previous surgeries and metal fusion is a very difficult clinical problem. There are multiple causes of pain that can include recurrent disc herniation, spinal stenosis, fibrosis, infection, nerve impingement by hardware or bone spurs, arachnoiditis, and drug-seeking behavior. Proper radiologic diagnosis is extremely important in these patients, and often difficult. Magnetic resonance imaging can provide an adequate evaluation in some patients, depending on the hardware present and system used. Multidetector CT with or without myelography is a very important supplemental or primary imaging modality for evaluating these patients.

Case 14.5: Cocaine Vasculitis

Clinical Information

A 52-year-old woman with headache, slurred speech, and right-sided weakness. Diffusion MRI shows a small focus of ischemia in the left parietal lobe. The patient reports a history of cocaine abuse and recent usage.

Postprocessing Techniques Used and Approach

Variable slab multiplanar MIP images are used for initial review of the circle of Willis (Table 14.5 and Figures 14.5.1 and 14.5.2). Volume-

Table 14.5. Scan Acquisition Parameters for Case 14.5, Cocaine Vasculitis

Slice No. and Thickness	**16 × 0.5 mm**
Coverage	**Through brain**
Helical Pitch	**1.25:1**
Rotation Speed	**0.75 sec**
Dose Parameters	**135 kVp, 195 mAs**
Contrast Dose	**75 mL Omnipaque 350**
Injection Rate	**3 mL/sec**
Bolus Timing Method	**Bolus triggering focused on the carotid artery**

rendered views are also used both with and without segmentation. The COW is isolated using manual segmentation from the 2D images. The resulting 3D VR image is viewed from multiple angles.

Diagnosis

Cocaine-induced vasculitis involving the left middle and posterior cerebral arteries with an associated cerebral infarction.

Teaching Points

Cocaine use is a well-known cause of acute stroke, which can be either ischemic or hemorrhagic. The mechanism is not entirely known but there appear to be several different contributory etiologies. Proposed mechanisms include acute hypertension, cerebral vasoconstriction, vasculitis, and acute intraarterial thrombosis. Hemorrhage is also commonly reported and can be either parenchymal or subarachnoid. Hemorrhages have been tentatively attributed to the hypertension caused by intranasal cocaine use, particularly in patients with an underlying vascular abnormality. The limited number of studies that have

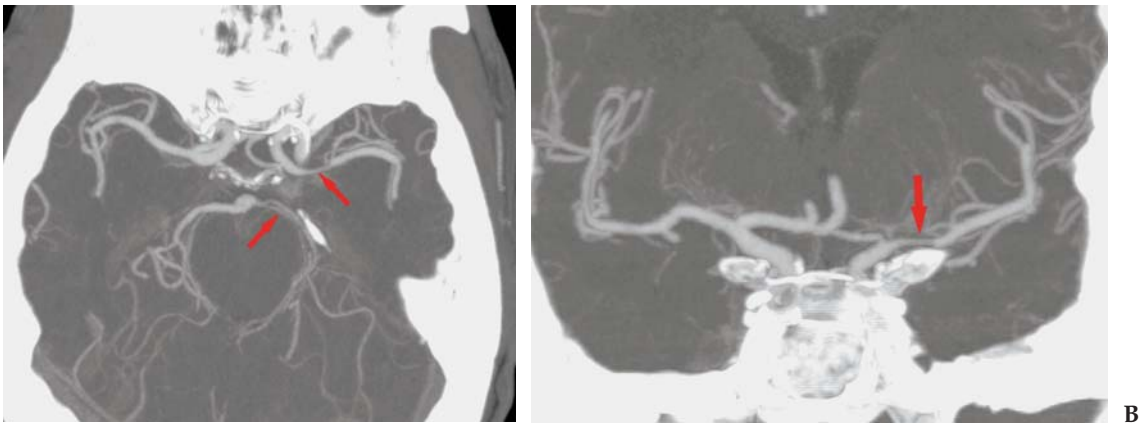

A B

Figure 14.5.1. (A and B) Axial and coronal thin slab MIP images through the COW. There is segmental high-grade narrowing involving the M1 segment of the left MCA (arrows). There is also diffuse narrowing and spasm of the left PCA.

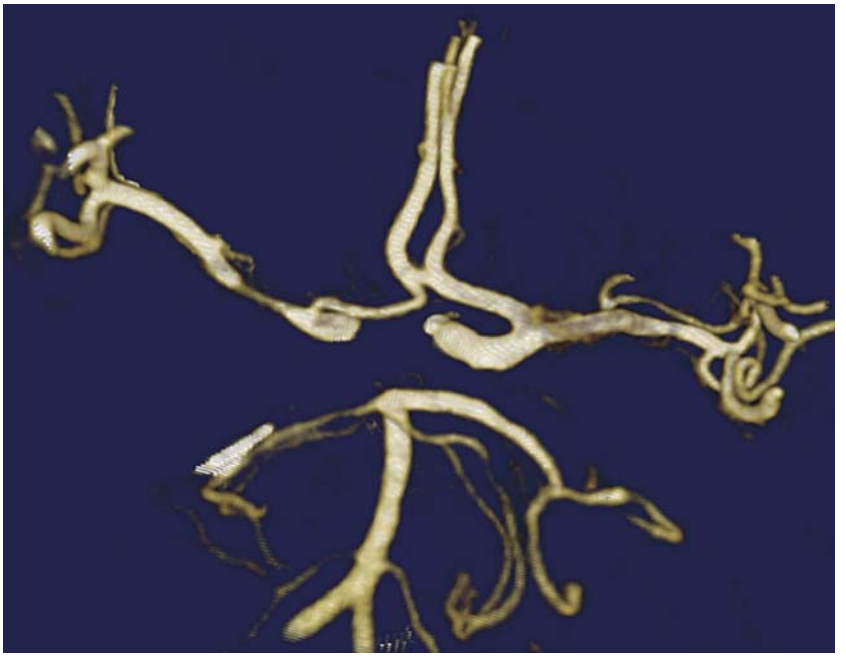

Figure 14.5.2. Segmented VR image offers excellent detail of the vascular pathology.

examined histopathologic specimens of arteries in patients with cocaine-associated stroke have proven to be conflicting; some show nonspecific inflammatory cells or normal findings, and others show changes consistent with vasculitis.

In this case the patient had other systemic evidence of vasculitis, and the presumed diagnosis for the cerebrovascular abnormality was cocaine-induced vasculitis. A CTA examination provided excellent detail of the stenotic, abnormal vascular segments in this case. The MIP images were adequate for basic diagnosis, but the segmented VR images offered a much better view of the abnormal vessels and the entire COW.

Case 14.6: Meningioma With Sinus Thrombosis

Clinical Information

A 40-year-old man with headaches and a known brain mass admitted for preoperative evaluation.

Postprocessing Techniques Used and Approach

Segmented MIP and VR (not shown) images in this case were created using threshold-based segmentation to remove the skull and leave the vascular structures (Table 14.6 and Figures 14.6.1 through 14.6.3). Manual editing of the 3D images was performed to leave only the dural

Table 14.6. Scan Acquisition Parameters for Case 14.6, Meningioma With Sinus Thrombosis

Slice No. and Thickness	16 × 0.5 mm
Coverage	Skull base through brain
Helical Pitch	1.25:1
Rotation Speed	0.75 sec
Dose Parameters	120 kVp, 160 mAs
Contrast Dose	75 mL Omnipaque 350
Injection Rate	3 mL/sec
Bolus Timing Method	Bolus triggering focused on the carotid artery

Figure 14.6.1. Precontrast axial CT image demonstrates a partially calcified extraaxial mass in the posterior midline suggestive of a meningioma.

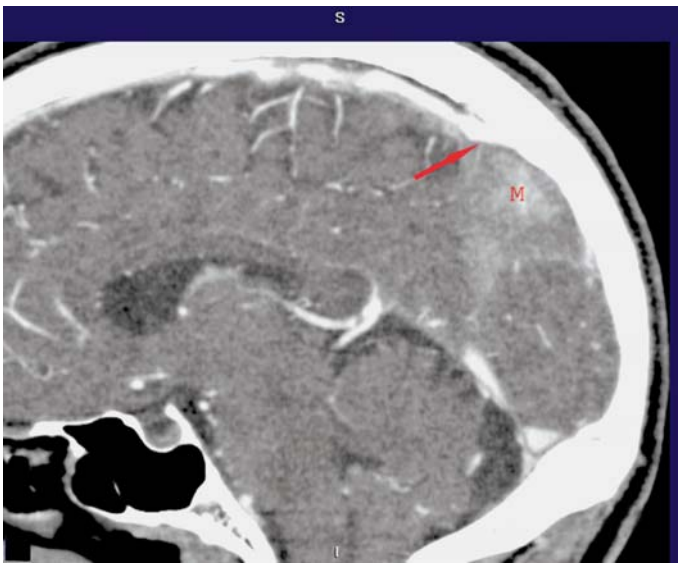

Figure 14.6.2. Sagittal postcontrast MPR. Mild enhancement of the mass is present. The superior sagittal sinus is patent proximal to the tumor (arrow) but is occluded at the site of the mass (M).

Figure 14.6.3. Three-dimensional segmented MIP reconstruction of the venous sinuses. The arterial structures and deep veins have been removed for clarity. Occlusion of the superior sagittal sinus at the site of the tumor is clearly shown. Collateral vessels bypass the tumor and reconstitute the sinus distal to the mass. Normal flow is present in the transverse sinuses.

venous sinuses. Images showing the arterial anatomy were performed separately.

Diagnosis

Meningioma with partial thrombosis of the superior sagittal sinus.

Teaching Points

Computed tomography provides a comprehensive diagnostic and preoperative workup in this patient. Multiplanar reconstructions are used to demonstrate the anatomy and pathology of the brain and tumor. Three-dimensional volume and MIP images provide a detailed picture of the arterial and venous anatomy for the surgeon, which facilitates removal of this tumor. The segmented volume and MIP images are particularly helpful for surgical planning.

Case 14.7: Spinal Arachnoid Cyst

Clinical Information

A 34-year-old woman with leg weakness and paresthesias.

Postprocessing Techniques Used and Approach

Multiplanar reconstructions only (Table 14.7 and Figure 14.7.1).

Diagnosis

Arachnoid cyst of the spinal canal.

Table 14.7. Scan Acquisition Parameters for Case 14.7, Spinal Arachnoid Cyst

Slice No. and Thickness	**16 × 0.5 mm**
Coverage	**Thoracolumbar spine**
Helical Pitch	**0.94:1**
Rotation Speed	**0.75 sec**
Dose Parameters	**120 kVp, 195 mAs**
Contrast Dose	**10 mL intrathecal Isovue 200**

Teaching Points

Spinal arachnoid cysts are most commonly found in the lower thoracic region in the posterolateral aspect of the spinal canal and result in anterior displacement of the spinal cord. Less commonly they can occur ventral to the cord. Cysts may arise in either a subdural or epidural location. Arachnoid cysts are thought to result from the proliferation of arachnoid adhesions as a result of trauma, hemorrhage, inflammation, or congenital abnormalities. Many are asymptomatic, but they can produce symptoms secondary to compression of the cord or nerve roots. Symptoms can include weakness, hyperreflexia, incontinence, neuropathic pain, and numbness. Syringomyelia may also occur.

Diagnosis of spinal cysts is most often made with MRI. A CT myelography was used in this case to look for communication between the cyst and the subarachnoid space. In this instance no uptake of contrast was seen within the cyst even on delayed images. Treatment usually involves laminectomy with cyst fenestration and cyst wall resection.

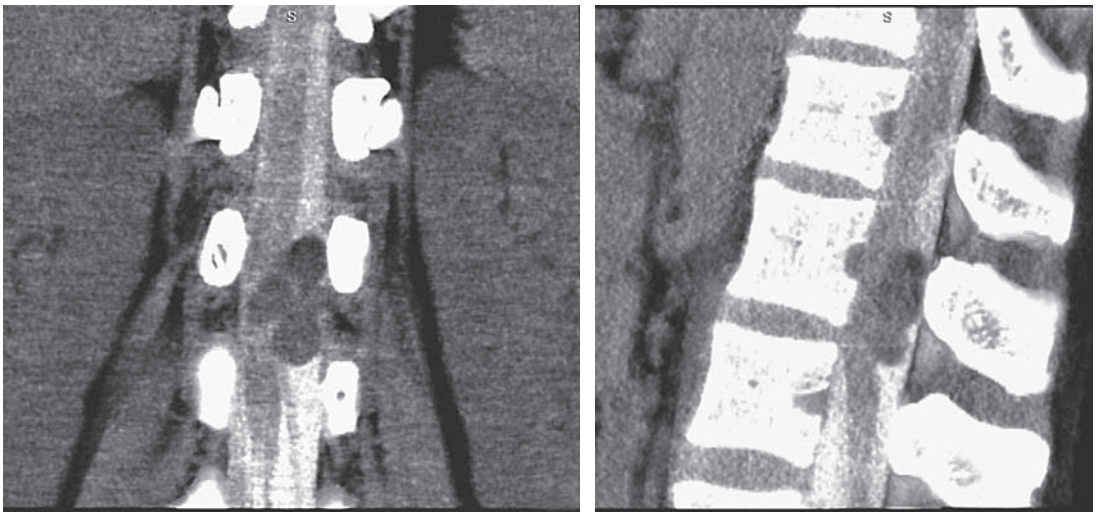

A B

Figure 14.7.1. (A and B) Coronal and sagittal MPR images from a delayed phase of a myelogram 3 hours postinjection. There is a multilobular cystic mass in the spinal canal. The mass is intradural, extramedullary. There is significant compression of the cord just above the conus.

Table 14.8. Scan Acquisition Parameters for Case 14.8, Occipital Arteriovenous Malformation

Slice No. and Thickness	**16 × 0.5 mm**
Coverage	**Through brain**
Helical Pitch	**0.94:1**
Rotation Speed	**0.5 sec**
Dose Parameters	**120 kVp, 150 mAs**
Contrast Dose	**75 mL Omnipaque 350**
Injection Rate	**4 mL/sec**
Bolus Timing Method	**Manual bolus triggering on the carotid artery**

Case 14.8: Occipital Arteriovenous Malformation

Clinical Information

A 17-year-old with headaches and an abnormality in the occipital lobe on noncontrast CT showing increased attenuation and a few foci of calcification.

Postprocessing Techniques Used and Approach

Maximum intensity projection images in the axial and sagittal planes are used to identify the AVM (Table 14.8 and Figures 14.8.1 through 14.8.3). Slab thickness is decreased to better show individual feeding arteries and draining veins, and increased to show the entire AVM nidus and venous drainage. Volume-rendered images are also very helpful. The skull is segmented using a threshold-based bone removal tool. Extraneous tissue and vessels are removed using 3D sculpting. Small veins are removed by windowing to make them less apparent.

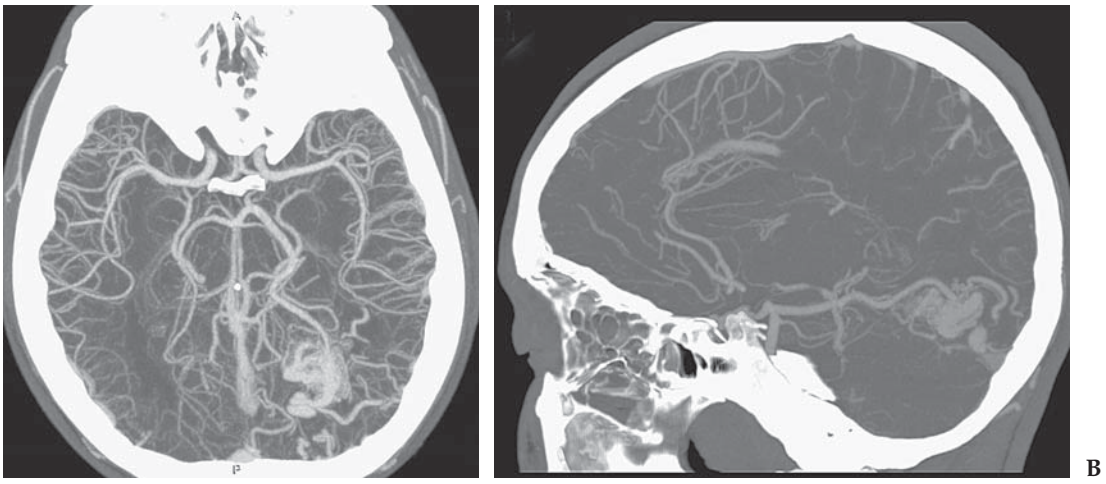

A B

Figure 14.8.1. (A and B) Axial thick slab MIP shows the nidus of the AVM with an overview of the arterial supply and venous drainage. Sagittal thinner-slab MIP image shows the dominant arterial supply from the left posterior cerebral artery.

Figure 14.8.2. Unsegmented VR image again demonstrates the arterial supply and venous drainage. Note the asymmetry of the transverse sinuses with enlargement on the left.

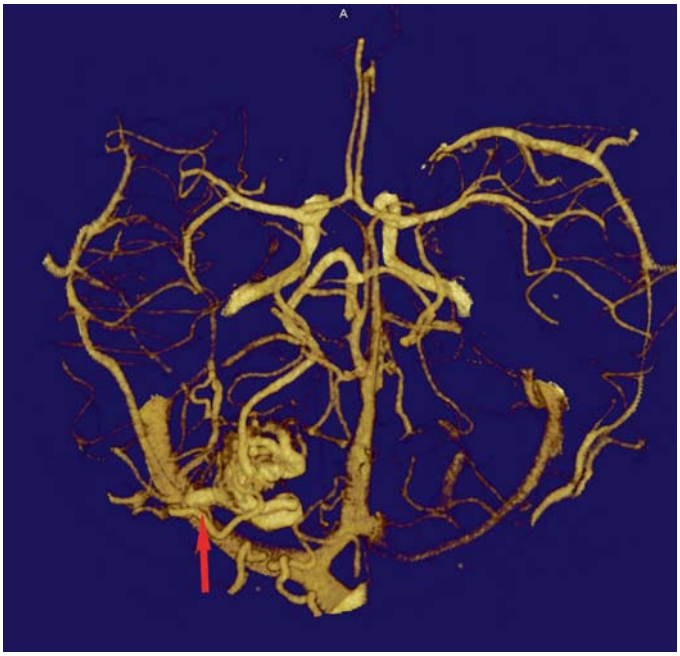

Figure 14.8.3. Segmented VR image with the skull and some smaller vessels removed. The arterial supply from the PCA is better shown. Also the dominant draining vein into the transverse sinus is visualized (arrow).

Diagnosis

Left occipital arteriovenous malformation.

Teaching Points

Computed tomographic angiography is the initial modality used for diagnosis in this patient, but it is also used for treatment planning. The information obtained on CTA is very similar to what would be available with MRA. The images can be reviewed by neurosurgery and interventional neuroradiology to determine an appropriate treatment plan for this young man. In this way, an extra step to perform a purely diagnostic catheter angiogram can be avoided. The catheter study can be combined with an embolization procedure.

The segmented images are quite helpful in this case to better demonstrate the arterial and venous anatomy of the malformation. Venous drainage can be better seen after the skull is removed. The neurosurgeons in particular appreciate the segmented volume images. Major arterial supply is easy to demonstrate on the volume and MIP images. In addition, CT angiography has proven useful for stereotactic localization before surgical resection or radiosurgical treatment, and it can lead to more accurate nidus localization in relationship to surrounding eloquent brain.

Cerebral vascular malformations are divided into four categories: arteriovenous malformation, capillary telangiectasia, cavernous malformation, and venous malformation. Arteriovenous malformations are defined as an abnormal network of arteries and veins with no intervening capillary bed. The main types are parenchymal (80%), usually with supply from the ICA or vertebrobasilar circulations; dural (10%), with supply from the ECA circulation; or mixed lesions (10%), with supply from both ICA or vertebral and ECA circulations. Noncontrast CT typically shows regions of increased attenuation at the site of the AVM with calcification in 25%. The risk of hemorrhage is reported to be approximately 3% per year. Noninvasive diagnosis can be made with either CTA or MRA demonstrating direct arteriovenous communication, usually with a nidus of abnormal vessels which replace but do not displace brain tissue.

Case 14.9: Right MCA Stroke: CT Brain Perfusion

Clinical Information

A 76-year-old woman with acute onset of left hemiplegia (approximately 8 hours earlier). She has a history of atrial fibrillation. (Case submitted by Dr. Alisa Watanabe.)

Postprocessing Techniques Used and Approach

Each slice is evaluated separately (Table 14.9 and Figures 14.9.1 through 14.9.3). A major artery (anterior cerebral) and vein (venous sinus) is identified for each level. Calculation of perfusion maps is performed automatically by the workstation.

Table 14.9. Scan Acquisition parameters for Case 14.9, Right MCA Stroke: CT Brain Perfusion

Slice No. and Thickness	**4 × 8 mm**
Coverage	**4 levels starting from top of ventricles**
Helical Pitch	**N/A**
Rotation Speed	**1 sec**
Dose Parameters	**120 kVp, 120 mAs**
Contrast Dose	**50 mL Omnipaque 350**
Injection Rate	**4 mL/sec**
Bolus Timing Method	**5-sec delay until scanning starts**

Diagnosis

Acute occlusion of the right MCA secondary to an embolus with a large infarct of the right MCA territory.

Teaching Points

Noncontrast CT of the head has been used as the mainstay imaging examination in the initial evaluation of stroke in the emergent setting. However, this study does not provide any physiological information. New treatments for stroke such as intravenous and intraarterial thrombolysis and intraarterial thrombectomy make it increasingly important to stratify patients who are the best candidates for these therapies based on pathophysiology rather than simply the temporal onset of an ischemic event.

Figure 14.9.1. Axial noncontrast CT image shows subtle hypodensity on the right side in the frontoparietal cortex suggesting an acute MCA distribution infarct.

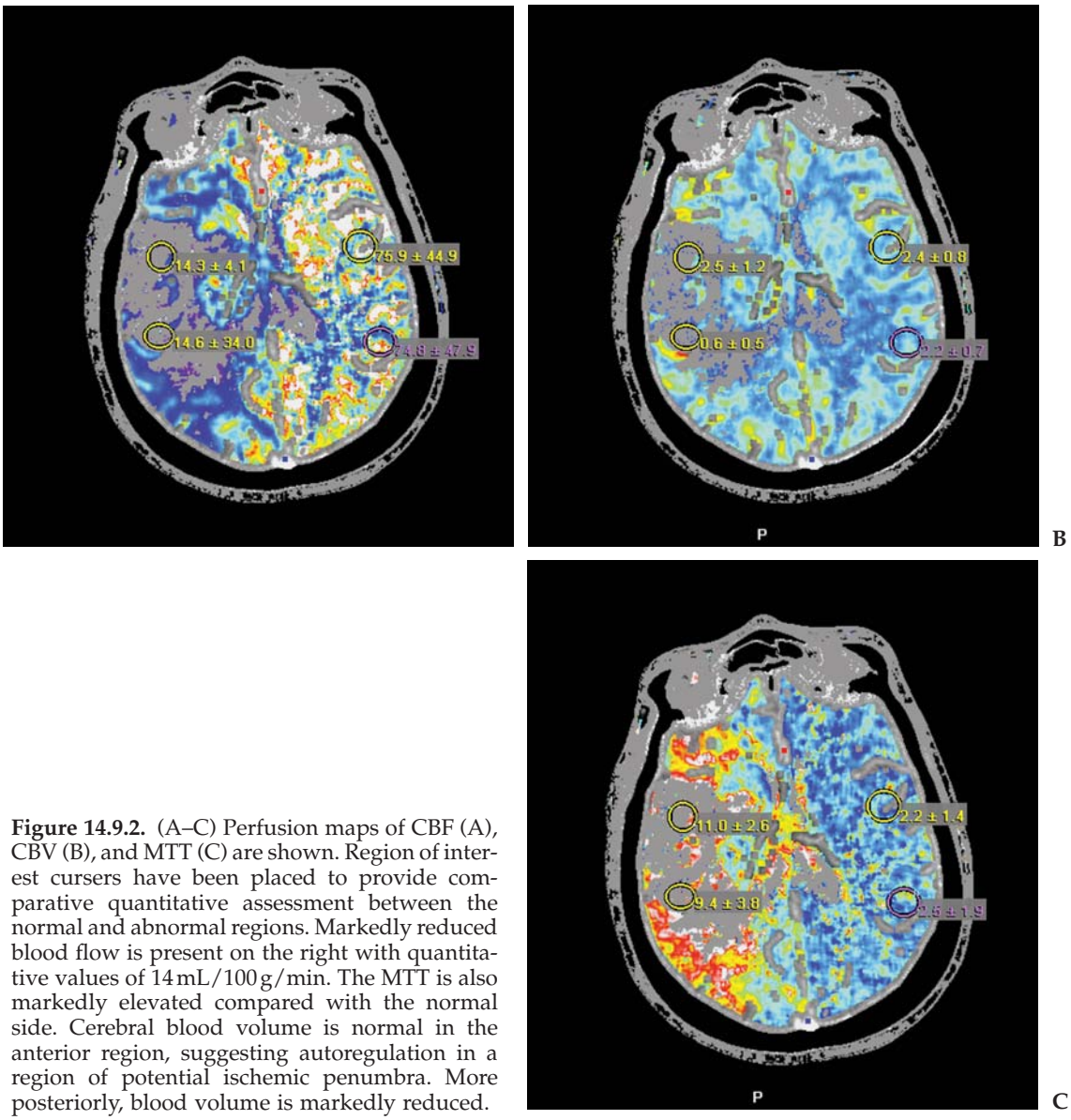

A B C

Figure 14.9.2. (A–C) Perfusion maps of CBF (A), CBV (B), and MTT (C) are shown. Region of interest cursers have been placed to provide comparative quantitative assessment between the normal and abnormal regions. Markedly reduced blood flow is present on the right with quantitative values of 14 mL/100 g/min. The MTT is also markedly elevated compared with the normal side. Cerebral blood volume is normal in the anterior region, suggesting autoregulation in a region of potential ischemic penumbra. More posteriorly, blood volume is markedly reduced.

Magnetic resonance imaging with diffusion-weighted imaging (DWI) has been shown to be significantly more sensitive in detection of acute ischemia and has a high degree of correlation with the eventual area of infarction. Diffusion-weighted imaging is 94% specific and 97% sensitive in the detection of acute ischemia. Both diffusion and perfusion imaging of the entire brain can be performed using MRI. The amount of salvageable brain can be inferred by determining a mismatch between the perfusion and diffusion abnormality. However, MRI is generally not readily available at most institutions in the emergent, setting and patients may have other contraindications, such as pacemakers, that preclude MRI.

Figure 14.9.3. Image from a CTA of the circle of Willis performed immediately following the perfusion study. There is acute cutoff of the right MCA at the trifurcation (arrow). The appearance is suggestive of an embolus to this region.

Computed tomography perfusion has evolved as a potential method for assessing cerebral ischemia in the clinical setting. Computed tomography scanners are readily available in the hospital inpatient setting, and the perfusion CT can be rapidly performed in conjunction with head CT and CTA. Disadvantages of CT perfusion include the lack of diffusion data, inability to scan the entire brain, ionizing radiation, and the need for intravenous injection of iodinated contrast. The rapid advancements in multidetector CT and postprocessing workstations do permit perfusion CT imaging of a significant portion of the brain. The amount of brain in the *z*-axis that can be evaluated with the perfusion technique is currently limited by the length of the CT detector itself. The longest detector available with 16-detector CT is 3.2 cm in length, and 40- and 64-detector scanners are now available with detectors up to 4.0 cm in length.

Computed tomography perfusion imaging is performed by rapidly injecting IV contrast and performing continuous scans in the same location to measure the changes in CT density of the brain over time. The iodinated contrast is assumed to be a nondiffusible agent, similar to xenon. The dynamic changes in CT attenuation are measured and converted into time vs. concentration curves. By manually placing cursors over representative arterial and venous structures (typically the anterior cerebral artery and superior sagittal sinus), attenuation curves are generated using a technique termed the deconvolution method. Typi-

Table 14.10. Summary of perfusion CT parameters

CBF: Cerebral Blood Flow	**30–100 = normal** **<20 = ischemia, possibly reversible** **<10 = strong correlation with infarction**
CBV: Cerebral Blood Volume	**<2.5 = strong correlation with infarction**
MTT: Mean Transit Time	**<3.5 sec = normal** **>7 sec = strong correlation with infarction**

cally, cerebral blood flow (CBF), cerebral blood volume (CBV), and mean transit time (MTT) are calculated by postprocessing software. Time to peak curves or maps can also be generated. These parameters can also be expressed by the central volume principle: MTT = CBV/CBF. Parametric maps can be displayed with a color scale to provide a visual overview of the dynamic data sets. In addition, ROIs can be selected to review exact values of particular parts of the brain.

Mean transit time and time to peak are prolonged in the setting of cerebral ischemia and are the most sensitive and reliable perfusion CT parameters for detecting acute ischemia (Table 14.10). Normal brain has an MTT of 3.5 sec or less. An MTT greater than 7 sec has a strong correlation with irreversible ischemia. A paradoxical decrease in MTT may be observed in an area of luxury perfusion. Also, a patient with collateral circulation may have a prolonged MTT but normal CBF and CBV.

Cerebral blood flow in the normal brain is typically fairly constant (30 mL/100 g brain/min–100 mL/100 g brain/min). This parameter is a measurement of blood delivery to the brain. A drop below 20 mL/100 g/min in CBF is usually associated with clinical stroke symptoms. Typically, CBF below 10 indicates irreversible infarction, also termed the ischemic core. A CBF between 10 and 20 corresponds with ischemic brain that is potentially salvageable, the so-called ischemic penumbra. The penumbra is usually found around the perimeter of the ischemic core. A CBF of less than 34% compared to the opposite (unaffected) side has a strong correlation with infarction. Comparison with the contralateral side may not be as useful if the patient has bilateral or multiple ischemic sites. Also, cerebral autoregulation may result in normal CBF in up to 25% of patients with acute stroke. It has also been shown that a paradoxical increase in CBF may occur in an infarcted territory due to luxury perfusion.

Cerebral blood volume is an indicator of autoregulation. This parameter is calculated in mL/100 g of brain tissue. This is parameter is less useful in detection of acute ischemia than MTT and CBF. A CBV of less than 2.5 has a strong correlation with infarction.

Selected Readings

Cerebral Aneurysms

1. Jayaraman M, Mayo-Smith WW, Tung GA, et al. Detection of intracranial aneurysms: multi–detector row CT angiography compared with DSA. Radiology 2004;230:510–518.

2. Kaminogo M, Hayashi H, Ishimaru H, et al. Depicting cerebral veins by three-dimensional CT angiography before surgical clipping of aneurysms. Am J Neuroradiol 2002;23:85–91.
3. Tomandl BF, Köstner NC, Schempershofe M, et al. CT angiography of intracranial aneurysms: a focus on postprocessing. Radiographics 2004; 24:637–655.
4. Velthuis BK, van Leeuwen MS, Witkamp TD, et al. Surgical anatomy of the cerebral arteries in patients with subarachnoid hemorrhage: comparison of computerized tomography angiography and digital subtraction angiography. J Neurosurg 2001;95:206–212.
5. Villablanca JP, Jahan R, Hooshi P, et al. Detection and characterization of very small cerebral aneurysms by using 2D and 3D helical CT angiography. Am J Neuroradiol 2002;23:1187–1198.

Carotid Thrombus

6. Alvarez-Linera J, Benito-Leon J, Escribano J, et al. Prospective evaluation of carotid artery stenosis: elliptic centric contrast-enhanced MR angiography and spiral CT angiography compared with digital subtraction angiography. Am J Neuroradiol 2003;24:1012–1019.
7. Barnett HJM, Taylor DW, Eliasziw M, et. al. Benefit of carotid endarterectomy in patients with symptomatic moderate or severe stenosis. N Engl J Med 1998;339:1415–1425.
8. Hirai T, Korogi Y, Ono K, et al. Maximum stenosis of extracranial internal carotid artery: effect of luminal morphology on stenosis measurement by using CT angiography and conventional DSA. Radiology 2001;221:802–809.
9. Josephson SA, Bryant SO, Mak HK, Johnston SC, Dillon WP, Smith WS. Evaluation of carotid stenosis using CT angiography in the initial evaluation of stroke and TIA. Neurology 2004 Aug;63(3):457–460.
10. Katano H, Kato K, Umemura A, Yamada K. Perioperative evaluation of carotid endarterectomy by 3D-CT angiography with refined reconstruction: preliminary experience of CEA without conventional angiography. Br J Neurosurg 2004 Apr;18(2):138–148.
11. Phillips CD, Bubash LA. CT angiography and MR angiography in the evaluation of extracranial carotid vascular disease. Radiol Clin North Am 2002;40:783–798.
12. Smith WS, Roberts HC, Chuang NA, et al. Safety and feasibility of a CT protocol for acute stroke: combined CT, CT angiography, and CT perfusion imaging in 53 consecutive patients. Am J Neuroradiol 2003;24: 688–690.

Sphenoidal Encephalocele

13. Barkovich AJ, Vandermarch P, Edwards MSB, Cogen PH. Congenital nasal masses: CT and MR imaging features in 16 cases. Am J Neuroradiol 1991;12:105–116.
14. Castillo M. Congenital abnormalities of the nose: CT and MR findings. Am J Roentgenol 1994;162:1211–1217.
15. Lowe LH, Booth TN, Joglar JM, Rollins NK. Midface anomalies in children. Radiographics 2000 Jul;20(4):907–922.
16. Schlosser RJ, Faust RA, Phillips CD, Gross CW. Three-dimensional computed tomography of congenital nasal anomalies. Int J Pediatr Otorhinolaryngol 2002 Sep;65(2):125–131.

Arachnoiditis

17. Chen YT, Wang MS. Three-dimensional reconstruction and fusion for multi-modality spinal images. Comput Med Imaging Graph 2004 Jan–Mar;28(1–2):21–31.
18. Miller GM, Krauss WE. Myelography: still the gold standard. Am J Neuroradiol 2003 Mar;24:298.
19. Tsuchiya K, Katase S, Aoki C, Hachiya J. Application of multi-detector row helical scanning to postmyelographic CT. Eur Radiol 2003 Jun;13(6): 1438–1443.

Cocaine Vasculitis

20. Bruno A. Cerebrovascular complications of alcohol and sympathomimetic drug abuse. Curr Neurol Neurosci Rep 2003 Jan;3(1):40–45. Review.
21. Jayaraman MV, Mayo-Smith WW. Multi-detector CT angiography of the intra-cranial circulation: normal anatomy and pathology with angiographic correlation. Clin Radiol 2004 Aug;59(8):690–698.
22. Scott RM. Moyamoya syndrome in cocaine-dependent patients. Am J Neuroradiol 2000 Nov–Dec;21(10):1977.
23. Storen EC, Wijdicks EF, Crum BA, Schultz G. Moyamoya-like vasculopathy from cocaine dependency. Am J Neuroradiol 2000 Jun;21: 1008–1010.

Meningioma With Sinus Thrombosis

24. Casey SO, Alberico RA, Patel M, et al. Cerebral CT venography. Radiology 1996;198:163–170.
25. Chawla S. Advances in multidetector computed tomography: applications in neuroradiology. J Comput Assist Tomogr 2004 Jul–Aug;28(suppl 1):S12–S16.
26. Jayaraman MV, Mayo-Smith WW. Multi-detector CT angiography of the intra-cranial circulation: normal anatomy and pathology with angiographic correlation. Clin Radiol 2004 Aug;59(8):690–698.
27. Majoie CBLM, van Straten M, Venema HW, den Heeten GJ. Multisection CT venography of the dural sinuses and cerebral veins by using matched mask bone elimination. Am J Neuroradiol 2004 May;25(5):787–791.

Spinal Arachnoid Cyst

28. Krings T, Lukas R, Reul J, et al. Diagnostic and therapeutic management of spinal arachnoid cysts. Acta Neurochir (Wien) 2001;143(3):227–234; discussion:234–235.
29. Lee HJ, Cho DY. Symptomatic spinal intradural arachnoid cysts in the pediatric age group: description of three new cases and review of the literature. Pediatr Neurosurg 2001 Oct;35(4):181–187.
30. In: Stark DD, Bradley WG, eds. Magnetic Resonance Imaging. 3rd ed. St. Louis, MO: Moseby; 1999:1861.
31. Wang MY, Levi AD, Green BA. Intradural spinal arachnoid cysts in adults. Surg Neurol 2003 Jul;60(1):49–55;discussion:55–56.

Occipital Arteriovenous Malformation

32. Aoki S, Sasaki Y, Machida T, et al. 3D-CT angiography of cerebral arteriovenous malformations. Radiat Med 1998 Jul–Aug;16(4):263–271.

33. Rieger J, Hosten N, Neumann K, et al. Initial clinical experience with spiral CT and 3D arterial reconstruction in intracranial aneurysms and arteriovenous malformations. Neuroradiology 1996 Apr;38(3):245–251.
34. Sanelli PC, Mifsud MJ, Stieg PE. Role of CT angiography in guiding management decisions of newly diagnosed and residual arteriovenous malformations. Am J Roentgenol 2004 Oct;183:1123–1126.
35. Tanaka H, Numaguchi Y, Konno S, et al. Initial experience with helical CT and 3D reconstruction in therapeutic planning of cerebral AVMs: comparison with 3D time-of-flight MRA and digital subtraction angiography. J Comput Assist Tomogr 1997;21:811–817.
36. Tsuchiya K, Katase S, Hachiya J, Shiokawa Y. Volume-rendered 3D display of MR angiograms in the diagnosis of cerebral arteriovenous malformations. Acta Radiol 2003 Nov;44(6):675–679.

Right MCA Stroke: CT Brain Perfusion

37. Eastwood JD, Lev MH, Wintermark M, et al. Correlation of early dynamic CT perfusion imaging with whole-brain MR diffusion and perfusion imaging in acute hemispheric stroke. Am J Neuroradiol 2003;24:1869–1875.
38. Galvez M, York GE, II, Eastwood JD. CT perfusion parameter values in regions of diffusion abnormalities. Am J Neuroradiol 2004 Aug;25: 1205–1210.
39. Mayer TE, Hamann GF, Baranczyk J, et al. Dynamic CT perfusion imaging of acute stroke. Am J Neuroradiol 2000;21:1441–1449.
40. Smith WS, Roberts HC, Chuang NA, et al. Safety and feasibility of a CT protocol for acute stroke: combined CT, CT angiography, and CT perfusion imaging in 53 consecutive patients. Am J Neuroradiol 2003;24:688–690.
41. Tomandl BF, Klotz E, Handschu R, et al. Comprehensive imaging of ischemic stroke with multisection CT. Radiographics 2003;23:565–592.
42. Wintermark M, Reichhart M, Cuisenaire O, et al. Comparison of admission perfusion computed tomography and qualitative diffusion- and perfusion-weighted magnetic resonance imaging in acute stroke patients. Stroke 2002;33:2025–2031.

Appendix
Sample CT Protocols

The protocols in the following Appendix are designed to serve as a general guide to setting up comprehensive CT protocols on your scanner. The protocols are independent of manufacturer; therefore they are not optimized for any individual scanner or patient and will generally require some modification before actual use. Some information such as specific reconstruction filters and algorithms is very manufacturer specific and cannot be included. This is also not meant to be a completely exhaustive list of protocols. Many specialty protocols for specific indications can be modified from the base protocols and created on the scanner.

The protocols are optimized for 16-detector scanners. Modification for 4- or 8-slice scanners will require changes primarily in acquisition slice thickness but may also affect contrast dose and timing and reconstructed image thickness.

The Appendix is divided into two sections. Appendix A contains general protocols for neuro, body and musculoskeletal imaging and Appendix B contains protocols for CT angiography. These protocols are designed for adult patients.

Special Note Regarding Pediatric CT Protocols

Pediatric patients require more attention than adults. In each case, the protocols need to be tailored to the individual patient, and special attention must be made to ensure that radiation dose is minimized. Pediatric patients, because of their smaller size, can generally be scanned at the thinnest slice thickness option available on a 16-detector scanner for almost every exam. If a 4-slice scanner is used, then submillimeter slice thickness should be used judiciously because of the increased radiation dose provided. Also, unlike adult patients, routine multiphase protocols should be avoided. Multiphase scanning should be employed only when truly needed for diagnosis in specific cases. Higher pitch values of 1.2–1.5 and short rotation times are both useful

techniques to increase the speed of the scan and to reduce motion artifacts as well as radiation dose.

Radiation dose parameters for pediatric CT patients must be carefully adjusted for body size and weight. Fortunately, the technologist can use advanced automated exposure control (AEC) software on the scanner to make many of these decisions automatically. If this software is not available, then a reference chart (Table A1) should be used to determine the appropriate mAs for weight. The kV should also be adjusted for children with 80 kV–100 kV used in smaller children (<50 kg) and 100 kV–120 kV used in larger children (>50 kg). Even when AEC software is used, the parameters set for the scan should undergo a "reality check" to make sure they fall within the expected range.

Contrast administration for pediatric patients can be more challenging than for adults because of the limited venous access. The standard contrast dose for pediatric patients is determined by weight and for most exams a contrast dose of 2 mL/kg is adequate. The contrast injection can be performed either manually or by power injector. Power injection is preferred but is often not possible. Peripheral small IVs, butterfly needles and central lines are usually injected manually. Scanning can begin at a predetermined delay (30–50 seconds for head, chest and abdomen scans depending on size) or started once all the contrast is in. If the manual injection is rapid, an additional delay may be needed before starting the scan (10–20 seconds).

CTA is best performed with a power injector, as this will routinely produce more uniform and denser vascular enhancement. Attempts should be made to place an angiocath into an antecubital vein. A 22-gauge catheter can be injected at 2–3 mL/sec and a 24-gauge catheter at 1.2 mL/sec. Delay will vary depending on injection rate; therefore, it is best to use bolus-triggering techniques to initiate the scan. If it is not possible to use a power injector, successful CTA can still be performed with a rapid manual injection.

Table A1. Recommended Dose Parameters for Pediatric Body MDCT

Patient Weight (kg)	Dose Parameters		
	kV	mAs Chest	mAs Abdomen
<15	80	20–30	30–40
15–24	80	30–40	50–60
25–34	80	50–60	70–80
35–44	80–100	70–80	90–100
45–54	100–120	90–100	110–125
>55	120	110+	140+

General Prolocols

Head Routine

Scan Parameters

Coverage	Scan Mode	kV	mA	AEC	Rotation Time	FOV	SliceThickness	Beam Pitch
Skull Base to Vertex	Helical or Sequence	120	250-300	No	1-1.5 sec	240mm	1 to 1.5mm	1

Injector Values

Contrast Needed	Contrast Volume	Saline Volume	Injection Rate
Optional	75-100cc	25 to 50cc	2cc/sec

Contrast Timing

Bolus Detection	Reference Location	Trigger Value (ROI)	Delay Before Monitoring	Scan Delay After Trigger
No				

Manual	Scan Delay
Yes	70 sec

Reconstructions

Algorithm	Thin Axials	Recon Interval	Thick Axials	Sagittal	Coronal
Head	no	same3	-5mm	No	No

Head High Resolution/3D

Scan Parameters

Coverage	Scan Mode	kV	mA	AEC	Rotation Time	FOV	SliceThickness	Beam Pitch
Skull Base to Vertex	Helical	120	400-500	No	0.5 sec	240mm	.5 to.75mm	1

Injector Values

Contrast Needed	Contrast Volume	Saline Volume	Injection Rate
Optional	75-100cc	25 to 50cc	2cc/sec

Contrast Timing

Bolus Detection	Reference Location	Trigger Value (ROI)	Delay Before Monitoring	Scan Delay After Trigger
No				

Manual	Scan Delay
Yes	70 sec

Reconstructions

Algorithm	Thin Axials	Recon Interval	Thick Axials	Sagittal	Coronal
Std + Bone	.5 to .75mm	.5mm	3mm	2mm	2mm

Sinus

Scan Parameters

Coverage	Scan Mode	kV	mA	AEC	Rotation Time	FOV	SliceThickness	Beam Pitch
Paranasal Sinuses	Helical	120	250-400	NO	0.5	240mm	.5 to .75mm	1

Injector Values

Contrast Needed	Contrast Volume	Saline Volume	Injection Rate
Optional	75-100cc	25 to 50cc	2cc/sec

Contrast Timing

Bolus Detection	Reference Location	Trigger Value (ROI)	Delay Before Monitoring	Scan Delay After Trigger
No				

Manual	Scan Delay
Yes	70 sec

Reconstructions

Algorithm	Thin Axials	Recon Interval	Thick Axials	Sagittal	Coronal
Std + Bone	.5 to .75mm	.5mm	2mm		2mm

Orbits/Facial Bones

Scan Parameters

Coverage	Scan Mode	kV	mA	AEC	Rotation Time	FOV	SliceThickness	Beam Pitch
Top of Orbits Through Mandible	Helical	120	250-400	NO	0.5	240mm	.5 to .75mm	1

Injector Values

Contrast Needed	Contrast Volume	Saline Volume	Injection Rate
Optional	75-100cc	25 to 50cc	2cc/sec

Contrast Timing

Bolus Detection	Reference Location	Trigger Value (ROI)	Delay Before Monitoring	Scan Delay After Trigger
No				

Manual	Scan Delay
Yes	70 sec

Reconstructions

Algorithm	Thin Axials	Recon Interval	Thick Axials	Sagittal	Coronal
Std + Bone	.5 to .75mm	.5mm	2mm	2mm	2mm

Neck

Scan Parameters

Coverage	Scan Mode	kV	mA	AEC	Rotation Time	FOV	SliceThickness	Beam Pitch
Lung Apex to Soft Palate	Helical	120	250-400	Yes	0.5 sec	240mm	.5 to .75mm	1.25

Injector Values

Contrast Needed	Contrast Volume	Saline Volume	Injection Rate
Optional	75-100cc	25 to 50cc	2cc/sec

Contrast Timing

Bolus Detection	Reference Location	Trigger Value (ROI)	Delay Before Monitoring	Scan Delay After Trigger
No				

Manual	Scan Delay
Yes	45 sec

Reconstructions

Algorithm	Thin Axials	Recon Interval	Thick Axials	Sagittal	Coronal
Standard	.5 to .75mm	.5mm	3mm	2mm	2mm

IAC

Scan Parameters

Coverage	Scan Mode	kV	mA	AEC	Rotation Time	FOV	SliceThickness	Beam Pitch
Tip of Mastoid to Sella	Helical	120	400	no	1 sec	240mm	.5 to .75mm	1

Injector Values

Contrast Needed	Contrast Volume	Saline Volume	Injection Rate
Optional	75-100cc	25 to 50cc	2cc/sec

Contrast Timing

Bolus Detection	Reference Location	Trigger Value (ROI)	Delay Before Monitoring	Scan Delay After Trigger
No				

Manual	Scan Delay
Yes	70 sec

Reconstructions

Algorithm	Thin Axials	Recon Interval	Thick Axials	Sagittal	Coronal
Std + Bone	.5 to .75mm	.4 to .5mm	1mm		1mm

Spine (C, T or L alone)

Scan Parameters

Coverage	Scan Mode	kV	mA	AEC	Rotation Time	FOV	SliceThickness	Beam Pitch
Spine Area of Interest	Helical	120	150-350	Yes	1 sec	240mm	.5 to .75mm	1

Injector Values

Contrast Needed	Contrast Volume	Saline Volume	Injection Rate
No			

Contrast Timing

Bolus Detection	Reference Location	Trigger Value (ROI)	Delay Before Monitoring	Scan Delay After Trigger	Manual	Scan Delay

Reconstructions

Algorithm	Thin Axials	Recon Interval	Thick Axials	Sagittal	Coronal
Std + Bone	.5 to .75mm	.5mm	2mm	2mm	2mm

Total Spine

Scan Parameters

Coverage	Scan Mode	kV	mA	AEC	Rotation Time	FOV	SliceThickness	Beam Pitch
Total Spine or Area of Interest	Helical	120	150-350	Yes	1 sec	240mm	1 to 1.5mm	1

Injector Values

Contrast Needed	Contrast Volume	Saline Volume	Injection Rate
No			

Contrast Timing

Bolus Detection	Reference Location	Trigger Value (ROI)	Delay Before Monitoring	Scan Delay After Trigger	Manual	Scan Delay

Reconstructions

Algorithm	Thin Axials	Recon Interval	Thick Axials	Sagittal	Coronal
Std + Bone	1 to 1.5mm	1mm	2mm	2mm	2mm

Chest

Scan Parameters

Coverage	Scan Mode	kV	mA	AEC	Rotation Time	FOV	SliceThickness	Beam Pitch
Lung Apex Through Adrenal Glands	Helical	120	200-350	Yes	0.5 sec	500mm	.5 to .75mm	1.25

Injector Values

Contrast Needed	Contrast Volume	Saline Volume	Injection Rate
Optional	75-100cc	25 to 50cc	2cc/sec

Contrast Timing

Bolus Detection	Reference Location	Trigger Value (ROI)	Delay Before Monitoring	Scan Delay After Trigger
Optional	Desc. aorta	200	20 sec	10 sec

Manual	Scan Delay
Yes (O)	50 to 60 sec

Reconstructions

Algorithm	Thin Axials	Recon Interval	Thick Axials	Sagittal	Coronal
Std + Lung	.5 to .75mm	.5mm	3mm	Optional	3mm

Chest High Resolution

Scan Parameters

Coverage	Scan Mode	kV	mA	AEC	Rotation Time	FOV	SliceThickness	Beam Pitch
Lung Apex Through Adrenal Glands	Helical	120	250-400	Yes	0.5 sec	500mm	.5 to .75mm	1.25

Injector Values

Contrast Needed	Contrast Volume	Saline Volume	Injection Rate
No			

Contrast Timing

Bolus Detection	Reference Location	Trigger Value (ROI)	Delay Before Monitoring	Scan Delay After Trigger

Manual	Scan Delay

Reconstruction #1

Algorithm	Thin Axials	Recon Interval	Thick Axials	Sagittal	Coronal
Std + Lung	.5 to .75mm	.5mm	3mm	Optional	3mm

Reconstruction #2

Algorithm	Thin Axials	Recon Interval	Thick Axials	Sagittal	Coronal
Lung	1mm	1 to 10mm			

Procedure note: Additional scans in the prone position can be obtained if needed. I also recommend obtaining a select series of expiratory scans. High resolution images can be reconstructed contiguously or at select intervals depending on radiologist preference.

Chest - Abdomen - Pelvis

Scan Parameters

Coverage	Scan Mode	kV	mA	AEC	Rotation Time	FOV	SliceThickness	Beam Pitch
Lung Apex Through Pubic Symphysis	Helical	120	250-500	Yes	0.5 sec	500mm	1 to 1.5mm	1.25

Injector Values

Contrast Needed	Contrast Volume	Saline Volume	Injection Rate
Yes	100-125cc	50 cc	2cc/sec

Contrast Timing

Bolus Detection	Reference Location	Trigger Value (ROI)	Delay Before Monitoring	Scan Delay After Trigger	Manual	Scan Delay
Optional	Desc. aorta	200	20	15 sec	Yes (O)	50 to 60 sec

Reconstructions

Algorithm	Thin Axials	Recon Interval	Thick Axials	Sagittal	Coronal
Std + Lung	1 to 1.5mm	1mm	3-5mm	Optional	3mm

Abdomen or Abd/Pelvis

Scan Parameters

Coverage	Scan Mode	kV	mA	AEC	Rotation Time	FOV	SliceThickness	Beam Pitch
Diaphragm Through Iliac Crest or Pubic Symphysis	Helical	120	300-500	Yes	0.5 sec	500mm	1 to 1.5mm	1.25

Injector Values

Contrast Needed	Contrast Volume	Saline Volume	Injection Rate
Yes	100cc	50cc	2cc/sec

Contrast Timing

Bolus Detection	Reference Location	Trigger Value (ROI)	Delay Before Monitoring	Scan Delay After Trigger	Manual	Scan Delay
Optional	Desc. aorta	200	40	15	Yes (O)	70 sec

Reconstructions

Algorithm	Thin Axials	Recon Interval	Thick Axials	Sagittal	Coronal
Standard	1 to 1.5mm	1mm	3-5mm	Optional	2mm

Multiphase Phase Liver

Scan Parameters

	Coverage	Scan Mode	kV	mA	AEC	Rotation Time	FOV	SliceThickness	Beam Pitch
Acquistion Scan #1	Liver - Late Arterial Phase	Helical	120	300-500	Yes	0.5 sec	500mm	1 to 1.5mm	1.25

	Coverage	Scan Mode	kV	mA	AEC	Rotation Time	FOV	SliceThickness	Beam Pitch
Acquistion Scan #2	Abd - Portal Venous Phase	Helical	120	300-500	Yes	0.5 sec	500mm	1 to 1.5mm	1.25

	Coverage	Scan Mode	kV	mA	AEC	Rotation Time	FOV	SliceThickness	Beam Pitch
Acquistion Scan #3	Liver - Delay Equilibrium Phase (Optional)	Helical	120	300-500	Yes	0.5 sec	500mm	1 to 1.5mm	1.25

Injector Values

Contrast Needed	Contrast Volume	Saline Volume	Injection Rate
Yes	125cc	50cc	4cc/sec

Contrast Timing

Bolus Detection	Reference Location	Trigger Value (ROI)	Delay Before Monitoring	Scan Delay After Trigger	Manual	Delay Scan #1	Delay Scan #2	Delay Scan #3
Optional	Abd aorta	200	15 sec	5 sec	Yes (O)	28 sec	60 sec	120 sec

	Algorithm	Thin Axials	Recon Interval	Thick Axials	Sagittal	Coronal
Reconstructions Scan #1	Standard	1 to 1.5mm	1mm	3mm	Optional	3mm

	Algorithm	Thin Axials	Recon Interval	Thick Axials	Sagittal	Coronal
Reconstructions Scans #2, #3	Standard	1 to 1.5mm	1mm	3mm	Optional	3mm

Pancreas Protocol

Scan Parameters

Acquistion

Coverage	Scan Mode	kV	mA	AEC	Rotation Time	FOV	SliceThickness	Beam Pitch
Pancreas - Pre contrast	Helical	120	300-500	Yes	0.5 sec	500mm	1 to 1.5mm	1.25

Scan#1

Acquistion

Coverage	Scan Mode	kV	mA	AEC	Rotation Time	FOV	SliceThickness	Beam Pitch
Pancreas - Pancreatic Phase	Helical	120	300-500	Yes	0.5 sec	500mm	.5 to .75mm	1.25

Scan #2

Acquistion

Coverage	Scan Mode	kV	mA	AEC	Rotation Time	FOV	SliceThickness	Beam Pitch
Abdomen - Venous Phase	Helical	120	300-500	Yes	0.5 sec	500mm	1 to 1.5mm	1.25

Scan #3

Injector Values

Contrast Needed	Contrast Volume	Saline Volume	Injection Rate
Yes	125cc	50cc	3cc/sec

Contrast Timing

Bolus Detection	Reference Location	Trigger Value (ROI)	Delay Before Monitoring	Scan Delay After Trigger
Optional	Abd aorta	200	20 sec	10 sec

Manual	Delay Scan #2	Delay Scan #3
Yes (O)	40 sec	70 sec

Reconstructions Scan #1

Algorithm	Thin Axials	Recon Interval	Thick Axials	Sagittal	Coronal
Standard	No		5mm		

Reconstructions Scan #2

Algorithm	Thin Axials	Recon Interval	Thick Axials	Sagittal	Coronal
Standard	.5 to .75mm	.5mm	2mm	Optional	2mm

Reconstructions Scan #3

Algorithm	Thin Axials	Recon Interval	Thick Axials	Sagittal	Coronal
Standard	1 to 1.5mm	1mm	3mm	Optional	3mm

Adrenal Gland

Scan Parameters

Acquistion	Coverage	Scan Mode	kV	mA	AEC	Rotation Time	FOV	SliceThickness	Beam Pitch
Scan#1	Non Contrast	Helical	120	300-500	Yes	0.5 sec	500mm	.5 to .75mm	1.25

Acquistion	Coverage	Scan Mode	kV	mA	AEC	Rotation Time	FOV	SliceThickness	Beam Pitch
Scan #2	Post Contrast - Venous Phase (Optional)	Helical	120	300-500	Yes	0.5 sec	500mm	.5 to .75mm	1.25

Injector Values	Contrast Needed	Contrast Volume	Saline Volume	Injection Rate
	Yes	100cc	25 to 50cc	2cc/sec

Contrast Timing	Bolus Detection	Reference Location	Trigger Value (ROI)	Delay Before Monitoring	Scan Delay After Trigger	Manual	Delay Scan #2
	No					Yes	70 sec

Reconstructions	Algorithm	Thin Axials	Recon Interval	Thick Axials	Sagittal	Coronal
Scan #1	Standard	.5 to .75mm	.5mm	3mm		3mm

Reconstructions	Algorithm	Thin Axials	Recon Interval	Thick Axials	Sagittal	Coronal
Scan #2	Standard	.5 to .75mm	.5mm	3-5mm	Optional	3mm

Abdomen/Pelvis Stone Survey

Scan Parameters

Scan Parameters	Coverage	Scan Mode	kV	mA	AEC	Rotation Time	AEC	SliceThickness	Beam Pitch
	Diaphragm Through Pubic Symphysis	Helical	120	250-400	Yes	0.5 sec	500mm	1 to 1.5mm	1.25

Injector Values	Contrast Needed	Contrast Volume	Saline Volume	Injection Rate
	No			

Contrast Timing	Bolus Detection	Reference Location	Trigger Value (ROI)	Delay Before Monitoring	Scan Delay After Trigger	Manual	Scan Delay

Reconstructions	Algorithm	Thin Axials	Recon Interval	Thick Axials	Sagittal	Coronal
	Standard	1 to 1.5mm	1mm	3mm	Optional	3mm

Renal Mass Protocol

Scan Parameters

Acquistion

Coverage	Scan Mode	kV	mA	AEC	Rotation Time	FOV	SliceThickness	Beam Pitch
Scan#1								
Kidney Pre Contrast	Helical	120	300-500	Yes	0.5 sec	500mm	1 to 1.5mm	1.25

Acquistion

Coverage	Scan Mode	kV	mA	AEC	Rotation Time	FOV	SliceThickness	Beam Pitch
Scan #2								
Abdomen - Venous Phase	Helical	120	300-500	Yes	0.5 sec	500mm	1 to 1.5mm	1.25

Acquistion

Coverage	Scan Mode	kV	mA	AEC	Rotation Time	FOV	SliceThickness	Beam Pitch
Scan #3								
Kidney Excretory Phase	Helical	120	300-500	yes	0.5 sec	500mm	1 to 1.5mm	1.25

Injector Values

Contrast Needed	Contrast Volume	Saline Volume	Injection Rate
Yes	125cc	50cc	2cc/sec

Contrast Timing

Bolus Detection	Reference Location	Trigger Value (ROI)	Delay Before Monitoring	Scan Delay After Trigger
No				

Manual	Delay Scan #2	Delay Scan #3
Yes	70 sec	3-5 minutes

Reconstructions

Scan #1

Algorithm	Thin Axials	Recon Interval	Thick Axials	Sagittal	Coronal
Standard	1 to 1.5mm	1mm	3mm	Optional	Optional

Reconstructions

Scan #2

Algorithm	Thin Axials	Recon Interval	Thick Axials	Sagittal	Coronal
Standard	1 to 1.5mm	1mm	3mm	Optional	3mm

Reconstructions

Scan #3

Algorithm	Thin Axials	Recon Interval	Thick Axials	Sagittal	Coronal
Standard	1 to 1.5mm	1mm	3mm	Optional	3mm

CT Urogram (hematuria protocol)

Scan Parameters

Acquistion	Coverage	Scan Mode	kV	mA	AEC	Rotation Time	FOV	SliceThickness	Beam Pitch
Scan#1	Abd/pel Pre Contrast	Helical	120	300-500	Yes	0.5 sec	500mm	1 to 1.5mm	1.25

Acquistion	Coverage	Scan Mode	kV	mA	AEC	Rotation Time	FOV	SliceThickness	Beam Pitch
Scan #2	Abdomen Mixed Nephrographic/Excretory	Helical	120	300-500	Yes	0.5 sec	500mm	1 to 1.5mm	1.25

Acquistion	Coverage	Scan Mode	kV	mA	AEC	Rotation Time	FOV	SliceThickness	Beam Pitch
Scan #3	Lower Abdomen and Pelvis Excretory Phase	Helical	120	300-500	Yes	0.5 sec	500mm	1 to 1.5mm	1.25

Injector Values	Contrast Needed	Contrast Volume	Saline Volume	Injection Rate
Injection 1	Yes	50cc	50cc	2cc/sec

	Contrast Needed	Contrast Volume	Saline Volume	Injection Rate
Injection 2	Yes	75cc	50cc	1.5cc/sec

Contrast Timing	Bolus Detection	Reference Location	Trigger Value (ROI)	Delay Before Monitoring	Scan Delay After Trigger	Manual	Delay Scan #2	Delay Scan #3
	No					Yes	See Note	See Note

Reconstructions	Algorithm	Thin Axials	Recon Interval	Thick Axials	Sagittal	Coronal
Scan #1	Standard	1 to 1.5mm	1mm	3mm	Optional	3mm

Reconstructions	Algorithm	Thin Axials	Recon Interval	Thick Axials	Sagittal	Coronal
Scan #2	Standard	1 to 1.5mm	1mm	3mm	Optional	3mm

Reconstructions	Algorithm	Thin Axials	Recon Interval	Thick Axials	Sagittal	Coronal
Scan #3	Standard	1 to 1.5mm	1mm	3mm	Optional	3mm

Procedure note: This protocol uses a split contrast injection. Inject 50 cc of contrast and apply abdominal compression. Wait 5 minutes then inject remaining 75 cc of contrast. Scan through kidneys at 60 seconds post start of second injection to obtain mixed nephrographic/excretory images. Wait an additional 3-5 minutes, release compression and immediately scan lower abdomen and pelvis.

CT Colography Protocol

Scan Parameters

Acquistion	Coverage	Scan Mode	kV	mA	AEC	Rotation Time	FOV	SliceThickness	Beam Pitch
Scan#1	Supine with Gas Insufflation	Helical	120	200-300	Yes	0.5 sec	500mm	1 to 1.5mm	1.25

Acquistion	Coverage	Scan Mode	kV	mA	AEC	Scan Time	FOV	SliceThickness	Beam Pitch
Scan #2	Prone with Gas Insufflation	Helical	120	200-300	Yes	0.5 sec	500mm	1 to 1.5mm	1.25

Injector Values	Contrast Needed	Contrast Volume	Saline Volume	Injection Rate
	No			

Contrast Timing	Bolus Detection	Reference Location	Trigger Value (ROI)	Delay Before Monitoring	Scan Delay After Trigger

Manual	Delay Scan #1	Delay Scan #2

Reconstructions Scan #1	Algorithm	Thin Axials	Recon Interval	Thick Axials	Sagittal	Coronal
	Standard	1 to 1.5mm	1mm	3mm		

Reconstructions Scan #2	Algorithm	Thin Axials	Recon Interval	Thick Axials	Sagittal	Coronal
	Standard	1 to 1.5mm	1mm	3mm		

Procedure note: Air or carbon dioxide gas insufflation needed to distend colon. Patient scanned supine and prone with low dose technique. Send thin section reconstructions to workstation for evaluation.

Peripheral Joint

Scan Parameters

	Coverage	Scan Mode	kV	mA	AEC	Rotation Time	FOV	SliceThickness	Beam Pitch
Scan Parameters	Knee, Ankle, Foot, Elbow, Wrist or Hand	Helical	120	200-300	No	0.5 sec	240mm	.5 to .75mm	1

Injector Values	Contrast Needed	Contrast Volume	Saline Volume	Injection Rate
	No			

Contrast Timing	Bolus Detection	Reference Location	Trigger Value (ROI)	Delay Before Monitoring	Scan Delay After Trigger		Manual	Scan Delay

Reconstructions	Algorithm	Thin Axials	Recon Interval	Thick Axials	Sagittal	Coronal
	Std + bone	.5 to .75mm	.4 to .5mm	2 to 3mm	2mm	2mm

Procedure note: Reconstruction with bone algorithm improves thick reconstructions for PACS, but 3D images are usually better with standard reconstruction algorithm. Oblique reconstructions made on the scanner or workstation are usually preferable to straight coronal and sagittal reconstructions, but must be individually tailored to anatomy.

Central Joint

Scan Parameters

	Coverage	Scan Mode	kV	mA	AEC	Rotation Time	FOV	SliceThickness	Beam Pitch
Scan Parameters	Shoulder, Scapula, Hip, Pelvis, Entire Arm or Leg	Helical	120	300-500	No	0.5 sec	500mm	1 to 1.5mm	1

Injector Values	Contrast Needed	Contrast Volume	Saline Volume	Injection Rate
	No			

Contrast Timing	Bolus Detection	Reference Location	Trigger Value (ROI)	Delay Before Monitoring	Scan Delay After Trigger		Manual	Scan Delay

Reconstructions	Algorithm	Thin Axials	Recon Interval	Thick Axials	Sagittal	Coronal
	Std + bone	1 to 1.5mm	.8 to 1mm	2mm	2mm	2mm

Procedure note: Reconstruction with bone algorithm improves thick reconstructions for PACS, but 3D images are usually better with standard reconstruction algorithm. Oblique reconstructions made on the scanner or workstation are usually preferable to straight coronal and sagittal reconstructions, but must be individually tailored to anatomy.

CTA Protocols

Head Angio (COW)

Scan Parameters

Coverage	Scan Mode	kV	mA	AEC	Rotation Time	FOV	SliceThickness	Beam Pitch
Skull Base to Vertex	Helical	135	400-500	no	0.5 sec	240mm	.5 to .75mm	1

Injector Values

Contrast Needed	Contrast Volume	Saline Volume	Injection Rate
Yes	75-100cc	50cc	4cc/sec

Contrast Timing

Bolus Detection	Reference Location	Trigger Value (ROI)	Delay Before Monitoring	Scan Delay After Trigger
Yes	Skull Base	Visual Blush	10 secs	0

Manual	Scan Delay
Yes (O)	15-20 sec

Reconstructions

Algorithm	Thin Axials	Recon Interval	Thick Axials	Sagittal	Coronal
Standard	.5 to .75mm	.4 to .5mm	2-3mm	Optional	Optional

Arch and Carotids

Scan Parameters

Coverage	Scan Mode	kV	mA	AEC	Rotation Time	FOV	SliceThickness	Beam Pitch
Aortic Arch to Skull Base	Helical	120	300-500	Yes	.4 to .5 sec	240mm	.5 to .75mm	1.25

Injector Values

Contrast Needed	Contrast Volume	Saline Volume	Injection Rate
Yes	75-100cc	50cc	4cc/sec

Contrast Timing

Bolus Detection	Reference Location	Trigger Value (ROI)	Delay Before Monitoring	Scan Delay After Trigger
Yes	Aortic Arch	150	10	0

Manual	Scan Delay
Optional	20 sec

Reconstructions

Algorithm	Thin Axials	Recon Interval	Thick Axials	Sagittal	Coronal
Standard	.5 to .75mm	.4 to .5mm	3mm	Optional	Optional

Chest Pulmonary Embolus

Scan Parameters

Coverage	Scan Mode	kV	mA	AEC	Rotation Time	FOV	SliceThickness	Beam Pitch
Diaphragm to Apex Inferior to Superior	Helical	120	300-500	Yes	.4 to .5 sec	500mm	.5 to .75mm	1.25

Injector Values

Contrast Needed	Contrast Volume	Saline Volume	Injection Rate
Yes	100 to 125cc	50cc	4cc/sec

Contrast Timing

Bolus Detection	Reference Location	Trigger Value (ROI)	Delay Before Monitoring	Scan Delay After Trigger	Manual	Scan Delay
Yes	Pulm Artery	150	10	0	Optional	20-25 sec

Reconstructions

Algorithm	Thin Axials	Recon Interval	Thick Axials	Sagittal	Coronal
Std + Lung	1 to 1.5mm	1mm	2mm	Optional	2mm

Chest Thoracic Aorta

Scan Parameters

Coverage	Scan Mode	kV	mA	AEC	Rotation Time	FOV	SliceThickness	Beam Pitch
Apex to Below Diaphragm	Helical	120	300-500	Yes	.4 to .5 sec	500mm	.5 to .75mm	1.25

Injector Values

Contrast Needed	Contrast Volume	Saline Volume	Injection Rate
Yes	100cc	50cc	4-5cc/sec

Contrast Timing

Bolus Detection	Reference Location	Trigger Value (ROI)	Delay Before Monitoring	Scan Delay After Trigger	Manual	Scan Delay
Yes	Arch	200	10	0	Optional	20-30 sec

Reconstructions

Algorithm	Thin Axials	Recon Interval	Thick Axials	Sagittal	Coronal
Std + Lung	.5 to .75mm	.4 to .5mm	3mm	2mm (oblique)	2mm

Total Aorta (Dissection Protocol)

Scan Parameters

	Coverage	Scan Mode	kV	mA	AEC	Rotation Time	FOV	SliceThickness	Beam Pitch
Scan Parameters	Apex to Below Bifurcation	Helical	120	400-500	Yes	.4 to .5 sec	500mm	1 to 1.5mm	1.25 to 1.5

	Contrast Needed	Contrast Volume	Saline Volume	Injection Rate
Injector Values	Yes	100 to 125cc	50cc	4-5cc/sec

	Bolus Detection	Reference Location	Trigger Value (ROI)	Delay Before Monitoring	Scan Delay After Trigger	Manual	Scan Delay
Contrast Timing	Yes	Arch	200	10	0	Yes (O)	20-30 sec

	Algorithm	Thin Axials	Recon Interval	Thick Axials	Sagittal	Coronal
Reconstructions	Standard	1 to 1.5mm	1mm	3mm	2mm (oblique)	3mm

Abdominal Angio

Scan Parameters

	Coverage	Scan Mode	kV	mA	AEC	Rotation Time	FOV	SliceThickness	Beam Pitch
Scan Parameters	Diaphragm to Below Bifurcation or to Groin	Helical	120	400-500	Yes	.5 sec	500mm	.5 to .75mm	1.25

	Contrast Needed	Contrast Volume	Saline Volume	Injection Rate
Injector Values	Yes	100cc	50cc	4-5cc/sec

	Bolus Detection	Reference Location	Trigger Value (ROI)	Delay Before Monitoring	Scan Delay After Trigger	Manual	Scan Delay
Contrast Timing	Yes	Abd Aorta	200	20	0	Yes (O)	25-30 sec

	Algorithm	Thin Axials	Recon Interval	Thick Axials	Sagittal	Coronal
Reconstructions	Standard	.5 to .75mm	.4 to .5mm	3mm	Optional	Optional

Procedure note: Aneurysm and mesenteric studies should extend all the way to the femoral bifurcation. Renal studies can end below the aortic bifurcation.

Cardiac CTA

Scan Parameters

Scan Parameters

Coverage	Scan Mode	kV	mA	AEC	Rotation Time	FOV	SliceThickness	Beam Pitch
Heart	Helical	120	400-500	no	.4 to .5 sec	320mm	.5 to .75mm	0.2-0.4

Injector Values

Contrast Needed	Contrast Volume	Saline Volume	Injection Rate
Yes	125 to 150cc	50cc	4cc/sec

Contrast Timing

Bolus Detection	Reference Location	Trigger Value (ROI)	Delay Before Monitoring	Scan Delay After Trigger	Manual	Scan Delay
Yes	Ascen Aorta	150	10 secs	0	Yes (O)	20 sec

Reconstructions

Algorithm	Thin Axials	Recon Interval	Thick Axials	Sagittal	Coronal
Standard	.5 to .75mm	.4 to .5mm	2mm	Optional	Optional

Procedure note: This exam must be performed with retrospective gating. Pitch will vary depending on heart rate with a typical range of .2 to .4. Reconstructions should be made at multiple phases of the R-R inverval.

Arm Angio

Scan Parameters

Scan Parameters

Coverage	Scan Mode	kV	mA	AEC	Rotation Time	FOV	SliceThickness	Beam Pitch
Arch to Hand	Helical	120	400-500	Yes	.5 sec	500mm	1mm	1.25

Injector Values

Contrast Needed	Contrast Volume	Saline Volume	Injection Rate
Yes	125cc	50cc	3cc/sec

Contrast Timing

Bolus Detection	Reference Location	Trigger Value (ROI)	Delay Before Monitoring	Scan Delay After trigger	Manual	Scan Delay
Yes	Aortic Arch	200	15s	0	Yes (O)	25-30 sec

Reconstructions

Algorithm	Thin Axials	Recon Interval	Thick Axials	Sagittal	Coronal
Standard	1mm	1mm	3mm	Optional	Optional

Procedure note: Position arm (or both arms if Needed) over the patients head. Be sure IV is not in arm of interest. A leg or femoral IV works best for evaluation of both arms and subclavian arteries.

Aorta with Runoff

Scan Parameters

Scan 1 Parameters

Coverage	Scan Mode	kV	mA	Real EC	Rotation Time	FOV	Slice Thickness	Beam Pitch
Diaphragm to Feet	Helical	120	400-500	no	.5 sec	500mm	1 to 1.5mm	1.25

Scan 2 if Needed

Coverage	Scan Mode	kV	mA	Real EC	Rotation Time	FOV	Slice Thickness	Beam Pitch
Above Knee to Feet	Helical	120	400-500	No	.5 sec	500mm	1mm	1.25

Injector Values

Contrast Needed	Contrast Volume	Saline Volume	Injection Rate
Yes	125 to 150cc	50cc	3cc/sec

Contrast Timing

Sure Start	Reference Location	Trigger Value (ROI)	Delay Before Monitoring	Scan Delay After Trigger	Manual	Scan Delay
Yes	Femoral Artery	Visual Blush	30 secs	0	Yes (O)	40s ecs

Reconstructions

Algorithm	Thin Axials	Recon Interval	Thick Axials	Sagittal	Coronal
Standard	1 to 1.5mm	1mm	3-5mm	Optional	Optional

Procedure note: Preprogrammed second run from above knee to feet. Use realtime image reconstruction. If no contrast below knees run the second pass. If contrast present, abort second run.

Index